PhD Thesis

Observational analysis of Cometary bodies in the Solar System

Submitted in partial fulfillment of the requirements
of the degree of

Doctor of Philosophy

by

Aravind K

(Roll No. 17330008)

Under the guidance of

Prof. Shashikiran Ganesh

Astronomy and Astrophysics Division

Physical Research Laboratory, Ahmedabad, India

Department of Physics

INDIAN INSTITUTE OF TECHNOLOGY GANDHINAGAR

2022

Dedicated to my beloved Family

Declaration

I, Aravind K, declare that this written submission represents my ideas in my own words and where others' ideas or words have been included, I have adequately cited the original sources. I also declare that I have adhered to all principles of academic honesty and integrity and have not misrepresented or fabricated or falsified any idea/data/fact/source in my submission. I understand that any violation of the above will be cause for disciplinary action by the Institute and can also evoke penal action from the sources which have thus not been properly cited or from whom proper permission has not been taken when needed.

Aravind K
(Roll. No. 17330008)

Date:

Certificate

It is certified that the work contained in the thesis entitled **"Observational analysis of Cometary bodies in the Solar system"** by Mr. Aravind K (Roll no 17330008), has been carried out under my supervision and that this work has not been submitted elsewhere for any degree or diploma.

(Shashikiran Ganesh)
Thesis Supervisor
Professor
Astronomy & Astrophysics Division
Physical Research Laboratory
Unit of Department of Space, Govt. of India
Ahmedabad-380009, Gujarat, India.

Date:

Acknowledgement

PhD has been journey of ups and downs. I would like to express my sincere gratitude to all those who have contributed to the completion of this doctoral thesis. Your support, guidance, and encouragement have been invaluable throughout this journey, and I am deeply thankful for your presence in my academic life.

First and foremost, I am indebted to my supervisor, *Prof. Shashikiran Ganesh* for his unwavering support, patience, and expertise. His guidance and mentorship have been instrumental in shaping my research and enabling me to reach this milestone. I am truly grateful for his dedication and commitment. Vastness of his knowledge, be it about the sky, telescope, electronics, science or general topics, has always envied me. I have learned a lot from him for which I will always be thankful.

I extend my heartfelt appreciation to the members of my Doctoral Study Committee, *Prof. Santosh Vadawale, Dr. Aveek Sarkar,* and *Dr. S. Vijayan*. Your insightful feedback, constructive criticism, and scholarly inputs have immensely enriched the quality of this thesis. I am grateful for the time and effort you have invested in reviewing and evaluating my work over these years.

I would like to acknowledge the academic and administrative sections of PRL and IITGN, as well as the library and computer centre of PRL. Your efficient administrative support and prompt assistance have facilitated the smooth progress of my research. I am grateful for your assistance in handling the various administrative requirements and processes.

A special mention goes to the staff of the Mt. Abu observatory and the Hanle observatory/CREST, Bangalore. Your tireless efforts in providing access to resources and technical support have been crucial in my research endeavors. I appreciate your willingness to go the extra mile in assisting me whenever I needed it.

I am indebted to the office group for creating a conducive work environment. Your camaraderie, teamwork, and shared experiences have made this academic journey more enjoyable and rewarding. While senior faculty members, *Prof. Baliyan, Prof. U.C.Joshi* and *A.B.Shah* have played major roles of being mentors, colleagues, *Prashanth, Deekshya, Alka*, and *Prachi* have been really supportive throughout this journey. I am thankful to *Navpreet* and *Kumar* for being wonderful super-seniors. I am grateful to *Archita* for introducing me to the facts of observational astronomy and guiding me as a senior when and where it was required during the initial days of my PhD. I thank *Namita* for being a joyful junior with whom there have been funny moments and intellectual discussions concerning Python coding as well as scientific topics which has largely helped me tackle various problems. I am grateful to the enthusiastic researcher in Prithish, with whom I have had extensive discussions regarding cometary dust particles. I also thank my junior colleague, *Goldy* for pointing out minor mistakes/typos in the thesis as well as for the deep comet discussions which have helped me perform better in my thesis defense. Thank you all for your friendship and the moments we have shared.

Hostel life has been a major part of this journey. There are lots of memories connected with it, having spent a good amount of time in both the hostels, Navrangpura and Thaltej. I am indebted to my lobby mates/seniors, *Vishnudath* and *Nijil*, who helped me smoothly settle into the new environment. We turned our lobby into a second home with all the parties, cooking, plastic bat cricket, fast badminton rallies, etc. Hostel life during course work turned out to be a wonderful time with the company of these two and other seniors like *Manu, Bivin, Aman* etc. Time spent at thaltej hostel will remain close to my heart for the funny moments with *Ankit, Satyajeet, Abhay, Shivani* and other batchmates, Holy celebrations, New year/Christmas parties, birthday celebrations and many more. Special mention to *Subith*, who has been an integral part during this journey, having given company in the random food outings, cooking, keeping movie checklist up-to-date, first 4D movies, out of the blue intellectual discussions, and the list goes on. To my colleagues, batchmates, and seniors, I express my heartfelt gratitude. Your support have been invaluable in shaping my ideas and broadening my horizons. I am grateful for the stimulating academic environment we have fostered together.

I would also like to acknowledge the presence of my inner circle of friends, both from school and college. The circle includes *Siyam, Adarsh, Ashwin, Praneeth, Tony, Sharath, Sandeep, Sachin* from school and *Ammu, Karthik, Hebin, Maria, Snehith, Amala* from college. Your unwavering support, encouragement, and taking pride in my achievements have been essential in maintaining balance and perspective in my life. Thank you for being there for me throughout this journey.

In addition, I am grateful for the sports activities that have kept life in the institute active. The games of football, badminton, volleyball, and table tennis have not only provided a much-needed physical outlet but have also fostered a sense of community and brotherhood. The badminton games with *Vishnu, Aman, Sandeep, Priyank, Harish* etc have helped me become a better player. I am grateful to have captained an energetic football team of the Astronomy division for three years, winning the inter-division football tournament in 2023 and to be a part of the PRL football team. Times spend at Vikram nagar football ground will always be close to my heart. I am also contended to have played and learned table tennis with good sportsmen like *Subir, Naval, Yash* etc. I am thankful for the sports facilities and the opportunities they have provided for recreation and stress relief, especially during the Covid times.

Furthermore, I am deeply indebted to my mother, *Geetha* and wife, *Silpa*, who have been my pillars of support throughout this PhD journey. Their unwavering belief in me, endless encouragement, and sacrifices have been the driving force behind my perseverance. My grandmother and brother have always believed in me and have looked forward to my success. I am forever grateful for all their love, understanding, and unwavering support.

Lastly, I would like to express my appreciation to my other family members, including my in-laws, *Vani, Mahadevan, Santhi, Sabari, Uma*, cousins, *Vishnu, Vibhu*, and aunty *Jaya*, who have been incredibly supportive throughout this endeavor. A special mention to my late uncle *Nandakumar* who have always been supportive of my research. With his immense knowledge in Sankrit and Vedas, we have had long interesting deep discussions blending both Veda and modern Astronomy, which I surely miss. Everyone's love, encouragement, and understanding have provided me with the necessary strength and motivation to overcome challenges and strive for excellence.

To all teachers and mentors who have helped me throughout the journey of my life, those mentioned above and to anyone whose support I may have inadvertently omitted, please accept my heartfelt appreciation. Your contributions, in various forms, directly or indirectly have been instrumental in the successful completion of this PhD thesis. I am humbled and honored to have received the support of such remarkable individuals and institutions, and I am forever grateful for their contributions which lead to the successful completion of this highest academic degree.

Abstract

As a supplementary to the eight major planets, there are countless minor bodies, belonging to various reservoirs, that go around the Sun in various orbits. They have their own characteristic behaviour and composition. Most of the minor bodies such as the comets, which are remnants of the proto-planetary disk that formed the Solar system, are faint and inactive at a large heliocentric distance. These bodies being the remnants contain pristine material from the early protosolar nebula. Owing to the small mass and long orbital periods of comets, they would have probably undergone less internal and external evolution. Hence, they embrace information regarding the composition and thermophysical conditions that existed in the protoplanetary disk. One of the key motivations to carry out research and study different comets and their characteristics is that they can advance our understanding of the Solar system and its evolution from the protosolar nebula.

Comets have been observed to be distributed into different reservoirs. Various theories suggests that these reservoirs would have formed as a result of multiple chaotic planetary migration that occurred at different stages of the Solar system formation. A major mixing up of the material distributed in the proto-planetary disk would have occurred during these chaotic movements. Hence, the average composition of a comet family or the overall composition of an individual comet cannot be linked to a particular place or time in the proto-planetary disk. As a result, observing and analysing predominantly all the comets originating from different reservoirs is essential for having a general idea regarding the distribution of cometary material.

At far off heliocentric distances, comets behave similar to asteroids as the ambient temperature would not be high enough to sublimate the volatile materials present in the comets. Short period and Long period comets keep orbiting in their respective orbital periods while new comets are injected into the Solar system from distant reservoirs like the Kuiper belt or the Oort cloud due to some external perturbations. As these objects start moving into the inner Solar system, based on the volatile nature of the materials present, sublimation occurs, producing an envelope made up of gas and dust, which is called the coma of the comet. It is at the onset of this phenomenon, comets are said to be active and hence become detectable. The observed coma is made up of material rising from the cometary nucleus, which formed at the initial stages of the Solar system. This makes comets a potential ticket to understand the history of the Solar system. Likewise, Interstellar comets, which were once part of another stellar system is a prospective messenger to understand and compare the composition of those systems with that of ours. Such comparisons can further help in confirming whether the formation of our Solar system was unique or general.

There are different aspects of a comet that needs to be studied. This includes the gaseous/dust activity and composition. The coma morphology can also speak for itself regarding the jet activity occurring within the coma. Therefore, the current work is intended in having a wide scale analysis of comets by examining the comets characteristics in different aspects. The gas activity/composition is studied by analysing the cometary emission spectra via low or high resolution spectroscopy. Dust activity/characteristics can be probed via imaging/spectroscopy and polarimetry, while the coma morphology and jet structures is studied by imaging the comet in various filters. The optical spectroscopic, polarimetric and imaging studies are carried out using the 1.2 m and 2 m telescopes at Mount Abu Infra-red Observatory and Indian Astronomical Observatory respectively.

In this work, a total of 22 comets, 10 Short Period Comets, 11 Long Period Comets and 1 Interstellar comet have been observed and studied. Out of these, all 22 of them have been studied via low resolution spectroscopy, 4 comets in high resolution spectroscopy and 5 comets by means of polarimetric observations. Low resolution spectroscopy has been used to analyse the relative abundance of various molecular emissions and Afρ profiles corresponding to different filter bands, while high resolution spectroscopy was employed to probe and separate the different blended emissions. High resolution was also effective in identifying the emission lines within each molecular bands and in investigating the forbidden Oxygen lines as well different bands of NH_2. Optical imaging and polarimetry were carried out to analyse the coma morphology and to evaluate the variation in degree of polarisation with phase angles for different comets, respectively.

The thesis commences with a basic introduction to the structure of the Solar system. The various major cometary reservoirs, their interconnection, classification of comets based on different criteria and the theories explaining the role of planetary migrations on the formation of these reservoirs have been briefly explained. A brief introduction to comets, including details regarding their activity, volatile composition, optical spectrum and detected species, dust properties, etc is provided. The roadmap of speculations related to the existence of the Interstellar comets alongside the presence of exocomets have been briefed.

Comet 156P/Russell-LINEAR was analysed with spectroscopic, polarimetric and imaging techniques to have a wider understanding of the comet's characteristics. Comets 46P/Wirtanen and C/2017 T2 (PANSTARRS) were observed extensively in low resolution spectroscopy to examine the fluctuations in the comet's activity along its orbit. The great comets of 2020 and 2021, C/2020 F3 (NEOWISE) and C/2021 A1 (Leonard), respectively, a peculiar Short Period Comet 29P/Schwassmann–Wachmann, interesting activity in comet 88P/Howell and many other interesting comets have been studied in optical spectroscopy and their activities have been examined and discussed. A few comets, including 46P, were observed in high resolution spectroscopy and different aspects of emission lines have been analysed. Once in a lifetime appearance of an Interstellar comet, 2I/Borisov, was observed in low resolution spectroscopy to report its pre and post perihelion activity to point at a possible heterogeneous nucleus of the comet. Imaging techniques were also employed to obtain the rough estimate of the comet's nucleus size.

Results obtained from each individual analysis have been discussed in their respective chapters and all the obtained results have been put together to achieve a collective understanding. This work demonstrates the importance of observing all possible cometary bodies and the advantage of simultaneously employing different observational techniques to analyse the characteristics of a comet. This work also exemplifies the significance of a common cometary database systematically updated with latest observational results, which can be later used for modelling and for cometary classification purpose.

List of Publications

Peer - Reviewed Journals

1. **Aravind, K.**, Ganesh, S., Venkataramani, K., et al. 2021, Activity of the first interstellar comet 2I/Borisov around perihelion: results from Indian observatories, MNRAS, 502, 3491.
   DOI: 10.1093/mnras/stab084

2. **Aravind, K.**, Halder, P., Ganesh, S., et al. 2022, Optical observations and dust modelling of comet 156P/Russell-LINEAR, Icarus, 383, 115042.
   DOI: 10.1016/j.icarus.2022.115042

3. **Aravind, K.**, Ganesh, S., et al., High resolution spectroscopy of comets using Hanle Echelle Spectrograph (HESP). Submitted to MNRAS.

Peer - Reviewed Journals - Not part of thesis

4. Bhatt M., W "ohler C., Rogall J., **Aravind K.**, Ganesh S., Bharadwaj A., 2023, *"Unique regolith characteristics of the Reiner Gamma swirl as revealed by imaging polarimetry at large phase angles"*, A&A.
   DOI: 10.1051/0004-6361/202245356

Astronomical Telegrams

5. **Krishnakumar, A.**, Angchuk, D., Venkataramani, K., et al. 2020, CN, C2, C3 production rates of Comet C/2020 F3 (NEOWISE) as observed from Himalayan Chandra Telescope, Hanle, India, The Astronomer's Telegram, 13897, 1

Conference Proceedings (Refereed)

6. Ganesh, S., **Krishnakumar, A.**, Venkataramani, K., et al. 2019, Solar system studies with the Indo-Belgian telescopes, Bulletin de la Societe Royale des Sciences de Liege, 88, 65

7. Ganesh, S., Rai, A., **Aravind, K.**, et al. 2020, in Society of Photo-Optical Instrumentation Engineers (SPIE) Conference Series, Vol. 11447, Society of Photo-Optical Instrumentation Engineers (SPIE) Conference Series, 114479E

Conference presentations (Posters)

1. **IPSC 2021** - Spectroscopy,polarization and dust modelling of short period comet 156P/Russel-Linear - Aravind.K et al

2. **RAS 2020** - *Spectroscopic and Imaging study of first Interstellar comet 2I/Borisov from two Indian Observatories* - Aravind.K et al

3. **ASI 2022** - Optical polarimetric study of cometary dust - Aravind.K et al

4. **LPSC 2021** - Regolith characteristics of the Reiner Gamma swirl as revealed by the polarimetric observations. - M. Bhatt, C. Wöhler, **Aravind K.**, S. Ganesh, A. Bhardwaj

Oral Presentations

Division Seminar

1. **Topic :** Evolution of the Solar System and the Importance of studies of the Minor Bodies
   Date : 25^{th} July 2019.

2. **Topic :** The case for Interstellar comets/Asteroid; Part I - Speculations and Conclusions
   Date : 17^{th} July 2020.

3. **Topic :** The case for Interstellar comets/Asteroids ; Part II - Detection and Analysis of first IS visitors
   Date : 28^{th} July 2020.

4. **Topic :** Spectroscopy, polarization and dust modelling of short period comet 156P/Russell-LINEAR
   Date : 29^{th} April 2021.

5. **Topic :** Scope of high resolution spectroscopy in cometary studies
   Date : 3^{rd} March 2022.

Other talks

6. Attended an International school , **IFAS5 - 5th Indo-French Astronomy School - Spectroscopy and Spectrograph**, held in IUCAA, Pune from August 16 - 24 2019.

7. **ASI 2020 :** Delivered a talk titled 'Contrasting behaviour of two Jupiter family comets' at the 38^{th} Meeting of the Astronomical Society of India held at IISER Tirupati, between 13^{th} - 17^{th} February 2020 **(Offline)**.

8. **ICDA 2020 :** Delivered a talk titled 'Spectroscopic and Imaging study of the first interstellar comet 2I/Borisov' at the International Conference on Dust in Astrophysics held at Assam University, between 31^{st} August - 1^{st} September 2020 **(Online)**.

9. Invited to deliver a talk on the 'Minor bodies in the Solar system' by the Department of Physics, School of Applied Sciences, REVA University, Bangalore, during the occasion of 'World Asteroid Day 2021' on June 30, 2021.

Contents

List of Figures

List of Tables

List of Abbreviations

MIRO	Mt. Abu Infrared Observatory
HCT	Himalayan Chandra Telescope
SPC	Short Period Comet
JFC	Jupiter Family Comet
LPC	Long Period Comet
HTC	Halley Type Comet
OCC	Oort Cloud Comet
LCHC	Long Chain HydroCarbons
LISA	Long slit Intermediate resolution Spectrograph for Astronomy
HFOSC	Hanle Faint Object Spectrograph & Camera
EMCCD	Electron Multiplying Charge Coupled Device
EMPOL	EMCCD based Polarimeter
HESP	Hanle Echelle Spectrograph
IRAF	Image Reduction and Analysis Facility
IHW	International Halley Watch
HA	Hierarchical Aggregates
OPR	Ortho-to-Para Ratio
G/R	Green-to-Red Doublet

Chapter 1

Introduction

"What we know is a drop, what we don't know is an ocean"

- Sir Isaac Newton

Comets have puzzled and fascinated the common man for a very long time. They were something to be feared for the primitive man, while they have turned out to be an attraction to the stargazers in recent times. From early times, the appearance of a comet has been considered to be a bad omen causing disasters, calamities and tragedies since they cause disturbance in the harmony of a usually starry sky. Aristotle (384 to 322 B.C.) believed the Earth's atmosphere to be source of these sightings. It was in the sixteenth century when the understanding regarding these 'mighty' celestial objects started to improve. It all started with Petrus Apianus who observed a Great comet in 1531 and realised that a comet's tail always pointed away from the Sun. Later in 1577 AD, it was the Danish astronomer Tycho Brahe who used accurate measurements to observe the Great comet of 1577 from various locations and determined from its parallax that the object was farther than the Moon. This marked the beginning of the understanding that comets were not just effects of the atmosphere, but individual celestial bodies.

Edmond Halley, after whom the Halley's comet is named, was the great English astronomer who proved that comets are part of the Solar system. His journey to understand the nature of comets started with the observation of the Great comet of 1680 (Kirch) followed by a bright comet in 1682 (Halley). Halley computed the orbits of a dozen comets with the help of Newtonian mechanics (Festou et al., 1993). To his surprise, the orbit of a comet appearance in 1531,1607 and 1682 had similar parameters. This led him to believe that this particular comet had a periodic orbit of $\sim$76 years and predicted that the same comet would return in 1758. Though Halley died in 1742, his prediction was proved right when the comet was recovered by Johann Palitzsch in 1758. Along with the proof of the periodic nature of the comet, this also helped in identifying the comet mentioned in ancient records until 240 BC.

Even though large number of comets had been observed and documented in the past, nobody knew what these objects were made of until Giovanni Donati (Donati, 1866) and Sir William Huggins (Huggins, 1868) performed the spectroscopic study of a comet. On visual comparison of the comet spectrum with that of a flame spectrum, the presence of the currently known "carbon bands" were found to be similar. These bands were later observed in all the comets which led to the understanding that carbon was an important constituent of comets (Festou et al., 1993). By this time (late 1860s) spectroscopy was recognised as a standard technique to study the light coming from the comets. This led to the discovery of new emissions at an increasing rate. Cyanogen (CN) was first discovered in comet C/1881 K1 and it was again observed in comet Halley in the apparition of 1910. The disclosure of the presence of CN in comets caused panic as people feared that they would be affected by the poison when the Earth passed through the tail of the comet Halley in 1910. Schwarzschild & Kron (1911) found out that fluorescence, absorption of Solar light and re-emission, could explain the emission from the comet during 1910 passage of Halley's comet. Even though molecules like CN, C_2, CH were identified by comparison with laboratory emissions, it was not understood why the violet CN bands observed in a comet spectrum did not appear like those seen in the laboratory spectrum. More interestingly, the peak intensity of the CN band also shifted slightly with heliocentric distance. (Swings, 1941) proposed that this phenomenon would be due to the variation in the number of CN molecule excited by certain specific transition caused by the crowding of absorption lines in the Solar spectrum. The location of these absorption lines is majorly affected by the comet's radial velocity with respect to the Sun. This is why the CN band of two comets at the same heliocentric distance would still be different due to the difference in their radial velocities. The long standing problem of this CN behaviour was hence solved and the phenomenon was named as *"Swings effect"*. All this while, the λ4050Å group remained unknown until Douglas (1951) produced the group in a laboratory experiment and assigned it to the linear triatomic carbon molecule, C_3. Cochran & Cochran (2002) provides a brief idea regarding the main emissions CN, C_2 and C_3 found in comets in the optical wavelength. Yamamoto (1981) have explained in detail the photochemical formation of CN, C_2 and C_3 radicals in the cometary coma and Weiler (2012) later revisited the formation mechanism of C_2 and C_3.

Extensive works were carried out in the period of 1930's and 1940's by Karl Wurm and Polydor Swings in understanding the spectra of the comets and their physical chemistry (eg., Wurm, 1939; Swings, 1942; Swings et al., 1943; Swings, 1943; Swings & Struve, 1943; Festou et al., 1993). As a result, the presence of chemically unstable radicals and ions like CN, C_2, CO^+, CH, N_2^+ etc in comet spectra were invoked to be the result of the photo chemistry (photo dissociation and photo ionisation) of a set of *parent molecules* thought to be residing in the nucleus inside the coma. Even though Swings was close enough to propose an *icy model* to suggest the presence of a nucleus where these parent molecules existed in solid state, the nature of the nucleus remained a speculation until the end of 1940's (Festou et al., 1993).

The next breakthrough in understanding the nature of comets came after 1950 when Lyttleton and F. Whipple tried to understand the structure of cometary nuclei and Jan Hendrik Oort proposed the existence of a comet reservoir by studying the kinematics of these objects (Oort, 1950). Lyttleton (1951) proposed that most of the comets did not posses a distinct nucleus, but was a loose swarm of ice and dust. He believed it was this collection of ice and dust responsible for the tail and coma as the comet came close to the Sun. But, to explain the periodic orbital nature of comet Encke, whose return was predicted successfully (after Halley) by Johann F. Encke in 1822, F. Whipple put forward a model, *icy conglomerate*, with the idea that the comet's nucleus was made up of water ice and dust and coined the term "dirty snowball" (Whipple, 1950). Even though there were numerous logical and observational evidences to support the latter model, the Whipple model of cometary nuclei was not confirmed until a spacecraft visited the Halley's comet in 1986.

After the Oort cloud model was proposed by Oort (1950) various theories emerged to explain the formation of our Solar system and different comet reservoirs (see Section 1.1 for details). Eventually, cometary science gained popularity among the astronomers since comets were understood to be the relics of the early Solar system. Analysing the composition and behaviour of these objects helps us gain knowledge regarding the thermo-chemical and physical conditions of the region in the proto-Solar nebula where they were formed (de Pater & Lissauer, 2015). In a way, comets turned out to be the tickets to the past of the Solar system. Intensive observations were carried out on all observable comets in an attempt to classify them based on composition. A'Hearn et al. (1995) had observed 85 comets using the International Halley Watch (IHW) narrow band comet filters (A'Hearn et al., 1984b, and references therein) and classified them based on their carbon abundances. Later on, various other extensive studies of comets have been carried out on an objective to refine our understanding of the distribution of comets based on composition and the reason behind it (eg., Cochran et al., 1992; Fink, 2009; Cochran et al., 2012; Langland-Shula & Smith, 2011, etc).

"Gathering physical data on as wide a sample of comets as possible is very important in understanding the formation of the Solar system" - Michael F. A'Hearn

1.1 Structure of the Solar system

As a supplementary to the eight major planets, there are countless minor bodies, belonging to various reservoirs, that go around the Sun in various orbits (see Figures 1.1, 1.2 and 1.3). They have their own characteristic behaviour and composition. The current defined orbits of planets and minor bodies as well as the different reservoirs have formed as a result of the evolution of the Solar system to the stage we currently know. The following subsections will discuss in brief the different models regarding the formation of planets, their effect on the planetesimal population present in the protoplanetary disk and the various cometary reservoirs present in the Solar system.

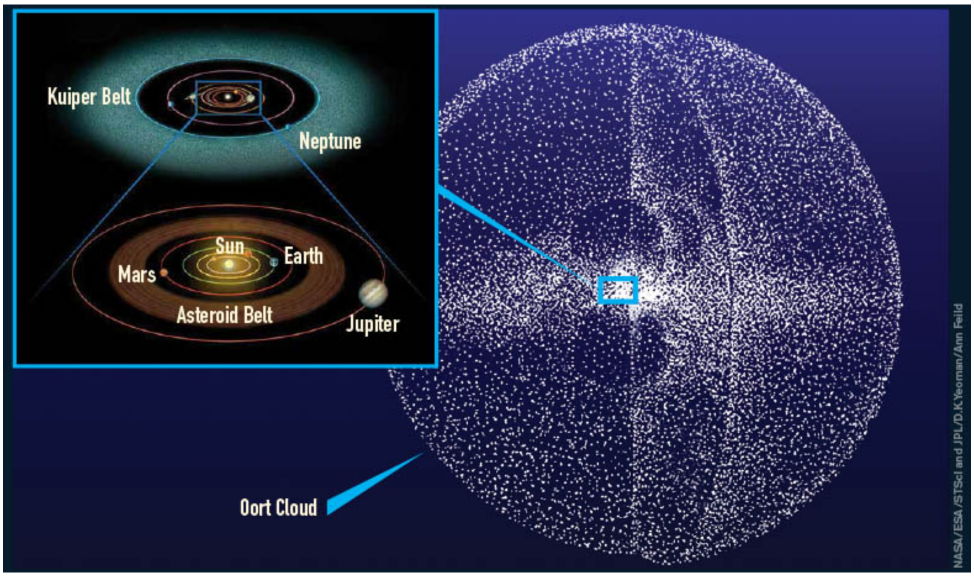

Figure 1.1: Overall structure of the Solar system. *Image credit: NASA*

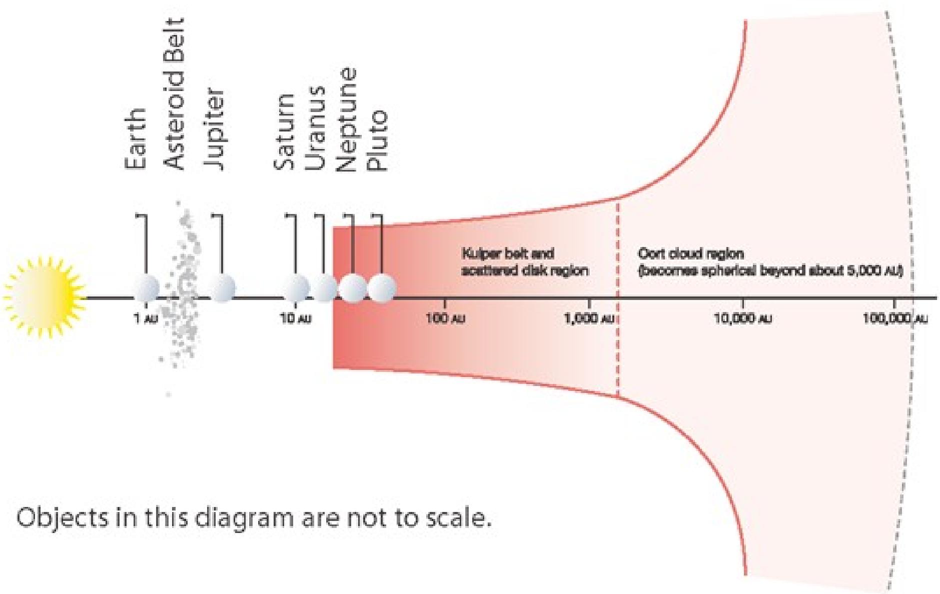

Figure 1.2: Detailed structure of the Solar system.*Image credit: Stern (2003)*

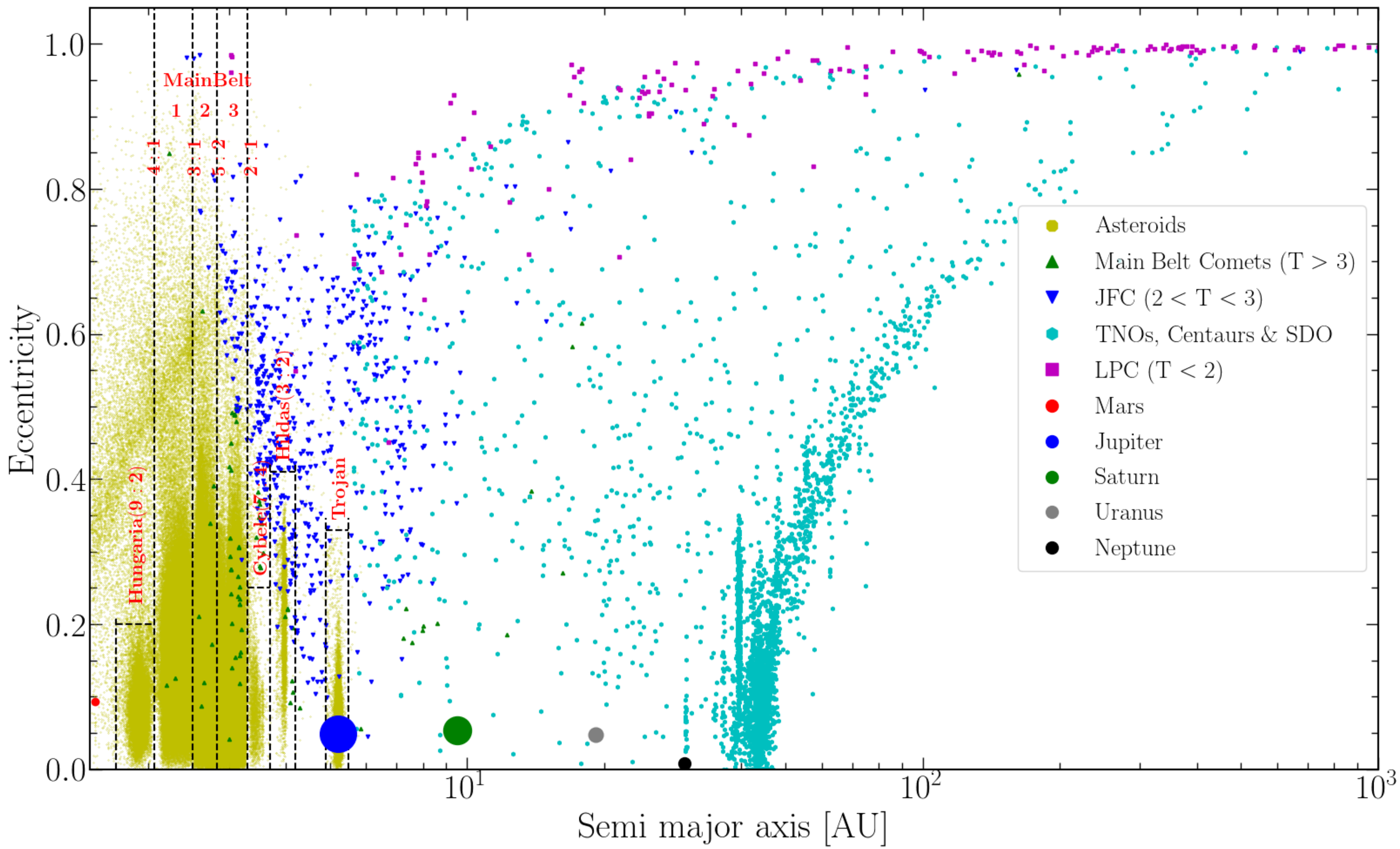

Figure 1.3: Minor body population in the Solar system: Plot by the author using data from the Minor Planet Centre - 2022

1.1.1 Comet Reservoirs

"From chaos, comes order"

Over the years of cometary observations, it was clear that there were different types of comet based on the orbital dynamics. The difference in orbits would be directly related to the origin of the comet in the current structure of the Solar system. From the study of a large set of comets, scientists confirmed that it is not assured that comets originating from a particular region of the Solar system should have similar composition. From this, it is clear that there should have been some large scale phenomenon which occurred in the initial stages of Solar system which caused such a mixing up. Planetary migration was one such major event that can explain the currently observed distribution of cometary bodies (see Section 1.1.2 for more details). Such a process would have every time created a large scale chaos by mixing up the planetesimal population present in the disk or throwing them away to a very large distance. Along with the planets getting settled into their currently observed orbits, the once scattered planetesimals (comets being referred) also came to order by getting sorted into different reservoirs namely Oort cloud (OC), Kuiper Belt (KB) and Jupiter Family Comets (JFC) (see Figures 1.1 and 1.2).

Comets are majorly classified into two groups based on their orbital period, Short Period Comets (SPC, P $<$ 200 years) and Long Period Comets (LPC, P $>$ 200 years). This margin of 200 years to separate SPC and LPC population is just a wisely chosen boundary to distinguish between comets that would have been observed multiple times from those that would have had only a single passage in the observational history of Astronomy, even though there are exceptions (comet 153P/Ikeya-Zhang (Hasegawa & Nakano, 2003)). The SPC family is further divided into JFC (P $<$ 20 years) and Halley Type Comets (HTC; 20 $<$ P $<$ 200 years) and the LPC family represent comets with orbital period greater than 200 years consisting of those which would have made multiple passages into the inner Solar system along with those making their first visit (generally called Oort Cloud Comets; OCC). But, such a classification simply based on orbital period was not robust enough which called for the introduction of another parameter known as the Tisserand's parameter.

1.1.1.1 Tisserand parameter

The orbits of comets can eventually evolve due to interactions with giant planets. Hence, classifying them based on their orbital period was not a robust method. As a result, Tisserand (1889) developed a parameter called the Tisserand's parameter to better distinguish the different classes of comets. Equation 1.1 is used to define the parameter, where a, e and i are semi-major axis, eccentricity and inclination of orbit of the body for which the parameter is being defined.

$$T_P = \frac{a_P}{a} + 2\left[(1-e^2)\frac{a}{a_P}\right]^{1/2}\cos(i) \tag{1.1}$$

A subscript P for a and T stands for the name of the perturbing planet in the system. Hence in the Solar System, Jupiter being the biggest and most influential of the planets, the above equation is written as:,

$$T_J = \frac{a_J}{a} + 2\left[(1-e^2)\frac{a}{a_J}\right]^{1/2}\cos(i) \tag{1.2}$$

where a_J represents the semi major axis of Jupiter's orbit.
With the help of these parameters and the current knowledge of comet population, Levison (1996) redefined the classification of comets as follows:

- JFC - 2 $<$ T$_J$ $<$ 3; a $<$ 7.35 AU & P $<$ 20 years.
- HTC - T$_J$ $<$ 2; q $>$ 0.01; a $<$ 34.2 AU & P $<$ 200 years.
- LPC - T$_J$ $<$ 2; q $>$ 0.01; 34.2 $<$ a $<$ 10,000 AU & P $>$ 200 years.
- OCC - T$_J$ $<$ 2; q $>$ 0.01; a $>$ 10,000 AU.

According to this classification, comets with T$_J$ $>$ 2 are known as Ecliptic Comets (EC) (majorly JFC) as their orbital inclination is more or less confined to the ecliptic plane and those with T$_J$ $<$ 2 are known as Nearly Isotropic Comets (NIC) (HTC, LPC and OCC), since their observed orbital inclinations are seen to be completely random

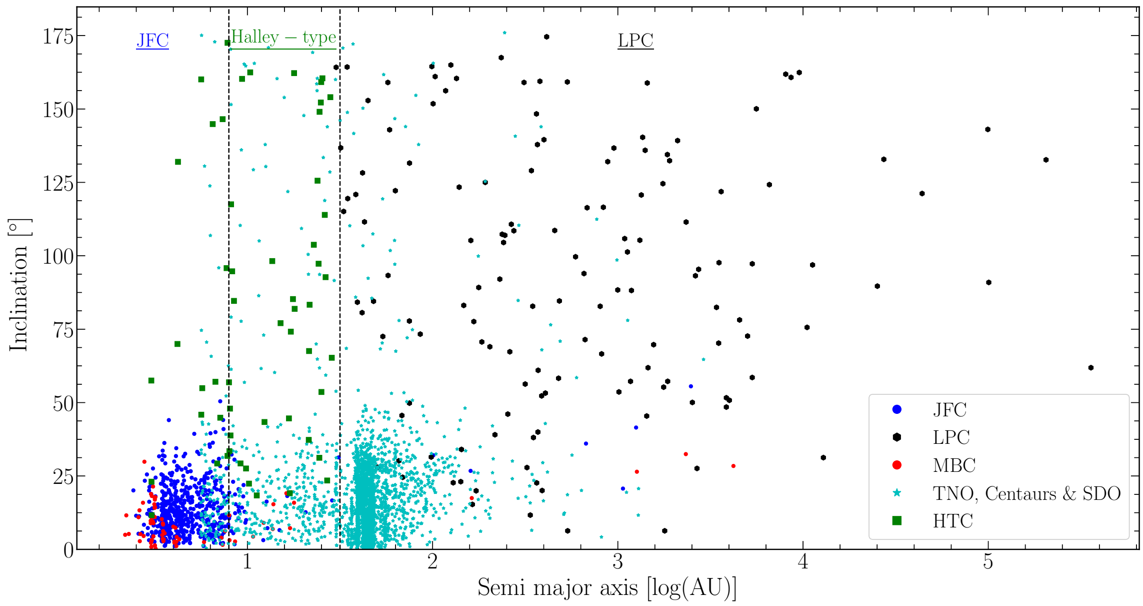

Figure 1.4: Family of comets: Plot by the author using data from the Minor Planet Centre - 2022

(see Figure.1.4). Certain other smaller families of comets, Encke type ($T_J > 3$, $a < a_J$), Centaurs/Chiron type ($T_J > 3$, $a > a_J$) also falls under the NIC category. The advantage of accepting this parameter as the base of classification is that the value of T_J remains a constant even if the orbit of the comet evolves over time to fall under a different class according to the orbital period classification. Such an example is the comet 96P/Machholz which was formerly considered a JFC due to an orbital period of 5.92 years and is now classified as an HTC as its T_J = 1.942 (Levison, 1996). The following sections describe in brief the 2 main reservoirs of comets, Oort cloud and the Scattered disk (including the Kuiper belt).

1.1.1.2 Oort cloud

Once the rate of comet detection had increased significantly, Jan Oort observed that a greater fraction of the comets were possessing large semi-major axis, $a > 10^4$ AU. In order to confirm this pattern, on plotting the histogram of the inverse of semi-major axis, as shown in Figure.1.5, he noticed a peak very close to $1/a < 5{\times}10^{-4}$ AU^{-1} implying a large number of comets originating from a population of comets lying far away from the Sun. In contrast to the other observed comets whose orbital inclination is confined to the ecliptic plane, this group of comets possessed random isotropic inclinations. This persuade him to propose the presence of a spherical shell made of cometary population with about 10^{11} comets surrounding the Solar system at a distance of 20,000–150,000 AU (Oort, 1950). This hypothetical spherical cloud of comets surrounding the Solar system is now called the Oort Cloud. The portion of the materials that were thrown out from the plane of the disk, by the giant planets, at high eccentricities, during the initial chaotic phase of evolution of the solar system (Brasser & Morbidelli, 2013) would have settled into a spherical shell surrounding the Solar system due to the gravitational influence of passing stars and galactic tides (Stern & Weissman, 2001). Fouchard et al. (2006) pointed out that the comets belonging to this reservoirs have been orbiting at these distances for about the age of the Solar system and it is when an external force acts upon it that these comets starts travelling to the inner Solar system to be detected. The external forces that can cause the comets belonging to OC to start towards the inner Solar system are either passing stars (Weissman, 1980; Hills, 1981) or galactic tide (Heisler & Tremaine, 1986; Delsemme, 1987; Levison et al., 2001b). Heisler & Tremaine (1986) and Levison et al. (2001b) mention that the 'new comets' on their first passage into inner Solar system would have evolved from the OC at distance beyond 20,000 AU since galactic tides are strong enough to change their perihelion from about $q>30$ AU to $q<1.5$ AU in a single orbit to jump across Jupiter and Saturn and not undergo perturbation. At the same time, comets interior to 10,000 AU would rarely make it directly into the inner Solar system, rather slowly leak into the domain of the giant planets having multiple passages beyond $\sim$5 AU and getting decoupled from the OC (Wang & Brasser, 2014). They are generally referred to as LPC and a subset of these comets which eventually fall into orbits with orbital period within 200 years are known as Halley Type Comet, named after the first known periodic comet 1P/Halley.

Halley Type Comets: Comets possessing a semi major axis in the range of 8 and 35 AU are referred to as HTCs. They are observed to have an orbital period between 20 and 200 years. Owing to their short orbital period, they were initially thought to originate from the Kuiper belt or Scattered Disk. This argument could not stand long enough due to the dispersion observed in the orbital inclination of the HTCs. KB and SDO were not able to account for the kind of nearly isotropic inclinations observed in

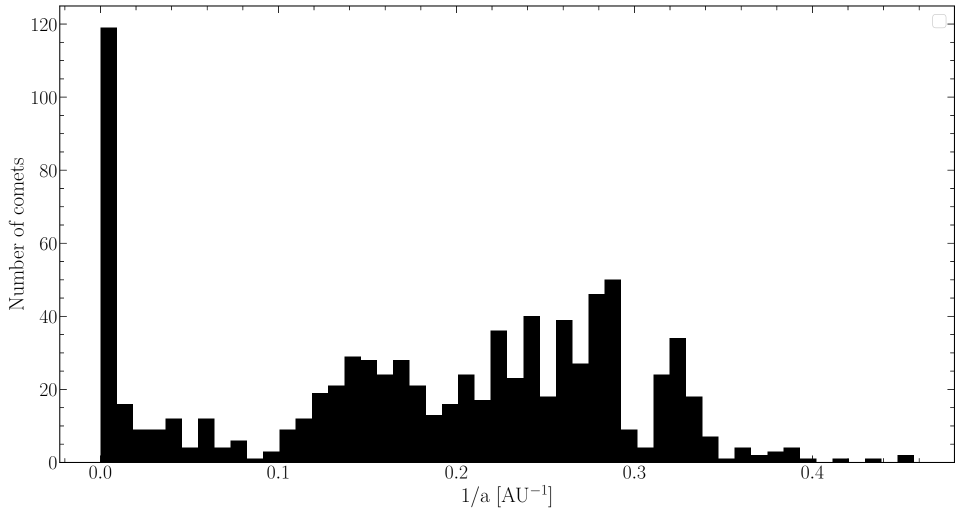

Figure 1.5: Histogram of the inverse of semi major axis of all the observed comets: Plot by the author using data from the Minor Planet Centre - 2022

these comets. This is when an explanation of an inner Oort cloud being a source of the HTCs came into existence (Wang & Brasser, 2014; Levison et al., 2001b; Morbidelli, 2005; van der Helm & Jeffers, 2012; Levison & Duncan, 1997a; Nesvorný et al., 2017). Hence, over the years, HTCs have been considered to be an extension of the returning long period comets once part of the Oort cloud to a short orbital period. Thus, HTCs acts as short cuts to probe the Oort cloud composition, atleast more than once, which is rather impossible during the human lifetime in the case of the other returning LPCs or new OCCs.

1.1.1.3 Kuiper Belt and Scattered Disk

Since the discovery of Pluto, Chiron and Albion in 1930, 1978 and 1992 respectively, the theory about the existence of a circumstellar disk outside the orbit of Neptune extending from about 30 AU to 50 AU having a nearly circular orbit with eccentricity as low as 0.1-0.2 is well established (Nesvorný et al., 2017; Morbidelli, 2005; Levison & Duncan, 1997a). This disk consists of objects belonging to a thick disk extending as far as ten degrees above the ecliptic plane, known as 'dynamically cold', and a more diffused population with inclinations varying till thirty degrees, known as 'dynamically hot'. Stephens & Noll (2006) observed that the dynamically cold and hot population in the KB differed in orbits as well as the colour and albedo, with the former being redder and brighter. Morbidelli (2005) pointed out that this distinction would be due to a difference in formation location with the cold population forming around the current region and hot population forming in the inner region to be scattered away by Neptune as it migrates into the Kuiper belt region (See Section.1.1.2.1).

Similarly, the existence of another class of objects called the Scattered Disk Objects (SDO) having an eccentricity as high as 0.8 extending from about 50 AU - 1000 AU was discovered (Luu et al., 1997). Both KBO and SDO together are known as the Trans-Neptunian Objects (TNOs). As per Grand Tack model (See Section.1.1.2.2), the outer disk planetesimals were pushed out as Uranus and Neptune moved out along with Jupiter till the depletion of planetesimal disk forming a thick disk spanning from about 16 AU to 35 AU. In the later stage, according to Nice model (See Section.1.1.2.1), as Neptune crossed Uranus orbit and penetrated into this planetesimal disk during the 1:2 resonance of Jupiter and Saturn, it would have scattered the inner disk population to form the major part of the dynamically hot KBO and the SDO (Levison & Morbidelli, 2003a,b; Stern & Colwell, 1997). The short period comets, Jupiter Family, are thought to have originated from this part of the Solar system due to its ecliptic nature.

Jupiter Family Comets: The KB was initially thought to be the source of the JFCs since a disk like structured source was a prerequisite owing to the average low orbital inclination and the absence of retrograde orbits of these comets (Morbidelli, 2005). After the discovery of SDO, they were considered a more probable source of JFC due to their unstable nature with higher eccentricity, compared to KB objects, making it possible for them to get scattered as they approach Neptune during perihelion (Levison & Duncan, 1997a; Nesvorný et al., 2017; Jewitt & Luu, 1997; Morbidelli, 2005). Cochran et al. (1995), Jewitt & Luu (1997) and Rickman (2010) had proposed a theory where the KBO were replenishing the JFCs by leaking through the Centaur population (Horner et al., 2004) which was later supported by Seligman et al. (2022). As seen from Figure.1.4, there is a clear bridge between the TNOs and the JFCs which could explain the theory mentioned above. Even though the major characteristics of a JFC is its low inclination and low orbital period, few comets classified as JFC are observed to have an orbital period P<20 with high inclination. These objects could be a part of the low period extension of the NICs (Nesvorný et al., 2017).

1.1.2 Planet migration

As mentioned in Section.1.1.1, scientists have been trying to connect planetary migrations with the formation of cometary reservoirs. Alongside, many theories have been developing to explain the clues regarding a possible 'Late Heavy Bombardment' (LHB) of planetesimals on the terrestrial planets and moon about 800 myr after the formation of the Solar system (Cohen et al., 2000). Levison et al. (2001a) tried explaining this phenomenon in connection to the formation of Uranus and Neptune. Based on these assumptions and modelling, a model named 'Nice model' (Gomes et al., 2005) was proposed to explain the current orbits of the planets along with the reason for the LHB and formation of various comet reservoirs (see Section 1.1.1). This model was further refined by Morbidelli et al. (2007) to address certain shortcomings in the previous model. Tsiganis et al. (2005) also proposed a theory to explain the current final semi major axis, eccentricities and mutual inclinations of the giant planets.
Another ambiguity related to the Solar system formation models was the low mass of Mars (Jin et al., 2008). Various assumptions and theories popped up trying to explain this ambiguity as a result of the rapid formation of Jupiter followed by Saturn, giant planet migration and the mean motion resonance between the two giant planets (eg., Montmerle et al., 2006; Masset & Snellgrove, 2001; Morbidelli & Crida, 2007). All of these theories were taken into consideration to fabricate a single model, the 'Grand Tack model' (Walsh et al., 2011), to explain the low mass of Mars, depletion of mass in asteroid belt, triggering the formation of various reservoirs etc. The following subsections will explain in brief the two models, Nice and Grand Tack, to point out the outcomes and difference in the time scale of the evolution of Solar system considered in them.

1.1.2.1 Nice model

In order to explain the currently observed orbits of the giant planets, presence of the Jupiter trojans (Morbidelli et al., 2005) and irregular satellites of Saturn, Uranus and Neptune, Gomes et al. (2005) and Tsiganis et al. (2005) proposed different models which talks about a later stage after the formation of the Solar system. In both the models, the orbits of Neptune and Uranus are considered to be flipped from what is observed now (latter one being the outer planet) followed by a massive planetesimal disk extending from about 1.5 AU outside the outer planet till about 30-35 AU. These model considers the end of the gas-disk phase where the fully evolved giant planets were placed in a tight configuration (Jupiter$\sim$5.45 AU, Saturn$\sim$8.18-8.65 AU, Neptune$\sim$11.5 and Uranus$\sim$14.2). Morbidelli et al. (2007) points out that the location of the icy giants (Neptune and Uranus) should have been much closer to the Sun than what is mentioned in the initial models. The interaction of the giant planets with the planetesimal disk would have forced them into a Mean Motion Resonance (MMR) causing a global instability. Both Gomes et al. (2005) and Tsiganis et al. (2005) points out that Jupiter and Saturn would have gone into a 1:2 MMR causing a large instability in the disk due to their increased eccentricities, similar to what is observed now, which forced Neptune to cross the orbit of Uranus with both ice giants penetrating into the massive planetesimal disk creating a chaos. Once the planetesimal disk was depleted, the planet migration stopped and settled into nearly circular orbit with orbital parameters similar to what is observed currently. While both theories are good enough in explaining the current observed orbits of the giant planets as well as the presence of Jupiter Trojans, Nice model (Gomes et al., 2005) is more successful in explaining the LHB which had occurred $\sim$700 myr after the formation of the Solar system. These models are also successful in explaining the mechanism by which the planetesimals present in the disk were distributed to different reservoirs.

1.1.2.2 Grand Tack model

A long-standing question was the anomaly in the observed low mass of Mars. In a standard Solar system formation without any planetary migration, Mars would have acquired more mass owing to the amount of material that was available at the location. Walsh et al. (2011) was successful in explaining this ambiguity by incorporating the rapid formation and migration of both Jupiter and Saturn during the initial stage of Solar system formation. In this model it is considered that only Jupiter was fully grown with Saturn, Uranus, Neptune in their growing phase and terrestrial planets were not formed. They pointed out that Jupiter started forming at around 3.5 AU,

just beyond the snow-line (Ciesla & Cuzzi, 2006), owing to perfect location for giant planet formation. Pollack et al. (1996) explained the three phases of formation for giant planets through which they initially form a massive core (20–30 $M_{\oplus}$) and undergo an exponential increase in mass to reach hundreds of Earth masses via the 'runaway' phase. The core of Saturn (30 $M_{\oplus}$) initially located at $\sim$4.5 AU keeps growing to 50 $M_{\oplus}$ while Jupiter was slowly migrating inwards till 1.5 AU through the Type-II migration (Lin & Papaloizou, 1986). Once Saturn reaches 50 $M_{\oplus}$, it starts migrating inwards, faster than Jupiter to fall into a 2:3 resonance with Jupiter (Masset & Snellgrove, 2001). The resonance causes a reverse in the direction of migration and the giant planets starts moving outwards along with Uranus and Neptune until Jupiter reaches 5.4 AU, as the migration decreases exponentially when the gas disk dissipates.
The migration of Jupiter to 1.5 AU truncated the inner planetesimal disk to 1 AU where the terrestrial planets formed later. The intrusion of Jupiter towards the Sun reduced the material available for the Mars planet embryo to grow, resulting in its low mass. While the inward and outward migration of the giant planets caused enormous mixing up of the S-type (volatile poor) and C-type (volatile rich) asteroids which were initially present before Jupiter (0.3–3 AU) and between the giant planets respectively, it pushed away the outer disk planetesimals initially present between 8–13 AU. Ultimately only a very small fraction of the initial asteroid belt was left after the giant planet migration and terrestrial planet formation. The rest of the planetesimals belonging to the S-type and C-type would have been either ejected out of the Solar system or distributed into the Oort cloud and the massive disk present outside Neptune.

Dones et al. (2015) proposes that the planetary dynamics explained in both Grand Tack model and Nice model would have been equally responsible for the creation of the different reservoirs, mainly Oort cloud. Morbidelli (2005) also states that Oort cloud should have formed in two stages, first during the formation of Giant planets and second during the period of LHB. The planetary migrations and formation of cometary reservoirs are still being studied to understand the detailed processes which would have caused the ordered distribution of minor bodies in the Solar system.

1.2 A brief introduction to comets

Most of the minor bodies such as the comets are faint and inactive at a large heliocentric distance. Hence, they are difficult to be distinguished from an asteroid unless they move closer to the Sun causing the ice present in the nucleus to sublimate forming a coma. As a consequence, the basic point of difference between an asteroid and a comet is the presence of a coma in comets. Comets spend most of the time far away from the Sun causing minimal evolutionary effects. Hence, comets can be considered to be the primordial remnants of our Solar system, containing pristine materials that were present in the cold regions of the protosolar nebula. The major regions of interest present in the comet are:

Nucleus

Comets comprise of a solid core structure made up of a coalescence of rock, dust and different types of ices. The ices present could be of water or frozen carbon dioxide, carbon monoxide, methane, and ammonia (Greenberg, 1998). Also, there have been detection of a variety of organic volatile compounds like CH_3OH, C_2H_2, C_2H_6, OCS, HCN, and H_2CO (Mumma et al., 2002). Possibility of presence of long chain hydrocarbons and amino acids cannot be neglected. The compounds present in the comet's nucleus are known as the parent molecules or primary volatiles. Comet nucleus are usually observed to be of 1-10 km in size. They cannot be directly observed during their active phase as they will be covered with a dense gaseous atmosphere known as coma.

Coma

Comets, the dirty snowballs, which are inactive at large heliocentric distance kick off their activity as the volatile species starts to sublimate during the onset of the comets journey into the inner Solar system. Different volatile species sublimate at different heliocentric distance due to their temperate dependence. The sublimated ices (primary volatiles) along with the dust forms an atmosphere around the nucleus (see Figure.1.6). It is this envelope which gives a fuzzy look to the comet differentiating it from asteroid or stars. Size of the coma can vary, even as large as the size of Jupiter, depending on the amount of activity in the comet. The UV radiation coming from the Sun is responsible for the photo dissociation and photo ionisation of the parent molecules giving rise to a number of daughter/grand-daughter molecules. The direct observation of parent molecules are principally possible in the infrared (Mumma & Charnley, 2011; Mumma et al., 2001) or radio wavelengths (Cordiner et al., 2014) while a large number of daughter/grand-daughter molecules can be detected in the visible region of the optical spectrum of the comet (A'Hearn et al., 1995; Cochran et al., 2012).

Dust tail

The dust particles rises from the surface of the comet nucleus due to the gas pressure of the sublimating volatiles. As the comet gets closer to the Sun, the radiation pressure from the Sun causes the dust particles to move out of the coma forming a tail like feature. Since, each dust particle would have different size and mass, they would have their unique velocity in an individual orbit around the Sun. This makes the dust tail a broad feature in a curved path (see Figure.1.6). Even though the dust tail is majorly made up of dust particles, spectroscopic studies are performed for dust tails to understand the volatile chemistry at different cometocentric locations.

Ion tail

The coma contains both primary volatiles as well as the product species produced via photo dissociation by the UV photons from the Sun. Certain primary volatiles like CO, H_2O, N_2 etc and product species like CH can be ionised by the strong Solar radiation. Since, these ionic species are extremely light, they are blown away by the Solar wind

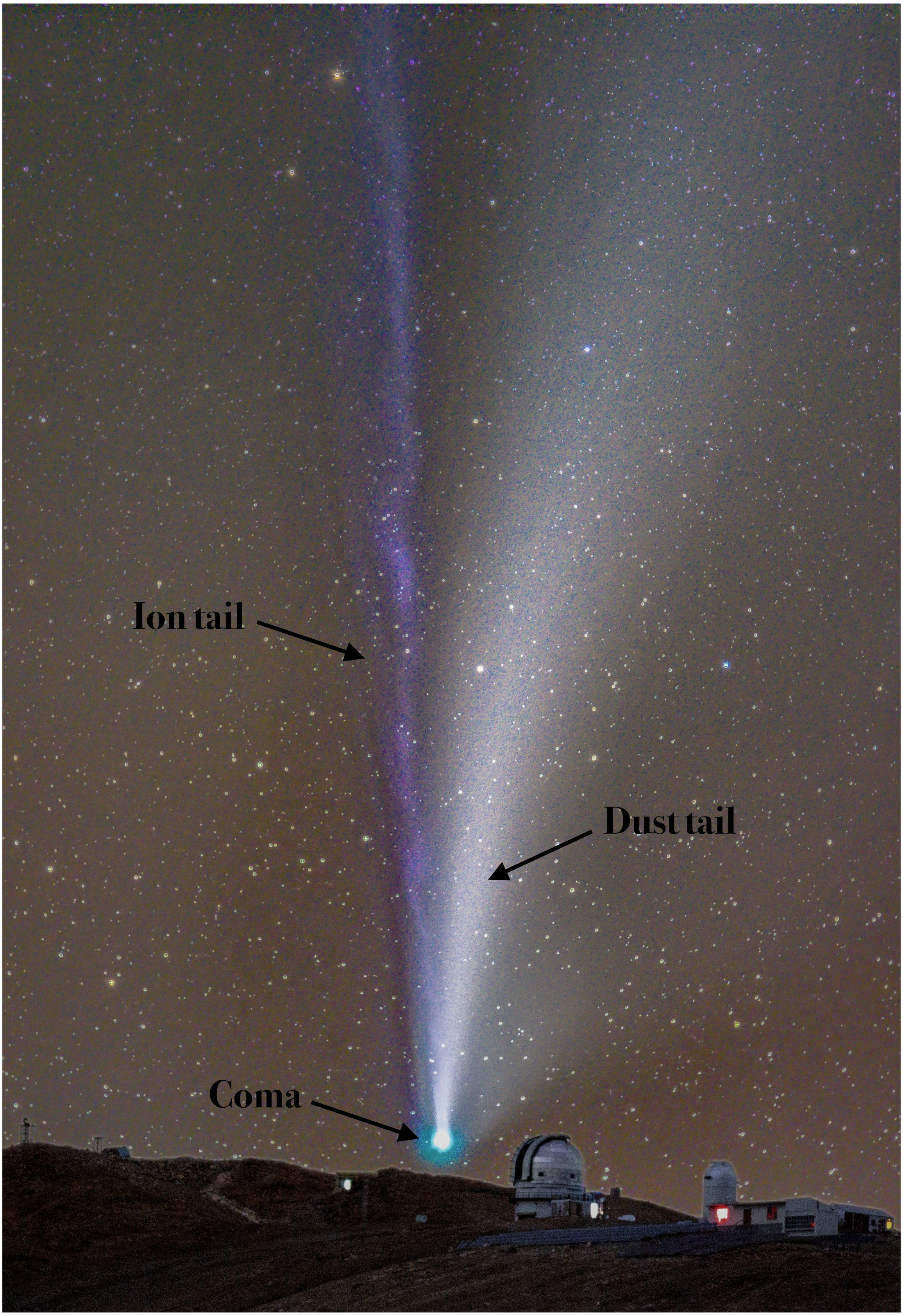

Figure 1.6: Image of comet C/2020 F3 taken on 22nd July from IAO, Hanle, *Credits:* Dorje Angchuk

giving rise to the ion tail in a direction opposite to that of Sun. Ion tails are observed to have a bluish tint due to the abundance of CO^+ species (see Figure.1.6). In spite of the fact that these ionic species are mostly observed only in the ion tail, there are exceptions like C/2016 R2 (PANSTARRS) (Venkataramani et al., 2020; Opitom et al., 2019b) where only ionic emissions were observed in the cometary coma.

Also, there have been reports of a third tail, a sodium (Na) tail, which has been observed only for a few comets with a very low perihelion passage (Cremonese et al., 2002; Kupperman et al., 1998; Lin et al., 2020b).

1.2.1 Beginning of activity in comets

Generally, a comet starts its activity when it crosses the water ice line at 5 AU, where the temperature is high enough to sublimate the water ice ($\sim$150 K) (Jewitt et al., 2007). It is at this moment the comet develops a coma and starts looking fuzzy when observed. In the optical spectra of these comets, gas emissions are not present above the reflected solar continuum spectra due to absence of ambient temperature to sublimate the different volatile species. As the comet moves closer to the Sun, emission from CN is the first one to be detected once the comet is around a heliocentric distance of 3 AU followed by C_3 and NH_2 at $\sim$2 AU and C_2 (Swan bands), CH etc at $\sim$ 1.5 AU (Swamy, 2010). Among these, CN and C_2 are the ones that dominate the optical spectra of a comet. At distances shorter than 1.5 AU, emissions from ionic species like CO^+, CH^+, N_2^+ starts appearing in the ion tail.
In rare cases, like comet C/2016 R2 (PANSTARRS), only ionic species were detected in the coma with the absence of all other main emissions (Venkataramani et al., 2020; Opitom et al., 2019b). Such detection opens up immense opportunity to study a comet which would have formed in a location completely different from that of the others. There have also been reports of comets which are active at very large heliocentric distance (Jewitt, 2009; Meech et al., 2009, 2017a; Kulyk et al., 2016; Womack et al., 2017). Mostly, at distances where temperature is favourable for amorphous ice to transform into crystalline form ($\sim$ 120 K), this exothermic runaway process is responsible for the

activity in the comet (Prialnik & Bar-Nun, 1992; Gronkowski & Smela, 1998; de Sanctis et al., 2002; Ivanova et al., 2011). But, at much larger distances, only the most volatile species like CO_2 ($\sim$ 80 K), CO ($\sim$25 K), N_2 ($\sim$ 22 K) can sublimate (Meech et al., 2009). A proof for CO sublimation being the primary reason for the activity was found in the comet C/2017 K2 (PANSTARRS), which was seen to be active at an unprecedented distance of $\sim$ 24 AU (Jewitt et al., 2017a, 2021; Meech et al., 2017a).

Considering the activity in comets coming from different reservoirs, a general distinction between the activities in SPCs and LPCs are observed. The SPCs tend to have an upper-shield relatively exhausted in the cometary volatile as a result of its multiple passages close to the Sun (Shustov et al., 2018). Such dust crusts are formed as the comet recedes from the Sun and sublimation ceases. Once the comet returns to the inner Solar system, these crusts can get depleted exposing the layer beneath (fresh volatile material or layers of ice that have different vaporization rates) Venkataramani et al. (2016). Hence, mostly SPCs show increased amount of activity very close to perihelion or after perihelion while LPCs tend to show an increased amount in activity on their way into the inner Solar system due to the availability of a fresh unexposed layer of volatile material. In this regard, observing and analysing the emissions from a SPC during its multiple apparition is a critical technique to understand the overall composition of the cometary nucleus.

1.2.2 Comet spectrum and classification

Spectrum is simply the variation of intensity with wavelength. A comet spectrum is comprised of both the coma gas emission spectrum (fluorescence emission) and the spectrum of the sunlight scattered by the dust particles (continuum). The optical regime of the cometary spectrum is filled with emissions from different radicals which are the daughter molecules of the parent ice species present in the comet nucleus. Figure.1.7 illustrates a typical spectrum of a comet with clear detection of emissions from different bands of various radicals like CN, C_2, C_3, CH, NH_2 along with the forbidden atomic Oxygen line, [OI]. Spectroscopic analysis of this region along the orbit of the comet can provide immense details regarding the relative abundance of different molecular emissions and their variations with heliocentric distances. The advantage of spectroscopic analysis is the luxury of obtaining emissions present in a given wavelength in a single shot avoiding effects of any temporal variation, if present.

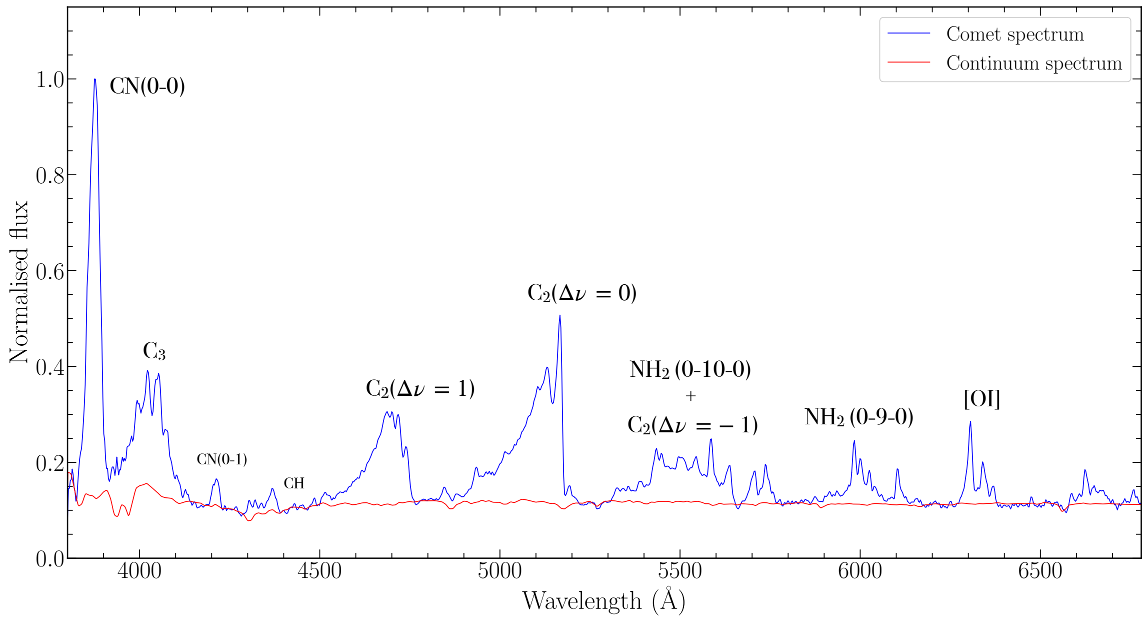

Figure 1.7: Optical spectrum of 46P/Wirtanen as observed on 2018-12-14. Further details of this observation can be found in Chapter 4

.

A'Hearn et al. (1995) have employed imaging in narrow band filters and Cochran et al. (2012), Fink (2009), and Langland-Shula & Smith (2011) utilised spectroscopic techniques to study a large number of comets originating from different reservoirs. From their observations they have defined classes for the comets, Typical and Carbon depleted, based on various production rate ratios, majorly with respect to CN. A'Hearn et al. (1995) classifies a comet to be carbon depleted if the production rate ratio of C_2 to CN [$Q(C_2)/Q(CN)$] is less than 0.66. Later, Cochran et al. (2012) slightly modified the classification to include the production rate ratio of C_3 too with respect to CN to decide the carbon depletion in comets. He stated that comets were depleted in carbon if $Q(C_2)/Q(CN) < 1.04$ and $Q(C_3)/Q(CN) < 0.13$. Both these classifications have been used extensively to segregate the cometary population, with the A'Hearn et al. (1995) method used more widely. Comets are also made up of dust grains which agglomerated at the time of formation of the Solar system. A'Hearn et al. (1984b) defined a parameter

Afρ, which is a proxy to the dust emission of the comet to classify the comet as dust rich or dust poor. These classifications have been globally used over the years to organise every new comet to make the sample space as large as possible in an attempt to correlate these characteristics with the formation location of different comets and understand the mixing up which occurred at the initial stages of the Solar system formation.

1.2.3 Dust in comets

Comets are termed 'dirty snowballs' due to the reason that it is built up of both dust and ice. Equivalent to the ice component, the dust particles can also provide a great deal of information regarding the composition of the comet. There has been various space missions to probe the dust particles present in asteroids[1] and comets[2]. Even though a large amount of information regarding the composition of minor bodies has been obtained from these missions, they are still restricted to probe only the ecliptic bodies, due to the limitations of space missions. In the case of comets, this would mean that *InSitu* observations are possible only for comets belonging to Jupiter family or Halley type not having significant difference in inclination from the ecliptic plane. Since it is practically not possible to send probes to every ecliptic body, ground based observations remain the most reliable method to study and understand the larger fraction of cometary bodies, both SPCs and LPCs. Cometary nucleus is made up of dust particles of different size, shape and composition. The dust present in the SPCs would be highly processed owing to its short orbital period allowing frequent weathering in contrast to that of LPCs which would contain material that has never been exposed to Sun light. Hence, systematic comparison of the dust composition present in comets originating from different reservoirs can help us in understanding the general composition of the dust present in them.

Polarisation measurement has been a preliminary technique to study the reflected light from a Solar system body starting from Arago in 1811 who observed the polarisation of Moon. Arago had also detected traces of polarisation in comets in 1819. The presence

[1]https://nssdc.gsfc.nasa.gov/planetary/planets/asteroidpage.html

[2]https://nssdc.gsfc.nasa.gov/planetary/planets/cometpage.html

of polarisation in comets were confirmed while observing comet Halley during its 1835 apparition. It was later in 1881, the comets 1881 III and IV were visually observed by Wright W. A. to understand that comets exhibit considerably high polarisation (Wright, 1881b,a). Öhman (1939) also visually observed the polarisation in comet 1927 VII but, it was Öhman (1941) who first recorded the polarisation measurements of comets Cunningham (1940 C) and Paraskevopoulos (1941 C) in their spectra. He was effectively able to distinguish the polarisation effects present in the molecular emission bands as well as in the Sun light scattered by the cometary dust (continuum region). The polarisation detected in different molecular bands (CN, C_2 etc) were attributed to the fluorescence emission while that detected in the continuum region was ascribed to the physio- compositional characteristics of the dust present in the comet. It was observed that the degree of polarisation varied with the Sun-Target-Observer (STO) angle, also known as phase angle and it was maximum (P_{max}) around 90°. Blackwell & Willstrop (1957) were the first one to study the polarisation effects separately in line spectrum and continuum spectrum.

The discovery of silicate minerals, a material that forms at high temperatures in the inner most region of proto-Solar nebula, in cometary dust (Bregman et al., 1987; Brownlee et al., 2006; Brownlee, 2014; McKeegan et al., 2006) also helped in confirming the extreme mixing up of proto-planetary disk material during the initial stage of Solar system. Polarisation measurement turned out to be a standard technique to probe the dust particles present in a comet. From the works that followed (eg., Kiselev & Chernova, 1978, 1981; Myers, 1985; Bastien et al., 1986; Sen et al., 1991; Joshi et al., 1992, 1997; Kolokolova et al., 2004; Ganesh et al., 1998, 2009) the phase dependence and wavelength dependence of polarisation values were studied to analyse the difference in positive polarisation in different comets. Backing these works, Zubko et al. (2016) proposed that the difference in polarisation-phase curve between distinct comets would be due to the variation in the physical and chemical composition of the dust present in these comets. He stated that there would be two types of materials making up the dust particles in comets, a weakly absorbing material (silicates) and a strongly absorbing (carbonaceous) one, whose relative composition is responsible for the slope of the polarisation-phase curve. As seen from the work carried out in Zubko et al. (2020), the high P_{max} in polarisation-phase curve corresponds to comets with relatively lower composition of weakly absorbing material (silicates) and vice versa.

Complex modelling methods can be employed to understand in depth the dust char-

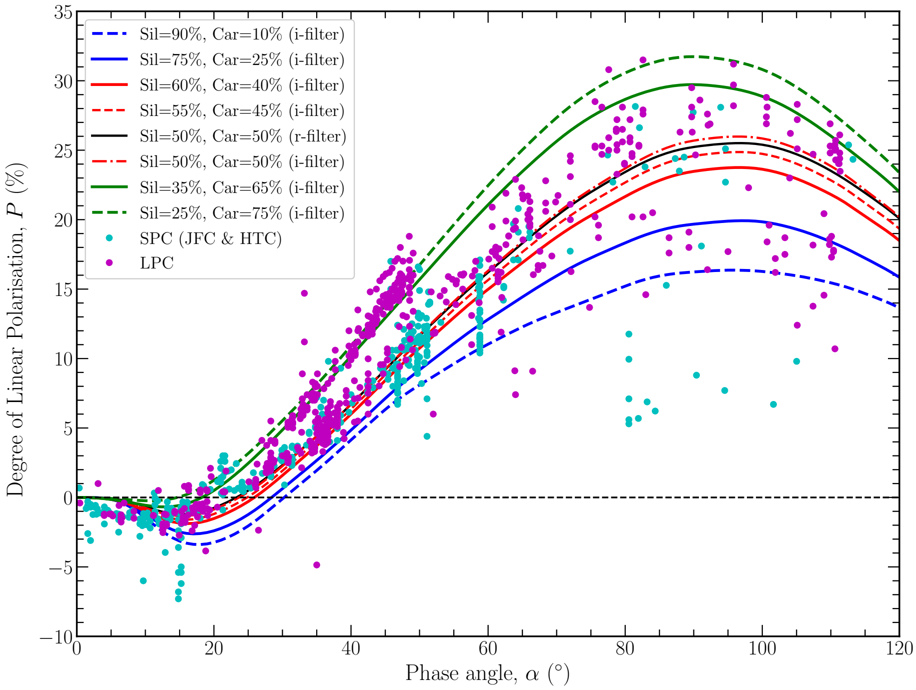

Figure 1.8: Variation of degree of linear polarisation for all observed comets in wavelengths greater than 6500 angstrom. The data has been taken from Kiselev et al. (2017) and models from Halder & Ganesh (2021) and Aravind et al. (2022).

acteristics (Halder & Ganesh, 2021). As a consequence, the variation of polarisation with phase and/or wavelength can be used to understand the general physical and compositional characteristics of the dust present in any comet. Figure.1.8 illustrates the distribution of polarisation with phase angle for a large number of comets (both SPCs and LPCs), compiled by Kiselev et al. (2017). The data has been filtered to include measurements which have been taken for an effective wavelength greater than 6500 Å. This ensures the exclusion of polarisation measurements carried out at shorter wavelength which can be contaminated by molecular emissions. This illustration clearly depicts an overlap in the dust compositions of SPCs and LPCs with the LPCs largely biased towards the higher slope indicating the presence of a larger fraction of carbonaceous material (highly absorbing). Any similarity/dissimilarity in the composition of SPCs and LPCs can be effectively used to streamline the theories related to the chaotic mixing up of proto-planetary disk material or to analyse the effects of evolutionary process in comets.

1.3 Comets exterior to our Solar system

Considering that the formation mechanism explained above for our Solar system is not unique, and can be applied to any other stellar system, it can be expected that they also have a history of comets bound to their system or expelled due to interactions with giant planets. This idea of considering similar formation mechanism in other stellar systems can be confirmed from the detected presence of hot Jupiters (please see the recent work by Khandelwal et al., 2022, and the references therein). The presence of such giant planets which would have migrated closer to the parent star would have caused excessive instability among the planetesimals, similar to what is currently being considered for our Solar system. Hence, one can expect other stellar systems to have comet families bound to them (Exocomets) as well as a large number of comets which have been expelled from such different stellar system, wandering in the interstellar medium (Interstellar comet). The upcoming subsections discuss in brief the initial theories related to the existence of such exocomet and interstellar comet families and our current understanding.

1.3.1 Exocomets

Unaltered remnants like comets are always the best source to access the history of a planetary system. Section.1.1.2 explains the different kind of planetary migration that would have occurred in the Solar system at different stages of its formulation. It is clear from these theories that such giant planet migrations can cause extreme chaos in the proto-planetary disk causing a large scale mix up or ejection of planetesimals leading to the formation of different comet reservoirs. If the process which led to the formation of our Solar system is not unique, then other stellar system would also have a comet population orbiting around its parent star. Lecavelier Des Etangs et al. (1999) had simulated the possibility of detecting an exocomet. He successfully simulated the stellar occultation light curve of a comet by taking into consideration the dust spatial distribution and extinction within the tail. The possibility of two types of light curves were presented, rounded triangle and symmetric, where the latter is difficult to be distinguished from what is observed in the case of a planetary occultation. It was clear that the structure and evolution of the planetary region in a nearby star can be studied by detecting and analysing the cometary activity around it. Since then various groups have been successful in detecting and establishing the presence of such exocomets (eg., Rappaport et al., 2018; Zieba et al., 2019; Rebollido et al., 2020; Pavlenko et al., 2021; Kiefer et al., 2017).

1.3.2 Interstellar comet

In 1950, Oort (1950) hypothesised the existence of a quasi-spherical comet cloud around the Solar system. Later it was understood that the physical process which led to the injection of comets into orbits at such large distances would have ejected as much number of comets out of the Solar system. These comets would not be bound to any system and would be travelling in the interstellar space. Hence, these loosely bound cometary bodies were termed as Interstellar Comets (ISC). As mentioned in the previous section, if other stellar systems also formed according to the theories predicted for our Solar systems, a significant number of ISCs would have been contributed by these systems. It was Sekanina (1976) who proposed the likelihood of the existence of these bodies and discussed the probability of their encounter with our Solar system, with not much conviction. Gaining interest in this topic, building on the work done by Marsden et al. (1978), Yabushita & Hasegawa (1978) discussed the probability of an incoming ISC with weakly hyperbolic orbit (hyperbolic excess) being perturbed and captured by the major planets into a weakly elliptical orbit. But, later Kresak (1992) discarded the origin of the hyperbolic excess observed in many comets to be of interstellar origin by including the effects of non-gravitational forces due to the out-gassing of cometary nuclei.

McGlynn & Chapman (1989) studied in detail the possible density of the ISC family and the theoretically expected number of ISC comets that can be detected in a year. Quoting that a stellar system similar to our Solar system retains only about 10% of the total initial cometary population and ejects the rest of them, they stated that the number of comets lost to interstellar space from a single stellar system should be about 10^{14} (considering the total comet population to be $\sim 10^{12}$ (Weissman, 1983)). Accepting the total matter density due to stars near Sun as defined by Bahcall (1984) and the probability of detection of a comet as defined by Everhart (1967a,b), McGlynn & Chapman (1989) proposed that 0.6 comets of interstellar origin should be detected per year. This implies that at least 6 ISCs should have been discovered in the 150 year old history of observational astronomy. This rate of detection points at a clear discrepancy with the detection rate at that time, which was zero. To explain the probable reasons behind the lack of these detection, McGlynn & Chapman (1989) takes into consideration certain minute possibilities like, an alternative origin of Oort cloud, uniqueness of our Solar system, we are currently in a comet shower (leading to wrong OCC population estimation) etc. Even though the outcomes of all these considerations were different, none of them could explain the lack of detection of these ISCs.

In an attempt to address the missing interstellar comets, Sen & Rana (1993) explored the method defined by McGlynn & Chapman (1989) but by tweaking certain parameters like the expected stellar mass in the Solar neighbourhood. Considering the work done by Basu & Rana (1992) on the mass function of stars in the Solar neighbourhood Sen & Rana (1993) were able to propose confidently that the number of ISCs expected to be detected in a century should be less than one rather than 4, as proposed by McGlynn & Chapman (1989). Hence, it was concluded that only one ISC can be expected to be discovered in about 200 years. This result portrayed the 150 year non-detection of ISCs as normal and the current models of Oort cloud and Solar system formation were stated to be reliable. It is well understood that studying the various aspects of a cometary body can help us gain insight into the conditions that prevailed during the formation of its parent star system. Therefore, comparing comets from our Solar system with interstellar ones can shed light on the difference/similarity in the formation mechanism and materials present in different proto-stellar systems.

Even after centuries of comet observations and decades after the initial prediction by Sen & Rana (1993), no one had observed an interstellar object, passing through the inner Solar system, until October 2017 when 'Oumuamua (1I/2017 U1) was discovered. Even though there was non-gravitational acceleration found in its orbit, around perihelion, which is usually a result of out-gassing (eg., Micheli et al., 2018), 'Oumuamua is observed to be completely asteroidal in nature (Meech et al., 2017b; Jewitt et al., 2017b). This behaviour limited the observation of the object due to its faintness. Later, on 30th August 2019, Gennady Borisov, using his self-built 0.65 m telescope discovered a comet like body. This was later identified to be the first ever interstellar comet observed to be passing through the inner Solar system. The comet possessed a very large eccentricity of e = *3.379* and a very high hyperbolic excess velocity of v $\sim$ 32 Km/s (Guzik et al., 2020), further confirming its interstellar origin. The interstellar comet, initially identified as C/2019 Q4, was later named 2I/Borisov[3] by IAU.

1.4 Mysteries related to the cometary population

Having understood the structure of the Solar system and the possible scenarios that would have resulted in the alignment and formation of various reservoirs, it is still an open question regarding the kind of mixing of planetesimals that would have occurred during the chaotic instabilities at different stages of the Solar system formation. Ideally, different types of comets should possess different origin. Hence, initially, it was assumed that a specific type of comet would have originated from a particular reservoir. But, A'Hearn et al. (2012) and Willacy et al. (2022) suggested that most of the comets would have formed in an overlapping region (current place of giant planets) as mentioned in the Nice model. Still, the average composition of a comet family or the observed compositions of the individual comets cannot be described by a specific place or time during the formation of Solar system (Willacy et al., 2022). It seems that the homogeneity/heterogeneity of a comet nucleus is predominantly a result of their formation process rather than evolutionary as pointed by Belton & Melosh (2009). If evolutionary signatures like thermal processing dominated the characteristics of a comet, then more volatile species would have been depleted in a comet relative to the less volatile species. Rather, it is observed that comets with fewest perihelion passage are most depleted in high volatile species (eg., CO, CO_2) in contrast to the evolutionary model. Any internal heterogeneity observed in the comet nucleus would be due to the

[3] https://minorplanetcenter.net/mpec/K19/K19S72.html

comparable duration of planetary migration and growth of cometesimal leading to a mixing of materials present at different locations in the proto-Solar nebula (A'Hearn et al., 2012).

According to the classification by A'Hearn et al. (1995), a large fraction of the carbon depleted comets were found to be JFCs. Even though the strict classification criterion by Cochran et al. (2012) (including C_3 production rate ratio) reduced the fraction, this biasness was still observed. Although a difference in composition between two families of comets point to a difference in the region of formation, a large scale mixing up of these comets is evident. Considering the possibility that carbon is a product of the long chain hydrocarbons (LCHC) present in comets, the depletion of carbon in JFCs would simply mean that they were formed in the colder regions of the proto-Solar nebula where the temperature was not ambient for these LCHCs to form de Pater & Lissauer (2015). But, A'Hearn et al. (2012) states that even though the LPC and JFC population would have formed in an overlapping region, JFCs would have formed in slightly warmer regions of the nebula owing to the observed exhaustion of CO in JFC when compared to the LPCs.

The polarisation distribution of a large number of comets imply that a larger fraction of LPCs contain more carbonaceous materials while SPCs are biased towards containing relatively more Silicate materials (see Section.1.2.3). However, a mixing up of the cometary population is apparently seen. Since, it is not possible that the SPCs would have formed at locations where the Silicate material was abundant in the proto-Solar nebula (very high temperature), this indicates a major mixing up of the proto-planetary disk material during the initial stages of the Solar system with no clues of where these bodies would have originally formed. But, the significant difference in the relative dust composition would definitely be the consequence of the location at which these bodies formed.

As mentioned in the beginning, the exact origin of different types of comets and the kind of mixing up that would have occurred during the formation of the planets in the Solar system is still unknown. It is also possible that, all these biasness in the different classifications are just a direct result of the observation limitations. Even though a large number of comets have been discovered (4410 as of April 2022 [4]) and observed,

[4] https://minorplanetcenter.net/

they account only for a tiny fraction of the entire comet population ($\sim 10^{12}$). Hence, continuous monitoring of new comets as well as periodic comets using different observation techniques is necessary to streamline the unanswered questions related to comet formation and improve our understanding of the Solar system formation.

1.5 Aim of the Thesis

One of the key motivations to carry out research and study different comets and their characteristics is that they can advance our understanding of the Solar system and its evolution from the proto-Solar nebula. Comets being the carriers of the most primordial material that were present in the proto-Solar nebula, they provide vital clues to the early history of the Solar system. These clues can be gathered from a larger set of comets belonging to different reservoirs to streamline the various theories on the evolution of the Solar system.
The different aspects of a comet to be studied in order to have a better understanding about their characteristics are:

1. Chemical composition from the molecular emission bands in the optical regime, their relative molecular abundances and variation in production rates with heliocentric distance with the help of low resolution spectroscopy.

2. Analyse the coma morphology and Afρ profile of different comets to have a comparison of the characteristic dust emission in each of them.

3. Probe the rotational-vibrational lines present within the different molecular bands, which are seen to be blended in low resolution, with the help of high resolution spectroscopy.

4. Understanding the variation in degree of polarisation with phase angle in order to have a deeper understanding of the physical and compositional properties of the dust present in the comets.

Simultaneous employment of low and high resolution spectroscopy to probe the gaseous emissions present in the comet, imaging/low resolution spectroscopy to study the dust emission characteristics of the comet, broad band/narrow band imaging to analyse the presence of dust jets or structures within the coma, along with polarisation analysis can help one gain greater insight into the type of material present in different comets. Similar works have been carried out on a few other comets like C/2014 A4 (SONEAR) (Ivanova et al., 2019b), C/2009 P1 (Garradd) (Ivanova et al., 2017), C/2011 KP36 (Spacewatch) (Ivanova et al., 2021c) and 156P/Russell-LINEAR (Aravind et al., 2022). Extensive comparison between such intensive studies of long period and short period comets would help in unravelling the mystery of primordial and evolutionary signatures present in the comets belonging to different reservoirs.

Chapter 2

Overview of Observational techniques

2.1 Introduction

Observations of comets were carried out using two Indian observatories, the 1.2 m telescope at Mount Abu InfraRed Observatory (MIRO) operated by the Physical Research Laboratory at Mount Abu, Rajasthan and the 2 m Himalayan Chandra Telescope (HCT) operated by the Indian Institute of Astrophysics at Hanle, Ladakh. The different types of comets covered in this work has been listed in Table.2.1.

The Hanle telescope facility has been used for observational techniques like imaging and spectroscopy (low resolution and high resolution) while the Mt. Abu telescope facility has been used for a wider range of observational techniques like broadband imaging, low resolution spectroscopy and optical polarimetry. The NASA JPL HORIZONS[1] service was used to generate the ephemerides for the observed comets at both the observing locations.

[1] https://ssd.jpl.nasa.gov/horizons.cgi

Table 2.1: Brief list of comets observed during the course of the thesis work. Complete details of observation are given in Table.2.2.

Object name	Type
46P	JFC
21P	JFC
260P	JFC
88P	JFC
156P	JFC
67P	JFC
4P	JFC
29P	JFC
123P	JFC
38P	HTC
C/2019 N1	LPC

Object name	Type
C/2018 Y1	LPC
C/2018 N2	LPC
C/2018 W2	LPC
C/2020 A2	LPC
C/2019 Y4	LPC
C/2017 T2	LPC
C/2020 F3	LPC
C/2020 M3	LPC
C/2021 A1	LPC
C/2019 L3	LPC
2I/Borisov	Interstellar

In the following sub-sections we describe, briefly, the details of both the observational facilities and the unique observational procedures like imaging (broad band and narrow band), spectroscopy (low and high resolution) and broad band polarimetry. The detailed reduction procedures and pipelines employed for each of the above mentioned techniques, including the acquisition script written in AndorBasic for the imaging polarimeter will be discussed in their respective subsections. The complete log of the observation, including the name of the observed object, observational facility used, the observational technique employed, and the epoch of observations are as given in Table 2.2.

Subsequently, the Narrow band comet filters (CN, C_2, C_3, Blue continuum, Green continuum and Red continuum) (Farnham et al., 2000), which were made for the observation of comet Hale-Bopp, hence known as Hale-Bopp (HB) filters, will be introduced. The behaviour of the transmission curves of these filters available with us over the years will be discussed so as to lay a foundation to the comparison of Narrow band filter transmission curve with the low resolution comet spectrum of different comets illustrated in Chapter.5.

Table 2.2: Complete observational data

Dates of observation	Observational technique	Observatory/Instrument
46P/Wirtanen - [*e = 0.658, i = 11°.74, q = 1.055 AU, a = 1.055 AU, P = 5.439 Years*] - JFC		
2018-10-05	Spectroscopy (Low res)	MIRO/LISA
2018-11-21	Spectroscopy (Low res)	MIRO/LISA
2018-11-28	Spectroscopy (Low res)	MIRO/LISA
2018-11-29	Spectroscopy (Low res)	MIRO/LISA
2018-11-30	Spectroscopy (Low res)	MIRO/LISA
2018-12-08	Spectroscopy (Low res)	MIRO/LISA
2018-12-09	Spectroscopy (Low res)	MIRO/LISA
2018-12-13	Spectroscopy (Low res)	MIRO/LISA
2018-12-14	Spectroscopy (Low res)	MIRO/LISA
2018-12-15	Spectroscopy (Low res)	MIRO/LISA
2018-12-27	Spectroscopy (Low res)	MIRO/LISA
2018-12-28	Spectroscopy (Low res)	MIRO/LISA
2019-01-11	Spectroscopy (Low res)	MIRO/LISA
2019-01-12	Spectroscopy (Low res)	MIRO/LISA
2019-01-13	Spectroscopy (Low res)	MIRO/LISA
2019-01-31	Spectroscopy (Low res)	MIRO/LISA
2019-02-01	Spectroscopy (Low res)	MIRO/LISA
2019-02-02	Spectroscopy (Low res)	MIRO/LISA
2019-02-03	Spectroscopy (Low res)	MIRO/LISA
2018-12-15	Spectroscopy (High res)	HCT/HESP
2018-12-28	Spectroscopy (High res)	HCT/HESP
2019-01-11	Spectroscopy (High res)	HCT/HESP
21P/Giacobini–Zinner - [*e = 0.710, i = 32°, q = 1.013 AU, a = 3.50 AU, P = 6.549 Years*] - JFC		
2018-04-10	Spectroscopy (Low res)	MIRO/LISA
260P/McNaught - [*e = 0.594, i = 15°.767, q = 1.49 AU, a = 3.67 AU, P = 7.048 Years*] - JFC		
2019-10-20	Spectroscopy (Low res)	HCT/HFOSC
2019-11-30	Spectroscopy (Low res)	HCT/HFOSC
2019-12-22	Spectroscopy (Low res)	HCT/HFOSC
88P/Howell - [*e = 0.563, i = 4°.38, q = 1.35 AU, a = 3.1 AU, P = 5.48 Years*] - JFC		
2020-05-18	Spectroscopy (Low res)	HCT/HFOSC
2020-06-25	Spectroscopy (Low res)	HCT/HFOSC
2020-09-22	Spectroscopy (Low res)	HCT/HFOSC
156P/Russell-LINEAR - [*e = 0.615, i = 17°.26, q = 1.33 AU, a = 3.46 AU, P = 6.44 Years*] - JFC		
18-10-2020	Spectroscopy (Low res)	HCT/HFOSC
13-11-2020	Polarimetry (Broad band)	MIRO/EMPOL
15-12-2020	Spectroscopy (Low res)	MIRO/LISA
16-12-2020	Polarimetry (Broad band)	MIRO/EMPOL
67P/Churyumov-Gerasimenko - [*e = 0.641, i = 7°.05, q = 1.24 AU, a = 3.46 AU, P = 6.44 Years*] - JFC		
2021-11-09	Spectroscopy (Low res)	HCT/HFOSC
2021-11-07	Polarimetry (Broad band)	MIRO/EMPOL
2021-11-09	Polarimetry (Broad band)	MIRO/EMPOL

Table 2.2 Continued

4P/Faye - [*e = 0.58, i = 8°.17, q = 1.57 AU, a = 3.795 AU, P = 7.395 Years*] - **JFC**		
09/11/2021	Spectroscopy (Low res)	HCT/HFOSC
29P/Schwassmann–Wachmann - [*e = 0.043, i = 9°.37, q = 5.738 AU, a = 6.002 AU, P = 14.698 Years*] - **JFC**		
2020-10-18	Spectroscopy (Low res)	HCT/HFOSC
2021-11-09	Spectroscopy (Low res)	HCT/HFOSC
123P/West-Hartley - [*e = 0.449, i = 15°.35, q = 2.12 AU, a = 3.86 AU, P = 7.584 Years*] - **JFC**		
2019-03-13	Spectroscopy (Low res)	MIRO/LISA
2019-04-01	Spectroscopy (Low res)	MIRO/LISA
2019-04-02	Spectroscopy (Low res)	MIRO/LISA
38P/Stephan–Oterma - [*e = 0.859, i = 18°.35, q = 1.588 AU, a = 11.288 AU, P = 37.93 Years*] - **HTC**		
2018-11-20	Spectroscopy (Low res)	MIRO/LISA
2018-11-28	Spectroscopy (Low res)	MIRO/LISA
2018-12-09	Spectroscopy (Low res)	MIRO/LISA
2018-12-13	Spectroscopy (Low res)	MIRO/LISA
2018-12-14	Spectroscopy (Low res)	MIRO/LISA
2018-11-28	Spectroscopy (High res)	HCT/HESP
C/2018 Y1 (Iwamoto) - [*e = 0.9904, i = 160°.40, q = 1.28 AU, a = 133.68 AU, P = 1,545.54 Years*] - **LPC**		
2019-01-11	Spectroscopy (Low res)	MIRO/LISA
2019-01-12	Spectroscopy (Low res)	MIRO/LISA
2019-01-31	Spectroscopy (Low res)	MIRO/LISA
2019-02-02	Spectroscopy (Low res)	MIRO/LISA
2019-02-03	Spectroscopy (Low res)	MIRO/LISA
C/2018 N2 (ASASSN) - [*e = 1.0006, i = 77°.55, q = 3.13 AU*] - **LPC**		
2019-11-30	Spectroscopy (Low res)	HCT/HFOSC
2019-12-22	Spectroscopy (Low res)	HCT/HFOSC
C/2018 W2 (Africano) - [*e = 1.0004, i = 116°.6, q = 1.458 AU*] - **LPC**		
2019-09-07	Spectroscopy (Low res)	HCT/HFOSC
2019-10-02	Spectroscopy (Low res)	HCT/HFOSC
C/2020 A2 (Iwamoto) - [*e = 0.999, i = 120°.70, q = 0.98 AU, a = 1,329.47 AU, P = 1,18,474 Years*] - **LPC**		
2020-01-31	Spectroscopy (Low res)	MIRO/LISA
2020-02-22	Spectroscopy (Low res)	MIRO/LISA
2020-02-23	Spectroscopy (Low res)	MIRO/LISA
C/2019 Y4 (ATLAS) - [*e = 1.002, i = 45.98°, q = 0.25 AU*] - **LPC**		
2020-02-22	Spectroscopy (Low res)	MIRO/LISA
2020-02-23	Spectroscopy (Low res)	MIRO/LISA
2020-03-15	Spectroscopy (Low res)	MIRO/LISA
2020-05-26	Spectroscopy (Low res)	MIRO/LISA
2020-03-13	Polarimetry (Broad band)	MIRO/EMPOL
C/2017 T2 (PANSTARRS) - [*e = 0.999, i = 57°.23, q = 1.615 AU, a = 5,004 AU, P = 3,54,071 Years*] - **LPC**		
2019-10-02	Spectroscopy (Low res)	HCT/HFOSC
2019-11-30	Spectroscopy (Low res)	HCT/HFOSC
2019-12-22	Spectroscopy (Low res)	MIRO/LISA
2020-01-30	Spectroscopy (Low res)	MIRO/LISA
2020-01-31	Spectroscopy (Low res)	MIRO/LISA
2020-02-23	Spectroscopy (Low res)	MIRO/LISA
2020-05-26	Spectroscopy (Low res)	MIRO/LISA
2020-06-09	Spectroscopy (Low res)	MIRO/LISA

Table 2.2 Continued

2020-06-25	Spectroscopy (Low res)	HCT/HFOSC
2019-12-28	Polarimetry (Broad band)	MIRO/EMPOL
2020-01-17	Polarimetry (Broad band)	MIRO/EMPOL
C/2020 F3 (NEOWISE) - [*e* = *0.999*, *i* = *128°.93*, *q* = *0.294 AU*, *a* = *358.46 AU*, *P* = *6,787 Years*] - LPC		
2020-07-22	Spectroscopy (Low res)	HCT/HFOSC
2020-07-24	Spectroscopy (Low res)	HCT/HFOSC
C/2020 M3 (ATLAS) - [*e* = *0.952*, *i* = *23°.47*, *q* = *1.26 AU*, *a* = *xx AU*, *P* = *138.87 Years*] - LPC		
2020-10-18	Spectroscopy (Low res)	HCT/HFOSC
2020-12-15	Spectroscopy (Low res)	MIRO/LISA
	Polarimetry (Broad band)	MIRO/EMPOL
C/2021 A1 (Leonard) - [*e* = *1.0001*, *i* = *132.68°*, *q* = *0.615 AU*] - LPC		
2021-11-09	Spectroscopy (Low res)	HCT/HFOSC
2021-11-03	Polarimetry (Broad band)	MIRO/EMPOL
2021-11-26	Polarimetry (Broad band)	MIRO/EMPOL
C/2019 L3 (ATLAS) - [*e* = *1.011*, *i* = *48°.36*, *q* = *3.55 AU*] - LPC		
2021-11-09	Spectroscopy (Low res)	HCT/HFOSC
2022-02-18	Spectroscopy (Low res)	HCT/HFOSC
C/2019 N1 (ATLAS) - [*e* = *0.9998*, *i* = *82°.42*, *q* = *1.704 AU*, *a* = *13,137 AU*, *P* = *15,05,765 Years*] - LPC		
2020-06-25	Spectroscopy (Low res)	HCT/HFOSC
2020-07-22	Spectroscopy (Low res)	HCT/HFOSC
2I/Borisov - [*e* = *3.57*, *i* = *44°.05*, *q* = *2.0062 AU*] - IC		
2019-11-30	Spectroscopy (Low res)	HCT/HFOSC
2019-12-22	Spectroscopy (Low res)	HCT/HFOSC
2019-12-24	Imaging (Broad band)	MIRO/EMCCD
2019-12-25	Imaging (Broad band)	MIRO/EMCCD
2019-12-24	Imaging (Broad band)	MIRO/EMCCD

2.2 Observational facilities

Optical instruments available on two different observational facilities in India have been extensively used for the observation of comets in multiple observational techniques. Himalayan Chandra Telescope and Mt. Abu Infrared Observatory encompasses different instruments using which various aspects of comets can be analysed.

2.2.1 Mount Abu InfraRed Observatory (MIRO)

The 1.2 m Mount Abu InfraRed Observatory (MIRO) is located at Mount Abu, Rajasthan (Longitude : $72^\circ\ 46'\ 47.5''$ East; Latitude: $24^\circ\ 39'\ 8.8''$ North; Altitude : 1680 m). It is an f/13 Ritchey-Chretien equatorial mount telescope. The control system of the telescope provides option for variable tracking of astronomical objects. The rate of motion of the object in RA and DEC can be computed and loaded in order to force the telescope to follow the object moving in a non-sidereal rate. In order to correct any possible movement of the objects position during long exposure (specially during spectroscopy), the telescope can be manually moved using the control switches or a remote. This technique has been successful even in observing fast moving Near-Earth asteroids too. The telescope houses multiple instruments that can be employed for various observational techniques like imaging, low resolution spectroscopy and polarimetry. The backend instruments that has been used are, Long slit Intermediate resolution Spectrograph for Astronomy (LISA), EMCCD based imaging Polarimeter (EMPOL) and an imaging system (filter wheel + EMCCD).

LISA: LISA[2] is an optical spectrograph designed for telescopes with focal ratio *f/5*. The 1.2 m MIRO being an *f/13* telescope requires a focal reducer in order to effectively use the LISA instrument without light loss. The GSO 2″ 0.5x Focal Reducer[3] can be used to reduce the native focal ratio of the telescope by 0.5 when mounted 53 mm from the focal plane (slit) of the instrument. At initial stages, the focal reducer was mounted on the detachable telescope mount of LISA. Due to the larger distance of the focal reducer lens to the focal plane, this setup brought down the reduction to ∼0.19x, bringing the focal ratio to *f/2.5*. Since, the best performance of the instrument is at *f/5*, efforts were made to build a mechanical setup that can hold the focal reducer at a closer distance from the LISA focal plane, so as to increase the reduction factor. Figure.2.1 illustrates the mechanical attachment which was built in-house for this purpose. Panel *(a)* displays the portion of the complete attachment which holds the focal reducer through threads. Panel *(b)* is the main body of the attachment which holds the attachment shown in panel

[2] https://www.shelyak.com/produit/pf0021vis-lisa-slit-visible/?lang=en

[3] https://agenaastro.com/gso-2-0-5x-focal-reducer.html

(a) and also connects LISA to the telescope as shown in Panel *(c)*. Through this setup we were able to vary the distance of the focal reducer from the detector focal plane by apt amount to set the reduction factor to 0.38x. Hence, the focal ratio was successfully reduced to *f/5*.

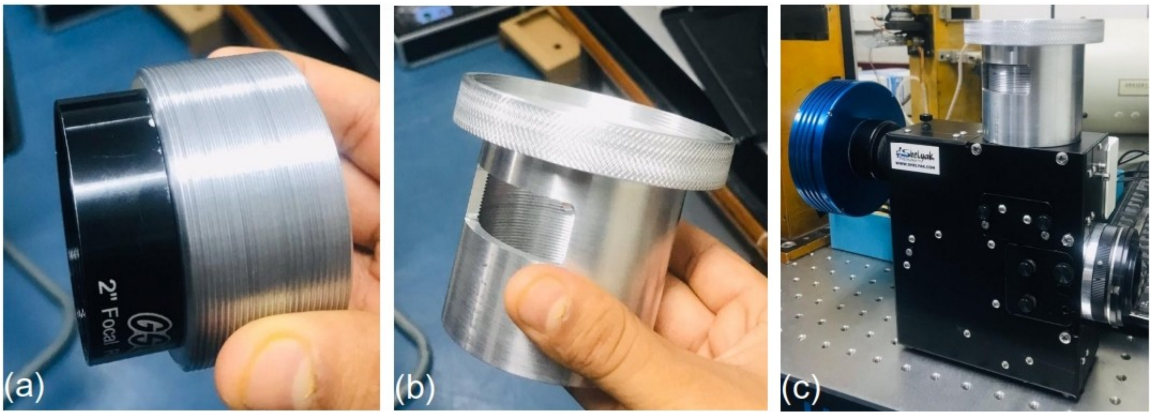

Figure 2.1: Mechanical attachments included in LISA for optimal performance

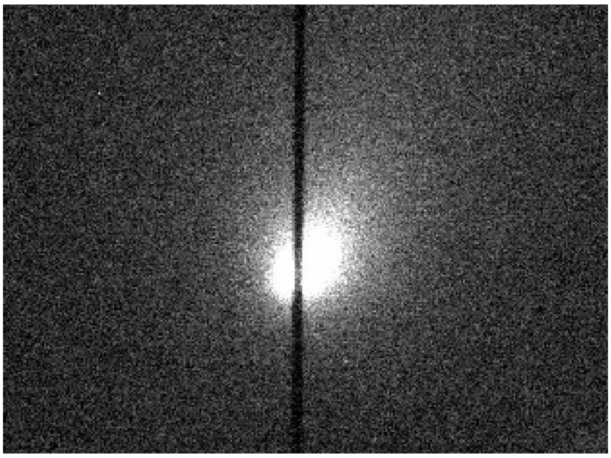

Figure 2.2: Snapshot of the guider CCD showing a comet placed on the slit

A detailed light path of the instrument is given by Venkataramani (2019). The instrument consists of two CCDs, one for data acquisition and one for guiding. The guider CCD, whose exposure can be set to user defined time interval, is helpful in live tracking the comets position on the slit (see Figure.2.2). The final spectrum is obtained on the acquisition CCD. The guider CCD is of 659×494, 7.4 μm square pixels and the acquisition CCD is of 1392×1040, 6.45 μm square pixels. The plate scale of the instrument initially was 0.665 arcsec per pixel. After the introduction of the mechanical attachment mentioned before, the plate scale decreased to 0.326 arcsec per pixel. The spectral range of this instrument covers the entire visible wavelength range of 3800-7000 Å at a resolving power of ~1000. A long slit, oriented in the N-S direction, 4 mm in length and 35 μm in width was used for the observation of both comet and standard. Considering the current plate scale of the instrument, the physical length and width of the slit corresponds to 3.36 arcmin and 1.76 arcsec. In this case, due to the narrow slit, there could be a loss of flux from the standard star resulting in an underestimation in the flux of the comet while performing flux calibration. Hence, a slit correction factor, as explained in Lee & Pak (2006), is introduced whenever necessary while extracting the spectrum. A tungsten lamp and an Argon-Neon lamp are also included within the instrument to acquire spectrum images to perform flat fielding and wavelength calibration respectively.

EMPOL: The 1.2 m MIRO telescope houses an EMCCD based optical polarimeter. It is an in house developed instrument (Ganesh et al., 2020) with a 1K × 1K ANDOR EMCCD having a plate scale of 0.72 arcsec per pixel in a 4 × 4 binning mode. Initially the instrument consisted of a retractable glan prism, rotating half wave plate, a foster prism, a 12 position filter wheel from Finger Lakes Instrumentation and an EMCCD as the detector. Currently, the foster prism has been replaced with a wire grid and a half wave plate has been introduced after the rotating component. The polarisation measurement is carried out using the rotating half-wave plate (48 steps per rotation) as the modulator and the wire grid polariser as the analyser. The foster prism was replaced with wire grid in order to utilise the entire Field of View (FoV) while the fixed half wave plate was introduced to cancel out the wavelength dependence of polarisation angle. The retractable glan prism is used to produce 100 percent polarised light in order to check the efficiency of the instrument (see Section.2.3.4 for more details). The filter wheel containing broadband Sloan and Bessel filters (u, g, r, i, z, U, B, V, R, I) is placed after the analyser to measure the degree of polarisation in different wavelength regions. An option to provide a user defined EM gain during observations makes this in-house developed instrument the perfect choice for the precise measurement of degree of polarisation (within 0.2 %) for even faint objects.

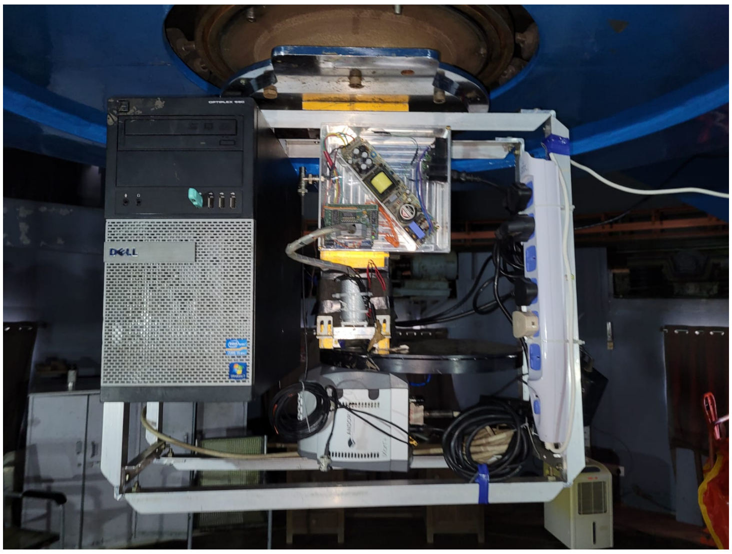

Figure 2.3: Image of optical polarimeter EMPOL

CCD Imaging: Apart from the regular instruments mounted on the 1.2 m MIRO, it also owns a simple imaging system consisting of a detector and a filter wheel. The detector is a 1K $\times$ 1K pixel EMCCD camera (Ixon) from Andor. The EMCCD is mounted at the Cassegrain focal plane. With 2×2 on-chip-binning mode we achieve a plate scale of 0.36 arcsec/pixel. A CFW-2-7 (7 position, 2 inch diameter per filter) model filter wheel, from Finger Lakes Instrumentation, holds the Johnson-Cousins (*UBVRI*, as described by Bessell, 2005) broadband filters. The 12 position filter wheel with the narrow band comet filters loaded can replace the filter wheel in this setup so as to perform narrow band comet imaging.

2.2.2 Himalayan Chandra Telescope (HCT)

The 2 m HCT is located at Hanle, Ladakh (Longitude: 78° $57'$ $49.8''$ East; Latitude : 32° $46'$ $46.3''$ Altitude : 4475 m). It is an f/9 Ritchey-Chretien alt-azimuth mount telescope. We use the Himalaya Faint Object Spectrograph and Camera (HFOSC)[4] for both imaging and low resolution spectroscopic observations while the Hanle Echelle Spectrograph (HESP)[5] is used for high resolution spectroscopy. Comets being solar system bodies move at a different rate across the sky. Hence these objects are tracked

[4] https://www.iiap.res.in/iao/hfosc.html
[5] https://www.iiap.res.in/hesp/

at non-sidereal rate during spectroscopic and imaging exposures, using the keystone mode available in the HCT telescope control system. In this mode a trackfile containing the comet's altitude-azimuth coordinates at regular intervals, is given as an input to the system. This mode of observation has been incorporated effectively in order to point the telescope at the comet and maintain the comet at a fixed location for desired amount of time. Once the comet is in the field of view of the instrument, using the trackfile, the bias offset is hence used to place the comet on the required location. This technique has been proved efficient for tracking the comet for even longer exposures which was not possible earlier. The sky frame required for comet (to remove the sky contribution in the comet spectrum) is obtained by changing the already set bias offset so as to point the telescope to the required position in sky with reference to the comet. The sky frames are usually taken at about 1° away from the photocentre since the coma contribution of the comet extends to a wide area in the sky.

HFOSC: HFOSC is an optical instrument with the capability of imaging and spectroscopic observation. It uses a 2K $\times$ 4K CCD having a pixel size of 15 $\times$ 15 μm with a CCD pixel scale of $0.296''$ per pixel. 2K $\times$ 2K portion of the CCD is used during imaging and 1.5K $\times$ 4K during spectroscopy in order to get a good spatial coverage for the comet. Multiple grism, providing distinct wavelength range for observations at different resolutions, are available. Our spectroscopic observations with HFOSC are usually carried out using grism 7 (Gr 7) providing a wavelength range of 3700 - 6840 Å. We have also used grism 8 (Gr 8), providing a wavelength range of 5800 - 8350 Å, for certain comets. In both the cases, a long slit, $11'$ in length and $1.92''$ in width, is used for the observation of comets and another long slit $15.41''$ in width, is used for the observation of spectroscopic standard star. Both the slits are placed horizontally in the E-W direction. With this configuration, we have a spectral resolving power of 1330 (Gr 7) and 2190 (Gr 8) for comet observations. The Johnson-Cousins *BVRI* filters are used in the imaging mode. A halogen lamp and an FeAr lamp are also available within the instrument to acquire spectrum images to perform flat fielding and wavelength calibration respectively during the reduction of spectroscopic data (see Section.2.3.1).

HESP: The HESP instrument is a bench mounted, dual fibre-fed spectrograph (Sriram et al., 2018). Using an R2 echelle grating along with 2 cross dispersing prisms and a 4K×4K E2V CCD, it covers a wavelength region 3500 - 10,000 Å at two modes of spectral resolution, 30,000 (medium-res) and 60,000 (high-res). A 100 micron slit is used as input slit in the low resolution mode while an image slicer helps achieve the high resolution. It posses two pinholes separated by 1.25 mm ($\sim$ 13 arcsec) to incorporate multiple modes of observation like star-sky, star-calib, and calib-calib. Comet observations make use of the star-sky mode where the sky fibre will also be contaminated by the cometary emissions owing to the close distance of the fibres. Hence, in principle, data from both the fibres can be used to analyse the emissions from the comet at two different locations in the coma. The slit width used in the high-res mode is 0.14 mm and 0.34 mm in the case of medium-res. Even though the telescope tracks comet with the help of the trackfile, the presence of a pinhole viewer camera gives the user the liberty to manually make sure that the pinhole is place on the photocentre throughout the exposure time. ThAr lamp and Quartz-Blue lamp present within the instrument are used for the calibration and flat fielding purpose.

2.3 Observation, Reduction and Analysis

The observational facilities and their respective instruments briefed in Section.2.2 have been used to obtain data for various comets. While getting data itself needs considerable luck and effort, their reduction and analysis to confirm their credibility is a herculean task. This section explains the intricate observational details involved in various techniques (spectroscopy, polarimetry and imaging) with their respective subsections providing details regarding the necessary steps involved in their reduction process as well as the scientific analysis of the reduced data.

2.3.1 Low resolution Spectroscopy

Observation and Reduction: Low resolution spectra of comets are obtained using both LISA and HFOSC. They differ slightly only in the spectral resolution. During these observations, a standard star from the catalogue of spectroscopic standards in IRAF[6] is observed for the purpose of flux calibration. Flat lamp spectra, zero exposure frames and calibration lamp spectra (details of lamps given in the respective subsection of the instrument) are also obtained at regular intervals for flat fielding, bias subtraction and wavelength calibration respectively. The placement of the comet at any location on the slit is a bit more easier in the case of LISA as compared to HFOSC, due to the availability of a guider CCD and manual control of the telescope. Hence, for bright comets, LISA gives us the luxury to obtain the spectra for tail part and head part in a rather easy manner.

In the case of both the instruments, since comets are tracked in the appropriate rate, exposures of desired duration, based on brightness of the comet, are obtained at the photocentre. While observing a comet, the comet frame and its corresponding sky frame are obtained with the same exposure settings. A raw spectrum obtained from low resolution spectroscopy is simply the distribution of photon intensity across the CCD. The spectrum is spread over the dispersion axis and the length of the slit decides the spatial extent covered (see Figure.2.4). In the case of comet observations, a longer slit helps in studying the spatial distribution of the various emissions present, as a function of distance from the photocentre. As part of the basic reduction procedure, the bias frames are used to remove the bias contribution from the CCD and flat frames are used to normalise the pixel to pixel sensitivity variation present in the CCD. Since, comet observations require relatively longer exposure, the frames are likely to be contaminated with the cosmic ray emissions which appear as bright spots on the CCD. In this work, the *cosmicrays* module available in IRAF is used to remove the cosmic rays present in comet frames observed from MIRO, while, the Laplacian Cosmic Ray Identification (van Dokkum, 2001)[7] procedure is used for observations made from HCT.

[6] The full list of spectroscopic standards available in IRAF can be found in http://stsdas.stsci.edu/cgi-bin/gethelp.cgi?onedstds

[7] http://www.astro.yale.edu/dokkum/lacosmic/

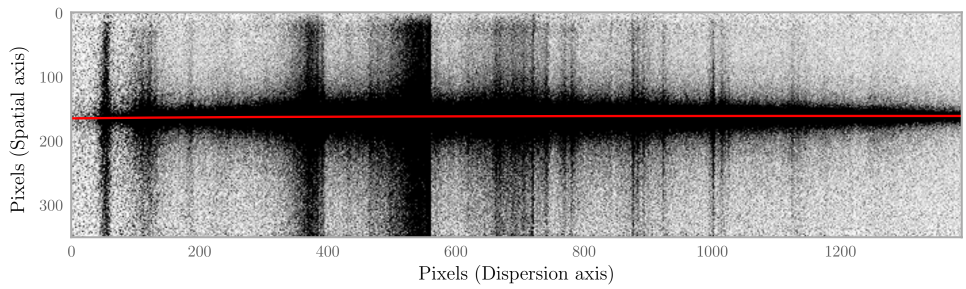

Figure 2.4: Raw image of a comet spectrum observed in low resolution

The reduced sky frame is subtracted from the corresponding comet frame in order to remove the background sky contribution like telluric lines and other bands. A separate sky frame is necessary for comet but not for standard star due to the spatial extent of the comet spectrum, which makes it difficult to extract a sky spectrum from the same frame. Hence, standard star spectrum can be extracted using the IRAF *apall* task, since it allows to perform an effective sky subtraction using regions on both sides of the target. The same module can be used for comets with the sky subtraction routine turned off. As mentioned before, since comet spectrum has a spatial extent, apertures of equivalent width can be used to analyse the behaviour of emissions as a function of cometocentric distance (see Figure.2.5).

Extraction of comet spectroscopic data (using IRAF) requires extensive attentiveness while extracting multiple apertures since care has to be given to use the same trace of extraction (along the dispersion axis) for all the apertures. A slight difference in fitting the trace from one aperture to another can cause changes in the final spectrum, in turn affecting the end results. Hence, a python code was scripted and stabilised to provide desired outputs for any comet data. The details regarding the PYTHON routine is given in APPENDIX.A. The end result of this routine would be a list of spectra corresponding to the increasing apertures defined to one side of the photocenter (see Figure.A.7).

The pixel scale in the dispersion axis is to be changed into wavelength in order to identify/extract the molecular bands corresponding to various species. In the case of LISA, an Argon-Neon lamp is used while an Fe-Ar lamp is used for HFOSC. Figure.2.6 illustrates the spectrum extracted for the above mentioned lamps. The lines present in these spectra are identified for their wavelength using *identify* module in IRAF, with the help of predefined line maps to create a wavelength solution. The pixel axis of the comet or standard star spectrum gets converted into wavelength scale once this solution

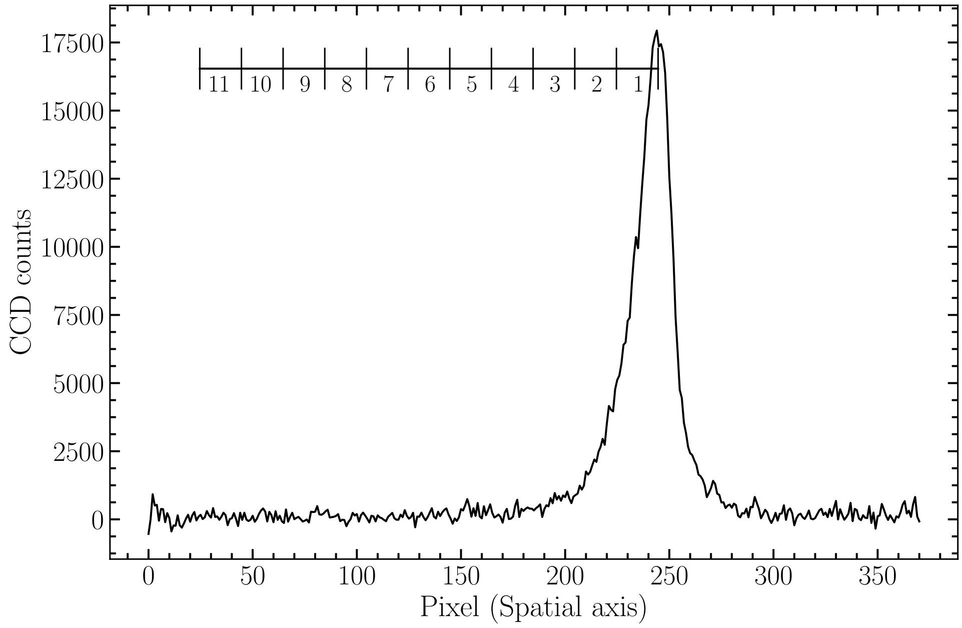

Figure 2.5: Schematic representation of aperture selection required for comet spectrum extraction

is applied with the help of *dispcor* module. After the spectrum has been wavelength calibrated, the next major step is to flux calibrate the comet spectrum. It is only after flux calibration we can extract the flux corresponding to each molecular emission bands.

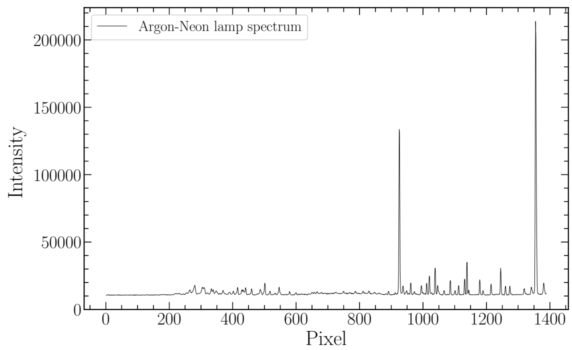

(a) Spectrum of Ar-Ne lamp present in LISA.

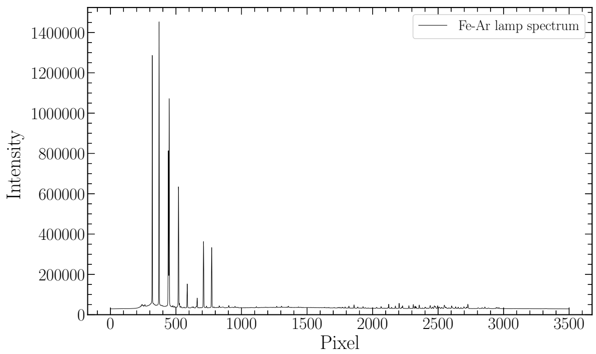

(b) Spectrum of Fe-Ar lamp present in HFOSC.

Figure 2.6: Wavelength calibration lamp spectra for LISA and HFOSC.

In order to convert the CCD counts to actual flux terms, a sensitivity curve of the instrument as a function of wavelength is required. Figure.2.7 displays the sensitivity function of both LISA and HFOSC. This function is obtained by making use of the already observed wavelength calibrated standard star spectrum along with the predefined flux catalogues of the same star in the *std* and *sensfunc* modules available in IRAF. Dividing these sensitivity functions with the comet spectrum converts the spectrum intensity into flux (ergs/cm^2/s/Å). These wavelength and flux calibrated spectra corresponding to all the apertures are further used in analysis to study the different molecular emission bands present in the spectrum to get a general understanding of the comet.

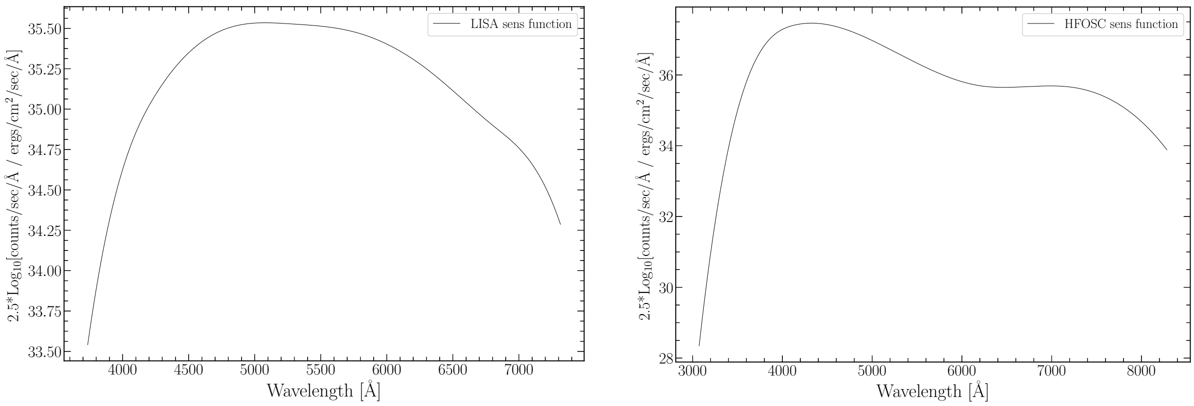

(a) Sensitivity function of LISA CCD.

(b) Sensitivity function of HFOSC CCD.

Figure 2.7: The CCD sensitivity of LISA and HFOSC.

The comet spectrum is comprised of both the coma gas emission spectrum and the spectrum of the sunlight scattered by the dust particles. Hence, it is necessary to remove the continuum signal in order to study the gaseous emissions. A Sun spectrum or a solar analog spectrum is used to remove the continuum signal. In this work, either a solar analog star or the high resolution Sun spectrum from Kurucz et al. (1984) has been used. Initially, in the case of the Solar high resolution spectrum, the spectrum is gaussian convolved to match the resolution of our instrument. Later, the degraded solar spectrum or observed solar analog spectrum is normalised and scaled to the comet continuum flux (see Figure.2.8a). A 5th degree polynomial is fitted to both the comet and solar analog spectrum for the continuum windows mentioned in Ivanova et al. (2021a). The scaled solar analog star spectrum is multiplied by the ratio of these polynomials (to correct for the redder nature of the cometary dust) in order to obtain a continuum spectrum of the comet as shown in Figure. 2.8b. This continuum spectrum is now subtracted from the original comet spectrum to obtain the pure emission spectrum.

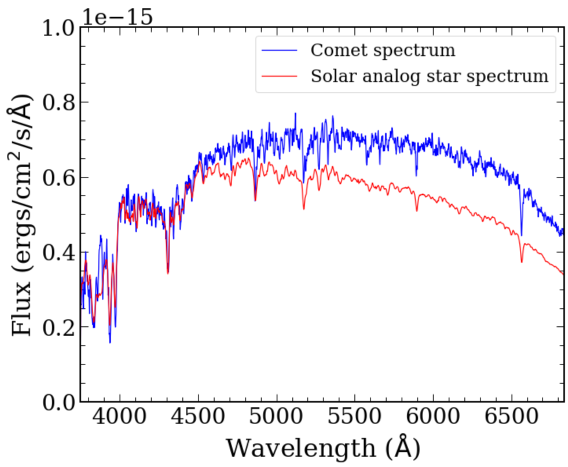

(a) Comet spectrum overplotted with the scaled spectrum of the solar analog star.

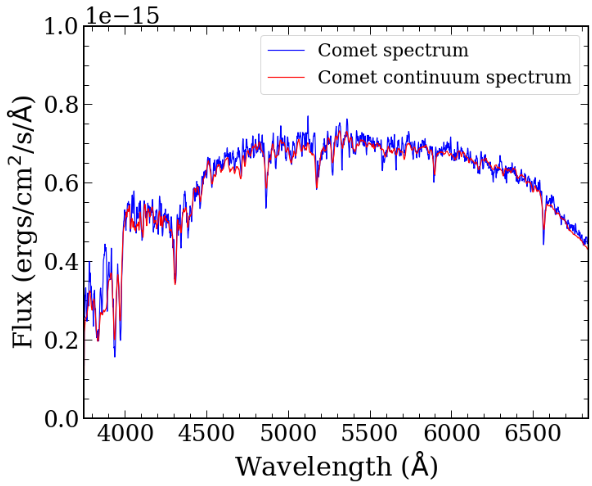

(b) Comet spectrum overplotted with the synthetic continuum spectrum.

Figure 2.8: Continuum fitting for a comet spectrum extracted at the photocentre using a single pixel aperture.

Analysis: As the comet spectrum is a combination of the fluorescence emission from the gaseous species and the continuum emission coming from the Sun light reflected by the dust particles, the continuum flux can be used to study the dust activity present in the comet. A'Hearn et al. (1984b) defined a parameter $Af\rho$, which is a proxy to the amount of dust produced. In our work we compute $Af\rho$ for the blue continuum (4390–4510 Å) (hereby called BC) and green continuum (5200–5320 Å) (hereby called GC) narrow-band filters regions. The specifications of the narrow band filters are discussed in (Farnham et al., 2000).

While using the spectroscopic data to compute $Af\rho$, it is necessary to convert the observed flux obtained using long slit into a full disk flux. To attain this, we have used a geometrical conversion factor, in a similar way as used by (Langland-Shula & Smith, 2011), for each column of fixed aperture moving outwards from the centre of the nucleus (see Figure.2.9). The geometrical conversion factor is defined as the ratio of area of the circular/annular area to the area of the aperture used. The spectrum extracted for each column of fixed aperture, as explained in APPENDIX A, is now multiplied with the corresponding conversion factor to convert the spectrum into circular/annular flux. In order to obtain the full disk flux within each increasing aperture radius, the flux computed for each circular/annular region within the required radius are added up.

The production rate of each molecular emission ($CN(\Delta v = 0)$, $C_3(\lambda 4050\text{Å})$, $C_2(\Delta v = +1)$

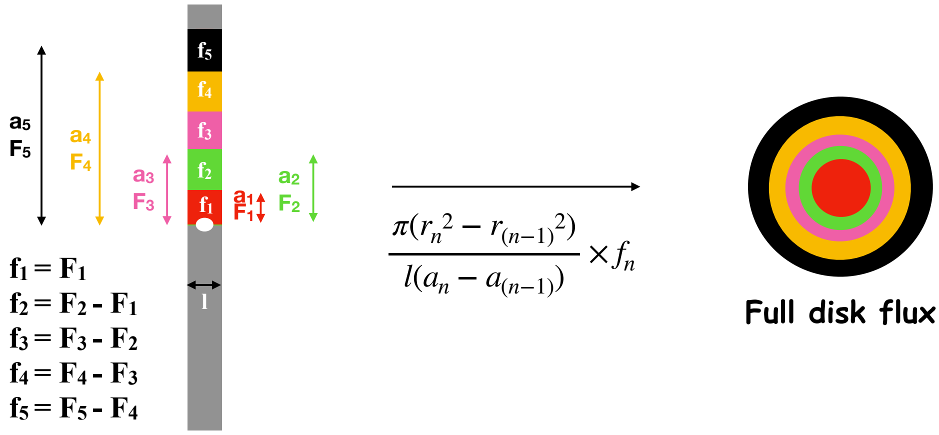

Figure 2.9: Pictorial representation of the method adopted for converting flux in long slit spectra into full disk.

and $C_2(\Delta v = 0)$) can be computed from its column density profile using the Haser model if the spectrum has good enough Signal to Noise Ratio (SNR) along the spatial axis. On the other hand, for a faint comet whose spectrum is not strong enough to provide a sufficient SNR along the spatial axis, the total flux (full disk flux) present in the wavelength range of each molecular band can be used directly to compute the production rate. Details regarding the computation of $Af\rho$ and production rates are given in APPENDIX B.

2.3.2 High resolution Spectroscopy

Observation and Reduction: Comets being Solar system bodies cannot be tracked in the normal observing mode. Hence, initially the comet was placed on the object pinhole with the help of feedback and its position was adjusted manually for its varying motion, time-to-time, using the direction keys in the keystone mode. Currently, the tracking technique explained in Section.2.2.2, being implemented for observation of comets using the HFOSC instrument on the HCT is applied for HESP observations so that the continuous manual correction of the comets position would not be required. Most of the observations are carried out in the medium-res mode, ($\lambda/\Delta\lambda \sim$ 30,000).

Comets being extended objects, observation in high-res mode, ($\lambda/\Delta\lambda \sim 60{,}000$) require the comet to be bright enough in order to obtain the necessary SNR. Hence, only a few comets can be observed in the high-res mode. Multiple frames with adequate exposure are obtained for most of the comets during every epoch. Figure 2.10 illustrates a snapshot of the raw data obtained for a comet in the HESP instrument. Along with the comet observation, sky frames are also obtained in order to analyse the strong atmospheric emissions present. Bias frames, Quartz-Blue lamp and Th-Ar lamp spectra are also obtained to perform the bias correction, flat fielding and wavelength calibration. All the observed data were reduced with the help of HESP python pipeline[8].

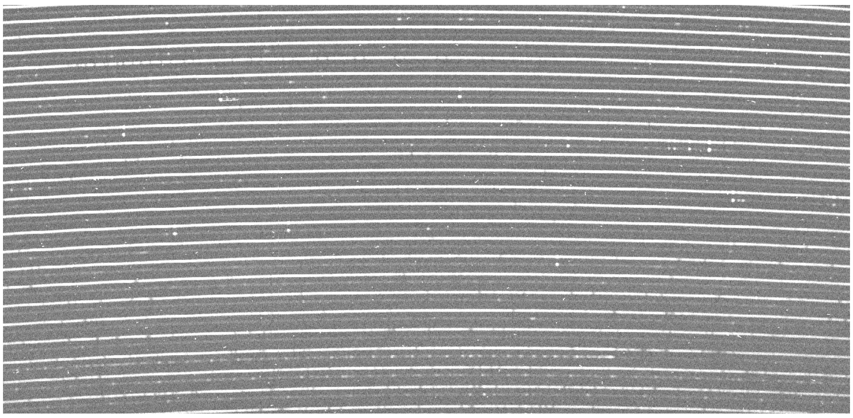

Figure 2.10: Raw image of the high resolution spectrum observed with HESP

The spectrum extracted from multiple frames for each comet are combined to increase the SNR. A Doppler shift correction is incorporated with the help of *dopcor* module in IRAF to account for the shift in emission lines due to the geocentric velocity ($\dot{\Delta}$) of the comet. The continuum present in each extracted order is removed by fitting a continuum to the spectrum using the generic continuum fitting function present in the specutils module of PYTHON. Since comet observations are carried out in Star-Sky mode, there would be comet high resolution spectrum corresponding to both pinhole inputs, Fibre 1 and Fibre 2. With the distance between both the fibres known to be 13 arcsec, the physical distance in the coma can be computed using the geocentric distance for each epoch. Hence, in principle, data from both the fibres can be used to analyse the emissions from the comet at two different locations in the coma.

[8] https://www.iiap.res.in/hesp/hesp_pipeline_manual.pdf

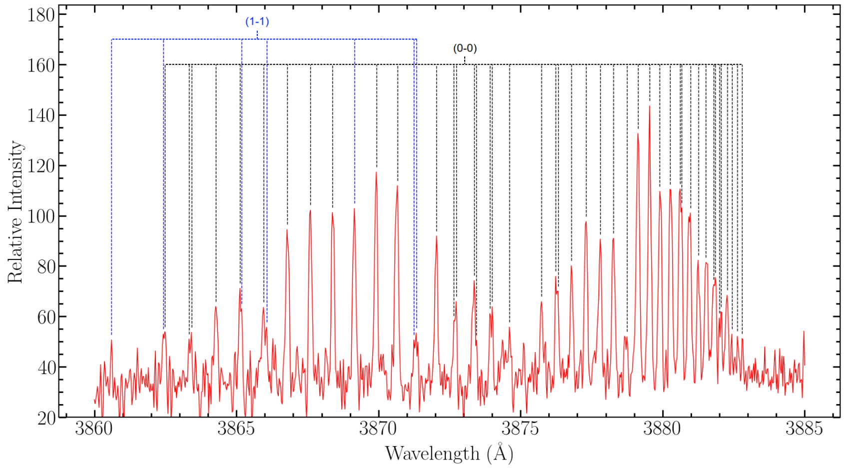

Figure 2.11: Cross identification of the vibrational transitions present in the CN ($B^2\Sigma^+$-$X^2\Sigma^+$) electronic band of comet C/2015 V2 observed on 2017-02-22.

Analysis: Among the other high resolution spectroscopic observations carried out on comets, there are few cometary emission line catalogues available which can be used to identify the emission lines present in the comets observed in this work. Even though the molecular line list provided by (Cambianica et al., 2021) is the latest and more exhaustive one, we have used the emission line catalogue provided by (Cochran & Cochran, 2002) due to the similarity in the wavelength range being considered along with the comparability of the resolution used. PYTHON scripts have been used to identify the peaks present in the spectrum and the STIL Tool Set (STILTS; Taylor, 2006) has been used to cross match the identified lines with the available line catalogues of different molecular bands. Since certain orders of the spectrum does not have very high SNR, special care has been taken to avoid matching noise as a detected line. We have considered the standard deviation in the continuum of each order as noise (1σ) and selected those lines with signal above 3σ level to be matched with the catalogue and identified (see figure 2.11 for cross-identification). Also, similar to what has been done in (Cambianica et al., 2021), the catalogue lines have been matched with the observed emission line only if the wavelength coincidence was within the spectral resolution (i.e $\pm 3\Delta\lambda = \lambda/R$, where R is the resolving power of the instrument). Considering the density of lines and relatively low SNR in certain orders of the spectrum, some line coincidences are believed to be accidental.

2.3.3 Optical Imaging

Observation, Reduction and Analysis: Imaging of comets are performed using both HFOSC and the optical imager available for MIRO. Imaging observation are carried out mostly in the *BVRI* filters. Exposure time required is fixed based on the brightness of the comet. Since, the comets are tracked in non-sidereal mode, long enough exposures are also possible. Acquiring multiple frames is necessary in order to improve the SNR and improve the contrast of any features present in the coma. Any photometric standard star or field is chosen to be used for photometric calibration. Mostly, the photometric standard star field Ru149 is chosen as it contains more number of standard stars. Twilight flats are obtained in all the filters used for observation to normalise the pixel to pixel response of the CCD. Zero exposure bias frames are also obtained so as to perform the bias correction.

A self scripted PYTHON routine is used to perform all basic data reduction techniques (bias subtraction, flat fielding and median combining) on both comet and standard star images. Aperture photometry is performed on the comet and standard stars using the PHOTUTILS package in Astropy. The instrumental magnitudes of the standard stars are then corrected for both extinction and colour. Extinction coefficient values (magnitude/airmass) of various filters, as given in Stalin et al. (2008), are used to apply the extinction correction to the instrumental magnitudes of the standard stars as well as the comet images obtained from HCT. The coefficients for Mount Abu are taken from an in-house project carried out for computing the extinction values for the site. The zero point offset in magnitude is computed with the help of Landolt's standard star magnitudes as given in Landolt (1992). The comet instrumental magnitude are then corrected for the zero point to obtain its apparent magnitude in various filters.

2.3.4 Optical Imaging Polarimetry

Observation and Reduction: Section.2.2.1 explains the working of the EMPOL instrument and the measurement of polarisation with the help of a rotating half wave plate (HWP). The maximum exposure that can be provided to a single frame is 0.5 s due to the constrain from the rotating HWP. The total number of frames to be acquired is decided based on the effective exposure required per frame. Considering the exposure per frame as 0.5 s, a complete rotation of the half wave plate consists of 48 frames and an effective exposure of 10 s per frame was required, a total of 1008 frames are acquired (See Equation.2.1). Depending on the brightness of the comet, an EM gain can be set for the CCD in order to improve the signal.

$$n = \left(\frac{Effective\ exposure}{0.5} + 1 \right) \times 48, \tag{2.1}$$

Since, the HWP is in continuous rotation, starting the exposure at different points for each set would affect the final computed polarisation angle of the object. Hence, it has to be made sure that the first exposure is triggered only when the HWP is at a particular location after which the rest of the frames follow. Other than the exposure time per frame which is fixed, various other parameters like binning, read out speed, location for auto save, output file format, acquisition mode etc are also to be set before starting each set of observation. Therefore, to make these tedious settings a bit more user friendly, a code was scripted in the ANDOR BASIC. The code makes sure that the series of CCD exposure is triggered only when it receives a signal from the rotating HWP as it reaches a predefined location. Along with this, it also designates the predefined settings mentioned previously. The user can beforehand provide the final path for saving the files and the amount of EM gain required, in the ANDOR BASIC code available in the system. Once the code is executed, it receives input from the user regarding the filename required, total effective exposure required (to decide the total number of frames to be acquired based on Equation.2.1) and an option to chose whether to turn on EM gain or not. Once the CCD receives the trigger signal from the instrument, the frame acquisition starts.

The raw frame corresponding to one of the 48 steps is as shown in Figure.2.12a. Another set of data, namely sky frames, using the same settings is also taken with the telescope pointed $\sim 1^\circ$ away from the comet. These would be used to remove any contribution of sky polarisation in the comet frames. Twilight flat frames and bias frames are also acquired as per requirement. During the observation, a few high polarised standards listed in Schmidt et al. (1992) are observed in order to confirm the operation of the instrument and to obtain the zero point correction of the polarisation angle. The observation can be carried out in either *Sloan* or *Bessell* broad band filters as per requirement. During the reduction of both comet and standard star frames, all the single frames were initially bias subtracted and flat fielded. Since there would be a slight shift in the object position from frame to frame due to the variable tracking, they were shifted to a common point and then median combined in order to build up the signal. After the reduction process we are left with 48 frames, each with the user defined effective exposure, (see Figure. 2.12b) which would now be used to compute the degree of polarisation and polarisation angle.

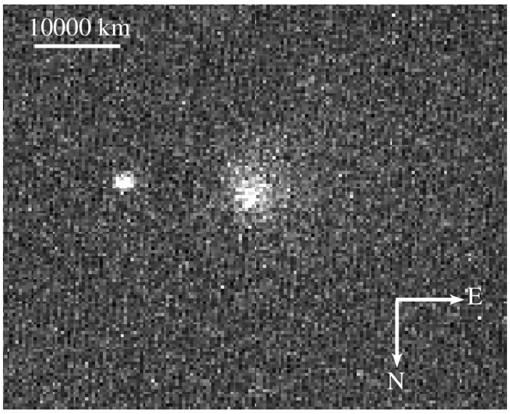

(a) Single raw frame (0.5 s exposure) of the comet obtained during the polarisation observation. Gain is used appropriately based on the comet brightness.

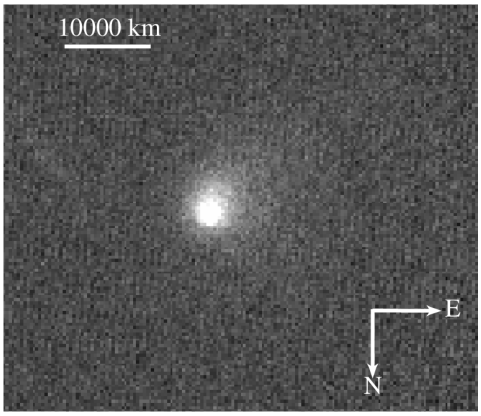

(b) One frame among the 48 final frames where the corresponding single frames have been reduced, shifted and combined to increase the SNR.

Figure 2.12: Comparison of the raw output of EMPOL instrument with the reduced and combined image.

Analysis: As previously mentioned, the final product after all the reduction process would be 48 frames of the standard star or comet which is to be used to compute the degree of polarisation and polarisation angle. The 48 frames correspond to 48 angles spanning from 0 to 360 degree. A PYTHON code is used to perform aperture photometry on all the frames of the object being analysed to obtain the counts within a fixed aperture (optimum aperture). Knowing the counts corresponding to each of the

48 angles, the equation

$$I_o = \frac{1}{2}[I + Q\cos 4\theta + U\sin 4\theta], \tag{2.2}$$

where I_o is the observed intensity corresponding to the θ in radians, is used to get the best fit Stokes' parameters I, Q, U. Figure. 2.13 illustrates the modulation of the observed intensity across the 48 frames of a random star observed with the glan prism introduced, over plotted with the best fit curve used to determine the Stokes' parameters. Once the Stokes' parameters are derived, the degree of polarisation (DoP) and the position angle for the plane of polarisation (PA) are calculated using the equations 2.3 and 2.4 respectively. Since, the glan prism is introduced in this case, the observed polarisation would be about 100% as expected. This implies that the instrument itself does not cause any decrease or increase in the measured polarisation.

$$DoP = \frac{\sqrt{Q^2 + U^2}}{I} \tag{2.3}$$

$$PA = \frac{1}{2}\tan^{-1}\left(\frac{U}{Q}\right) \tag{2.4}$$

The uncertainties in the measured quantities are determined using error propagation (eg. Dolan & Tapia, 1986), making use of the uncertainties in the derived Stokes' parameters obtained from the curve fitting. These analysis techniques are performed on the observed comet and the standard star frames. Radially increasing apertures can also be used to check for any spatial variation in the degree of polarisation as observed in comet 67P (Rosenbush et al., 2017).

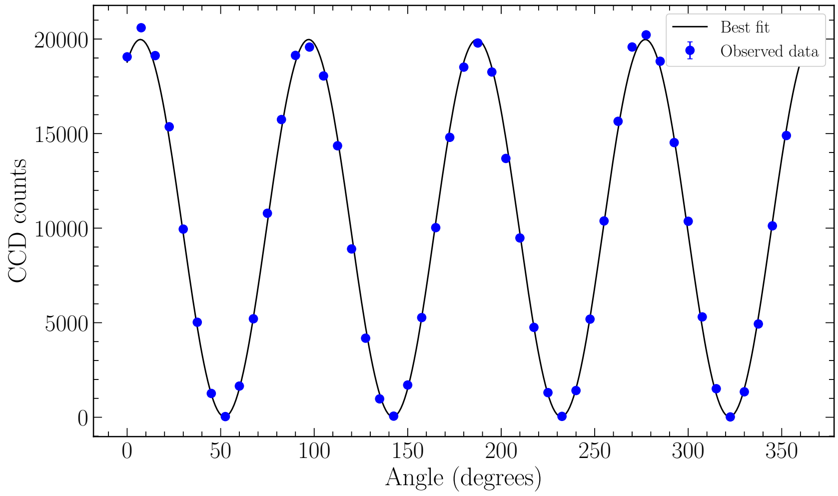

Figure 2.13: Intensity modulation derived from the 48 final frames obtained from the polarisation observation a star with the glan prism introduced. The black solid line portray the best fit for the equation.2.2 used to compute Stokes' parameters.

2.4 Narrow band filter system

Generally, the bandwidth of the usual broad band filters are highly contaminated with emissions from different molecular bands as shown in Figure.2.14a. Hence, broad band imaging techniques are not efficient in differentiating and analysing the flux corresponding to various emissions or the continuum region. The *Bessell* broadband R filter can be used to analyse the dust present in the redder region as this region is not majorly populated by different emission lines as observed for other broadband filters. With an objective to isolate and study the major emissions and continuum region present in comets through imaging, different observers implemented different filters. This led to discrepancies in the conclusion due to the variation in the filters. The first standardised filter set consisting of filters to isolate the three main emissions, CN, C_2, C_3 and their corresponding continuum points was first used by A'Hearn & Cowan (1975) and A'Hearn et al. (1977) and later up to 1983.

Later, in order to better standardise the filter set, the IAU funded International Halley Watch (IHW) narrow bands filters (See Osborn et al., 1990) was developed in 1984 keeping in mind the approaching perihelion of the great Halley's comet. The IHW filter was in use for around 25 years observing a large number of comets (eg., A'Hearn et al., 1995). Later, close to 2000, in order to enhance the narrow band filter set and to establish a standard star system, Farnham et al. (2000) developed a new set of narrow band filters. They contained filters to study the flux corresponding to OH, NH, CN, C_2, C_3, CO^+, H_2O^+ emissions and continuum in the UV, blue, green and red region of the spectrum (see Figure.2.14b for transmission profile of few filters). These filters, developed primarily for the observation of the next great comet Hale-Bopp are hence known as Hale-Bopp (HB) filter set. The entire set was designed incorporating a better understanding of the different emissions so as to reduce the contamination of the undesired species as compared to the previous filter set.

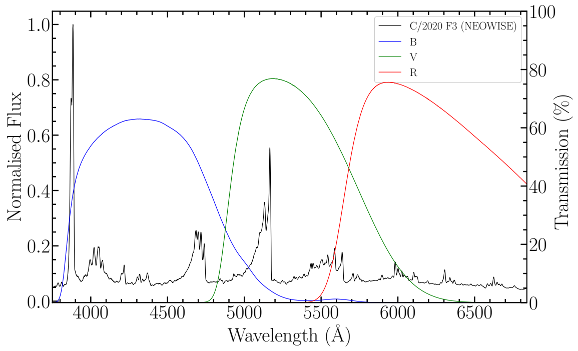

(a) Bessell Broad band filter profiles overplotted on comet spectrum

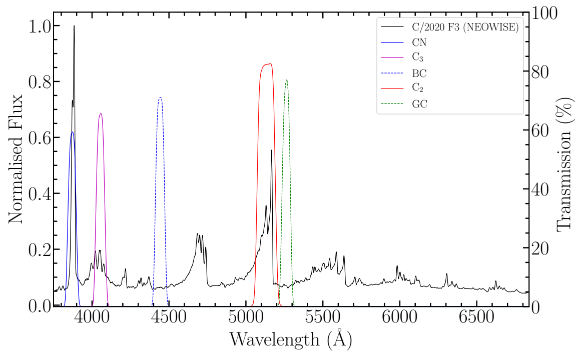

(b) Narrow band filter profiles overplotted on comet spectrum

Figure 2.14: Comparison of the available broad band and narrow band filter transmission profiles with comet spectrum in the optical regime.

The narrow band filter set was developed, characterised and sold across the world for comet observations. The filters for CN, C_2, C_3, BC, GC and RC were acquired by PRL in 1997. They have been employed in various comet observations (Venkataramani, 2019). In Figure.2.15 the filter profiles of the above mentioned filters over the years have been compared. The dashed lines and solid lines corresponds to the peak transmission and central wavelength respectively for the filter reported by Farnham et al. (2000). The numbers in red represent the measured full width at the corresponding power points for the filters available with us. Even though the measured values for the available filters have certain discrepancies with the reported values, it can be seen that there is not much variation in the transmission profile over the years. Possibility of improvements in any of the filters or requirement of an additional filter is discussed further in Section.8.1.3.

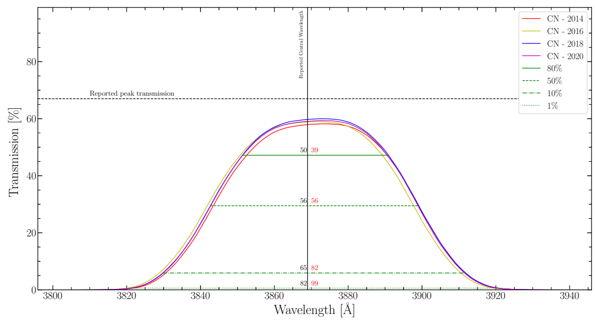

(a) CN filter transmission

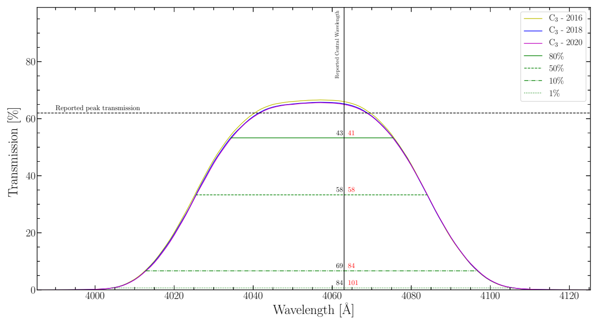

(b) C_3 filter transmission

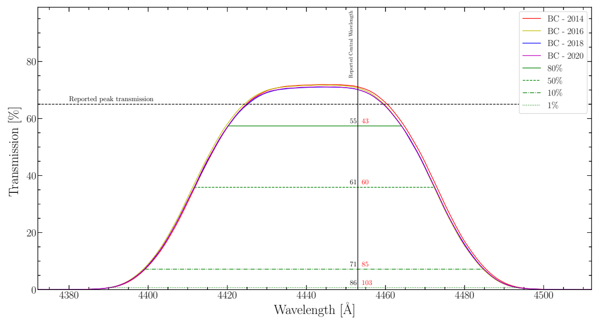

(c) BC filter transmission

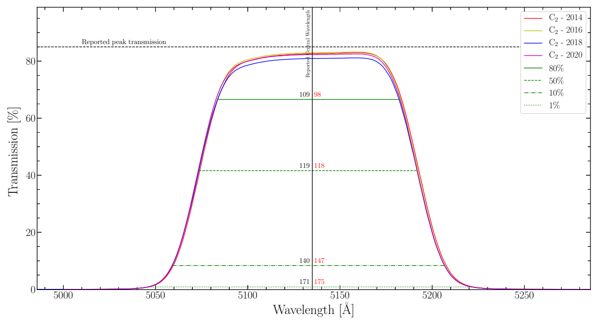

(d) C_2 filter transmission

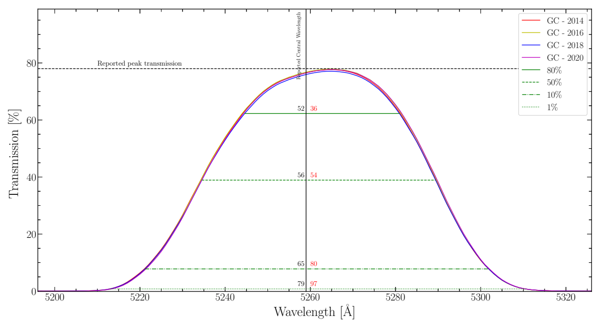

(e) GC filter transmission

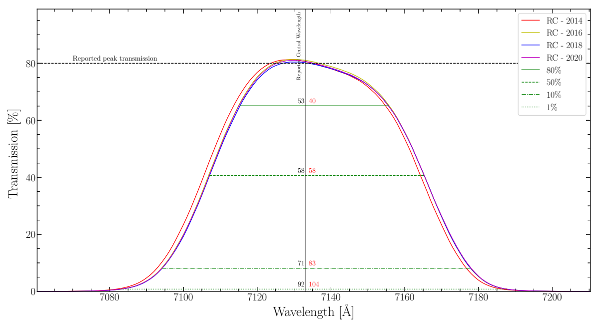

(f) RC filter transmission

Figure 2.15: Comparison of the transmission curve for different narrow band filter profiles over the years. The various values reported in Farnham et al. (2000) are mentioned or marked accordingly.

2.5 Summary

Observational astronomy demands quality in both observed data as well as the reduction and analysis techniques. Any unknown error due to manual or natural reasons might end up in a wrong scientific interpretation of the data. Understanding when an observed data or the analysed result can be deemed accurate is principal in this field. Keeping this in mind, a well defined observational techniques and reduction and analysis methods have been fabricated to make best use of the observational facilities and the corresponding instruments. These methods have been used to observe and study the set of comets mentioned in Table.2.2, whose details will be discussed in the upcoming chapters.

This page was intentionally left blank.

Chapter 3

Comet 156P/Russell-LINEAR

3.1 Introduction

Importance of intensive studies of essentially all the observable comets belonging to various reservoirs is pointed out in Chapter.1. Considering the idea that the Jupiter family comets (JFC) have evolved from the Kuiper belt objects (Levison & Duncan, 1997b) due to planetary interactions, it is important to study these objects in detail to get a better understanding on the effects of evolution in the material present in the icy bodies (Tancredi & Rickman, 1992; Farnham, 2009). Simultaneous study of the gaseous and dust emission from the comet, along with polarisation analysis can help one gain greater insight into the type of material present in the comet. Similar works have been carried out on a few other comets like C/2014 A4 (SONEAR) (Ivanova et al., 2019b), C/2009 P1 (Garradd) (Ivanova et al., 2017) and C/2011 KP36 (Spacewatch) (Ivanova et al., 2021c). Comparison between such intensive studies of long period and short period comets would help in unravelling the mystery of primordial and evolutionary signatures present in the comets.

In this Chapter, the results from spectroscopic, photometric and polarimetric observations along with some dust modelling studies of a short period Comet 156P/Russell-LINEAR (hereafter 156P) is presented. Comet 156P is a short period Jupiter family comet discovered by Kenneth S. Russell on 1986 September 3. The comet has an orbital period of 6.44 years, a perihelion distance of 1.30 AU and an aphelion distance of 5.6 AU. Comet 156P had a new passage in 2020, with a perihelion on November 17 and the closest approach to Earth (0.38 AU) on 2020 October 29. Despite the multiple passages of the comet through the inner Solar system, there are no reports on its properties or activity in the earlier literature. The NASA JPL Orbit viewer[1] shows that the comet is well placed for observations during alternate apparitions. This could be the primary reason for the comet not being properly observed and documented. The next favourable apparition would be in 2033 with the closest approach to Earth being 0.514 AU. During the 2020 apparition, Jehin et al. (2020b) and Jehin et al. (2020a) reported the activity of 156P in 2020 October and November.

Here we report the pre and post-perihelion spectroscopic activity of the comet 156P, during 2020 October and December, observed from the 2 m Himalayan Chandra Telescope (HCT) of the Indian Astronomical Observatory (IAO) and 1.2 m telescope of the Mount Abu Infrared Observatory (MIRO), respectively. We also combine the imaging data obtained from both HCT as well as the 0.82 m IAC80, Teide observatory telescope to study the evolution of dust jets present in the coma and the variation of the observed Afρ profile over a period of time. We also report the optical polarimetric observations of the comet observed from MIRO, at two different phase angles. Using the results of the polarimetric observation, dust modelling has been performed with the help of Vikram-100 HPC supercomputing facility at PRL. With the basic details of observation, reduction and analysis of spectroscopic, imaging and polarimetric data already discussed, a brief detail of the observations made for this comet will be looked into and hence the main results are discussed in Section.3.4.

[1]https://ssd.jpl.nasa.gov/tools/orbit_viewer.html

3.2 Observations

The comet 156P was observed from the two Indian observatories HCT and MIRO as well as the Teide Observatory, Tenerife, Spain during multiple epochs. The 2 m HCT, at the IAO, was used for imaging and spectroscopy. At MIRO, the 1.2m telescope was used for spectroscopy and polarimetry. The 0.82 m IAC-80 telescope at the Teide observatory was used for imaging the comet over the period of 2020 November and December. The following sub-sections describe in brief, the details of the observations. The observational log, detailing the telescope facility used, observational technique employed, exposure time, number of frames acquired, heliocentric distance, geocentric distance and phase angle at the time of observations are as given in Table.3.1.

3.2.1 Spectroscopy

Considering the perihelion date of the comet, 2020 November 17, we have covered two epochs in spectroscopy, pre-perihelion and post-perihelion. Even though the two epochs are pre and post-perihelion, it is interesting to observe that the heliocentric distance at the time of observations are similar for both.

During the first epoch, the comet was observed from HCT using the HFOSC instrument. The instrument details are given in Section.2.2.2. Spectroscopic standard star, BD+28 4211 was observed for flux calibration using a slit of width 15.41 arcsec in order to avoid light loss. Frames of necessary calibration lamps were also obtained.

During the second epoch, the comet was observed from MIRO with the help of LISA. The complete details regarding the instrument is given in Section.2.2.1. The comet and a separate sky frame were obtained with an exposure of 900 seconds each. During this epoch, standard star HD 74721 was observed for flux calibration. The required frames for basic reduction purpose are also obtained along with the observation. During both epochs, solar analog HD 81809 (G2V) (Farnham et al., 2000) was observed in order to remove the continuum from the comet spectrum.

As mentioned earlier in Section.2.2.1 and 2.2.2, the comet was observed in non-sidereal

Table 3.1: Observation Log for comet 156P

Date (UT)	Time (UT)	Telescope Facility	Observational Technique	Filter/ Wavelength range ()	Exposure (seconds)	N	Heliocentric Distance (r_H) (AU)	Geocentric Distance (Δ) (AU)	Distance scale at photo-centre (km pixel^{-1})	Phase angle (°)
18/10/2020	15.21	HCT[a]	Imaging	R	30	5	1.380	0.483	103	30.93
18/10/2020	15.28	HCT[a]	Spectroscopy	3800-6840	1200	1	1.380	0.483	103	30.93
13/11/2020	18.70	MIRO[b]	Polarimetry	i	10	48*	1.334	0.509	266	38.90
18/11/2020	21.53	IAC80[c]	Imaging	Open	25	32	1.333	0.526	128	39.86
21/11/2020	00.01	IAC80[c]	Imaging	Open	25	32	1.334	0.537	130	40.42
07/12/2020	19.08	IAC80[c]	Imaging	Open	25	24	1.351	0.618	150	42.17
08/12/2020	19.10	IAC80[c]	Imaging	Open	25	24	1.353	0.624	152	42.25
14/12/2020	19.49	IAC80[c]	Imaging	Open	30	28	1.367	0.663	161	42.36
15/12/2020	17.28	MIRO[d]	Spectroscopy	3800-7000	900	1	1.370	0.670	158	42.35
16/12/2020	14.60	MIRO[b]	Polarimetry	i	10	48*	1.372	0.684	355	42.34
18/12/2020	19.55	IAC80[c]	Imaging	Open	30	24	1.378	0.692	168	42.32
20/12/2020	23.63	IAC80[c]	Imaging	Open	30	20	1.384	0.707	172	42.27
29/12/2020	19.36	IAC80[c]	Imaging	Open	25	19	1.415	0.779	190	41.82

*Explained in Section.3.2.3

[a]IAU-MPC code: N50, HFOSC Resolution: 0.296 arcsec/pixel.

[b]EMPOL Resolution: 0.720 arcsec/pixel.

[c]IAU-MPC code: 954 , Camelot-2 Resolution: 0.336 arcsec/pixel.

[d]LISA Resolution: 0.326 arcsec/pixel.

mode available and on both the epochs, sky frame was obtained 1° away from the photocentre of the comet. The basic reductions, calibrations and spectrum extraction for all the frames were performed as explained in Section.2.3.1.

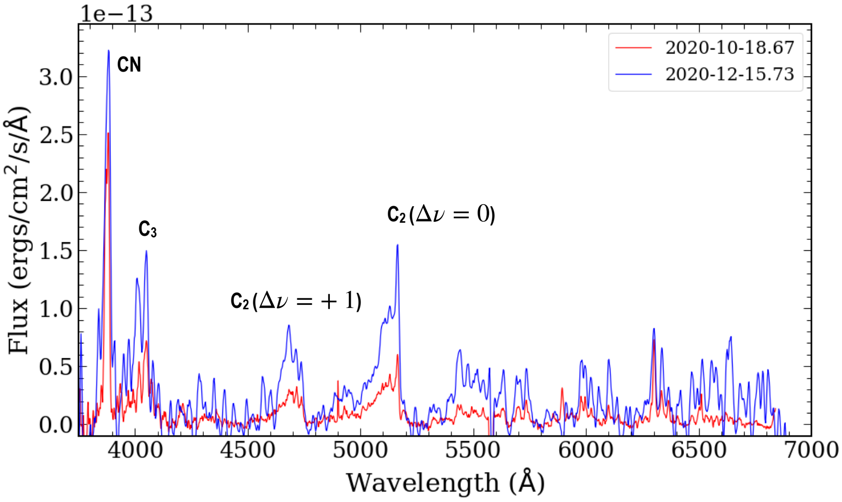

Figure 3.1: *Red:* Optical spectrum of 156P observed pre-perihelion with the HFOSC instrument on HCT on 2020-10-18.67 UT; *Blue:* Optical spectrum of 156P post-perihelion observed with the LISA instrument on MIRO on 2020-12-15.73 UT.

3.2.2 Imaging

The comet 156P was observed in imaging mode from both HCT and IAC-80 telescopes across the months 2020 October to December. As described in Table.3.1, the comet was observed from HCT on 2020 October 18 in the broadband *R* filter. The Landolt's standard star field (Landolt, 1992) Ru 149 in filter *R*, twilight flat and bias frames were also acquired so as to perform the standard photometric analysis (see Section.2.3.3). During the rest of the imaging epochs using the IAC-80 telescope, the comet was observed under the Pro-Am Cometary Morphological Evolution Study (COMES) project[2] using the CAMELOT-2[3] camera containing a 4K $\times$ 4K pixels CCD with a resolution of 0.336 arcsec per pixel. Dark, flat and bias frames were also obtained during all the epochs in order to perform the standard reductions. Firstly, the standard reduction was performed using Python subroutines. Then, the object images with the worst FWHM and deviation from median background level were rejected using PixInsight software. Finally, all the images were aligned to stars, then aligned to comet using the Maxim-DL software and then integrated with the average method.

[2]https://cometografia.es/comes/imagenes/
[3]http://research.iac.es/OOCC/iac-managed-telescopes/iac80/camelot2-2/

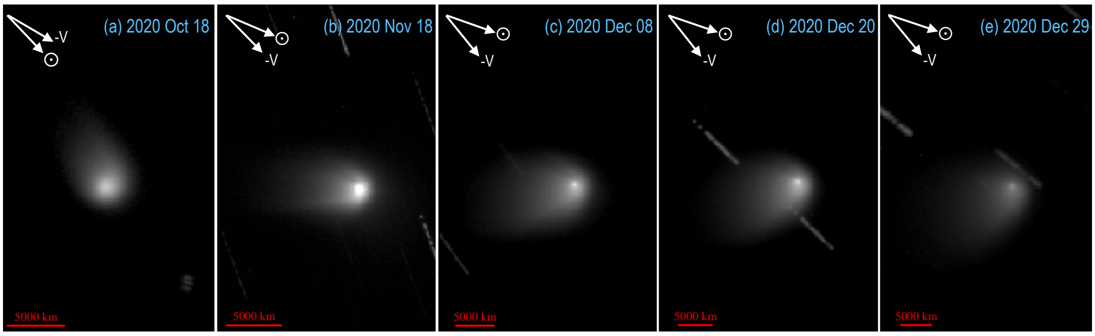

Figure 3.2: Compilation of few of the reduced imaging data obtained for comet 156P/Russell-LINEAR. North is up and East is on left for all the panels and the red solid line depicts 5000 km on the sky at the distance of the comet. The date of observation, direction to the Sun and the direction of negative heliocentric velocity are also mentioned in all the panels. Panel *(a)* depicts observation from HCT R filter and the rest are from IAC observed in the absence of any filter. All the images have been scaled for the best visualization and the resulting gray scale does not represent their actual magnitude.

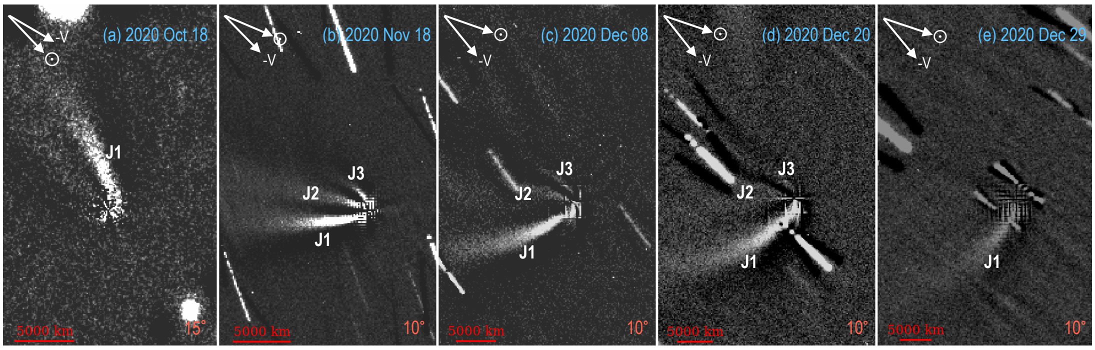

Figure 3.3: Compilation of LS processed outputs of imaging data of multiple epochs displayed in Figure.3.2. North is upwards and East is towards the left for all the panels. The angle of rotation employed for the technique is mentioned in orange coloured text on the bottom right of each panel. The red solid line depicts 5000 km on the sky at the distance of the comet. The date of observation, direction to the Sun and the direction of the negative heliocentric velocity vector are also mentioned in all the panels.

Figure.3.2 compiles few of the imaging observations carried out for comet 156P. To an extent, it illustrates the variation in strength of the coma as the comet crossed perihelion and moved away from the Sun. At a glance, most of the images reveals the presence of probable dust jets arising from the comet nucleus. Further analysis and detailing of these features are described in Section.3.4.2.1.

3.2.3 Polarisation

The EMPOL instrument (see Section.2.3) was used to observe the comet 156P at two different phase angles, 38.9° and 42.34°, in the *Sloan i* filter in order to make sure that the light observed was solely the scattered light from the dust present in the coma. Twilight flat frames and bias frames were also acquired as per requirement. On both the epochs, out of a few high polarised standards listed in Schmidt et al. (1992), BD+64 106 and HD 25443 were observed in order to confirm the operation of the instrument and to obtain the zero point correction of the polarisation angle. Both the standards were observed in *sloan i* filter with an effective exposure of 1 s per frame. The reduction of both comet and standard star frames as well as the analysis procedures are as explained in 2.3.4.

3.3 Data Analysis

3.3.1 Spectroscopy

3.3.1.1 Gas production rates

Strong emissions from $CN(\Delta\nu = 0)$, $C_3(\lambda4050\text{Å})$, $C_2(\Delta\nu = +1)$ and $C_2(\Delta\nu = 0)$ can be observed during both the epochs. Comparing the pre and post-perihelion spectra (see Figure.3.1), it can be inferred that there has been an increase in the activity, post-perihelion, even though the heliocentric distance was almost the same during both the epochs. The production rates of the various molecules detected are computed as elucidated in APPENDIX.B. The values that have been used for $g,\ l_p\ and\ l_d$ at the respective epochs are given in Table.3.2.

Figure.3.4 illustrates the observed column density profile of CN, plotted along with the best fit Haser model used to compute the production rate as mentioned in Table.3.3.

Table 3.2: Scale lengths and fluorescence efficiency of different molecules at both epochs of observation.

	2020-10-18			2020-12-15		
	g-factor	l_p	l_d	g-factor	l_p	l_d
Molecule	$(ergsmol^{-1}s^{-1})$	(10^4 km)	(10^4 km)	$(ergsmol^{-1}s^{-1})$	(10^4 km)	(10^4 km)
CN(0-0)	1.89×10^{-13}	2.47	39.99	2.36×10^{-13}	2.44	39.94
$C_2(\Delta\nu=0)$	2.36×10^{-13}	4.18	12.56	2.40×10^{-13}	4.13	12.38
C_3	5.25×10^{-13}	0.53	5.14	5.33×10^{-13}	0.52	5.06

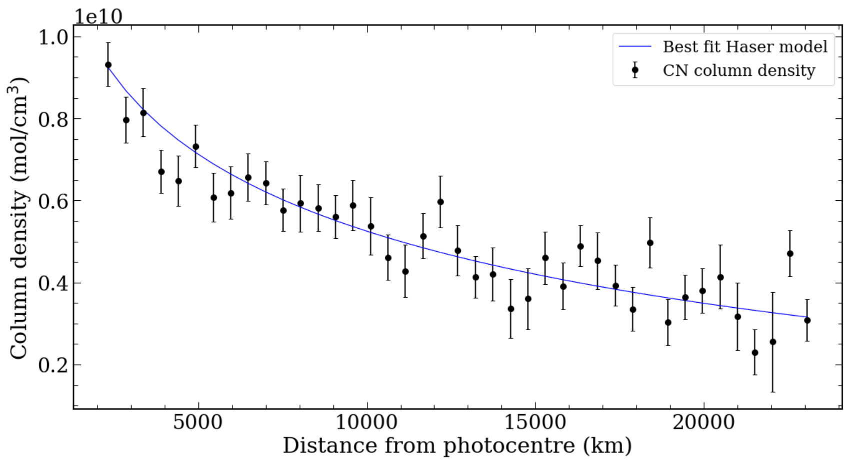

Figure 3.4: Column density profile of CN in the comet as observed on 2020-10-18. The blue solid line depicts the best Haser model fit. Error bars represent the standard error in column density at each respective points.

Table 3.3: Activity of comet 156P at different epochs

Date (UT)	Exposure (s)	r_H (AU)	Δ (AU)	Production Rate (molecules per sec) CN $\times10^{24}$	$C_2(\Delta\nu=0)$ $\times10^{24}$	C_3 $\times10^{24}$	Production rate ratio $Q(C_2)/Q(CN)$	Dust to gas ratio[a] $\log[(Af\rho)_{BC}/Q(CN)]$
2020-10-18.67	1200	1.38	0.48	3.06 ± 0.12	3.32 ± 0.41	0.51 ± 0.05	1.08 ± 0.17	-22.48 ± 0.29
2020-12-15.73	900	1.37	0.67	9.43 ± 0.16	12.5 ± 0.9	2.32 ± 0.26	1.32 ± 0.12	-22.24 ± 0.16

[a] $Af\rho$ corresponding to an aperture size of 10,000 Km has been used to compute the ratio

The production rates of other detected molecules, C_2 and C_3, were also computed in a similar manner for both epochs. The error obtained from the Haser model fitting is taken as the standard error in production rate while the standard errors in the column density are obtained from the propagation of errors in the parameters mentioned in Equation.B.3. The error in flux is computed from the continuum region close to the bandpass of the molecule of interest.

3.3.1.2 Dust production

The computation of the proxy to the dust parameter, $Af\rho$, defined by A'Hearn et al. (1984b) is described in APPENDIX.B. In this work we have computed $Af\rho$ in the narrow band filters BC (4390–4510 Å) and GC (5200–5320 Å) (hereby called GC) using the spectroscopic data of both the epochs and in the Johnson-Cousins R filter using an imaging data obtained on the first epoch using HCT. The specifications of the narrow band filters are discussed in Farnham et al. (2000).
Due to the absence of proper calibration standard stars during the imaging epochs of 156P obtained from IAC-80, the observed data were used to analyse any variation in Afρ profile over the period. Even though the observations are made in the absence of any filter, the contribution from the molecular emissions to the Afρ profile would be very less considering the physical scale at which the variations are seen. Also, the similarity of the Afρ profiles obtained on 2020-10-18 and 2020-12-15, derived for wavelength range corresponding to proper dust emissions, with those obtained on 2020-11-18 and 2020-12-08 in clear filter also suggests that the profile characteristics are dominated by the dust present in the coma. Hence, as shown in Figure.3.6, the profiles do not indicate the actual numbers of Afρ, rather are normalised to their peak values in order to compare the variation in the characteristics of the profile across the dates. In addition, the dominance of dust in the comet, especially in the inner coma, was explicitly seen in spectra extracted from the inner regions where the solar continuum is matching the comet spectrum over the entire wavelength range without any sign of emissions from other molecules. The gas emissions from different molecules starts to dominate only when the spectrum is extracted for larger apertures.

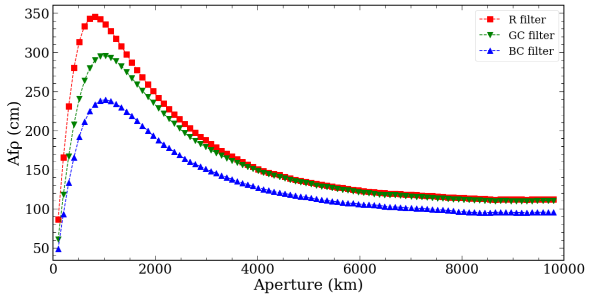

(a) Pre-perihelion (2020-10-18) Afρ profiles of the comet computed for broadband R filter and narrow band blue and green continuum filters. R filter profile is obtained from the imaging data and the narrow band filter profiles are obtained using the spectroscopic data. The standard error in the measurements are 23 cms.

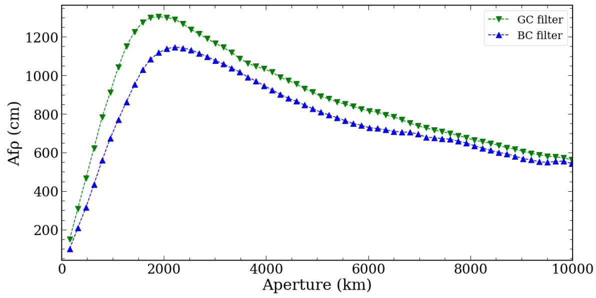

(b) Post-perihelion (2020-12-15) Afρ profiles of the comet in narrow band continuum filters. The spectroscopic data has been used to obtain the profiles. The standard error in the measurements are 81 cms.

Figure 3.5: Pre and post perihelion Afρ profiles in various filters.

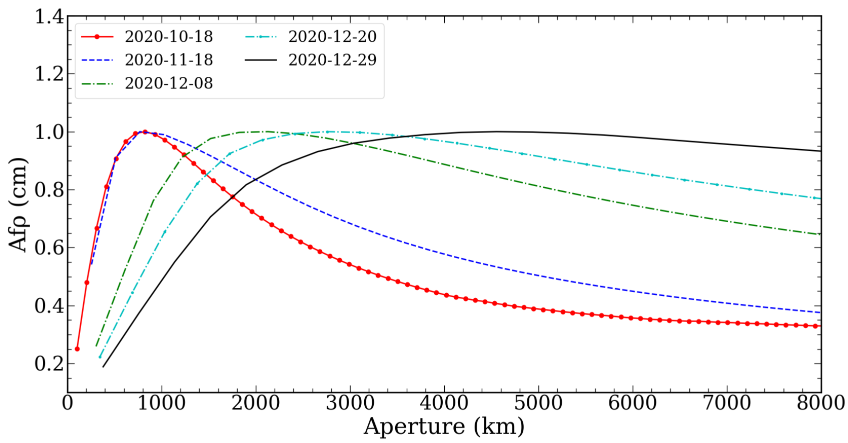

Figure 3.6: Comparison of the normalised Afρ profiles derived from a few selected imaging data observed using the HCT and IAC-80 telescope. The profile represented by the black solid line closely resembles the Afρ profile of a comet with a steady state outflow of dust.

3.3.2 Polarisation

The degree of polarisation and polarisation angle at a particular phase angle can be observed and computed as mentioned in Section.2.3.4. Figure.3.7 illustrates the modulation in the comet intensity measurement overplotted with the best fit line for computing the Stokes' parameters.

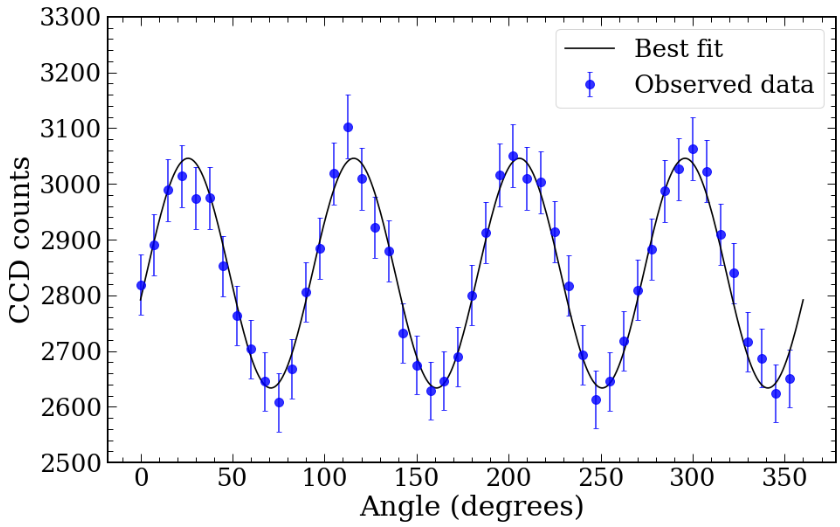

Figure 3.7: Intensity modulation derived from the 48 final frames obtained from the polarisation observation of the comet. The black solid line portray the best fit line for the equation.2.2 used to compute Stokes' parameters. The error bar represents the standard error in photometry at each angle

These analysis techniques are performed on the comet and the standard star frames observed on both epochs. The observational results for the observed standards are as mentioned in Table.3.4, where p_{obs} and θ_{obs} depicts the directly measured degree of polarisation and polarisation angle, p_0 and θ_0 represents the actual values taken from Schmidt et al. (1992) (for Johnson-Cousins *I* filter) and θ_{off} portrays the zero point offset in the polarisation angle. The values of degree of polarisation and polarisation angle of the comet observed for an aperture of 10000 km are specified in Table.3.5.
Radially increasing apertures were used to check for any spatial variation in the degree of polarisation as observed in comet 67P (Rosenbush et al., 2017). The observed degree of polarisation for multiple increasing apertures were similar within error bars, ruling out the presence of any systematic changes in the physical properties of the dust particles present in the coma. Average of the zero point offset in the polarisation angle, for each epoch, obtained from Table.3.4 is used to obtain the actual polarisation angle of the light from the coma of the comet (θ_{corr}). The observed polarisation is found to be positive over the whole coma since the angle of linear polarisation is observed to be

Table 3.4: Observational results of polarized standard stars.

Date	Star	Filter	p_0 (percent)	θ_0 (∘)	p_{obs} (percent)	θ_{obs} (∘)	$\theta_{off}=\theta_0-\theta_{obs}$ (∘)
13-11-2020	HD 25443	i	4.249 ± 0.041	134.21 ± 0.28	4.12 ± 0.29	19 ± 2	115 ± 2
	BD +64 106	i	4.696 ± 0.052	96.89 ± 0.32	4.60 ± 0.32	-15 ± 3	112 ± 4
16-12-2020	HD 25443	i	4.249 ± 0.041	134.21 ± 0.28	3.97 ± 0.31	27 ± 4	107 ± 4
	BD +64 106	i	4.696 ± 0.052	96.89 ± 0.32	4.76 ± 0.33	-9 ± 2	106 ± 3

Table 3.5: Observational results of comet 156P.

Date	Filter	Phase Angle (∘)	p_{obs} (percent)	θ_{obs} (∘)	$\theta_{corr}=\theta_{obs}+\theta^*_{off(avg)}$ (∘)
13-11-2020	i	38.9	5.26 ± 0.39	27.86 ± 4.80	141 ± 5
16-12-2020	i	42.3	6.80 ± 0.21	43.93 ± 1.10	151 ± 2

* The average values of zero point offset in polarisation angle for each epoch are 113.458 ± 2.07 and 106.73 ± 2.24 respectively.

perpendicular to the scattering plane.

3.4 Discussion

This section will discuss in detail the significance of the results of the spectroscopic, imaging and polarimetric observations of the comet 156P and also consider the results obtained from the modelling of the observed degree of polarisation in order to have a deeper understanding of the dust present in the comet.

3.4.1 Gaseous emissions

During the pre and post-perihelion optical spectroscopic observation of the comet, there were clear detection of the emissions from CN ($\Delta\nu = 0$) (λ3880Å), C_3 (λ4050Å), C_2

$(\Delta v = +1)(\lambda 4690\text{Å})$ and C_2 $(\Delta v = 0)(\lambda 5165\text{Å})$, as illustrated in Figure.3.1. The computed production rates at both epochs are as mentioned in Table.3.3. Considering that the perihelion date of the comet was on 2020 November 17, it is observed that the production rates have increased significantly when observed about 5 weeks post-perihelion. Similar increase in production rates, a few weeks after perihelion, has been observed in comet 67P (Opitom et al., 2017). Due to the lack of observational data, it is difficult to remark on the kind of evolution in the production rate which would have occurred in 156P. Still, increase in production rates as observed in the span of 2 months would require an increased level of activity as the comet approached perihelion. Short-period comets tend to have an upper-shield relatively exhausted in the cometary volatile as a result of its multiple passages close to the Sun (Shustov et al., 2018). Such dust crusts are formed as the comet recedes from the Sun and sublimation ceases. Once the comet returns to the inner Solar system, these crusts can get depleted exposing the layer beneath (fresh volatile material or layers of ice that have different vaporization rates) Venkataramani et al. (2016). This could result in an increased activity in the comet in turn giving rise to an increase in the observed production rates of various molecules. But, as pointed out by Marshall et al. (2019), the reason for a significant increase in cometary out-gassing cannot be clearly understood without prior knowledge of basic parameters (shape, spin axis orientation, activity locations) of the comet nucleus.

According to A'Hearn et al. (1995), comets with production rate ratio $Q(C_2)/Q(CN) < 0.66$ are classified as carbon-chain depleted comets and the others are classified as typical comets. The values of the production rate ratio at both epochs given in Table.3.3 implies that the comet 156P belongs to the typical class of comets. Also, even after considering the strict definition of carbon depletion in comets as mentioned in Cochran et al. (2012), the comet can be clearly seen to be belonging to the typical class of comets. Even though a significant difference in the activity of the comet is observed between both the epochs, the production rate ratios are estimated to be consistent. In the same line, the dust-gas ratio (see Table.3.3) is also measured to be consistent during both epochs. This could mean that the comet had possibly formed in a part of the proto-Solar nebula where the availability of volatile components and other building blocks of the comet nucleus were uniform.

3.4.2 Dust emission

The amount of dust in the coma is estimated with the help of a proxy parameter, $Af\rho$, as described in Section.3.3.1.2. The computed $Af\rho$ is expected to be independent of the aperture size (ρ) in the case of a steady state outflow in the coma (A'Hearn et al., 1984b). In such a case, the profile of the parameter would attain a constant value beyond a particular aperture. Hence, the value of $Af\rho$ at a larger aperture can be directly used to study the activity of dust production in the cometary coma.

Figure.3.5a and 3.5b illustrates the observed profile of $Af\rho$ in the comet, pre and post-perihelion, corresponding to various filter bands. It is seen that on both epochs the profile does not behave as expected in the case of a simple radial outflow model. Hence, it can be inferred that the coma of 156P has a non-steady state dust emission. Also, a possibility of dust grain destruction with nucleocentric distance cannot be ruled out. This results in the fall of column density (N(ρ)) and hence the $Af\rho$ at larger apertures. Similar kind of behaviour in the dust emission has been observed in a few other short period comets, 221P/LINEAR (Garcia et al., 2020), 52P/Slaughter-Burnham and 78P/Gehrels (Mazzotta Epifani & Palumbo, 2011) as well as a few long-period comets C/2001 Q4 (Tozzi et al., 2003), C/2000 WM1 (Lara et al., 2004), C/2010 FB87 and C/2011 L4 (Garcia et al., 2020). Hence, this behaviour can be considered to be irrespective of the dynamical age of the comet but as a characteristics of the activity in the comet.

According to Figure.3.5a, in the pre-perihelion epoch, the steep rise in the $Af\rho$ profile in the inner coma around 1000 Km might be due to the presence of a compact dust coma (as mentioned in Jehin et al., 2020b). The gradual decrease in the profile with the increase in nucleocentric distance can either be due to the destruction of a fraction of the dust present in the coma as they move outward or due to a difference in population of dust grains, with different physical properties, between the inner and outer coma (eg., Lara et al., 2004). Even though a similar trend in $Af\rho$ profile is observed post-perihelion (see Figure.3.5b), it is noticed that the peak which was observed around 1000 km (pre-perihelion), is observed at around 2000 km (post-perihelion) and has broadened by a few thousand kilometres. This shifting and broadening can be due to an expanded outer boundary of the compact dense inner coma caused by a slightly increased outflow of the dust in the coma owing to the increased activity in the comet. Figure.3.6 compares the characteristics of the Afρ profile over a few selected dates of observation. It is seen that the profile observed on 2020 November 18 is similar to what has been observed on 2020 October 18. As the comet moves in its orbit, away from the Sun, the observed profile is seen to be widening as if the difference in the presence of amount of dust in the inner and outer coma has reduced. The Afρ profile observed on 2020 December 8 has a trend is similar to what is observed on 2020 December 15 (see Figure.3.5b). Later, it is observed that the peak continues to widen and on December 29 the observed profile is similar to an expected Afρ profile for a comet with steady state outflow of dust emission. Hence, over the period of observation during pre and post-perihelion epochs, the dust emission in the comet has changed from a strong non-steady state outflow to a steady state. This could be possible if there were certain strong activity in the comet around perihelion which decreased by the end of December, few weeks after perihelion, as the comet started moving away from the Sun. Detailed dust modelling studies are required to understand the dust distribution in the coma to explain such abnormal Afρ profiles.

3.4.2.1 Coma morphology

Dust structures present in the coma can be identified by analysing the coma morphology in broadband filters like R or I since the light observed in these bands directly corresponds to the light scattered by the dust present in the coma. Open/clear filter can be used to get more SNR in case of a faint comet or small telescope, with the only issue being the contamination from the molecular emissions. Still, this technique can be employed to get a general understanding of the coma morphology present in the comet. There are various techniques (eg., Sekanina & Larson, 1984; Samarasinha et al., 2006; Schwarz et al., 1989; Larson & Slaughter, 1992; Schleicher & Farnham, 2004) that can be employed to carry out the analysis. In the current work the Larson-Sekanina (LS) processing method proposed by Sekanina & Larson (1984) is being used. We use a similar technique followed in Garcia et al. (2020) for comet 221P, where two images rotated with same angle in the opposite direction are individually subtracted from the original image and then co-added to increase the contrast between any faint structure present in the coma. The angle of rotation is chosen in such a way that the feature is best highlighted.

All the images available, as mentioned in Table.3.1, few of which are shown in Figure.3.2, were processed using this technique. The selected outputs of the LS processing are illustrated in Figure.3.3 with the angle of rotation used for the processing and directions of Sun and heliocentric velocity marked in all the panels. In panel (a), which is the only observation before perihelion, the presence of a strong feature, marked J1, probably a part of the main dust tail, is clearly visible along with a few faint features. As the comet moved in its orbit, there is a projection effect which causes a flip in the position of J1. Two other strong features, J2 and J3, are detected in the rest of the images indicating an increase in activity of the comet around perihelion. It is also observed that the jets, J2 and J3, remains active in December (see panel (c) for observation on 2020 December 08). This increase in activity could explain the increase in the production rates when the comet was observed on 2020 December 15.

Even if it is not demonstrable here, the prominent feature J1 can be suspected to be a part of the dust tail arising from an active region facing the Sun, being bent into the tail direction by the Solar radiation pressure. Farnham (2009) named such jets which appear unchanged for a long period of time as fixed jets. These fixed jets are usually centred on the rotation axis. According to the collimated jet model (Sekanina, 1987), isolated active regions producing such fixed jets can produce spatial variations in the density or particle size of the dust particles present in the coma. Detailed measurement of the comet's position along its orbit, analysis of dust particle size etc are required to confirm this assumption.

Comparing the panel (b) with the other panels in Figure.3.3, it can be observed that the jets are more compact and streamlined during the initial epochs of observation =with the angle between *J1 and J2* being only 25.7°. In the later epochs the coma opens up or the jets move apart systematically with the angles between *J1 and J2* being 49.9° and 59.7° on 2020 December 08 (Fig.3.3 panel (c)) and 2020 December 20 (Fig.3.3 panel (d)) respectively. This angular variation between the observed jets more or less corresponds to the epochs when the Afρ profiles are observed to start widening (see Afρ profile corresponding to 2020-12-08 illustrated in Fig.3.6). Hence, there is a possibility that, such a process would have resulted in an increased outflow of dust into the outer coma causing the widening of Afρ profile peak as seen in Figure.3.5b. From Figure.3.3, it can be observed that the jets which were most prominent during the first half of December starts to loose strength and subsides towards the end of December. Figure.3.6 illustrates that the Afρ profile started widening as the coma/jets opened up during the beginning of December and then attained a normal profile towards the end of December, once the jets subsided significantly. Hence, in the current case it can be inferred that the non-steady state outflow of dust resulting in the abnormal Afρ profile could be a result of the presence of strong dust jets arising from the nucleus. As the prominence of the jets subsided, the dust outflow would have tended more or less towards a steady state, reducing the spatial variation in the coma, causing the Afρ profile to attain a constant value independent of the aperture size, as it is normally expected.

3.4.3 Polarisation and dust properties

The degree of polarisation and polarisation angle were measured for the comet at two different phase angles. The observed values are tabulated in Table.3.5. Dust modelling was performed on the obtained polarisation data (see Aravind et al. (2022) for more details) to understand the possible composition and characteristics of the dust particles present in the comet. Fig.3.8 shows the best fit modelled data for the observed polarimetric response obtained for comet 156P at the *sloan i* filter for 75 percent Solids + 25 percent Hierarchical Aggregates (HA) having power-law size distribution $n = 2.4$. The modelled data indicates the presence of high amount of silicate/low absorbing material (50 to 60 percent) as obtained in the case of 67P (Halder & Ganesh, 2021). The polarimetric study of 156P reveals dust properties similar to those obtained in the case of the comet 67P. The shallow polarimetric slope indicates the presence of highly processed large size dust particles. The short orbital period allows frequent weathering of the dust reducing the amount of small fractals leaving behind the solids with low porosity in the coma.

It was observed that there are strong fixed jets present in the coma. As mentioned earlier, presence of such jets can create spatial variation in the particle size of the dust, which can produce a spatial variation of the degree of polarisation in the coma. Since,

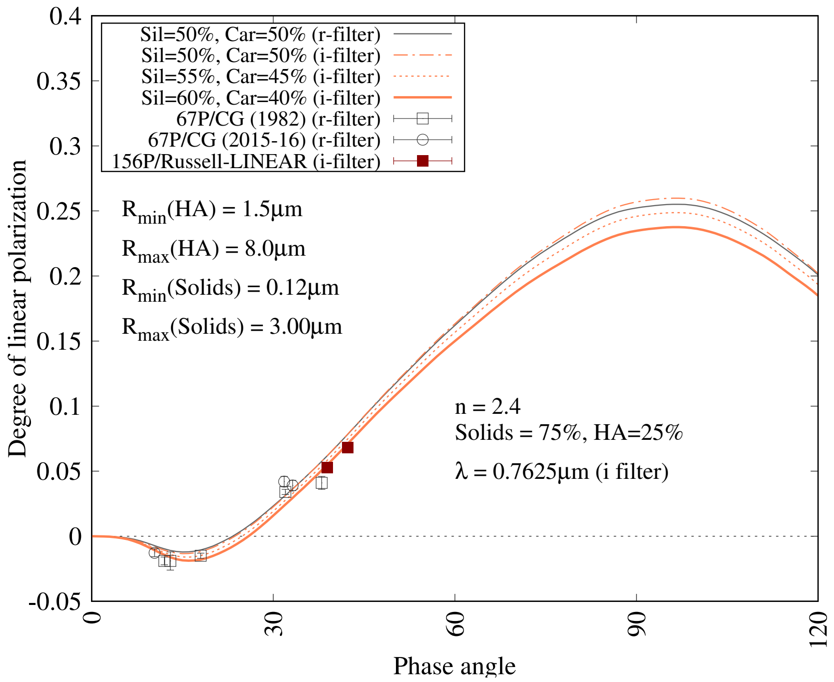

Figure 3.8: Best fit results for the comet 156P/Russell-LINEAR with the observations (dark-red solid squares). The light-red coloured lines indicate the best fit modelled polarisation-phase curves obtained from this study in the *sloan i* filter and the grey solid line indicate the best fit model obtained for 67P from Halder & Ganesh (2021). The grey hollow squares/circles denote the observations of 67P in *R* filter (Myers & Nordsieck, 1984; Rosenbush et al., 2017).

the presence of any systematic change in degree of polarisation with increasing aperture was already ruled out, an analysis was carried out on the 2020 December 16 polarimetric data in order to explore the possibility of difference in degree of polarisation at different locations in the coma due to the presence of the strong jets. The polarimetric data obtained for 2020 November 13 could only be used for computing the total coma polarisation as the comet was not bright enough to determine the polarisation at different locations within the coma. As shown in Figure.3.9 panel (a), for the 2020 December 16 data, various locations in the coma were chosen to compute the corresponding polarisation for a circular aperture of 2 pixel (706 km) diameter. Similar computational techniques as mentioned in Section.3.3.2 were employed at all the locations. The degree of polarisation corresponding to each location is illustrated in the form of polarisation vectors as well as rounded off to integers and mentioned at each location in yellow. The actual observed degree of polarisation is also mentioned in Table.3.6. Even though the errors are larger as compared to the earlier analysis, it is noticed that there is a variation in the observed degree of polarisation from point to point. At the same time, the jet features can not be distinguished in the polarimetric image due to the low resolution of the polarimeter. Hence, the jet features can be expected to be similar to what is observed on 2020 December 18 (see panel (b) of Figure.3.9).

A pattern in the variation of polarisation can not be definitively concluded due to the large errors in the observed values. It is observed that the degree of polarisation computed at the points 3, 4, 5, 12, 13, 14 and 15 are distinctly higher than what is observed at the other points. Upon careful comparison with panel (b) in Figure.3.9, it is spotted that these points lie in the area dominated by the observed strong jets *J1, J2, J3*. The presence of such jets would have created a localised difference in the physical characteristics of the dust population giving rise to a difference in the observed polarisation (eg., Rosenbush et al., 2017). The degree of polarisation is observed to be lower a few thousand kilometres away from the nucleus. Even though it is not a conclusive evidence, it can be indirectly presumed that, despite the jets being strong, their dominance is only in the inner coma within a few thousand kilometres. The dust particles arising from these jets could be getting destroyed as they move into the outer coma (giving rise to the dip in the Afρ profile as discussed in Section.3.4.2) causing the observed polarisation to be lower.

3.5 Conclusions

In this work, we have studied the short period Jupiter family comet 156P/Russell-LINEAR using spectroscopic, photometric and polarimetric techniques with the help of HCT, MIRO and IAC-80 telescopes. Emissions from $CN(\Delta v = 0)$, C_3 (λ4050Å), C_2 (Δv = +1) and C_2 (Δv = 0) are detected on both epochs of spectroscopic observation. The observational results from spectroscopy, imaging and polarimetry along with dust modelling help us in arriving at the following conclusions:

1. The production rates observed for CN, C_2 and C_3 are comparable to those observed for Jupiter family comets. From the spectroscopic results obtained for the two

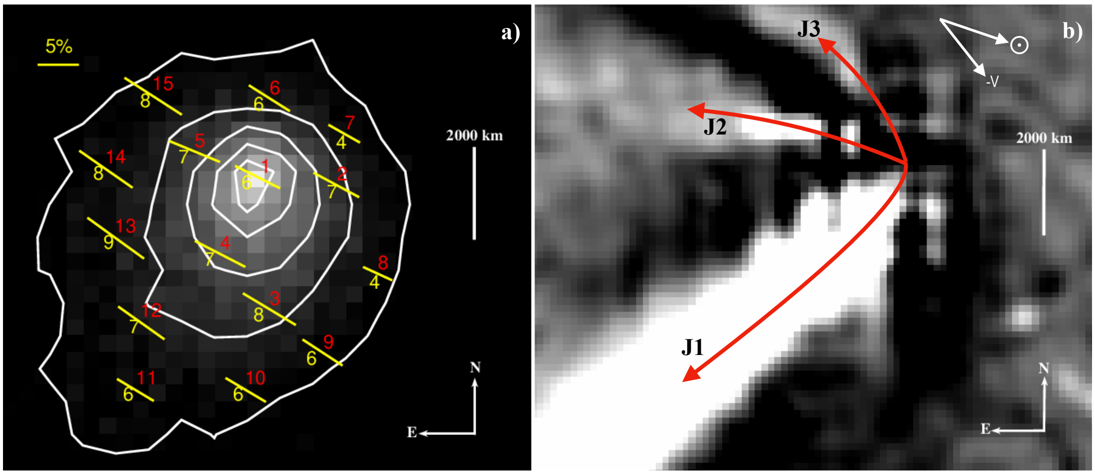

Figure 3.9: a) Illustration of spread of polarisation vectors in the coma of the comet 156P observed on 2020-12-16. The direction of the local polarisation plane is indicated by the orientation of the vectors, and their length denotes the degree of polarisation. Numbers in yellow represent the degree of polarisation rounded off to integer and red represents the aperture number (see Table.3.6). The contours simply represent the intensity variation in the coma. The vertical solid white line depicts the physical scale on the sky at the comet. b) Illustration of the observed jet directions in the LS processed image obtained on 2020-12-18.

epochs of observation, an increase in activity is observed post perihelion.

2. The value of $Q(C_2)/Q(CN)$ evidently classifies the comet as a typical comet.

3. The images processed through Larson-Sekanina technique, indicating the presence of strong jets throughout the observational period. This, along with the observed increase in production rates, suggests that there has been an increase in the activity as the comet crossed perihelion.

4. A non-steady state outflow of dust emission is observed during the initial epochs of observation. The jets which are arising from the isolated active regions in the comet nucleus can create spatial variation in the density or particle size of the dust present in the coma generating an abnormality in the observed Afρ profiles.

5. Towards the end of 2020 December, about 6 weeks after perihelion, the dust jets are observed to subside, which could have reduced the spatial variations in the coma. This may be a possible reason for the Afρ profiles to tends towards a

Table 3.6: Degree of polarisation corresponding to the locations displayed in Figure.3.9 panel (a).

Aperture number	p_{obs} (%)	θ_{corr} (°)
1	6.11 ± 0.41	154 ± 4
2	6.63 ± 0.46	152 ± 4
3	7.52 ± 0.45	149 ± 4
4	6.91 ± 0.49	153 ± 4
5	6.74 ± 0.47	158 ± 5
6	5.95 ± 0.50	148 ± 5
7	4.44 ± 0.52	151 ± 4
8	3.91 ± 0.56	155 ± 5
9	5.87 ± 0.58	147 ± 5
10	5.71 ± 0.62	149 ± 5
11	5.52 ± 0.62	149 ± 5
12	6.90 ± 0.60	145 ± 5
13	8.52 ± 0.50	144 ± 5
14	7.93 ± 0.55	145 ± 5
15	8.34 ± 0.48	147 ± 5

general profile as in the case of a steady state outflow of dust.

6. The degree of polarisation of the comet obtained on both the epochs are in good agreement with the values observed for Jupiter family comets at similar phase angles.

7. A variation in the degree of polarisation at various locations in the coma, dominated by the dust jets, has been observed. This suggests a probability of dust jets being a prominent reason for producing localised differences in the density or size of the dust particles present in the coma.

8. The best fit model for the observed polarisation of the comet 156P suggests the presence of higher percentage ($> 50\%$) of silicates or low absorbing material. The model also indicates the coma to be dominated by higher amount of larger

particles with lower porosity, having a power law size distribution index $n = 2.4$. This can be due to the short orbital period and/or frequent weathering of the smaller materials with high porosity similar to what is seen in the case of the comet 67P.

The comet 156P/Russell-LINEAR has not been well studied in any of its previous apparitions due to its unfavourable orbital positioning. This restricts us from generalising the characteristics of the comet with our set of data or to compare it with other data sets. However, the behaviour of the activity in the comet around perihelion and the modelled dust properties obtained with the help of polarisation data, points to a similarity to another Jupiter family comet 67P. Further study of the comet in its upcoming favourable apparitions would be welcome to have a better understanding of this comet.

Chapter 4

Long term evaluation of activity in an SPC and an LPC

4.1 Introduction

Comets are unpredictable Solar system bodies. The dynamical life of a comet is not a mere implication of the level of activity expected in it. In a general case, LPCs show higher activity than SPCs. This is because surface of the LPCs contain fresh material that has never been exposed or exposed very few times to the Solar radiation compared to the processed surfaces of SPCs. Due to this, LPCs are expected to be more gaseous rather than being dusty. Still, as explained in Section.1.1.1 in Chapter.1, there could be objects whose primordial nucleus formed in a more dusty inner region of the proto-Solar nebula and later got ejected into the Oort cloud to preserve the accumulated icy materials. In order to understand the overall activity in a comet during its apparition, extensive coverage along its orbit is necessary. In the case of LPCs it is important as these objects would not again return to the inner Solar system during the current human life time. At the same time, it is important for SPCs in order to track the similarity/dissimilarity of activities from previous apparition. This could provide a great deal of information regarding the composition of the nucleus of the comet.

In this chapter, we discuss the long term observations of two comets, one SPC 46P/ Wirtanen (46P hereafter) and one dynamically new LPC C/2017 T2 (T2 hereafter). Table.2.2 indicates the orbital parameters of both the objects. 46P was the original target of the comet mission *Rosetta* after which it was changed to 67P due to certain delays in the launch (Schulz, 2005). 46P being an SPC has been observed during its previous apparitions (eg., A'Hearn et al., 1995; Langland-Shula & Smith, 2011; Kidger, 2004; Combi et al., 2020). But, the 2018 apparition of 46P presented the closest approach of the comet with Earth ($\sim$0.068 AU) in the last four centuries. This enabled to probe the very interior of the coma even with seeing limited observations. The comet exhibited significant activity despite of a 1.055 AU perihelion distance. The exceptional passage of 46P resulted in the detailed study of the comet in imaging, IR/UV/optical spectroscopy, polarisation etc (eg., Farnham et al., 2021; Noonan et al., 2021; Knight et al., 2021; Bauer et al., 2021; McKay et al., 2021; Protopapa et al., 2021; Rosenbush et al., 2021a; Roth et al., 2021; Kelley et al., 2021). Even though T2 did not have such close heliocentric or geocentric encounters (q$\sim$1.615 AU), the comet was spectroscopically observable from large heliocentric distances as it approached perihelion. The availability of the comet across many months enabled its extensive study in different regimes (eg., Combi et al., 2021b; Schleicher et al., 2020; Moulane et al., 2020a; Manzini et al., 2020).

4.2 Observation

The availability of a telescope facility and compatible instruments does not guarantee the possibility of long term coverage of a comet. The orbital parameters and Earth's orbital position plays a major role in determining the observability. The apparitions of comet 46P and T2 in 2018 and 2019 respectively presented a prospect for long term coverage in spectroscopy. As part of the long term coverage, comet 46P was observed for 19 epochs spanning across 2018 October to 2019 February and comet T2 was observed for 9 epochs spanning across 2019 October to 2020 June. Only instrument LISA was used for the complete observation of 46P while both HFOSC and LISA were used for the complete coverage of T2 (see Table.2.2 for details). The brief details of the observational epochs for both the comets are as given in Table.4.1 and 4.2. The entire data set was reduced and analysed as mentioned in Section.2.3.1. The spectrum of few selected epochs of comets 46P and T2 are shown in Figure.4.1 and 4.2 respectively.

Table 4.1: Observation Log for 46P

Date [UT]	Heliocentric Distance (r_H) [AU]	Heliocentric velocity ($\dot{r_H}$) [km s^{-1}]	Geocentric Distance (Δ) [AU]	Distance scale at photo-centre [Km $pixel^{-1}$]	Phase angle [°]
2018-10-05	1.379	-13.53	0.441	212	25.66
2018-11-21	1.093	-6.07	0.164	79	46.65
2018-11-28	1.072	-4.19	0.13	62	46.03
2018-11-29	1.07	-3.9	0.126	61	45.61
2018-11-30	1.068	-3.622	0.121	58	45.09
2018-12-08	1.057	-1.301	0.09	43	36.07
2018-12-09	1.056	-0.962	0.0874	40	33.99
2018-12-13	1.055	0.248	0.079	38	25.42
2018-12-14	1.0556	0.55	0.078	37	23.31
2018-12-15	1.056	0.852	0.077	37	21.4
2018-12-27	1.074	4.36	0.103	49	27.01
2018-12-28	1.077	4.64	0.107	51	28.13
2019-01-11	1.129	8.149	0.18	86	33.41
2019-01-12	1.133	8.36	0.186	89	33.34
2019-01-13	1.138	8.58	0.192	92	33.24
2019-01-31	1.244	11.66	0.31	149	29.2
2019-02-01	1.252	11.81	0.318	153	28.93
2019-02-02	1.259	11.94	0.326	156	28.7
2019-02-03	1.265	12.06	0.333	160	28.48

Table 4.2: Observation Log for T2

Date [UT]	Heliocentric Distance (r_H) [AU]	Heliocentric velocity ($\dot{r_H}$) [km s^{-1}]	Geocentric Distance (Δ) [AU]	Distance scale at photo-centre [Km $pixel^{-1}$]	Phase angle [°]
2019-10-02	3.13	-16.56	2.73	584	18.0
2019-11-30	2.58	-16.03	1.65	353	9.46
2019-12-22	2.37	-15.46	1.52	325	14.88
2020-01-30	2.05	-13.54	1.62	346	28.16
2020-01-31	2.04	-13.47	1.62	346	28.37
2020-02-23	1.87	-11.44	1.72	368	31.57
2020-05-26	1.64	4.185	1.66	355	35.74
2020-06-09	1.69	6.63	1.67	360	35.14
2020-06-25	1.75	9.06	1.75	374	33.64

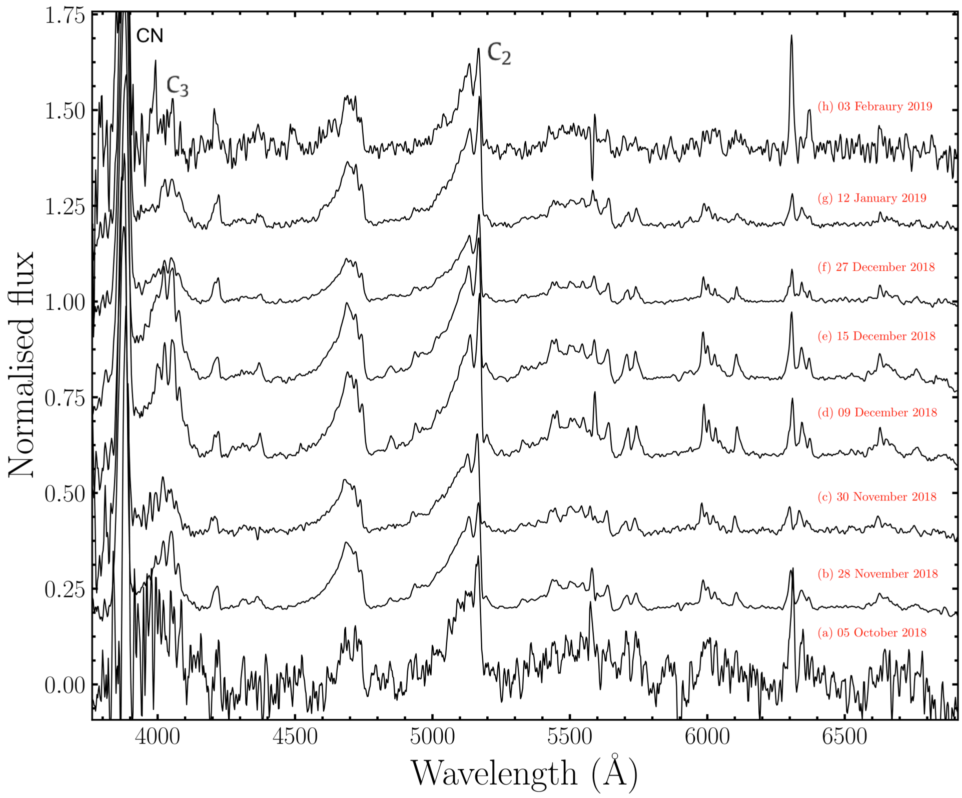

Figure 4.1: Optical spectrum of 46P for selected observational epochs

.

4.3 Discussion

The latest apparition of 46P presented a great opportunity to observe various molecular emissions. As the comet was approaching perihelion, the activity increased significantly resulting in the appearance of a large number of emission lines in the optical spectrum (see Figure.4.1). Detailed analysis of the evolution of these lines can be performed to understand the comet composition in depth. On the other hand, the long period comet T2 did not posses such abundance of emission lines (see Figure.4.2), which could be due to the larger perihelion distance as compared to 46P. The major emissions detected in both the comets were CN, C_2, C_3 and NH_2.

Observations of the comets with the long slit in both the instruments were utilised to study the spatial variation in column density of various molecules (CN, C_2, C_3) so as to compute the evolution of their production rates with heliocentric distance. The characteristic Afρ profile of both comets in BC and GC narrow band filters for various

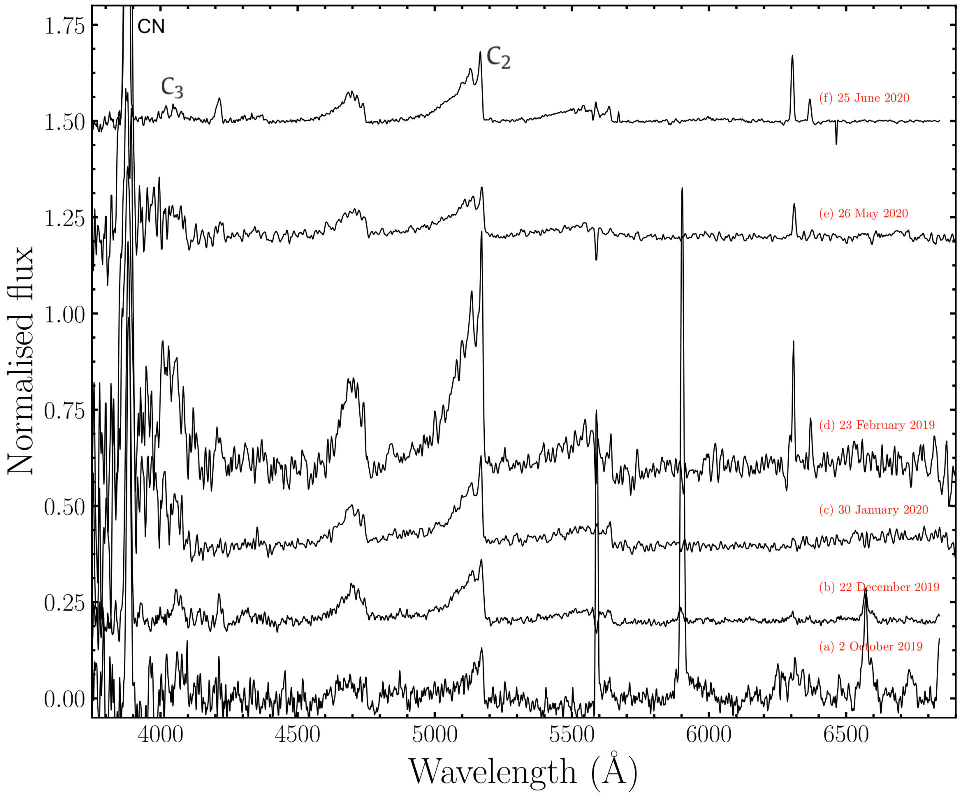

Figure 4.2: Optical spectrum of T2 for selected observational epochs

.

epochs are also analysed to study any variation in the dust emission. The following subsections discuss the results obtained from these analysis for both the comets.

4.3.1 46P

Extensive coverage of a comet along its orbit provides enough details to understand the basic compositional characteristics of a comet. But, the current apparition of 46P being special due to its very close approach to Earth provides a different scenario. The close geocentric approach of the comet implies that we are always looking at the innermost part of the coma where there can be drastic changes in activity due to the presence of jets or outburst. In such scenario, imaging analysis would have an advantage over long slit spectroscopy in investigating the general production rate characteristics of the comet. This is because, imaging analysis would be considering the emission arising from the total disk rather than a particular spatial axis as in the case of long slit spectroscopy. Due

Table 4.3: Activity of comet 46P at different epochs

Date	r_H	Δ	Production Rate (molecules per sec)			Production rate ratio	Afρ (cm)		Dust to gas ratio
(UT)	(AU)	(AU)	CN	$C_2(\Delta v = 0)$	C_3	$Q(C_2)/Q(CN)$	BC	GC	$(Af\rho)_{BC}/Q(CN)$
2018-10-05	1.38	0.44	24.56(0.09)	24.64(0.15)	23.58(0.29)	0.08(0.18)	1.77(0.32)	1.74(0.35)	-22.79(0.33)
2018-11-21	1.09	0.16	25.23(0.02)	25.31(0.03)	24.19(0.06)	0.08(0.04)	2.24(0.09)	2.26(0.08)	-22.99(0.09)
2018-11-28	1.07	0.13	25.44(0.02)	25.53(0.02)	24.38(0.03)	0.09(0.03)	2.57(0.06)	2.56(0.06)	-22.87(0.06)
2018-11-29	1.07	0.13	25.74(0.01)	25.78(0.01)	24.50(0.02)	0.04(0.01)	2.65(0.04)	2.73(0.03)	-23.08(0.04)
2018-11-30	1.07	0.12	25.79(0.01)	25.81(0.01)	24.62(0.09)	0.03(0.01)	2.74(0.04)	2.84(0.03)	-23.05(0.04)
2018-12-08	1.06	0.09	25.25(0.01)	25.238(0.01)	24.17(0.04)	0.13(0.02)	2.45(0.04)	2.44(0.04)	-22.80(0.04)
018-12-09	1.06	0.09	25.30(0.01)	25.39(0.02)	24.26(0.04)	0.10(0.02)	2.44(0.03)	2.49(0.02)	-22.86(0.03)
2018-12-13	1.05	0.08	25.44(0.01)	25.50(0.02)	24.41(0.04)	0.06(0.02)	2.57(0.04)	2.62(0.03)	-22.88(0.04)
2018-12-14	1.06	0.08	25.38(0.01)	25.44(0.00)	24.32(0.11)	0.07(0.01)	2.49(0.03)	2.54(0.03)	-22.89(0.03)
2018-12-15	1.06	0.08	25.39(0.02)	25.44(0.01)	24.34(0.06)	0.06(0.02)	2.43(0.03)	2.48(0.02)	-22.96(0.03)
2018-12-27	1.07	0.10	25.27(0.02)	25.28(0.02)	24.14(0.05)	0.01(0.03)	2.33(0.03)	2.47(0.02)	-22.94(0.04)
2018-12-28	1.08	0.11	25.23(0.03)	25.25(0.02)	24.04(0.09)	0.02(0.03)	2.42(0.03)	2.48(0.03)	-22.81(0.04)
2019-01-11	1.13	0.18	25.20(0.01)	25.36(0.02)	24.07(0.13)	0.16(0.03)	2.43(0.09)	2.46(0.08)	-22.77(0.09)
2019-01-12	1.13	0.19	25.19(0.01)	25.36(0.03)	24.04(0.12)	0.17(0.03)	2.23(0.06)	2.34(0.05)	-22.95(0.07)
2019-01-13	1.14	0.19	25.20(0.02)	25.29(0.03)	24.07(0.13)	0.09(0.03)	2.42(0.06)	2.42(0.06)	-22.77(0.06)
2019-01-31	1.24	0.31	24.95(0.05)	25.03(0.05)	23.84(0.42)	0.08(0.07)	1.92(0.14)	2.06(0.10)	-23.03(0.15)
2019-02-01	1.25	0.32	24.97(0.02)	25.04(0.05)	23.87(0.19)	0.06(0.05)	2.11(0.11)	2.13(0.10)	-22.86(0.11)
2019-02-02	1.26	0.33	24.96(0.03)	25.03(0.04)	23.83(0.23)	0.07(0.05)	2.15(0.11)	2.18(0.10)	-22.81(0.11)
2019-02-03	1.26	0.33	24.84(0.04)	24.85(0.06)	23.77(0.37)	0.01(0.07)	1.79(0.21)	1.77(0.22)	-23.06(0.22)

Values in the parenthesis represents the corresponding errors.
Production rates and ratios are in log scale.

to this disadvantage in spectroscopy, presence of any localised jet or outburst varying from day to day at the location of the slit can affect the column density of the molecules and hence the computed production rates. But, while imaging is restricted to analysing only the emissions corresponding to various filters available, spectroscopy is always advantageous in having a complete analysis of the different emissions occurring in the optical regime.

Figure.4.3a illustrates the variation in production rate of CN, $C_2(\Delta v = 0)$ and C_3 across perihelion (see Table.4.3 for corresponding values). It is clearly seen that there has been a drastic increase in the production rate of all the three molecules around 2018-11-28, after which it dropped significantly as the comet reached perihelion. Kelley et al. (2021) and Farnham et al. (2021) reports multiple outbursts and strong presence of CN jets as the comet approached perihelion with a rotation period of nucleus to be around 9 hours. As mentioned before, these outbursts and presence of strong jets along with the nucleus rotation could contaminate the slit in a different manner from day to

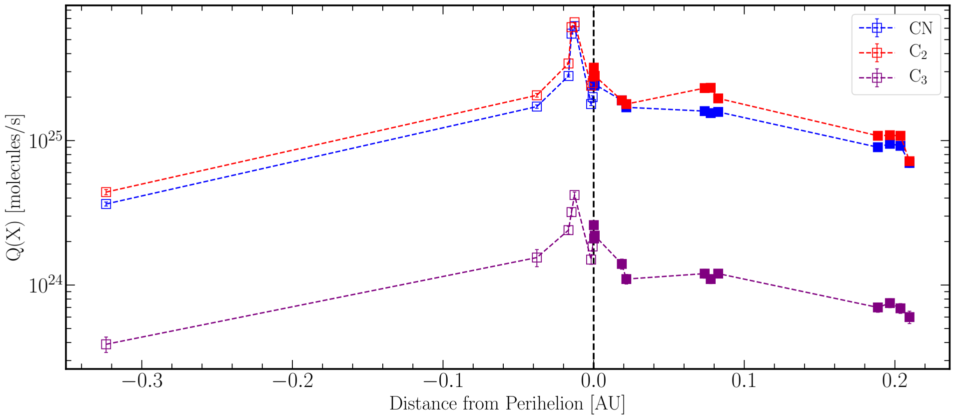

(a) Variation of production rates in CN, C_2 and C_3. The vertical dashed line represents the perihelion of the comet. .

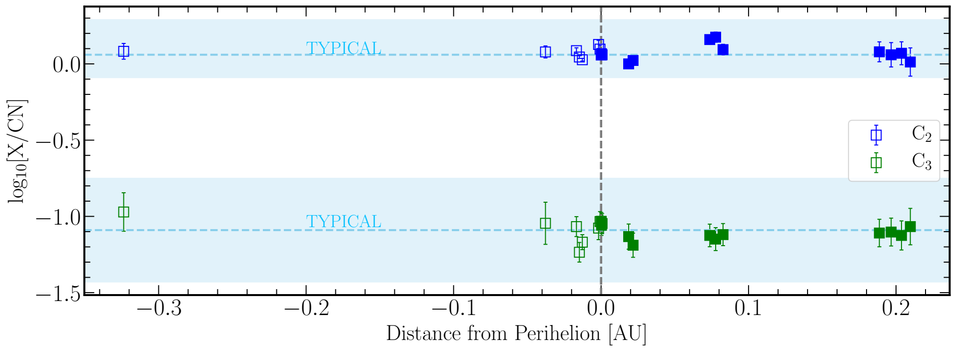

(b) Observed trend in the computed production rate ratios. The vertical dashed line represents the perihelion of the comet. The horizontal dashed lines represents the mean value of production rate ratios for comets reported in A'Hearn et al. (1995).

Figure 4.3: Variation of gas production in comet 46P as a function of distance from perihelion. Open squares represent pre-perihelion epochs while filled squares represent post-perihelion epochs.

day. Roth et al. (2021) reports the rapid variation of outgassing in the inner coma close to perihelion. But, the unavailability of production rate numbers for the molecules corresponding to these dates in Knight et al. (2021) limits us from confirming whether this variation is due to a total short term increase in activity in the comet or due to the alignment of slit along the jet features during these dates. Still, it can be seen from Figure.4.3b that such drastic variation in the production rates of C_2 and CN have not notably affected the $Q(C_2)/Q(CN)$ ratio. It is interesting to see that the $Q(C_3)/Q(CN)$ ratio which lied in the typical region according to the classification given by Cochran et al. (2012) moves into the depleted region during and after the short term increase in

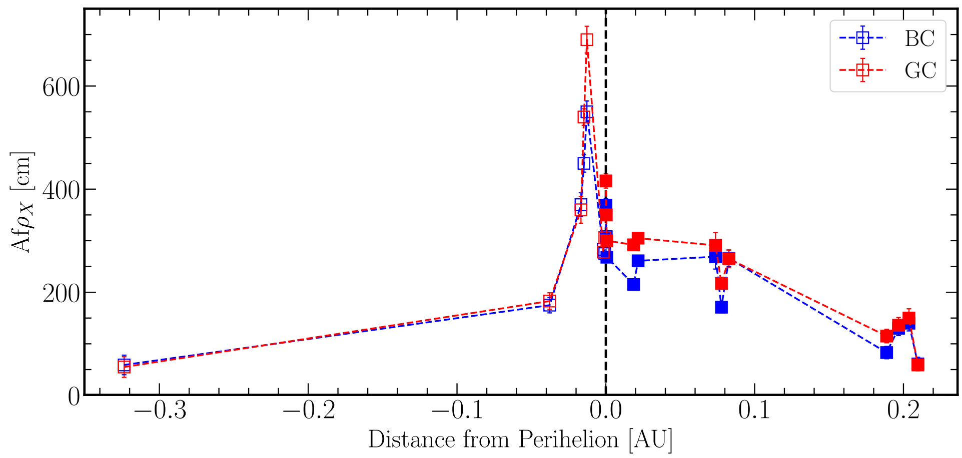

(a) Variation in the dust activity (denoted by Afρ) measured in the Blue and Green continuum filters. The vertical dashed vertical line represents the perihelion of the comet.

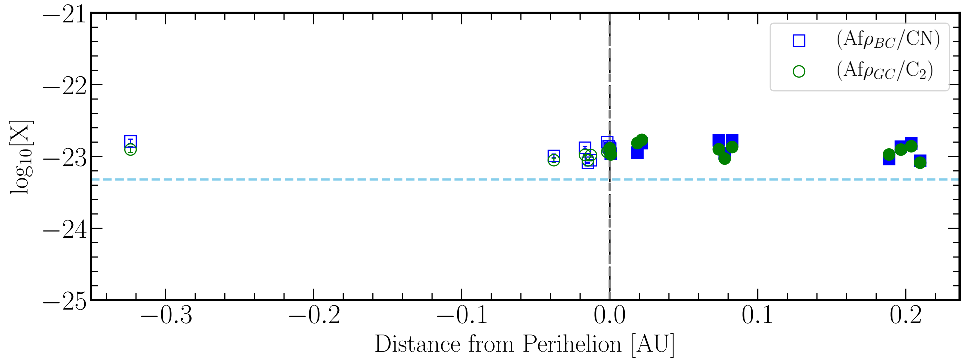

(b) Observed trend in dust to gas ratio at two different regions of the spectrum. The vertical dashed line represents the perihelion of the comet. The horizontal dashed line represents the mean value of dust to gas ratio for comets reported in A'Hearn et al. (1995).

Figure 4.4: Variation of dust activity in comet 46P as a function of distance from perihelion. Open squares represent pre-perihelion epochs while filled squares represent post-perihelion epochs.

activity. Even though the activity in 46P reported by Knight et al. (2021) and Rosenbush et al. (2021b) shows an increase in dust activity after perihelion, our dataset reveals an increase in both gas and dust activity before perihelion. As mentioned, while the imaging studies analyse the average activity in the coma, long slit spectroscopic studies can be affected by localised strong activities in the inner coma falling in the slit direction.

The general dust activity in the comet along the orbit was inspected by analysing the variation in the Afρ characteristic profile in the narrow band BC and GC filters.

As seen in Figure.4.4a, the dust emission was in a perfect steady state emission during majority of the observational epochs. It is only during 2018-12-27 there is a non-steady emission observed after which it again goes back into the steady state. From Table.4.3 it can be seen that Afρ computed for both BC and GC filter bands reach their peak value at the same time the production rates of the different molecules peak. Hence, the chances of the increased activity being only a mere effect of molecular jets aligned in the slit direction should be checked further. At the same time, as pointed out by A'Hearn et al. (1995), in the case of 46P also, the dust to gas ratio does not vary significantly for the observed range of heliocentric distance (see Figure.4.4b). 46P having had a historic close flyby with Earth during this apparition, effects of domination by localised activity in the inner coma can be significant. However, further analysing the spectra of each individual epoch can reveal a great amount of detail regarding the coma composition during its hyperactivity..

4.3.2 C/2017 T2

Long term observational studies of LPCs are of great importance as these are objects which will not be returning to the inner Solar system during the current human lifetime. Comet C/2017 T2 with an orbital period of 3,54,071 years is classified as a dynamically new object travelling to the inner Solar system for the first time Combi et al. (2021b). The comet was bright enough to be observed in low resolution spectroscopy even at a distance of 3.13 AU. The spectrum of the object initially appeared to be dominated by dust as the gaseous emissions would not be strong enough at the observed distance. Figure.4.5a demonstrate the variation in production rates of CN, C_2 and C_3 as a function of distance from perihelion (see Table.4.4 for corresponding values). Unlike comet 46P, the activity in T2 was gradual as the comet approached perihelion. This is because the comet contains fresh unexposed volatile materials which gradually sublimates as the comet moves closer to the Sun, thereby increasing the production rates. Even after increased activities in CN and C_2, the emission from C_3 was not so evident except in few epochs (see Figure.4.2) as compared to other LPCs. Similarly the dust activity depicted by the Afρ values reaches a peak value of 6760 cm and 8128 cm in the BC and GC filter bands (see Figure.4.6a), 93 days before perihelion similar to what has been reported by Moulane et al. (2020a).

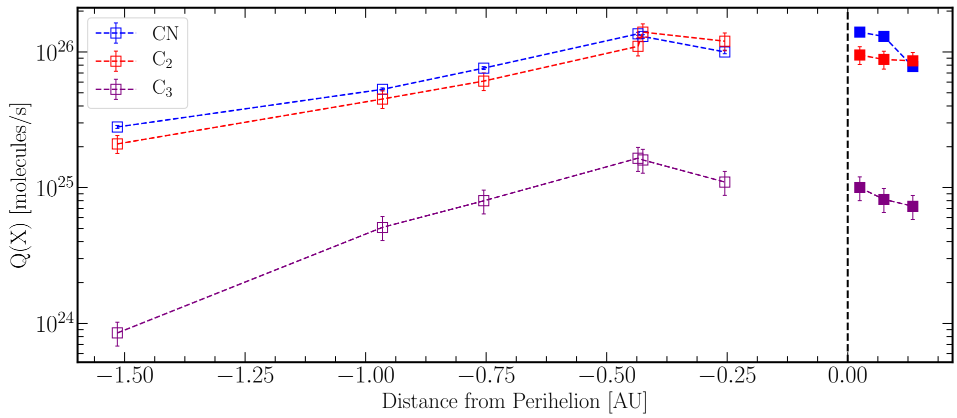

(a) Variation of production rates in CN, C_2 and C_3. The vertical dashed line represents the perihelion of the comet.

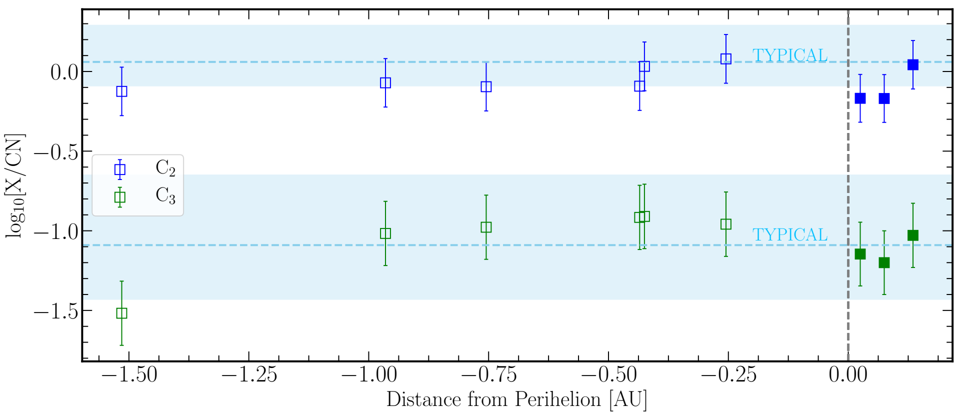

(b) Observed trend in the computed production rate ratios. The vertical dashed line represents the perihelion of the comet. The horizontal dashed line represents the mean value of dust to gas ratio for comets reported in A'Hearn et al. (1995).

Figure 4.5: Variation of gas production in comet C/2017 T2 as a function of distance from perihelion. Open squares represent pre-perihelion epochs while filled squares represent post-perihelion epochs.

On the other hand, a difference in the activity is observed in the epochs after perihelion. Combi et al. (2021b) reports an asymmetric variation of water production about perihelion while Manzini et al. (2020) reports the observation of concentric structures in the broadband images of T2 pointing at a strong activity driven by the rotation of the nucleus. However, the lack of observations connecting the pre and post perihelion

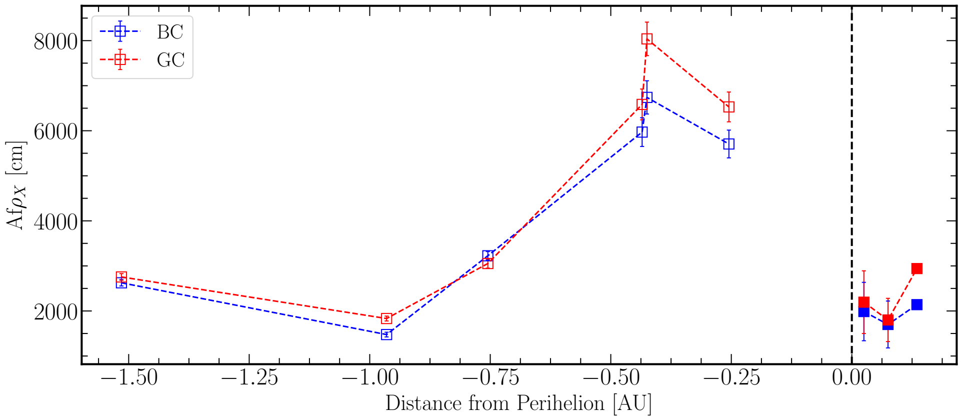

(a) Variation in the dust activity (denoted by Afρ) measured in the Blue and Green continuum filter regions. The vertical dashed line represents the perihelion of the comet.

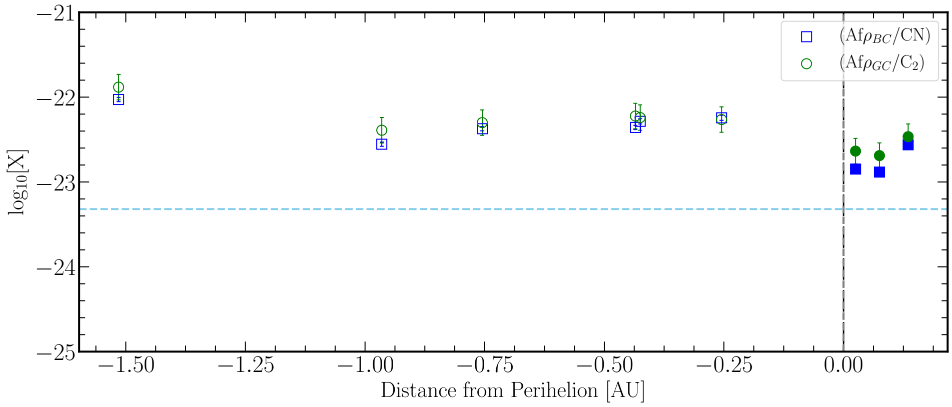

(b) Observed trend in dust to gas ratio at two different regions of the spectrum. The vertical dashed line represents the perihelion of the comet. The horizontal dashed line represents the mean value of dust to gas ratio for comets reported in A'Hearn et al. (1995).

Figure 4.6: Variation of dust activity in comet C/2017 T2 as a function of distance from perihelion. Open squares represent pre-perihelion epochs while filled squares represent post-perihelion epochs

epochs, due to the onset of a national lockdown as a consequence of COVID, makes it difficult to analyse the behaviour of dust and gas activity that would have occurred in the comet as it reached perihelion. Asymmetry is observed in both production rate ratios and dust to gas ratios after the perihelion (see Figure.4.5b and 4.6b. The absence of any other published literature studying the comet's activity in the optical regime during these epochs leaves the door open for understanding what happened to the comet as it approached perihelion.

Table 4.4: Activity of comet T2 at different epochs

Date	r_H	Δ	Production Rate (molecules per sec)			Production rate ratio	Afρ (cm)		Dust to gas ratio
(UT)	(AU)	(AU)	CN	$C_2(\Delta\nu = 0)$	C_3	$Q(C_2)/Q(CN)$	BC	GC	$(Af\rho)_{BC}/Q(CN)$
2019-10-02	3.13	2.73	25.45(0.02)	25.32(0.26)	23.92(0.16)	-0.12(0.26)	3.42(0.03)	3.44(0.03)	-22.03(0.04)
2019-11-30	2.58	1.65	25.72(0.06)	25.65(0.10)	24.71(0.46)	-0.07(0.12)	3.17(0.04)	3.26(0.03)	-22.56(0.07)
2019-12-22	2.37	1.52	25.88(0.04)	25.79(0.09)	24.90(0.47)	-0.10(0.10)	3.51(0.03)	3.48(0.03)	-22.37(0.05)
2020-01-30	2.05	1.62	26.13(0.07)	26.04(0.13)	25.21(0.37)	-0.09(0.15)	3.78(0.05)	3.82(0.05)	-22.36(0.08)
2020-01-31	2.04	1.62	26.00(0.05)	26.07(0.09)	25.04(0.39)	0.03(0.11)	3.83(0.05)	3.91(0.05)	-22.28(0.08)
2020-02-23	1.87	1.72	26.14(0.05)	25.97(0.06)	25.00(0.27)	0.07(0.07)	3.76(0.05)	3.81(0.05)	-22.24(0.07)
2020-05-26	1.64	1.66	26.40(0.03)	25.98(0.06)	25.08(0.58)	-0.17(0.06)	3.30(0.33)	3.34(0.30)	-22.84(0.33)
2020-06-09	1.69	1.67	26.11(0.04)	25.94 (0.07)	24.91 (0.5)	-0.17 (0.06)	3.23(0.30)	3.25(0.26)	-22.88(0.04)
2020-06-25	1.75	1.75	25.89(0.01)	25.93(0.02)	24.86(0.24)	0.04(0.02)	3.33(0.04)	3.47(0.03)	-22.56(0.04)

Values in the parenthesis represents the corresponding errors.
Production rates and ratios are in log scale.

4.4 Conclusion

Two different comets, one SPC and one LPC, were observed for a long duration in low resolution spectroscopy as the comet crossed perihelion. The SPC, 46P, was followed for about 19 epochs while the LPC, T2, was followed for 8 epochs. Few major points to be noted are:

1. Both the comets with a completely different dynamical origin were observed to be having a Typical carbon chain composition across the observational epochs. This points to a possibility of a homogeneous nucleus in both 46P and T2.

2. While 46P showed steep increase in activity as it approached perihelion, the activity in T2 appeared to be gradual. This was in agreement to the basic understanding of activity in an SPC and LPC with differences in the volatile depletion in the outer surfaces.

3. 46P had a lower dust to gas ratio when compared to T2 even though T2 was on its first trip to the inner Solar system while 46P has already made a large number of trips. This implies that the production rate ratios or dust to gas ratios are evidences of its primordial composition rather than being an evolutionary effect.

Chapter 5

Miscellaneous studies on comets

5.1 Introduction

In the current scenario, different classes of comets are observed to be originating from different reservoirs. As explained in Chapter.1, even though the JFCs are thought to be supplied by the Kuiper belt or Scattered disk and the LPCs and HTCs by the Oort cloud, the primitive origin of these bodies are unknown. There are large possibilities that they could have formed in an inner part of the Solar system and later got mixed and thrown into different reservoirs. Hence, comets belonging to a specific class need not necessarily have similar characteristics. This is why it is necessary to observe and analyse all possible comets originating from different reservoirs. Such extensive study combined with the current data set can improve our understanding of the compositions of comets distributed at various regions.

This chapter mainly investigates the results obtained from the low resolution spectroscopic study of a large number of comets belonging to different reservoirs. The understanding regarding the dust composition of a few comets obtained from the polarisation study along with the prospect of improving the transmission profiles of the narrow band filter profiles are discussed towards the end.

5.2 Observations

For the purpose of a having a comparative study in the composition observed in comets originating from different reservoirs, a total of 18 comets, 8 SPCs and 10 LPCs were observed in low resolution spectroscopy with the help of LISA and HFOSC instruments. Table.5.1 lay out the observational log for the spectroscopic observations carried out for different comets. Polarisation observation was also carried out for 5 different comets at different phase angles to study the variation of degree of polarisation with phase angle. The basic orbital parameters of the comet and the instruments and techniques employed on different epochs are given in Table.2.2. All the spectroscopic data have been reduced and analysed with the techniques explained in Section.2.3.1 while the polarisation data reduction and analysis have been explained in Section.3.3.2. Broad band images of a few comets have also be been acquired on certain epochs. They have been used to compute the Afρ in broad band filters as well as check for any morphological features through LS processing.

Table 5.1: Observation log of comets observed in low resolution spectroscopy.

Object*	Date [UT]	Heliocentric Distance (r_H) [AU]	Heliocentric velocity ($\dot{r_H}$) [km s^{-1}]	Geocentric Distance (Δ) [AU]	Distance scale at photo-centre [Km pixel^{-1}]	Phase angle [°]
4P	2021-11-09	1.73	6.23	0.99	212	28.75
21P	2018-10-05	1.07	8.3	0.48	231	67.7
38P	2018-11-20	1.59	1.71	0.82	394	31.4
	2018-11-28	1.6	3.07	0.79	379	28.9
	2018-12-13	1.64	5.47	0.76	365	23.2
	2018-12-14	1.65	5.63	0.76	365	22.7
67P	2020-05-18	1.21	1.74	0.42	90	48.83
88P	2020-06-25	1.68	-10.24	1.18	252	36.7
	2020-07-22	1.53	-8.5	1.25	267	41.2
	2020-05-18	1.92	-11.35	1.08	231	23.0
260P	2019-10-02	1.44	3.46	0.56	120	31.04
	2019-11-30	1.67	9.7	0.77	165	20.3
	2019-12-22	1.8	10.86	0.98	210	23.25

Table 5.1 Continued

29P	2020-10-18	5.83	0.35	4.90	1047	3.9
	2021-11-09	5.92	0.50	5.04	1077	4.67
123P	2019-03-13	2.142	3.46	1.221	587	12.93
	2019-04-01	2.171	9.7	1.317	633	17.61
	2019-04-02	2.173	10.86	1.324	636	17.9
C/2018 N2	2019-11-30	3.13	1.03	2.52	539	15.9
	2019-12-22	3.15	2.16	2.83	605	17.9
C/2018 W2	2019-09-07	1.45	0.5	0.8	171	41.6
	2019-10-02	1.5	6.25	0.52	112	12.9
C/2018 Y1	2019-01-11	1.35	-7.78	1.26	605	44.1
	2019-01-12	1.35	-7.5	1.23	591	44.6
	2019-01-31	1.29	-1.87	0.55	264	45.4
	2019-02-02	1.29	-1.26	0.49	235	42.5
	2019-02-03	1.28	-0.96	0.46	221	40.7
C/2019 L3	2021-11-09	3.6	-2.46	3.08	658	14.6
	2022-02-18	3.57	1.61	2.87	614	12.46
C/2019 N1	2020-06-25	2.62	-15.4	2.84	607	20.91
	2020-07-22	2.39	-14.61	2.85	609	20.05
C/2019 Y4	2020-02-22	2.11	-27.11	1.3	306	19.52
	2020-02-23	2.1	-27.21	1.29	304	19.9
	2020-03-15	1.76	-29.32	1.11	261	31.33
	2020-05-26	0.29	0.0	0.8	188	132.0
C/2020 A2	2020-01-31	1.05	10.98	1.14	268	52.51
	2020-02-22	1.24	17.52	0.914	221	51.7
	2020-02-23	1.25	17.71	0.916	216	51.24
C/2020 F3	2020-07-22	0.62	38.72	0.692	148	101.35
	2020-07-24	0.66	38.52	0.695	149	96.65
C/2020 M3	2020-10-18	1.27	-2.045	0.43	101	42.6
	2020-12-15	1.47	12.6	0.5	118	10.2
C/2021 A1	2021-11-09	1.25	-26.84	1.26	269	46.25

*See Table.2.2 for orbital details of the objects

5.3 Discussion

Low resolution spectroscopy and polarisation studies are two unique stand alone techniques that can be used to understand the basic compositional characteristics of a comet. While spectroscopy provides information regarding the relative abundance of the volatile materials and a general understanding of the dust activity in the comet, polarisation study of comets at different phase angle combined with dust modelling studies helps in unveiling the physical and compositional characteristics of the dust present in the comet. The following subsections discuss the results obtained from the spectroscopic and polarisation study of various comets.

5.3.1 Spectroscopy

This section will discuss the results obtained from low resolution spectroscopy of multiple comets. Certain comets have been observed for multiple epochs while certain comets could be observed only for two or single epochs due to orbital constraints or unavailability of observational facility. Even a single epoch of spectroscopic observation for a comet is important as they provide great deal of information regarding the composition of the comet. The results from different comets, classified as short period and long period are discussed below.

5.3.1.1 Short period comets

4P/Faye

Comet 4P/Faye (hereafter 4P) is a short period comet which has been previously observed and studied by A'Hearn et al. (1995), Cochran et al. (2012) and Langland-Shula & Smith (2011). In this work, 4P could be observed only for one epoch during the current apparition. The observed spectrum of the comet is displayed in Figure.5.1a. While emissions from CN and C_2 are visible, C_3 lies within the detection limit. The analysis results (see table 5.2) shows that the comet belongs to the typical class of comets with a dust to gas ratio of -22.00$\pm$0.21 which is similar to the dust to gas ratio mentioned for SPCs in A'Hearn et al. (1995). While A'Hearn et al. (1995) detects emissions from CN, C_2 and C_3 and classifies the object as a depleted comet, Langland-Shula & Smith (2011) and Cochran et al. (2012) clearly detects only CN emission, hence classifying the object as extremely carbon chain depleted. Lin et al. (2021) reports an outburst in the comet as it was approaching perihelion. The characteristic Afρ profile as shown in Figure.5.1b implies that the dust outflow was in a steady state even after an outburst. The production rate and rate ratios reported in this work and Jehin et al. (2021b) (for observation on 2021-11-09 and 2021-11-30 respectively) are similar with the C_2 production rate higher

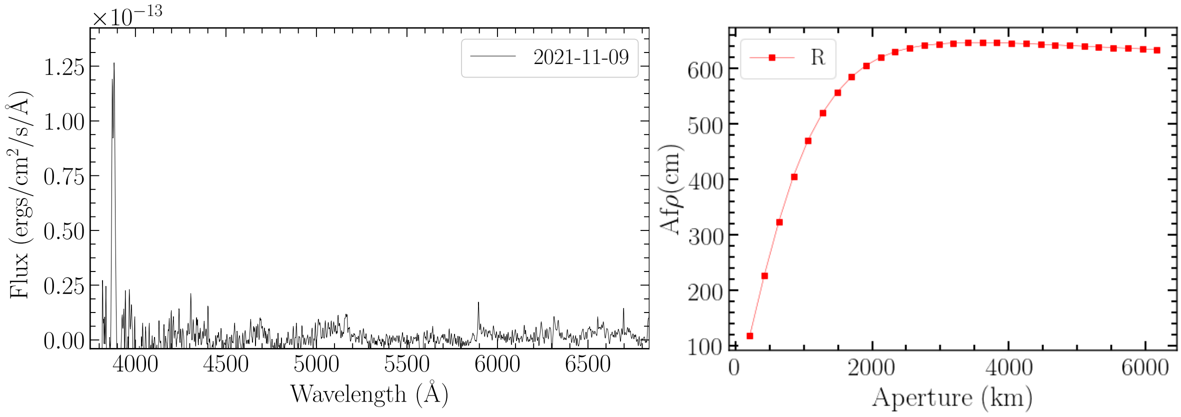

(a) 4P spectrum

(b) dust activity in R filter

Figure 5.1: Observed spectrum and Afρ profile for comet 4P

in the latter. A major difference in the depletion of carbon reported in observations for previous and current apparition is visible. The outburst would have resulted in unveiling a previously unexposed region in the nucleus which is rich in carbon chain molecules. From these comparisons, there is high possibility that the nucleus of comet 4P is highly heterogeneous.

Table 5.2: Activity of comet 4P

Date	r_H	Δ	Production Rate (molecules per sec)			Production rate ratio	Afρ (cm)		Dust to gas ratio
(UT)	(AU)	(AU)	CN	$C_2(\Delta v = 0)$	C_3	$Q(C_2)/Q(CN)$	BC	GC	$(Af\rho)_{BC}/Q(CN)$
20211109	1.73	0.99	24.66(0.18)	24.68(0.47)	<24.02(0.88)	0.02(0.50)	2.67(0.11)	2.71(0.10)	-22.00(0.21)

Values in the parenthesis represents the corresponding errors.
Production rates and ratios are in log scale.

21P/Giacobini–Zinner

Comet 21P/Giacobini–Zinner (hereafter 21P) has been studied extensively by Lara et al. (2003), Cochran et al. (2012), Pittichová et al. (2008), Schleicher (2022), Ehlert et al. (2019), Cochran et al. (2020), Shinnaka et al. (2020) and Moulane et al. (2020b) and is considered a prototype for carbon-chain depleted comets. The dust or gas behaviour of this comet is observed to be consistent over multiple apparitions (Moulane et al., 2020b). In this work comet 21P was observed for a single epoch from which it was observed that it contains large amount of CN emission compared to C_3 and C_2 (see Figure.5.2). Table.5.3 represents the results obtained for the comet. It is seen that the gas and dust activity obtained in this work is similar to what has been observed for the comet in nearby epochs reported in Schleicher (2022), Moulane et al. (2020b) and Ehlert et al. (2019) respectively. The dust colour (BC-GC) was computed to be 0.759±0.03 which is similar to the dust colour reported by Jewitt (2015) for active JFCs. The consistency in dust and gas activity as well as the relative abundances over multiple apparitions point to a highly homogeneous nucleus of the comet.

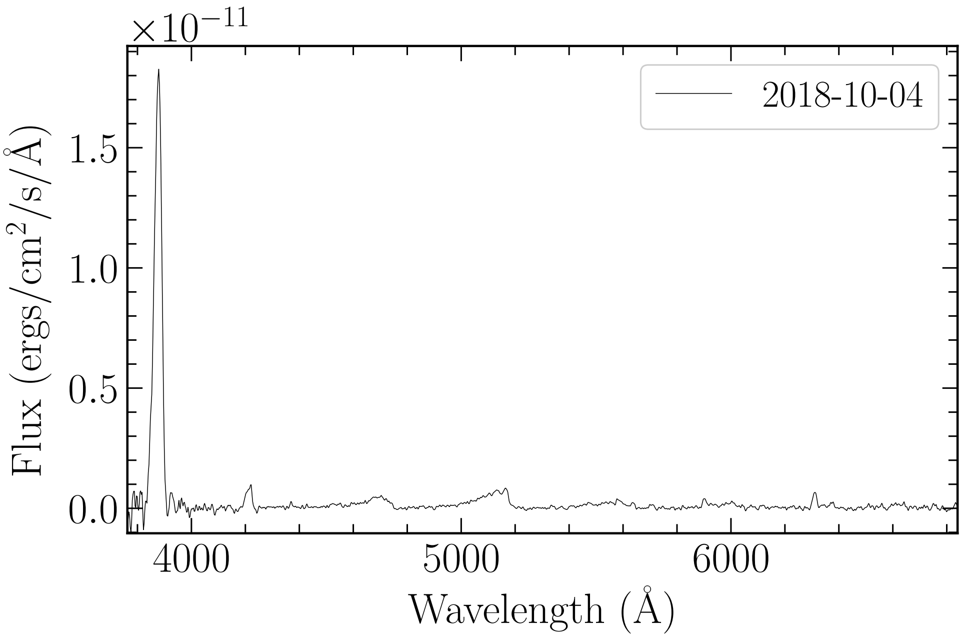

Figure 5.2: Optical spectrum of comet 21P as observed on 2018-10-04.

Table 5.3: Activity of comet 21P at different epochs

Date	r_H	Δ	Production Rate (molecules per sec)			Production rate ratio	$Af\rho$ (cm)		Dust to gas ratio
(UT)	(AU)	(AU)	CN	$C_2(\Delta v = 0)$	C_3	$Q(C_2)/Q(CN)$	BC	GC	$(Af\rho)_{BC}/Q(CN)$
20181004	1.07	0.48	25.38(0.01)	24.84(0.07)	<23.83(0.50)	-0.54(0.07)	2.37(0.10)	2.50(0.07)	-23.01(0.10)

Values in the parenthesis represents the corresponding errors.
Production rates and ratios are in log scale.

38P/Stephan-Oterma

Comet 38P/Stephan-Oterma (hereafter 38P) is the only HCT among all the observed comets in this work. As discussed in Chapter.1, HTCs are considered to be the extension of returning LPC having slowly moved into the realms of the giant planets. Hence, they are a short cut to observe the composition of a past LPC during multiple epochs which is not possible in the case of an actual LPC. A'Hearn et al. (1995) and Cochran et al. (2012) have observed the comet in its previous apparition and classified it to be a typical comet with dust to gas ratio in the range observed for JFCs. In the current apparition, we observed 38P for 4 epochs across November and December 2018 (see Figure.5.3). The production rates of various molecules, Afρ and dust to gas ratio observed in the distinct epochs are given in Table.5.4. It is observed that the comets composition has remained to be typical with a slight cutback in the $Q(C_2)/Q(CN)$ ratio, but is seen to be more dusty. Further observations during the comets next apparition could confirm whether there is a systematic reduction in the production rate ratio and increase in the dustiness of the comet. Any such change can confirm the presence of layering in the cometary nucleus with slightly different compositions.

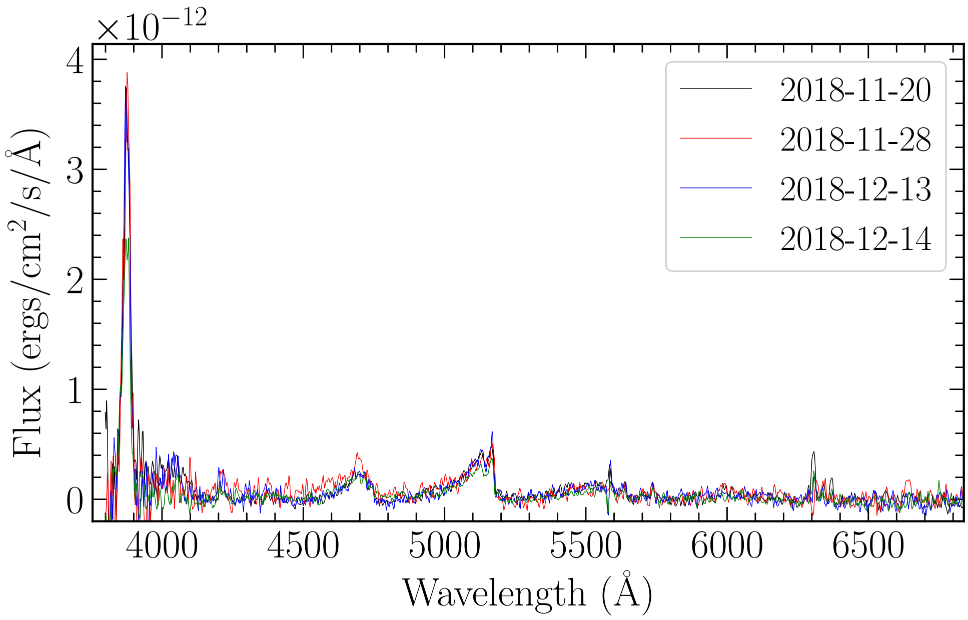

Figure 5.3: Optical spectra of comet 38P observed on 4 different epochs. Spectra extracted for aperture size of 69.16, 61.18,90.44 and 79.8 arcsec in chronological order.

67P/Churyumov–Gerasimenko

A short period comet 67P/Churyumov–Gerasimenko (hereafter 67P) became the main target for a space mission *Rosetta* launched in 2004. The successful space mission studied the comet in great detail. Repeated ground based observation of the comet during multiple apparition can provide more details regarding the comets composition.

Table 5.4: Activity of comet 38P at different epochs

Date	r_H	Δ	Production Rate (molecules per sec)				Production rate ratio	$Af\rho$ (cm)		Dust to gas ratio
(UT)	(AU)	(AU)	CN	$C_2(\Delta v = 0)$	$C_2(\Delta v = 1)$	C_3	$Q(C_2)/Q(CN)$	BC	GC	$(Af\rho)_{BC}/Q(CN)$
20181120	1.59	0.82	24.89(0.06)	24.81(0.30)	24.73(0.31)	24.11(0.28)	-0.09(0.30)	2.82(0.09)	2.95(0.07)	-22.07(0.11)
20181128	1.60	0.79	24.88(0.05)	24.80(0.33)	24.72(0.34)	24.04(0.29)	-0.08(0.34)	2.81(0.09)	2.91(0.07)	-22.07(0.10)
20181213	1.64	0.76	24.75(0.11)	24.66(0.33)	24.55(0.33)	24.08(0.61)	-0.09(0.34)	2.83(0.09)	2.89(0.08)	-21.92(0.14)
20181214	1.65	0.76	24.72(0.16)	24.63(0.33)	24.57(0.33)	24.04(0.75)	-0.08(0.36)	2.80(0.05)	2.86(0.04)	-21.92(0.17)

Values in the parenthesis represents the corresponding errors.
Production rates and ratios are in log scale.

A'Hearn et al. (1995), Fink (2009) and Cochran et al. (2012) have carried out optical ground based observations of 67P in various apparitions. Even though the comet was observed to be depleted in carbon-chain as reported by A'Hearn et al. (1995) and Fink (2009), Cochran et al. (2012) reports the comet to be highly typical. Sharma et al. (2021) reports 2 outburst in the comet in October and November 2021 out of which the second outburst was seen to be larger than the strongest outburst observed by *Rosetta* in 2015. In this work, the comet was observed for a single epoch in spectroscopy and two epochs in polarisation (see Section.5.3.2). The final spectrum of the comet is illustrated in Figure.5.4 and the computed results are displayed in Table.5.5. From the observation of the comet in the current apparition, we found the composition to be typical in the boundary region of the classification. This is similar to what has been reported by Jehin et al. (2021b) for observations on 2021-12-02. But later, for an observation on 2022-01-21, Jehin et al. (2022b) reports an increase in the C_2 production rate making the comet highly typical. A long term study of the activity in the comet during the current apparition might be crucial in understanding the observed variations in the production rates and ratios.

In addition, the $Af\rho$ profile shown in Figure.5.5a implies a non-steady state of dust outflow and Figure.5.5b illustrating the variation of colour with cometocentric distance indicates the dominance of larger sized particles in the outercoma. The variation in colour is similar to what has been reported by Rosenbush et al. (2017) during the comet's previous apparition. Further analysing an image of the comet acquired in broad band R filter through LS processing, as mentioned in Section.3.4.2.1, for a rotation angle of 20° reveals the presence of strong jets within the coma (see Figure.5.6). Such jets being be the main reason for a non-steady state of dust outflow in the coma was previously observed in comet 156P/Russell-LINEAR (Aravind et al., 2022). The dust outflow would be causing a difference in the dominance of dust population radially in the coma resulting in the observed variation in colour.

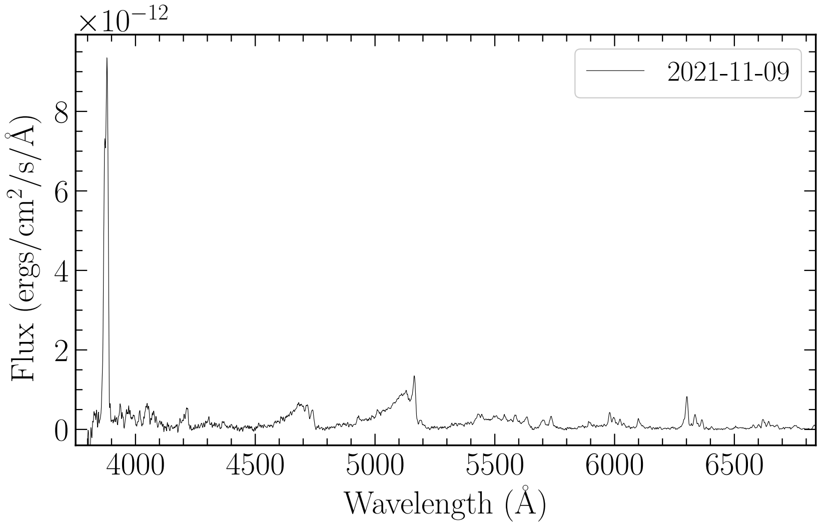

Figure 5.4: Optical spectra of comet 67P observed on 2021-11-09

Table 5.5: Activity of comet 67P

Date	r_H	Δ	Production Rate (molecules per sec)				Production rate ratio	Afρ (cm)		Dust to gas ratio
(UT)	(AU)	(AU)	CN	$C_2(\Delta v = 0)$	$C_2(\Delta v = 1)$	C_3	$Q(C_2)/Q(CN)$	BC	GC	$(Af\rho)_{BC}/Q(CN)$
20211109	1.21	0.42	25.12(0.03)	24.97(0.08)	24.87(0.06)	24.09(0.29)	-0.15(0.08)	2.84(0.04)	2.95(0.03)	-22.28(0.05)

Values in the parenthesis represents the corresponding errors.
Production rates and ratios are in log scale.

88P/Howell

Comet 88P/Howell (hereafter 88P) in spite being an SPC is one comet which has not been studied in depth due to its unfavourable apparitions. A'Hearn et al. (1995) and Cochran et al. (2012) reports the activity in the comet during one of its previous favourable apparitions. Both report the comet to be typical in composition with a dust to gas ratio in the range observed for SPCs. In this work, 88P was observed for 3 epochs as the comet was approaching perihelion. As given in Table.5.6, it was observed that the activity in the comet increased drastically from 18 May 2020 to 22 July 2020. The optical spectrum corresponding to the observation on 22 July is given in Figure.5.7. In the 2 initial epochs the production rate ratio ($Q(C_2)/Q(CN)$) and dust to gas ratio

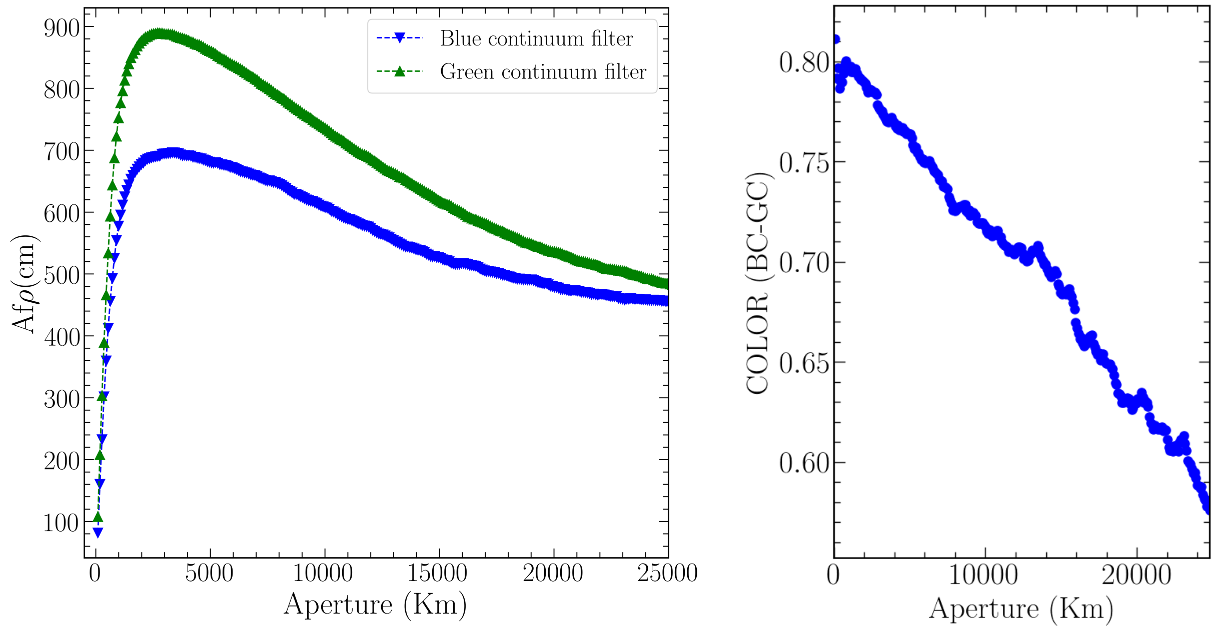

(a) 67P afrho

(b) Colour with nucleocentric distance

Figure 5.5: Variation in Afρ and dust colour as a function of the aperture size in comet 67P

was found to be similar to that reported by A'Hearn et al. (1995) while it changed significantly for the observation in July. In the due course, the dust to gas ratio during the initial 2 epochs, which was in the range expected for SPCs, also decreased to the range observed for LPCs making it gas dominated. Schleicher et al. (2020) reports an extremely steep increase in water production rate between mid-May and mid-August with an r dependence of -9.1. As they suggest, the movement of a dominant isolated source from winter to summer could be the major reason for the currently observed drastic increase in activity over the epochs. Jehin et al. (2020b) and Jehin et al. (2020a) reports the activity in 88P during October and November 2020 which is of the same order of the numbers reported for our observation in June 2020. Combining these trends, it could be expected that the activity, majorly driven by the water, would have peaked around August as the comet approached perihelion and started dropping as the comet receded. Even with such drastic changes in the activity, it is interesting to see that, the production rate ratio ($Q(C_3)/Q(CN)$) remains consistent, similar to that reported by A'Hearn et al. (1995), while the $Q(C_2)/Q(CN)$ changes significantly. Along

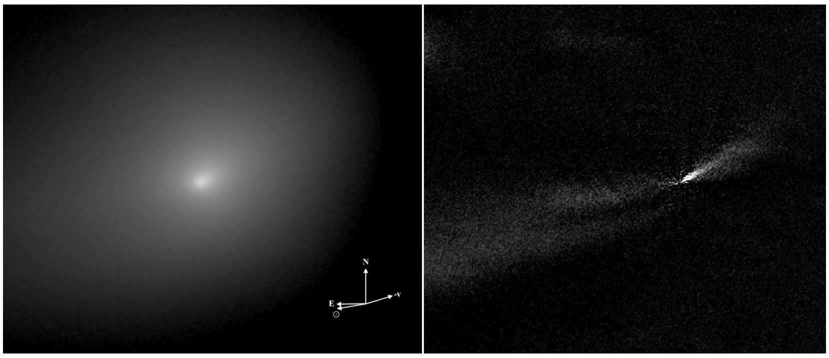

Figure 5.6: Comparison of comet 67P imaged in R filter and processed through LS filtering technique.

with further studies, this could be a major point in establishing the link between activity in water and observed production rate in C_2 molecule.

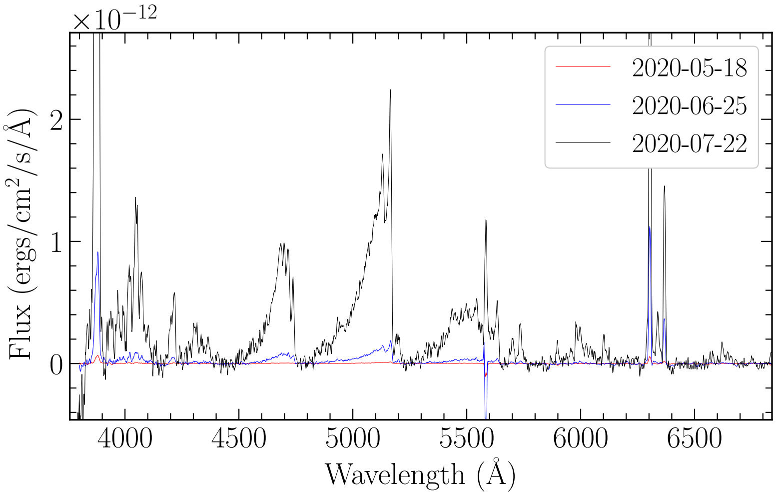

Figure 5.7: Optical spectra of comet 88P observed on different epochs. The aperture size used for spectra extraction in chronological order are 53.28 arcsec, 33.74 arcsec and 41.44 arcsec.

260P/McNaught

Comet 260P/McNaught (hereafter 260P) is another short period comet which has not been properly studied in spite of its comparatively short orbital period. Only Manzini et al. (2014) is the peer-reviewed publication on 260P investigating the spin-axis orientation of the comet during its previous apparition while Kelley et al. (2019a) have reported a small outburst in the comet during its current apparition. In this work,

Table 5.6: Activity of comet 88P at different epochs

Date	r_H	Δ	Production Rate (molecules per sec)				Production rate ratio	Afρ (cm)		Dust to gas ratio
(UT)	(AU)	(AU)	CN	$C_2(\Delta v = 0)$	$C_2(\Delta v = 1)$	C_3	$Q(C_2)/Q(CN)$	BC	GC	$(Af\rho)_{BC}/Q(CN)$
20200518	1.92	1.08	24.36(0.03)	24.29(0.12)	–	23.37(0.27)	-0.07(0.12)	1.51(0.16)	1.56(0.14)	-22.86(0.16)
20200625	1.68	1.18	25.23(0.01)	25.18(0.06)	25.02(0.06)	24.26(0.10)	-0.04(0.06)	2.42(0.11)	2.49(0.09)	-22.81(0.11)
20200722	1.53	1.25	26.38(0.02)	26.43(0.03)	26.27(0.01)	25.36(0.11)	0.05(0.04)	2.85(0.07)	2.96(0.06)	-23.53(0.07)

Values in the parenthesis represents the corresponding errors.
Production rates and ratios are in log scale.

we have observed the comet for 3 epochs as it was receding after perihelion. Table.5.7 shows the various results computed from the observation. It is seen that 260P is another comet similar to 21P which is depleted in Carbon-chain molecules. As expected, 260P is also a dust dominated comet with dust to gas ratio consistently lying in the range observed for other SPCs. Figure.5.8 illustrates the Afρ profile of the comet in BC and GC filter bands as seen on the different dates. An Afρ profile depicting a non-steady state outflow of dust is observed during the first epoch while it flattens out for the next two epochs. On further analysing the broadband image of the comet available for these epochs, the presence of jets were seen during the first epoch. During the same epoch, a variation in the colour with increasing aperture size is also observed similar to what is seen in 67P (see Figure.5.9b). This implies, a strong dust jet was causing a non-steady state outflow of dust resulting in the differentiation of dust population within the coma which is in turn observed as the variation in colour.

Table 5.7: Activity of comet 260P at different epochs

Date	r_H	Δ	Production Rate (molecules per sec)			Production rate ratio	Afρ (cm)		Dust to gas ratio
(UT)	(AU)	(AU)	CN	$C_2(\Delta v = 0)$	C_3	$Q(C_2)/Q(CN)$	BC	GC	$(Af\rho)_{BC}/Q(CN)$
20191002	1.44	0.56	24.41(0.04)	24.00(0.36)	22.89(0.71)	-0.41(0.37)	2.06(0.04)	2.16(0.03)	-22.35(0.06)
20191130	1.67	0.77	24.10(0.20)	23.82(0.59)	22.56(0.47)	-0.29(0.62)	2.18(0.10)	2.16(0.10)	-21.93(0.22)
20191222	1.80	0.98	24.02(0.14)	23.69(0.63)	22.49(0.61)	-0.33(0.65)	1.83(0.12)	1.81(0.12)	-22.19(0.18)

Values in the parenthesis represents the corresponding errors.
Production rates and ratios are in log scale.

123P/West-Hartley

Comet 123P/West-Hartley (hereafter 123P) is a peculiar comet belonging to the Jupiter Family. Other than Kelley et al. (2019b) reporting an apparent outburst in the comet,

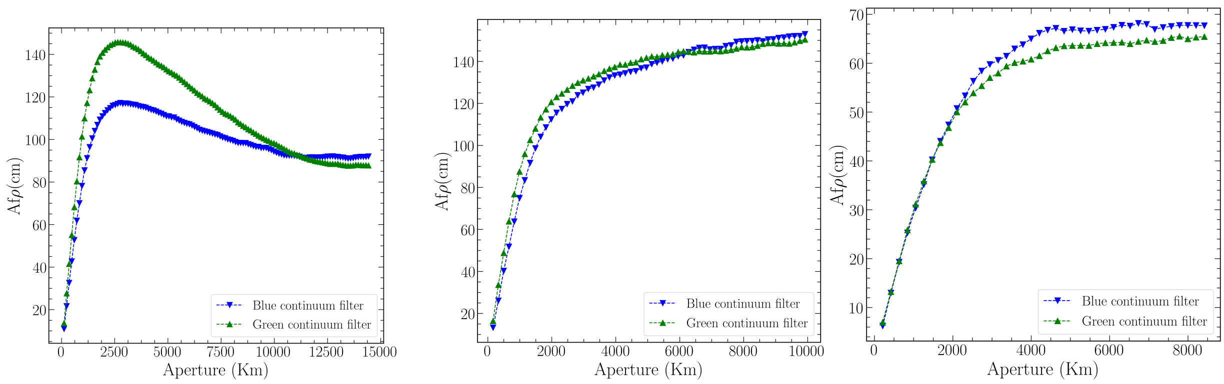

(a) 2019-10-02 (b) 2019-11-30 (c) 2019-12-22

Figure 5.8: Afρ computed for BC and GC filter bands for observation of comet 260P on various epochs.

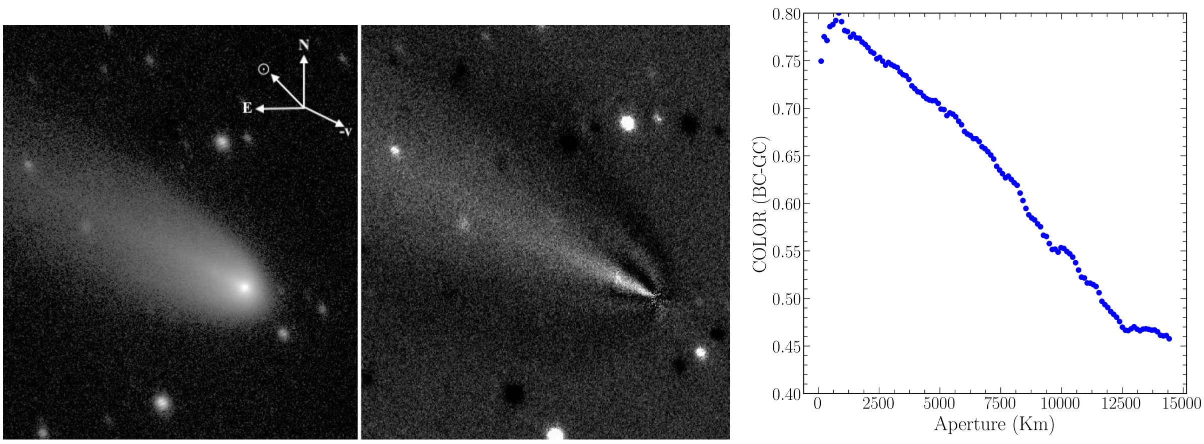

(a) R filter image of 260P observed on 2019-10-02 processed in LS technique for an angle of 20°

(b) colour variation in 260P with increasing aperture size

Figure 5.9: Analysing the morphology and colour variation in 260P

Kelley et al. (2013) reports the detection of 123P but mentions that it was not bright enough to be studied. Other than this there is no other published work reporting the activity in this comet. We observed this comet in spectroscopy for 3 epochs during which the spectrum was featureless. It was enthralling to see that the object displayed a prominent coma (see Figure.5.10a) while the spectrum showed no signs of emissions in the optical regime. The observed spectrum was used to compute the Afρ in different filter bands as given in Table.5.8. The observed coma producing adequate dust activity should be driven by some sort of emission. Either there is some strong emissions going on in the other wavelength regimes or the signal of the observed spectrum is not high enough to detect any sort of emissions present in it. Due to the absence of emissions, the reflectance spectrum obtained by dividing the object spectrum with a solar analog star spectrum observed on the same day, was matched with those of different types of asteroids to obtain a match with S-Type (see Figure.5.10b). This object could either be a dead comet or an active asteroid. Further study of the object in its upcoming apparition with larger telescopes could prove worthy in understanding the hidden activity in a less probed object.

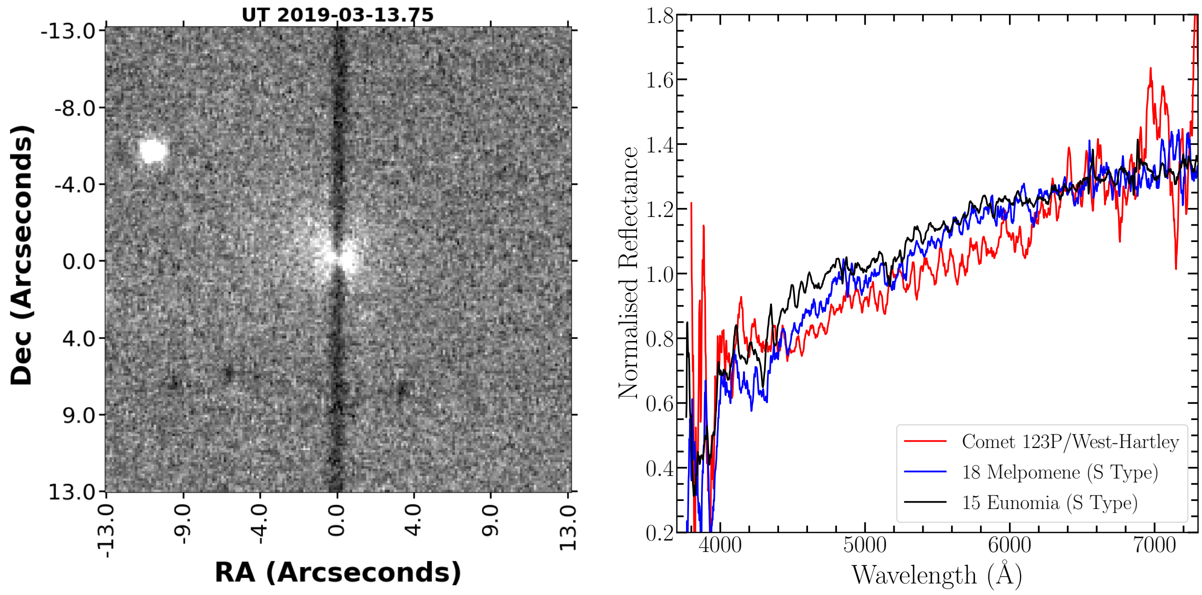

(a) 123P imager

(b) 123P reflectance

Figure 5.10: Comet 123P observed using LISA

Table 5.8: Dust activity of comet 123P at different epochs

Date	r_H	Δ	Afρ (cm)	
(UT)	(AU)	(AU)	BC	GC
20190313	2.14	1.22	2.78(0.08)	2.81(0.07)
20190401	2.17	1.31	2.60(0.08)	2.73(0.07)
20190402	2.17	1.32	2.45(0.11)	2.50(0.10)

Values in the parenthesis represents the corresponding errors
Afρ values are in log scale

29P/Schwassmann–Wachmann

Out of all the comets observed in the Solar system, there only few of them, 29P/Schwassmann-Wachmann (hereafter 29P), C/2002 VQ9 (LINEAR) and C/2016 R2 (PANSTARRS) which shows strong emissions from different bands of CO^+ and N_2^+ (Cochran et al., 1980, 1991; Korsun et al., 2008; Ivanova et al., 2016, 2019a, 2011; Picazzio et al., 2019; Opitom et al., 2019b; Venkataramani et al., 2020). Among these comets only 29P has showed emission features from CN (Cochran et al., 1980; Cochran & Cochran, 1991; Bockelée-Morvan et al., 2022) with other emissions from C_2 and C_3 absent. In this work, 29P was observed for 2 epochs, 2020-10-18 and 2021-11-09, among which the first epoch showed clear emissions from different bands of CO^+ and feeble emission from N_2^+(0-0) band while the detection was not so clear in the second epoch in spite of a brighter coma (see Figure.5.11).

Table 5.9: Relative intensities of different CO^+ bands with reference to (3-0) band observed on 202-10-18

Band	Flux (ergs cm^2 s^{-1})	Relative intensity
(3-0)	3.9E-15	1
(2-0)	3.71E-15	0.95
(2-1)	1.89E-15	0.48
(3-2)	2.3E-15	0.58
(1-0)	1.93E-15	0.49

Figure.5.12a illustrates the CO^+ (A-X) emissions observed in 29P. The emission bands of CO^+ have been identified by overlaying the optical spectrum of comet C/2016 R2 reported in Venkataramani et al. (2020) (see Figure.5.12b). The intensities of all the detected CO^+ bands were measured and the relative strength of the bands in reference to the (3-0) band are given in Table.5.9. They are in agreement to the observational and theoretical values reported by Venkataramani et al. (2020), Arpigny (1964), Magnani & A'Hearn (1986) and Krishna Swamy (1979). The $[N_2^+]/[CO^+]$ ratio was computed using both (3-0) and (2-0) bands of CO^+ emission. The column densities of both (3-0) and (2-0) bands were computed using the fluorescence efficiency (g) given in Magnani & A'Hearn (1986) and the fluorescence efficiency for the N_2^+ band was taken from Lutz et al. (1993). The ratio computed using the (3-0) band is found to be 0.012±0.002 and

(2-0) band is found to be 0.0102±0.002. These are well in agreement with the ratios reported by Ivanova et al. (2016) and Picazzio et al. (2019). The Afρ values corresponding to R and V filters (see Figure.5.13) implies a comparatively high dust activity in the comet. Further detailed studies are required to understand the frequent outbursts and source of the emissions observed in 29P.

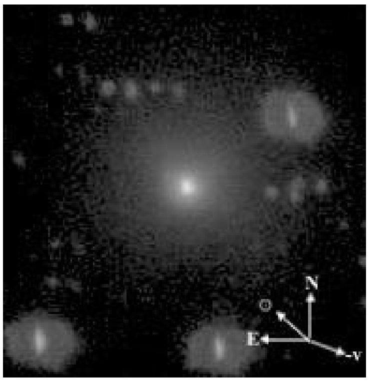

(a) 29P on 2020-10-18

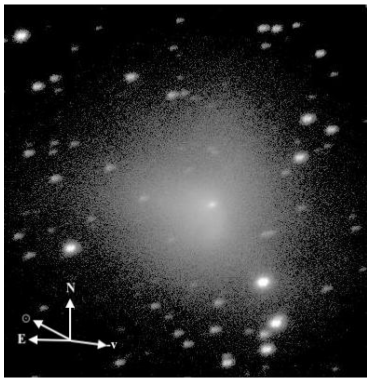

(b) 29P on 2021-11-09

Figure 5.11: Comet 29P images in R

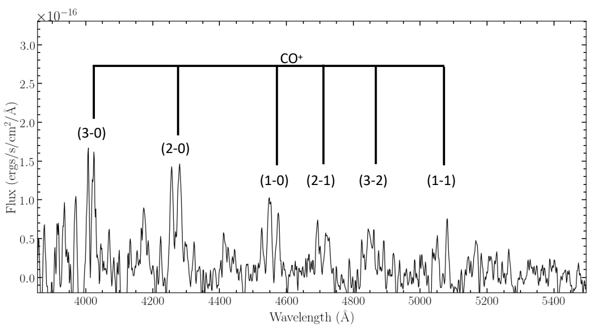

(a) 29P spectrum observed on 2020-10-18

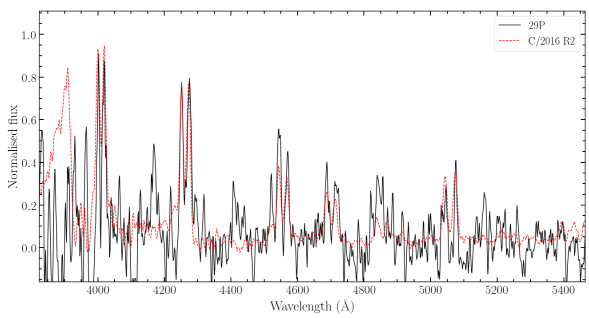

(b) Comparison of emissions in 29P and C/2016 R2

Figure 5.12: Emissions observed in comet 29P

5.3.1.2 Long period comets

C/2018 N2 (PANSTARRS)

Certain comets travelling into the inner Solar system interacts with the giant planets for their orbits to get converted into hyperbolic. C/2018 N2 (ASASSN) (hereafter N2) is one

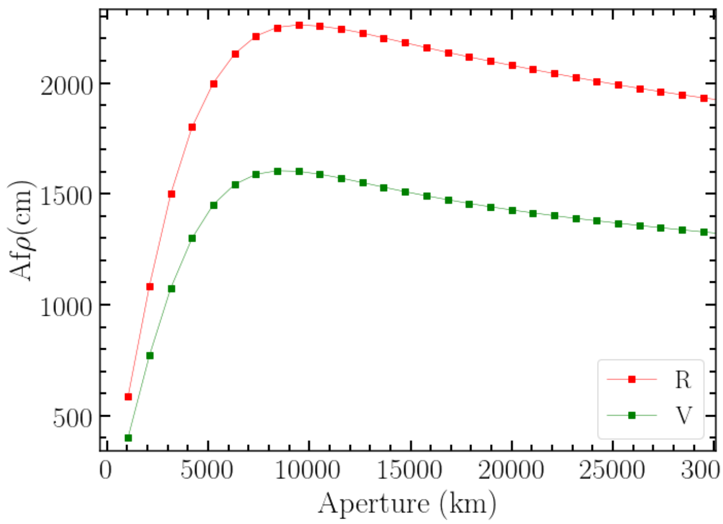

Figure 5.13: Afρ profile of comet 29P observed in broadband R and V filters on 2020-10-18.

such comet which had a very large perihelion. In this work, comet N2 was observed after perihelion for 2 epochs. The comet showed strong emissions from CN and C_2 and detectable emission from C_3 despite being at a large heliocentric distance. Figure.5.14 illustrates the spectrum of the object observed on both the epochs. Table.5.10 lays out the production rates and ratios computed for the corresponding epochs. It is observed that N2 belongs to the depleted class of comets and the dust to gas ratio is similar to that observed for SPCs. There is a possibility that this depletion and dusty nature could be a result of the distance at which the comet is observed where the temperature is not ambient enough to sublimate the major parent molecules of C_2 as well as other ices. But, the detection of strong emissions at this distance in turn implies the possibility of the presence of very pristine materials in this object. Combining bits of observation of this object observed around the world would be vital in understanding the activity in a comet that would never return back to the Solar system.

Table 5.10: Activity of comet C/2018 N2 at different epochs

Date	r_H	Δ	Production Rate (molecules per sec)			Production rate ratio	Afρ (cm)		Dust to gas ratio
(UT)	(AU)	(AU)	CN	$C_2(\Delta v = 0)$	C_3	$Q(C_2)/Q(CN)$	BC	GC	$(Af\rho)_{BC}/Q(CN)$
20191130	3.13	2.52	25.55(0.05)	25.18(0.46)	24.39(0.37)	-0.37(0.46)	3.42(0.04)	3.49(0.03)	-22.13(0.07)
20191222	3.15	2.83	25.58(0.06)	25.19(0.38)	24.54(0.37)	-0.40(0.38)	3.46(0.05)	3.43(0.05)	-22.13(0.08)

Values in the parenthesis represents the corresponding errors.
Production rates and ratios are in log scale.

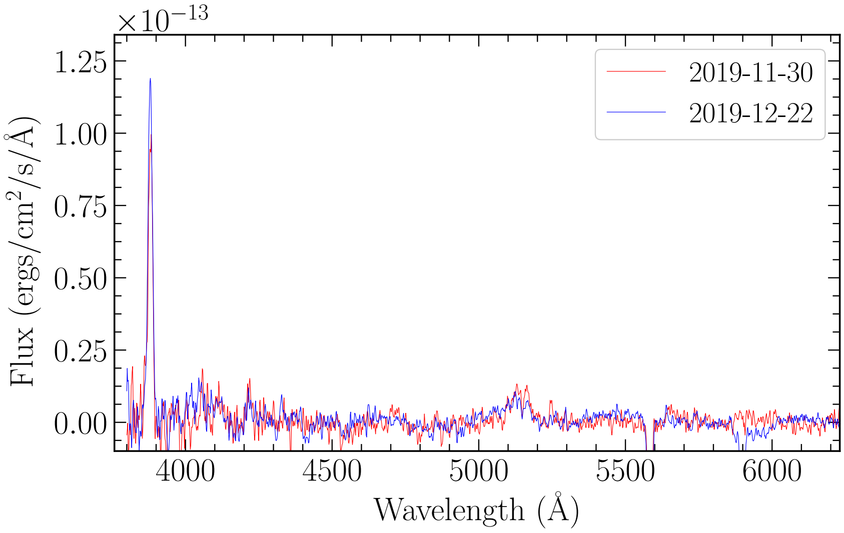

Figure 5.14: Optical spectrum acquired for comet C/2018 N2.

Optical spectrum acquired for comet C/2018 N2. Both Spectra extracted for an aperture size of 35.52 arcsec.

C/2018 W2 (PANSTARRS)

Long period comet C/2018 W2 (PANSTARRS) (hereafter W2) had its perihelion passage on September 05 2019 during which the TRAPPIST telescopes have observed the activity in the comet (Moulane et al., 2020a). There has been no publications on the comet discussing the emissions or activity displayed by the comet. In this work, we observed W2 for two epochs, one month apart, just after perihelion. Figure.5.15 shows the strong emissions detected in the comet. The various emissions and continuum flux were analysed to compute the production rates and ratios as shown in Table.5.11. The comet was seen to be a normal LPC with typical composition but having dust to gas ratio similar to that of SPC. The various other emissions seen in the spectrum can be analysed in depth to get a better understanding of the composition of the comet.

Table 5.11: Activity of comet C/2018 W2 at different epochs

Date	r_H	Δ	Production Rate (molecules per sec)				Production rate ratio	$Af\rho$ (cm)		Dust to gas ratio
(UT)	(AU)	(AU)	CN	$C_2(\Delta v = 0)$	$C_2(\Delta v = 1)$	C_3	$Q(C_2)/Q(CN)$	BC	GC	$(Af\rho)_{BC}/Q(CN)$
20190907	1.45	0.80	25.14(0.03)	25.21(0.04)	25.10(0.04)	24.11(0.35)	0.07(0.05)	2.39(0.07)	2.52(0.05)	-22.75(0.08)
20191002	1.50	0.52	24.98(0.04)	25.02(0.03)	24.83(0.03)	23.99(0.45)	0.04(0.05)	2.26(0.04)	2.40(0.03)	-22.72(0.05)

Values in the parenthesis represents the corresponding errors.
Production rates and ratios are in log scale.

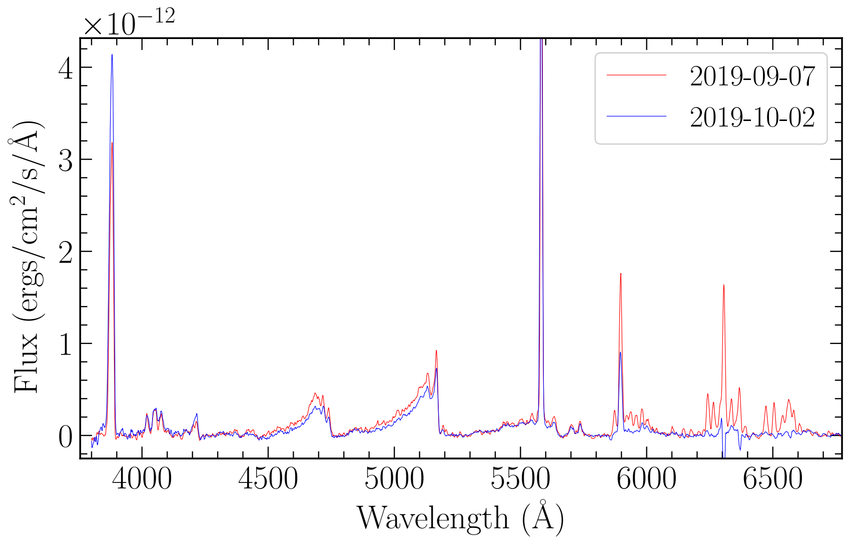

Figure 5.15: Optical spectrum acquired for comet C/2018 W2. Aperture size of 103.6 arcsec used on both epochs for extracting the spectrum.

C/2018 Y1 (Iwamoto)

LPCs are usually seen to be rich in both gas and dust. An LPC poor in dust could imply that it would have formed in a region dominated by volatile ices with a smaller fraction of dust present to accumulate. C/2018 Y1 (Iwamoto) (hereafter Y1) was a moderately bright LPC with a retrograde orbit. DiSanti et al. (2021) observed Y1 in the IR regime to detect certain parent molecules while Moulane et al. (2020a) has reported their observation of Y1 using the narrow band optical imaging to study the activity in the comet. In this work, we have observed Y1 for 5 epochs before perihelion. It was observed that the continuum contribution to the spectrum was very feeble. Figure.5.16 illustrates spectra corresponding to a few observational epochs. The computed results are displayed in Table.5.12. As observed from the spectrum, Y1 was seen to be poor in dust with a dust to gas ratio pointing too a gas rich comet. Only a few LPCs have been observed exhibiting such dust poor behaviour. Discovery of more such objects would help in constraining the location where such objects were formed.

C/2019 L3 (ATLAS)

It is rarely that comets with large heliocentric distance become bright enough to show detectable emissions in the optical wavelengths. C/2018 N2 was one such comet which

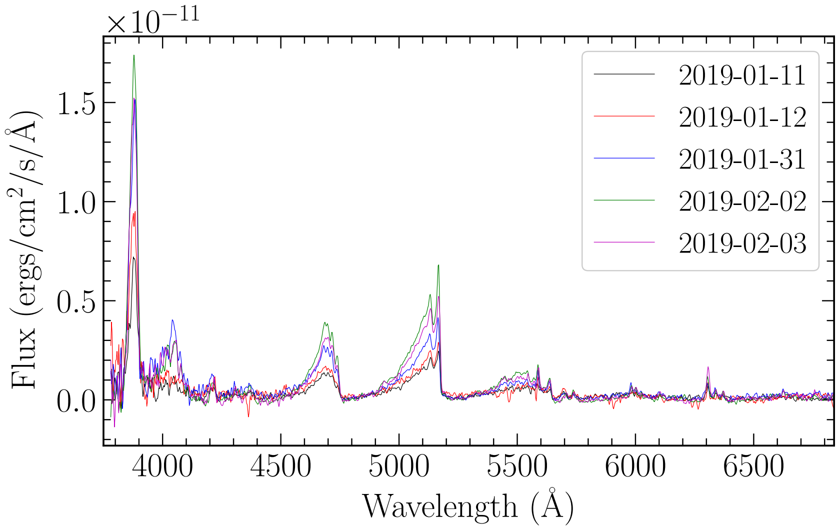

Figure 5.16: Optical spectrum acquired for comet C/2018 Y1. Aperture size used for spectra extraction in chronological order are 76.48 arcsec, 76.48 arcsec, 89.77 arcsec, 93.1 arcsec and 103.075 arcsec.

Table 5.12: Activity of comet C/2018 Y1 at different epochs

Date	r_H	Δ	Production Rate (molecules per sec)			Production rate ratio	$Af\rho$ (cm)		Dust to gas ratio
(UT)	(AU)	(AU)	CN	$C_2(\Delta v = 0)$	C_3	$Q(C_2)/Q(CN)$	BC	GC	$(Af\rho)_{BC}/Q(CN)$
20190111	1.35	1.26	26.01(0.05)	25.95(0.09)	24.33(0.11)	-0.06(0.10)	1.62(0.26)	1.63(0.26)	-24.39(0.27)
20190112	1.35	1.23	26.02(0.05)	25.96(0.10)	24.38(0.13)	-0.05(0.11)	1.64(0.27)	1.67(0.26)	-24.37(0.28)
20190131	1.29	0.55	25.79(0.09)	25.74(0.04)	24.08(0.42)	-0.06(0.10)	1.76(0.11)	1.70(0.12)	-24.04(0.14)
20190202	1.29	0.49	25.96(0.06)	25.91(0.01)	24.26(0.22)	-0.05(0.06)	1.76(0.10)	1.71(0.12)	-24.20(0.12)
20190203	1.28	0.46	25.80(0.09)	25.74(0.03)	24.14(0.09)	-0.06(0.09)	1.60(0.10)	1.52(0.12)	-24.20(0.13)

Values in the parenthesis represents the corresponding errors.
Production rates and ratios are in log scale.

has already been discussed. Another long period comet, C/2019 L3 (ATLAS) with its large perihelion in January 2022, was bright enough to be observed from 2 m class telescope. We observed this peculiar comet for 2 epochs, pre and post-perihelion to probe the emissions at such far off distances. Figure.5.17 presents the spectrum observed on both the epochs. The computed production rates and ratios given in Table.5.13 classifies the comet as a typical one with a very dusty nature as compared to other LPCs. These results are in agreement to that reported by Jehin et al. (2022b). Figure.5.18a indicates how bright the comet was despite being at a distance of ~3.6 AU. As mentioned before, the dust activity in the comet was observed to be relatively high for a comet at this distance (see Figure.5.18b). Even though the production rate ratios and dust to gas ratio remains consistent in pre and post perihelion observation, the activity is seen to increase around perihelion. It will be interesting to combine various data sets to study the activity curve in this peculiar hyperbolic comet.

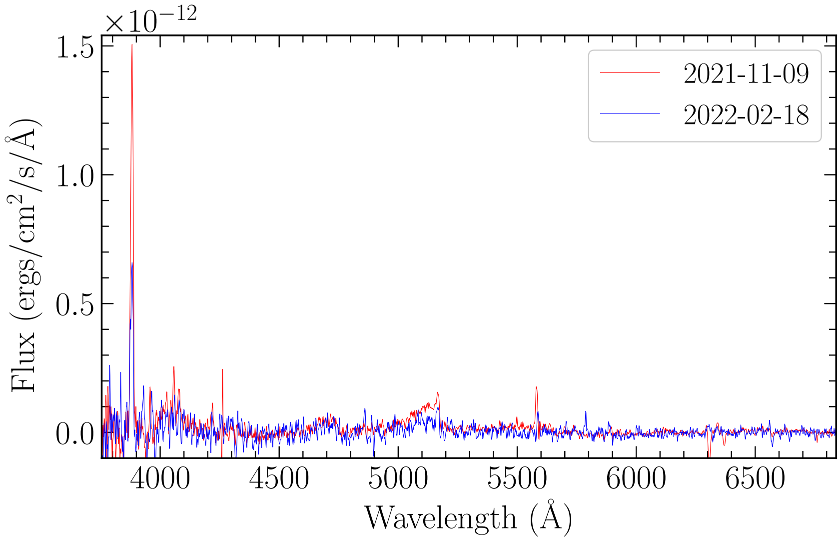

Figure 5.17: Optical spectrum acquired for comet C/2019 L3. Aperture size used to spectrum extraction are 59.2 arcsec (red) and 29.6 arcsec (blue).

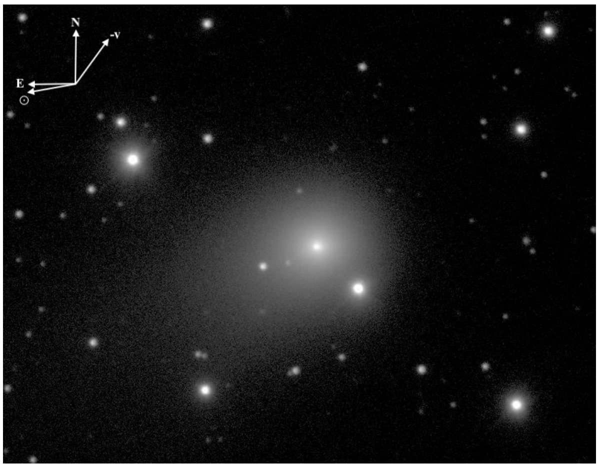

(a) C/2019 L3 comet imaged in broad band R filter

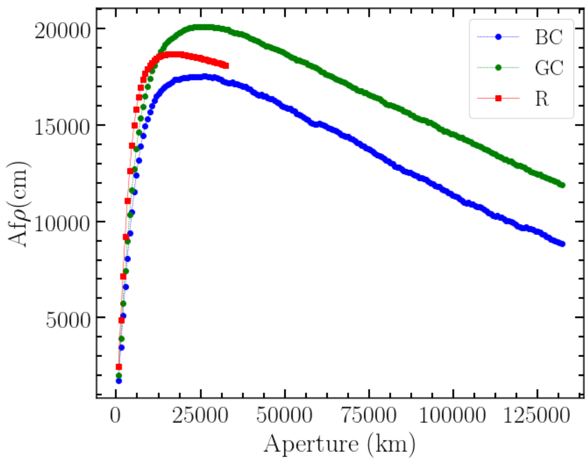

(b) Observed Afρ profiles in different filter bands

Figure 5.18: Broad band image and Afρ profile for Comet C/2019 L3

Table 5.13: Activity of comet C/2019 L3 at different epochs

Date (UT)	r_H (AU)	Δ (AU)	Production Rate (molecules per sec) CN	$C_2(\Delta\nu = 0)$	C_3	Production rate ratio $Q(C_2)/Q(CN)$	$Af\rho$ (cm) BC	GC	Dust to gas ratio $(Af\rho)_{BC}/Q(CN)$
20211109	3.60	3.08	26.32(0.06)	26.25(0.20)	25.56(0.30)	-0.07(0.21)	4.24(0.04)	4.30(0.03)	-22.08(0.07)
20220218	3.57	2.87	26.61(0.11)	26.52(0.36)	25.63(0.51)	-0.10(0.38)	4.50(0.06)	4.56(0.05)	-22.11(0.13)

Values in the parenthesis represents the corresponding errors.
Production rates and ratios are in log scale.

C/2019 N1 (PANSTARRS)

After the discovery of C/2019 L3 at a very large heliocentric distance, another LPC C/2019 N1 (PANSTARRS) (hereafter N1) was discovered to be on its way into the inner Solar system. Even though this comet was observable, no particular reports on the comet could mean that it was unobservable during most part of its orbit as it reached perihelion. In this work, we observed this comet for 2 epochs about 130 days before perihelion. Even though it was long before N1 reached perihelion, there was significant activity going on in the comet. Significant increase in the activity was observed for slight change (∼0.3 AU) in heliocentric distance. The acquired spectra is shown in Figure.5.19 and computed results are shown in Table.5.14. Although the absolute value of the production rate ratio has increased, the ratio observed for both epochs are comparable within errorbars. The measured dust to gas ratio, comparable to those of SPCs, is seen to be consistent over both the epochs. As explained earlier, the observed dust to gas ratio similar to SPCs could be a direct effect of the heliocentric distance at which the comet is observed. Currently, no known (published) observations are available to have a full scale understanding of the activity in the comet as it closed in on perihelion.

Table 5.14: Activity of comet C/2019 N1 at different epochs

Date (UT)	r_H (AU)	Δ (AU)	Production Rate (molecules per sec) CN	$C_2(\Delta\nu = 0)$	C_3	Production rate ratio $Q(C_2)/Q(CN)$	$Af\rho$ (cm) BC	GC	Dust to gas ratio $(Af\rho)_{BC}/Q(CN)$
20200625	2.62	2.84	25.46(0.08)	25.03(0.29)	24.11(0.78)	-0.42(0.30)	2.83(0.10)	3.03(0.07)	-22.62(0.13)
20200722	2.39	2.84	26.41(0.29)	26.18(0.44)	25.33(0.54)	-0.22(0.53)	3.75(0.21)	3.93(0.14)	-22.66(0.36)

Values in the parenthesis represents the corresponding errors.
Production rates and ratios are in log scale.

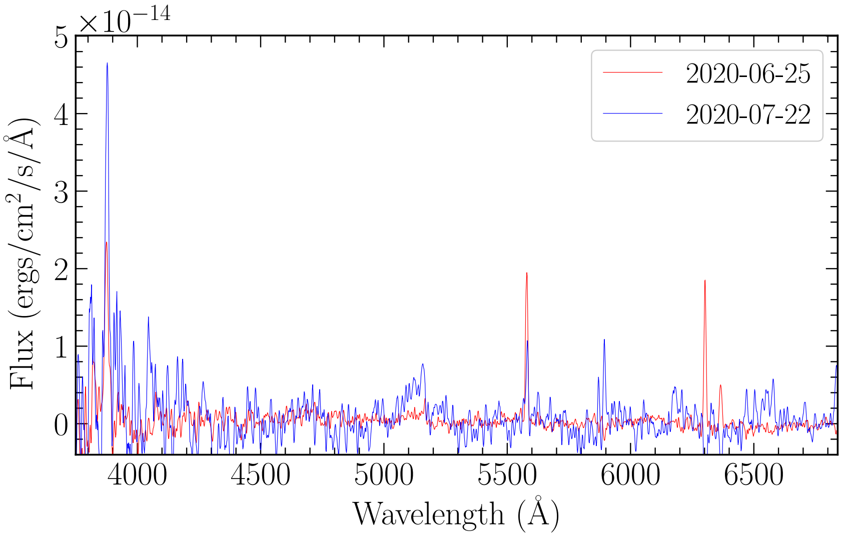

Figure 5.19: Optical spectrum acquired for comet C/2019 N1. Spectra extracted for aperture size of 11.8 arcsec (blue) and 4.2 arcsec (red)

C/2019 Y4 (ATLAS)

Comets are bodies made up of ices and dust sticking to each other. There are high chances that these objects can disintegrate due to the Solar radiation once they reach very close to the Sun. The chance of disintegration depends on both the perihelion distance as well the nucleus structure. Many comets, mostly LPCs, have been observed to get disintegrated as they reach or cross perihelion (eg., Sekanina & Kracht, 2014; Sekanina & Chodas, 2012; Zhang et al., 2022). Hui et al. (2022) reports the observations of disintegration of a first SPC. The SOHO space observatory has observed a number of Sun grazing comets out of which many have disintegrated (Biesecker et al., 1999). In 2020, comet C/2019 Y4 (ATLAS) (hereafter Y4) was the first LPC to get disintegrated well before perihelion. Moulane et al. (2020a) studied the evolution of activity in the comet and stated that the comet had reached its peak intensity around 22 March 2022. Hui & Ye (2020) reports that comet Y4 is a sibling of the comet C/1844 Y1 (Great Comet) which came into the Solar system ~ 5000 years ago and the disintegration in the comet nucleus had started by mid-March. Clear disintegration was observed in the comet by April (Ye & Zhang, 2020) and Ye et al. (2021) have studied in detail the fragmented parts and the possible reasons for fragmentation. (Ivanova et al., 2021b) reports photometric and spectroscopic observation of Y4 during the disintegration, studying the various emission arising from the comet and the variation in dust colour with nucleocentric distance. They also oppose the idea of both Y4 and C/1844 Y1 having the same origin. In this work, we observed comet Y4 for 4 epochs, 2 in February well before the disintegration, 1 in March around the time the disintegration started and 1 to the end of May well after reports of the total disintegration of the comet. Table.5.15 displays the results computed for the comets at different epochs. During the initial 2 epochs, Y4 seemed like normal LPC with typical carbon chain composition and dust to gas ratio. During the observational epoch close to the beginning of disintegration, a significant increase in the activity and emission lines were observed. A slight increase in the dust to gas ratio is observed which might be due to the large amount of dust released during the commencement of the disintegration. Reports from amateur astronomers suggested that Y4 had completely disintegrated by May 21^{st} after which it was not observable even through telescopes. Surprisingly we could obtain a spectrum of the comet on 26 May 2020 from a fuzzy region corresponding to the actual location of the comet. Figure.5.20 illustrates the comet spectra before and after disintegration. It is clearly seen that there are detectable emissions even when there wasn't a comet nucleus releasing the volatiles. Studying in detail the difference in spectra and production rate ratios before and after disintegration could help in much more detailed understanding of the coma chemistry.

Table 5.15: Activity of comet C/2019 Y4 at different epochs

Date	r_H	Δ	Production Rate (molecules per sec)				Production rate ratio	$Af\rho$ (cm)		Dust to gas ratio
(UT)	(AU)	(AU)	CN	$C_2(\Delta v = 0)$	$C_2(\Delta v = 1)$	C_3	$Q(C_2)/Q(CN)$	BC	GC	$(Af\rho)_{BC}/Q(CN)$
20200222	2.11	1.30	25.61(0.10)	25.52(0.15)	25.63(0.15)	24.90(0.29)	-0.09(0.18)	2.54(0.07)	2.44(0.09)	-23.07(0.12)
20200223	2.10	1.29	25.76(0.08)	25.65(0.16)	25.68(0.16)	25.01(0.25)	-0.11(0.18)	2.42(0.07)	2.44(0.07)	-23.35(0.11)
20200315	1.76	1.11	25.99(0.04)	25.96(0.03)	25.87(0.03)	25.22(0.23)	-0.03(0.05)	3.07(0.04)	3.04(0.04)	-22.92(0.06)
20200526	0.29	0.80	22.11(0.02)	21.79(0.13)	–	21.73(0.14)	-0.33(0.13)	–	–	–

Values in the parenthesis represents the corresponding errors.
Production rates and ratios are in log scale.

C/2020 A2 (Iwamoto)

Comet C/2020 A2 (Iwamoto) (hereafter A2) adds to the list of long period comets that has not been properly studied during its apparition. A2 was discovered during its perihelion on January 8 and had its closest approach to Earth on February 21. We observed the comet for 3 epochs after the perihelion. A2 was a faint patch requiring

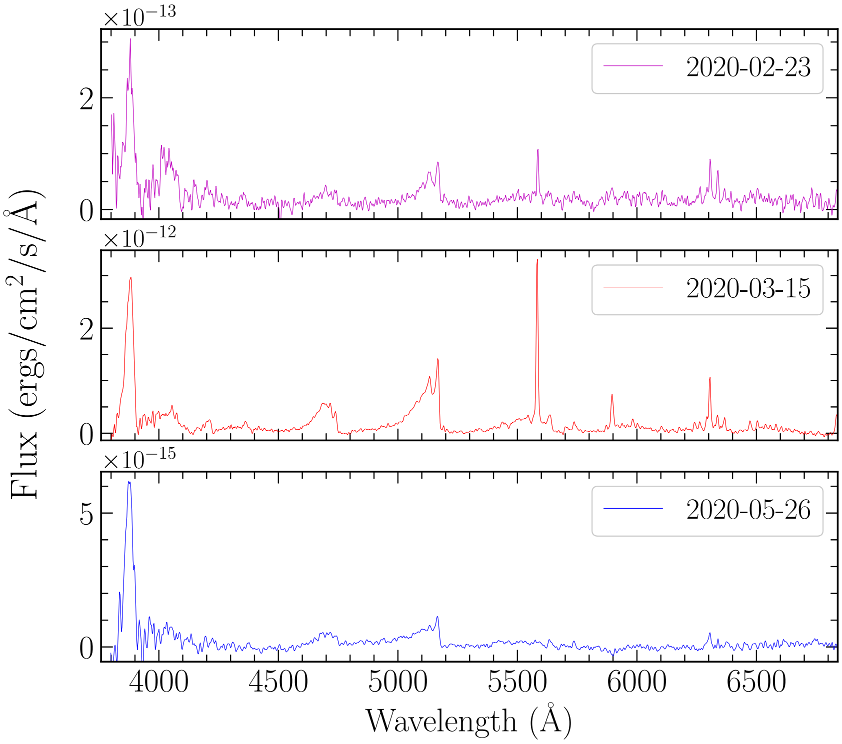

Figure 5.20: Optical spectrum acquired for comet C/2019 Y4. Aperture size used to for spectra extraction are 35.86 arcsec (top panel), 79.87 arcsec (middle panel) and 32.6 arcsec (bottom panel).

large exposures to get the ambient signal to study the spectrum. Figure.5.21 illustrates the spectrum of the comet observed on 3 different epochs. It is seen that the CN emission bands is broadened on 31 Jan 2020 when compared to the other two epochs. On detailed analysis, it was found that the N_2^+ (0-0) bands observed in C/2016 R2 (Venkataramani et al., 2020) exactly coincides with the emission seen in A2 (see Figure.5.22). This broadening of the CN bands due to possible blending with the N_2^+ (0-0) band disappears for the next two observational epochs. It could be possible that the orientation of the Earth-Comet line would have favoured the integration of any faint ionic emissions during the long exposures. This orientation would have changed as the comet came closer to Earth making it difficult to observe these emissions. Such a possible blending can be confirmed only if the comet and tail orientation during its orbit is studied in detail. From the analysis of the spectrum, A2 was seen to be a comet with typical carbon chain composition and dust to gas ratio similar to that of LPCs (see Table.5.16). The possible blending of other emissions along with CN could be the reason for the difference in the production rates between the first and second epochs. Once the presence of these ionic emissions can be further confirmed, incorporation of modelling techniques will be important to understand the composition of comet A2 in greater detail.

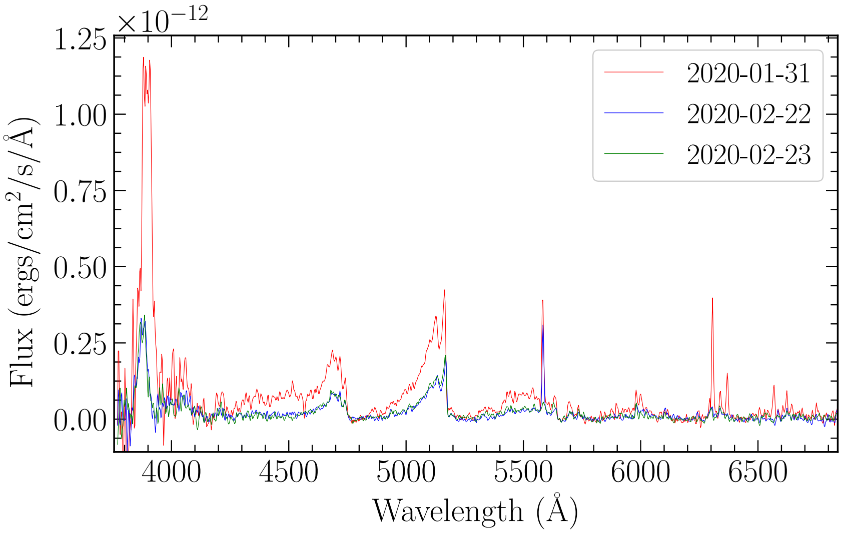

Figure 5.21: Optical spectrum acquired for comet C/2020 A2. Aperture size used to for spectrum extraction in chronological order are 27.71 arcsec, 29.34 arcsec and 29.34 arcsec.

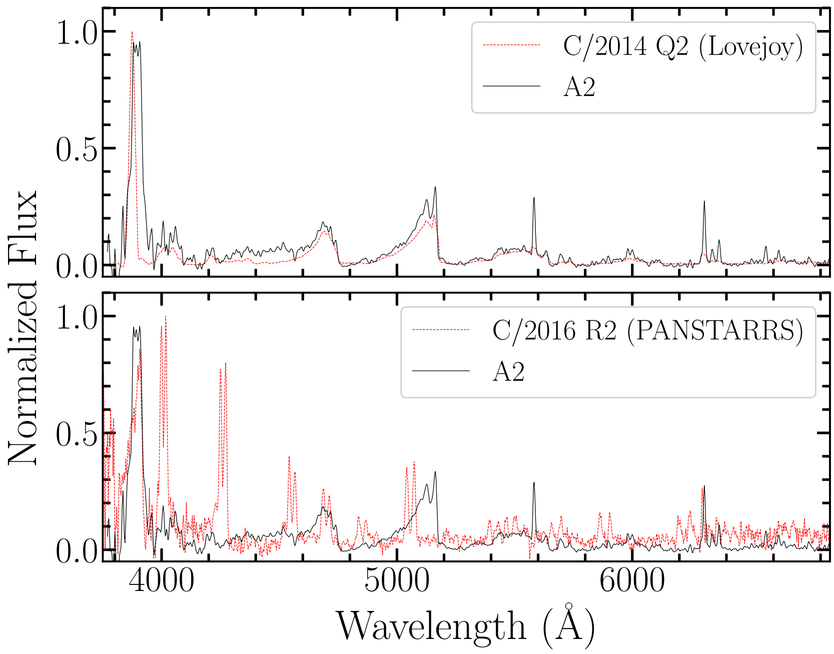

Figure 5.22: Comparison between optical spectrum acquired for A2 and comets C/2014 Q2 (Venkataramani et al., 2016) and comet C/2016 R2 (Venkataramani et al., 2020).

Table 5.16: Activity of comet C/2020 A2 at different epochs

Date (UT)	r_H (AU)	Δ (AU)	Production Rate (molecules per sec) CN	$C_2(\Delta v=0)$	$C_2(\Delta v=1)$	C_3	Production rate ratio $Q(C_2)/Q(CN)$	Afρ (cm) BC	GC	Dust to gas ratio $(Af\rho)_{BC}/Q(CN)$
20200131	1.05	1.14	25.50(0.02)	25.46(0.03)	25.36(0.03)	25.01(0.07)	-0.03(0.04)	2.30(0.07)	2.04(0.14)	-23.20(0.08)
20200222	1.24	0.91	25.23(0.02)	25.26(0.05)	25.17(0.05)	24.64(0.08)	0.03(0.06)	1.51(0.22)	1.38(0.29)	-23.73(0.22)
20200223	1.25	0.92	25.23(0.01)	25.27(0.06)	25.16(0.10)	24.57(0.04)	0.04(0.06)	1.64(0.20)	1.51(0.28)	-23.58(0.20)

Values in the parenthesis represents the corresponding errors.
Production rates and ratios are in log scale.

C/2020 F3 (NEOWISE)

There has been many great comets in the history of comet observations with 5 being observed in the last 30 years. The latest one was comet C/2020 F3 (NEOWISE) (hereafter F3) which became the brightest comet in the Northern hemisphere after comet Hale-Bopp. F3 was observable even from the light polluted skies of Indian cities. Figure.1.6 is one such spectacular image of the comet taken from the location of IAO, Hanle. The comet was too bright that a number of works including high and low resolution spectroscopy in optical and IR regime, morphology studies, polarisation studies, OH detection in radio band, water production from SOHO observations, CN jets etc has already been carried out (eg., Cambianica et al., 2021; Faggi et al., 2021; Krishnakumar et al., 2020; Manzini et al., 2021; Smith et al., 2021; Maslov, 2021; Combi et al., 2021a; Schleicher et al., 2020). Even though the comet was available at an observable altitude only for a very short time after the Sunset, we were fortunate enough to obtain the spectrum of this breathtaking comet during two epochs in July. Figure.5.23a shows the impressive spectra of the comet observed on both the epochs for an exposure time of only 3 minutes. The comet was also observed with the Gr8 grism available in HFOSC to probe the redder side (5800 – 8350 Å) at a resolution of 2190. Figure.5.23b illustrates the over-abundance of emission lines, NH_2(0-8-0), NH_2(0-7-0), NH_2(0-6-0), NH_2(0-5-0) etc, available in this region of the spectrum. From the computed production rates and ratio as given in Table.5.17, it is seen that this great comet as a highly typical carbon chain composition with dust to gas ratio similar to those expected for LPCs. The sharp variations in the production rates between two epochs could be a direct effect of the intense jets and activity going on within the coma.

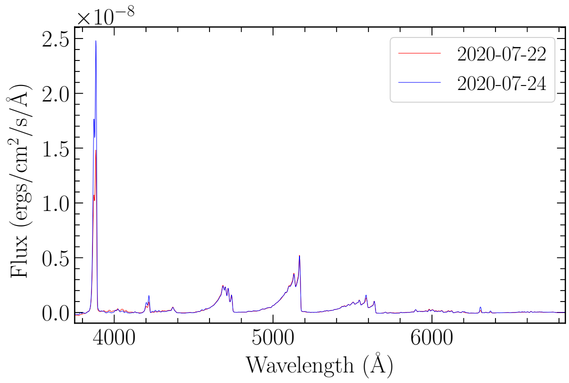

(a) Optical spectrum acquired in Grism 7 of HFOSC

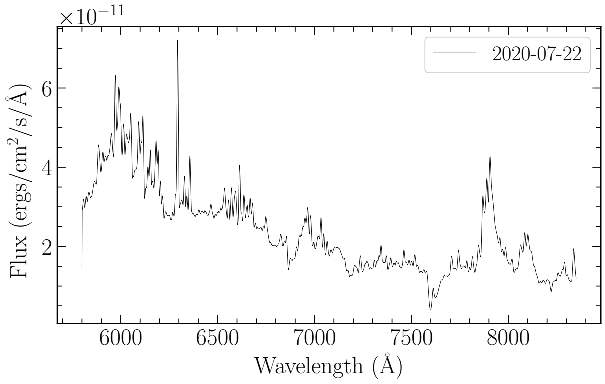

(b) Optical spectrum (red side) acquired in Grism 8 of HFOSC

Figure 5.23: Aperture size used to for spectra extraction are 66.6 arcsec (red) and 190.92 arcsec (blue).

Owing to the high SNR of the spectrum and the spatial extent available with the long slit in HFOSC, we studied the spatial variation of column density corresponding to various molecules (CN, C_3, $C_2(\Delta\nu = 0)$, $C_2(\Delta\nu = 1)$, NH_2(0-10-0) and, NH_2(0-8-0)) (see Figure.5.24). It was amusing to see the difference in spatial locations at which the column densities of each of these molecules peaked. Variation in the slope of the profile for each molecule is also observed. To an extent, it can be speculated that the spatial location of the column density profile peak of a particular molecule corresponds to the in situ region in the coma where this daughter/grand-daughter specie are largely formed. A major difference in the column density profiles are observed between the left and right side of the slit. The orientation of the slit and direction of Sun and negative heliocentric velocity of the comet are as shown in Figure.5.25. The right side of the slit corresponds to the Sun illuminated side while the left side is in the antisolar direction. This difference would be majorly affecting the amount of material released on both the sides and hence changing the photochemistry in these two directions resulting in the observed column density variation.

C/2020 M3 (ATLAS)

Among the long list of LPCs for which minimal details of their activity is known belongs comet C/2020 M3 (ATLAS) (hereafter M3). The comet with orbital period

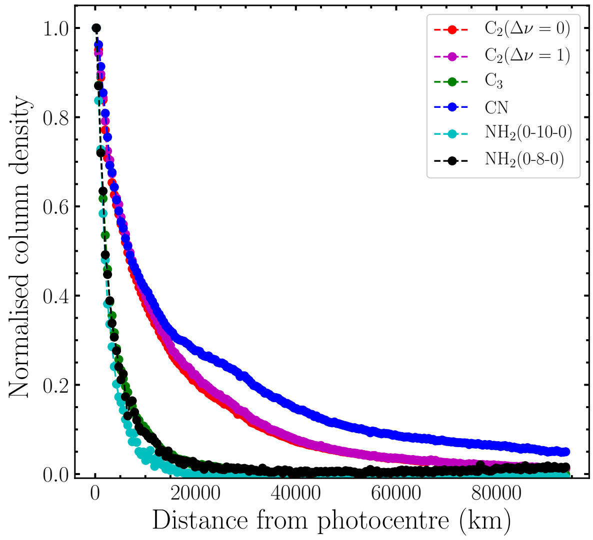

(a) Profile towards the left side of slit

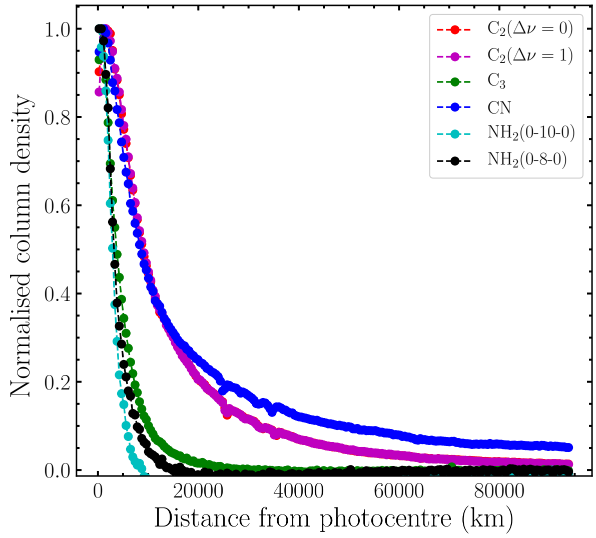

(b) Profile towards the right side of slit

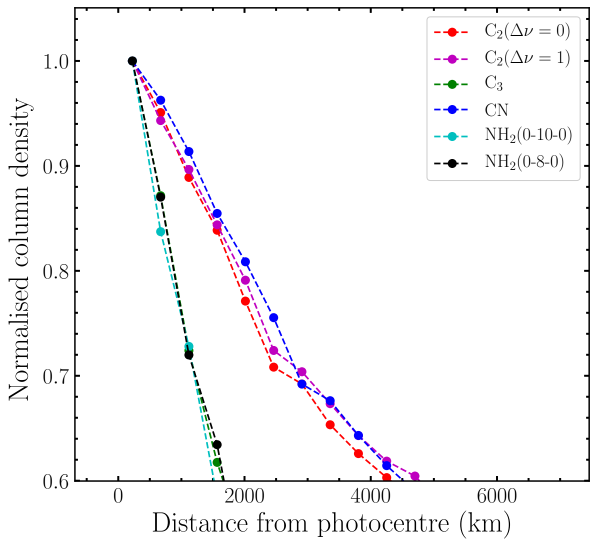

(c) Blown up version of Figure.5.24a

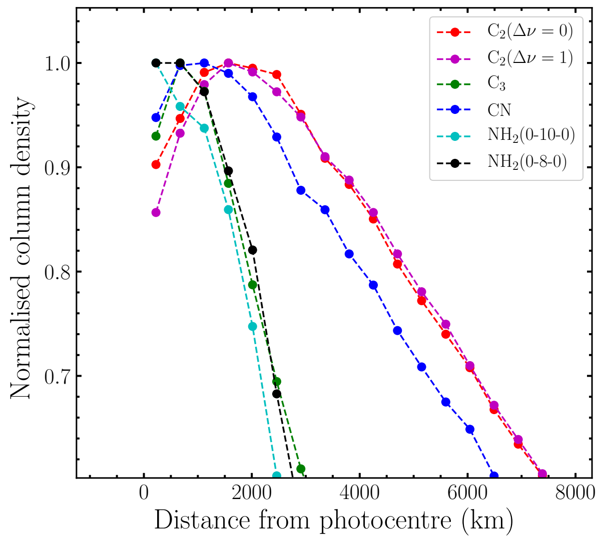

(d) Blown up version of Figure.5.24b

Figure 5.24: Column density profile of various molecules, towards both sides of the slit, observed in comet C/2020 F3

less than 200 years is classified as an LPC since it is making its first approach into the inner Solar system. In this work we have observed this comet 1 epoch each on pre and post perihelion. Figure.5.26 depicts the observed spectrum for each epoch. The production rates corresponding to the observed regular emissions (CN, C_2, and C_3) and dust activity (given by Afρ) are as given in Table.5.18. The production rate ratio as well as the dust to gas ratio was also computed for both the epochs. The computed values classify M3 as a comet with typical carbon chain composition having dust to gas

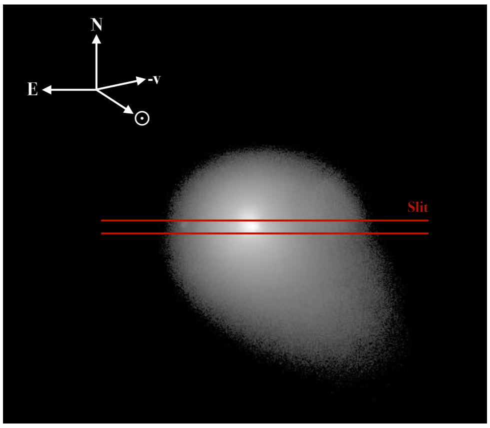

Figure 5.25: Illustration of the orientation of slit and direction of Sun and negative heliocentric velocity on 2020-07-22 during the observation of comet C/2020 F3. The displayed slit is simply for illustrative purpose and is not to scale.

Table 5.17: Activity of comet C/2020 F3 at different epochs

Date	r_H	Δ	Production Rate (molecules per sec)				Production rate ratio	$Af\rho$ (cm)		Dust to gas ratio
(UT)	(AU)	(AU)	CN	$C_2(\Delta v = 0)$	$C_2(\Delta v = 1)$	C_3	$Q(C_2)/Q(CN)$	BC	GC	$(Af\rho)_{BC}/Q(CN)$
20200722	0.62	0.69	28.11(0.00)	28.31(0.00)	28.24(0.00)	27.00(0.03)	0.20(0.01)	4.98(0.03)	5.02(0.03)	-23.13(0.03)
20200724	0.66	0.69	28.06(0.00)	28.20(0.00)	28.15(0.00)	26.76(0.04)	0.14(0.01)	4.55(0.04)	4.66(0.03)	-23.51(0.04)

Values in the parenthesis represents the corresponding errors.
Production rates and ratios are in log scale.

ratio similar to that seen in LPCs. Our results for the first epoch are in good agreement with the activity reported by Jehin et al. (2020b) for nearby epoch (2020-10-14). Even though our second epoch is one month away from the reported observation in (Jehin et al., 2020a), the gas activity and production rate ratio are similar except for the dust activity which is seen to be on a higher side in our observation. As mentioned, since these two epochs of observation are one month apart, possibilities of an increased dust activity cannot be ruled out. A study combining the available observation would help in understanding the evolution of comet activity across perihelion.

Table 5.18: Activity of comet C/2020 M3 at different epochs

Date	r_H	Δ	Production Rate (molecules per sec)				Production rate ratio	$Af\rho$ (cm)		Dust to gas ratio
(UT)	(AU)	(AU)	CN	$C_2(\Delta v = 0)$	$C_2(\Delta v = 1)$	C_3	$Q(C_2)/Q(CN)$	BC	GC	$(Af\rho)_{BC}/Q(CN)$
20201018	1.27	0.43	25.21(0.01)	25.34(0.01)	25.22(0.01)	24.28(0.06)	0.13(0.01)	2.14(0.05)	2.24(0.04)	-23.07(0.05)
20201215	1.47	0.50	25.19(0.02)	25.30(0.02)	25.24(0.02)	24.43(0.08)	0.11(0.03)	2.51(0.10)	2.54(0.09)	-22.68(0.10)

Values in the parenthesis represents the corresponding errors.
Production rates and ratios are in log scale.

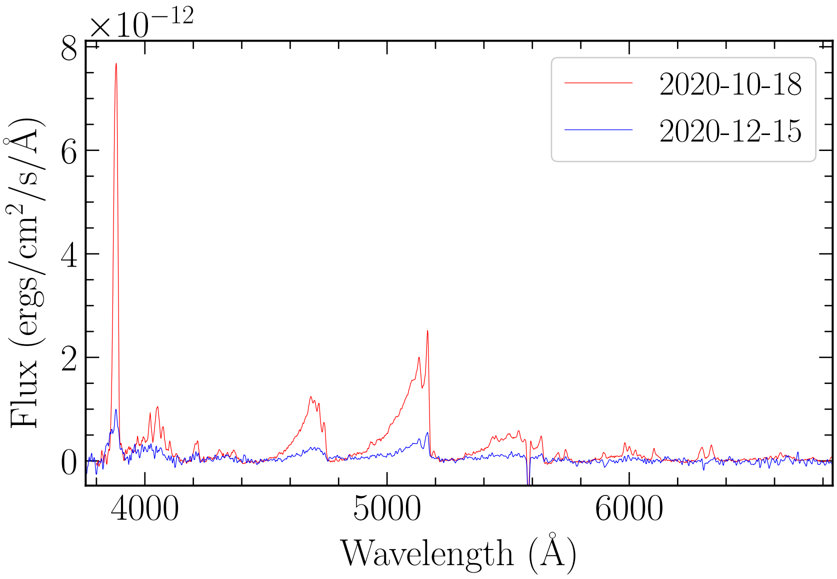

Figure 5.26: Optical spectrum acquired for comet C/2020 M3. Aperture size used to for spectra extraction are 114.1 arcsec (red) and 45.64 arcsec (blue).

C/2021 A1 (Leonard)

Similar to the year 2020, 2021 also had its own bright comet, C/2021 A1 (Leonard) (hereafter A1) which reached a brightness of about 3-4 magnitude. The comet was observed in January and March by Zhang et al. (2021) after its discovery on January 3rd by Gregory J. Leonard. They observed the comet through imaging and spectroscopy to study the dust size, activity and colour while any sort of emissions were absent. They also discuss the prospective close encounter of A1 with Venus (∼0.029 AU), closer than any known encounter of an LPC with Earth, to occur on 18 December 2021. Other than Jehin et al. (2022a) who reports the outburst of A1 around January 7 2022, the light curve of A1 given in Seiichi Yoshida's website[1] and other unconfirmed sources mentions a periodic outburst of the comet after 19 December 2021. In this work, we observed the comet on 2021-11-09, much before these possible outbursts have occurred. The observed spectrum for the epoch is as shown in Figure.5.27a. The computed results given in Table.5.19 implies a typical carbon chain composition of the comet but with a dust to gas ratio in the range observed for SPCs. The colour of the comet dust, BC-GC is observed to be 0.756±0.028 for an aperture of $\rho \sim 10^4$km, similar to the B-V colour of A1 that has been reported by Zhang et al. (2021) and similar to the colour of LPCs

[1] http://www.aerith.net/comet/catalog/2021A1/2021A1.html

as given in Jewitt (2015). But, for a larger range of aperture, the colour is found to vary significantly (see Figure.5.28b). The Afρ computed from the image available in broadband R filter shows numbers similar those computed for BC and GC filters. But, the Afρ profile shows a steep decline after 5000 km (see Figure.5.27b) as observed for comet 156P/Russell-LINEAR (Aravind et al., 2022). Such a behaviour of the profile implies a non-steady state of dust outflow present in the comet. The reports of a sharp and bright false nucleus in A1 (Jehin et al., 2021a) and the observed non-steady outflow of dust could imply a connection between the dust activity in the comet and the observation of such features (similar coincidence in reports of a bright and compact inner coma and non-steady state dust outflow were seen in comet 156P (refer Jehin et al. (2020b) and Aravind et al. (2022) for more details).

Even though the dust activity and general class of the comet is similar to what is

Table 5.19: Activity of comet C/2021 A1 at different epochs

Date	r_H	Δ	Production Rate (molecules per sec)				Production rate ratio	Afρ (cm)		Dust to gas ratio[a]
(UT)	(AU)	(AU)	CN	$C_2(\Delta v = 0)$	$C_2(\Delta v = 1)$	C_3	$Q(C_2)/Q(CN)$	BC	GC	$(Af\rho)_{BC}/Q(CN)$
20211109	1.25	1.26	25.57(0.01)	25.50(0.03)	25.46(0.03)	24.32(0.54)	-0.06(0.03)	2.92(0.06)	3.05(0.04)	-22.64(0.06)

Values in the parenthesis represents the corresponding errors.
Production rates and ratios are in log scale.

reported by Jehin et al. (2021a) for observations on 19 December 2021, one month later, an increase in the activity of C_2 is seen ($Q(C_2)$ becomes greater than Q(CN)) for the later epoch. As seen from the reports of activity in A1 for 2 epochs in January after the reported outburst (Jehin et al., 2022a,b), production rate of C_2 increases more steeply than that of CN. This implies there could have been some short outbursts in the comet in December which increased the C_2 production rate beyond CN. A combined study of the available data of A1 is required to understand the possible link between outbursts and increase in C_2 production rate.

5.3.2 Polarisation study of a few comets

The light coming from a comet is polarised to an extent due to the reflection by the dust particles present in it. Hence, analysing the modulation present in this light through

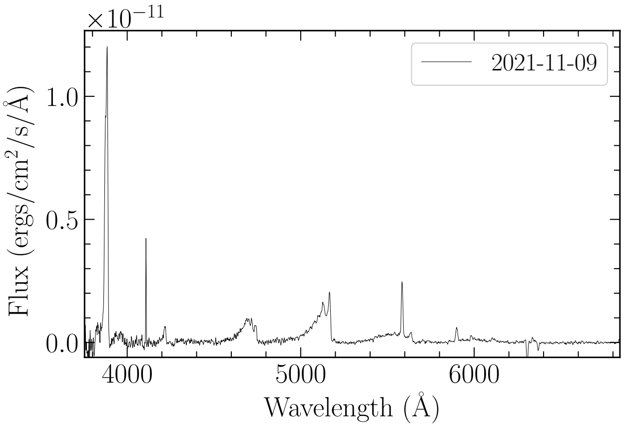

(a) Optical spectrum acquired for comet C/2021 A1

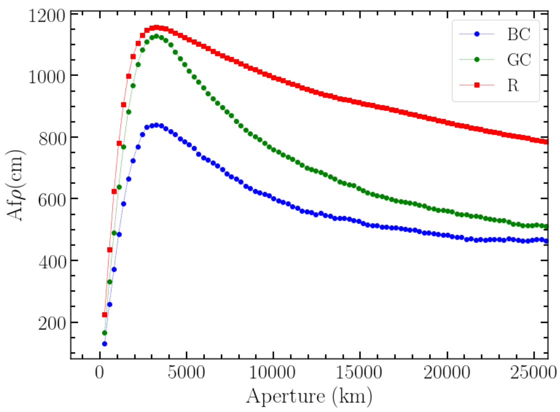

(b) Afρ profile observed in different filters

Figure 5.27: Observational results of comet C/2021 A1

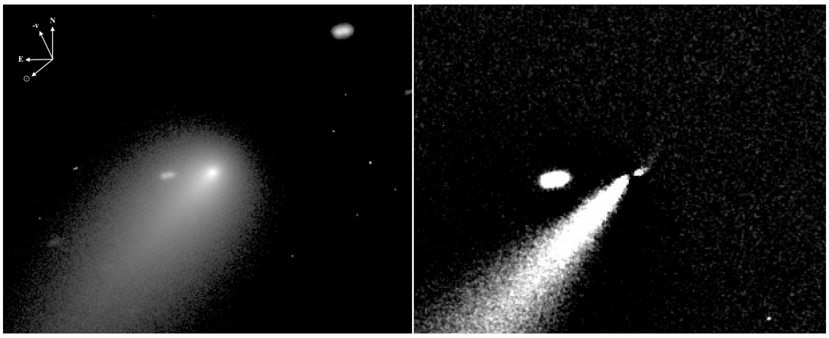

(a) Ls processed image of comet C/2021 A1

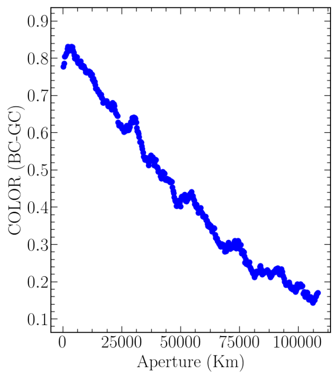

(b) Variation of colour with increasing aperture

Figure 5.28: Analysis of coma morphology and colour in comet C/2021 A2

filter bands mildly contaminated by molecular emissions (eg., Red broadband filters or the narrow band continuum filters). With the significance of polarisation studies for comets explained in Section.1.2.3, this section briefs the observational studies of a few comets, LPC and SPC, to compare their degree of polarisation as a function of phase angle. Table.2.2 mentions the epochs for which certain comets were observed for polarisation study. Polarisation standard stars are also observed on the same epochs to check for the consistency in the observed polarisation as well as to correct the observed polarisation angle of the comet (see Section.3.3.2 for more details). The EMPOL instrument briefed in Section.2.2.1 is used for all the observations. Section.2.3.4

explains the details related to the observation, reduction and analysis of polarimetric data.

Table 5.20: Actual degree of polarisation and polarisation angle of the observed standard stars.

Star	Filter	p_0 (percent)	θ_0 ($\circ$)
HD 25443	V	5.127 ± 0.061	134.23 ± 0.34
	R	4.734 ± 0.045	133.65 ± 0.28
	I	4.249 ± 0.041	134.21 ± 0.28
BD +64 106	R	5.150 ± 0.098	96.74 ± 0.54
HD 19820	R	4.562 ± 0.025	114.46 ± 0.16
HD 204827	R	4.893 ± 0.029	59.10 ± 0.17

The actual degree of polarisation and polarisation angle[2] and the computed degree of polarisation and polarisation angle of the different polarisation standard stars are given in Table.5.20 and 5.21 respectively. The degree of polarisation and polarisation angle of comets observed on various dates are laid out in Table.5.22. The observed degree of polarisation of the comets was then plotted as function of the phase angle during the observational epoch to analyse the variation between the comets (see Figure.5.29a). For a better understanding and comparison, the observed polarisation values of comet 156P as mentioned in Chapter.3, reported polarisation values of comet C/2019 Y4 in Zubko et al. (2020) and the modelled polarisation phase curves as explained in Halder & Ganesh (2021) and Aravind et al. (2022) are plotted together as illustrated in Figure.5.29b.

It is seen that the degree of polarisation measured for C/2019 Y4 is in agreement to the values reported by Zubko et al. (2020) and that of C/2020 M3 lies in the same line implying a possible similar composition in the comets. Comet C/2017 T2 having been observed at low phase angle displays a negative polarisation as the observed polarisation angle was parallel to the scattering plane. The inversion angle of C/2017 T2

[2] http://www.not.iac.es/instruments/turpol/std/hpstd.html

Table 5.21: Observational results of polarised standard stars observed on various dates.

Date	Star	Filter	p_{obs} (percent)	θ_{obs} ($\circ$)	$\theta_{\text{off}}=\theta_0-\theta_{\text{obs}}$ ($\circ$)
28-12-2018	BD +64 106	R	5.24 ± 0.6	30 ± 3	66 ± 4
17-01-2020	HD 19820	R	4.83 ± 0.65	9 ± 4	106 ± 4
	HD 25443	R	4.87 ± 0.54	25 ± 3	109 ± 4
13-03-2020	HD 25443	V	5.22 ± 0.83	38 ± 4	96 ± 5
	HD 25443	R	5.02 ± 0.21	35 ± 2	98 ± 3
12-11-2020	BD +64 106	R	5.02 ± 0.36	-8 ± 3	104 ± 3
	HD 25443	R	4.85 ± 0.38	26 ± 5	108 ± 6
03-11-2021	HD 25443	R	4.6 ± 0.22	-55 ± 1	188 ± 2
	HD 25443	R	4.49 ± 0.19	-62 ± 2	195 ± 2
	HD 25443	R	4.63 ± 0.3	-55 ± 2	188 ± 2
07-11-2021	HD 25443	R	4.84 ± 0.36	-60 ± 2	194 ± 2
	HD 19820	R	4.78 ± 0.31	-75 ± 2	189 ± 2
09-11-2021	HD 25443	R	4.98 ± 0.24	-68 ± 1	202 ± 1
	HD 25443	I	4.29 ± 0.21	-69 ± 1	203 ± 2
26-11-2021	HD 204827	R	4.88 ± 0.19	40 ± 1	19 ± 2

lies in the range 20°-30°. Comet C/2021 A1 is observed to have a polarisation similar to objects with higher silicate contents. Even though, generally, LPCs are expected to have a higher carbonaceous content displaying higher polarisation, it is seen from Figure.5.29b that a major mix up is present within the different comet population. Hence, C/2021 A1 could have a different region of origin as compared to other LPCs. Comet 67P displayed polarisation similar to what has been observed earlier and similar to that of 156P as reported in Aravind et al. (2022). But, there was significant variation in the observed polarisation between the 3 days of observation. The presence of strong jets, as shown in Figure.5.6, along with the rotation of the nucleus could be varying the dust population within the coma thereby affecting the measured polarisation. The analysis of variation in polarisation for 67P over a larger range of phase angle is required to have a better understanding. Such studies could also help in probing the compositional

Table 5.22: Observational results of different comets.

Comet	Date	Filter	Phase Angle (∘)	p_{obs} (percent)	θ_{obs} (∘)	$\theta_{\text{corr}}=\theta_{obs}+\theta^{*}_{\text{off(avg)}}$ (∘)
C/2017 T2	28-12-2019	R	17.22	-1.79 ± 0.3	45 ± 4	111 ± 5
	17-01-2020	R	24	-0.89 ± 0.22	75 ± 13	182 ± 14
C/2019 Y4	13-03-2020	R	30	4.79 ± 0.34	-34 ± 4	63 ± 5
C/2020 M3	12-11-2020	R	26.57	3.41 ± 0.23	-89 ± 5	17 ± 5
C/2021 A1	03-11-2021	R	40.2	5.98 ± 0.52	70 ± 1	80 ± 2
	26-11-2021	R	69.9	16.95 ± 0.23	63 ± 1	82 ± 2
67P	07-11-2021	R	49.15	9.71 ± 0.21	-33 ± 1	158 ± 2
	07-11-2021	R	49.15	8.61 ± 0.19	-28 ± 1	163 ± 2
	09-11-2021	R	48.97	5.0 ± 0.15	-39 ± 1	163 ± 2

* The average values of zero point offset in polarisation angle for each epoch are used for comets observed on the same epoch.

difference at two different locations in the comet.

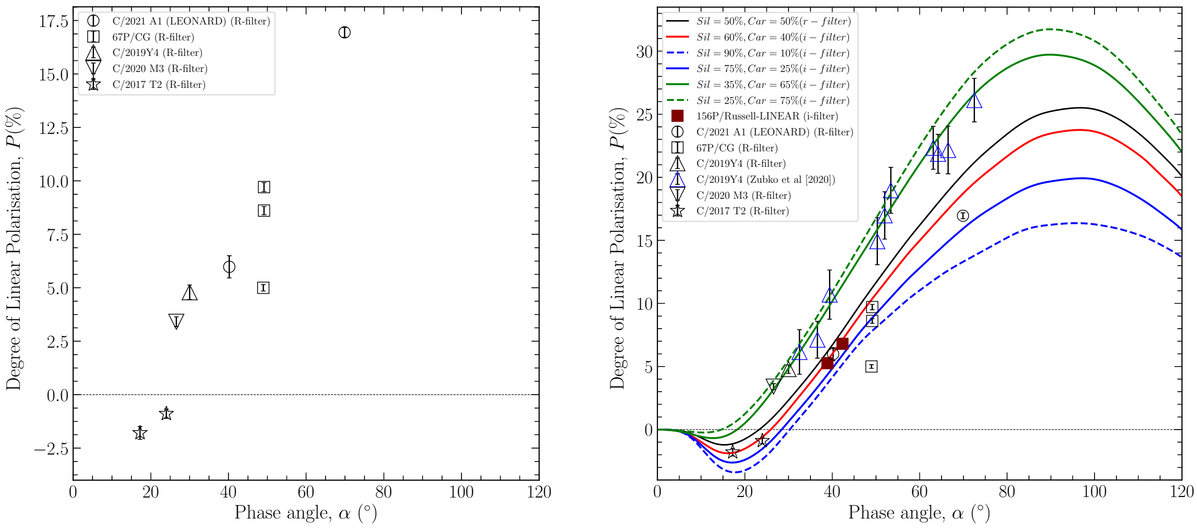

(a) Observed degree of linear polarisation for various comets at different phase angles

(b) Comparison of observed polarisation values with modelled phase polarisation curves

Figure 5.29: Phase angle variation of linear degree of polarisation observed for different comets

5.4 Conclusion

In order to have broad scale understanding of different comets, about 18 comets, 8 SPC and 10 LPC, have been observed in low resolution spectroscopy. The gas and dust activity in all the comets have been analysed and reported. A few major points to be noted are:

- Comets 29P and 123P were two comets which behaved completely different from the rest. The regular emission lines seen in comets were absent in 29P while it showed emissions from CO^+ and N_2^+. Comet 123P had a detectable coma while it did not posses any emission features in the optical regime. The reflectance slope of 123P similar to that of stony S-type asteroids could imply that this object initially formed in the inner part of the Solar system.
- Comet 88P demonstrated a drastic increase in the activity as it was approaching perihelion. The increase in activity by one order for every month of observation would have been observed only for a few SPCs. A detailed study of the activity in the comet along its orbit with understanding of its spin-axis geometry is necessary to narrow down the reasons for the observed activity.
- C/2020 A2 was another peculiar object which showed blended emissions in the CN region which matches N_2^+ emissions while it was absent for the other observational epochs. Such short term detection could be a direct effect of the viewing geometry at the time of observation.
- C/2019 Y4 was a normal cometary body before it gained attention due to its disintegration. We were able to acquire the objects spectrum around the starting of the disintegration and after reports of complete disintegration. The presence of clear emissions even after the complete disintegration of the nucleus is yet to be explained.
- C/2018 N2, C/2019 N1 and C/2019 L3 are three comets observed at comparatively large heliocentric distances to show strong emissions in their optical spectrum. It is rarely that comets with perihelion distance similar to these objects put up such

noticeable activity. The reason for activities at these distances are to be studied in detail.

- Few comets like 260P, 67P and C/2021 A1 were seen to have an Afρ profile depicting a non-steady state outflow of dust. The analysis of their images revealed presence of dust jets which could be a contributor to non-steady state outflow.
- The great comet of 2020, C/2020 F3, was observed to show enormous activity giving spectra of very high SNR even for very short exposures. The analysis of column density profiles of various molecules points at a difference in their in situ formation locations. The profiles obtained from spectra extracted from the Sun lit side displayed such behaviours while that from the anti-Solar direction showed differences only in the slope of the profile.
- Study of variation in degree of linear polarisation as a function of phase angle proves to be a prominent technique in probing the dust present in the comets. While simple phase polarisation curve can help in having a general understanding of the comets behaviour in comparison to other observed bodies, clubbing it with dust models can benefit it understanding the physical and compositional properties of the dust particles.

Chapter 6

High resolution spectroscopy of Comets

6.1 Introduction

Among different aspects of a comet that needs to be studied in detail, includes the chemical composition from the molecular emission bands in different wavelength ranges. This is done by analysing the cometary emission spectra. The rotational lines of a particular vibrational band in a comet molecular emission cannot be resolved with low resolution spectroscopy since they will be blended with each other. In case of some molecules (C_2) the bands arising with the same change in vibrational quantum number in going from one electronic state to another have wavelengths close to each other resulting in a blended feature (Swan bands) (Swan, 1857). High resolution is required to separate various bands from this blended feature. Even much higher resolution is required to resolve the rotational structures [Swamy (2010)]. Lambert & Danks (1983) have given a detailed study of the (C_2) swan bands using high resolution spectroscopy. From the high resolution spectroscopic observations of comets Swift-Tuttle and Brorsen-Metcalf, Brown et al. (1996) have identified 2997 lines including those of H, C_2, O, NH_2,

CN, C_3, CH, H_2O^+ and CH^+. High resolution spectra of Comet C/1996 B2 (Hyakutake) and Comet C/1995 O1 (Hale-Bopp) were obtained by Morrison et al. (1997) and Zhang et al. (2001) respectively. Similar observations have also been done for comets 153P/ (Cremonese et al., 2007), 21P/ (Shinnaka et al., 2020) and C/2000 WM1 (Picazzio et al., 2002). Cochran et al. (2020) used high resolution spectroscopy to illustrate what it means to be a highly depleted comet and laid down comparison with a typical comet. Also, high resolution spectroscopy was used by Opitom et al. (2021) to study the emissions present in the first interstellar comet in detail and to establish the similarity of the comet with Solar system comets. However, the high resolution spectra of comets still contain many unidentified lines. With the help of a resolving power of 60,000, Cochran & Cochran (2002) have identified 12,219 lines in the wavelength range 3800 - 10,192 Å in the spectrum of the comet 122P/de Vico using laboratory molecular line lists. This has been the most exhaustive line list until Cambianica et al. (2021) observed C/2020 F3 (NEOWISE) at a resolving power of 1,15,000 to identify and catalog 4488 cometary emission lines in the wavelength range 3830 - 6930 Å.
In this Chapter, the feasibility of using an echelle spectrograph mounted on an Indian telescope for the high resolution spectroscopic observation of cometary bodies is discussed. The various aspects regarding the instrument, observation and data reduction has already been discussed in Section.2.3.2 of Chapter.2. The following Sections cover the various emissions detected in different comets during distinct epochs and lays down a comparison among the observed band sequences and lines observed with the help of the available catalogues. The understanding of a few comets obtained from the basic analysis of the forbidden oxygen lines and NH_2 Ortho and Para lines are also discussed subsequently.

6.2 Observation and Analysis

We observed multiple comets during distinct epochs using the HESP mounted on the HCT. Most of the observations were carried out in the medium-res mode, ($\lambda/\Delta\lambda \sim$ 30,000). Comets being extended objects, observation in high-res mode, ($\lambda/\Delta\lambda \sim$ 60,000) require the comet to be bright enough in order to obtain the necessary SNR. Hence, only 46P/Wirtanen was observed in the high-res mode owing to its closest approach during its 2018 apparition. The complete list of observed comets along with the basic information related to the observations are provided in table 6.1. Multiple frames were obtained for most of the comets during each epochs. The orbital parameters of these comets are given in Table.2.2. Out of the 4 comets observed in high resolution, 46P and 41P/Tuttle–Giacobini–Kresák (hereafter 41P) are JFCs while 38P is an HTC and C/2015 V2 (Johnson) (hereafter V2) is a hyperbolic long period comet. 46P was observed before and after perihelion, V2 was observed as the comet was approaching perihelion and 38P and 41P were observed only for one epoch each. As mentioned in Section.2.3.2, cometary emission catalogues were used to identify the emission lines present in each comet. While Figures 6.1, 6.2, 6.3, and 6.4 illustrates the overall picture of the lines identified in each comet for its brightest epoch. Section.6.3 discuss in brief the various strong emissions detected in each comet for multiple epochs and lay down a basic comparison between the strength of the emissions observed in the two fibres.

Object	Date (UT)	Exposure time* (sec)	Δ (au)	$\dot{\Delta}$ (km s^{-1})	r (au)	$\dot{r}$ (km s^{-1})	Resolution ($\lambda/\delta\lambda$)
46P/Wirtanen	2018-11-28	1800[5]	0.13	-8.32	1.07	-4.23	30000
	2018-12-15	1800[5]	0.08	-0.32	1.05	0.90	30000
	2018-12-28	1800[5]	0.11	7.6	1.08	4.70	30000
		2700[4]					60000
	2019-01-11	2700[6]	0.18	10.32	1.13	8.20	30000
C/2015 V2 (Johnson)	2017-02-22	3600[5]	1.78	-21.2	2.18	-14.2	30000
	2017-05-02	1800[5]	0.99	-16.35	1.72	-7.23	30000
	2017-05-28	2400[4]	0.82	-4.57	1.65	-2.74	30000
38P/Stephan–Oterma	2018-11-28	1800[1]	0.76	-5.34	1.60	3.10	30000
41P/Tuttle–Giacobini–Kresák	2017-02-22	3600[2]	0.25	-10.1	1.23	-11.80	30000

* Numbers in the parentheses represent the number of frames obtained for each exposure time.

Table 6.1: Basic observational details of high resolution spectroscopy.

6.3 Discussion

The low/high resolution mode of HESP instrument was used to observe 3 short period comets, 46P, 38P, 41P and one long period comet V2. Emissions from various bands of

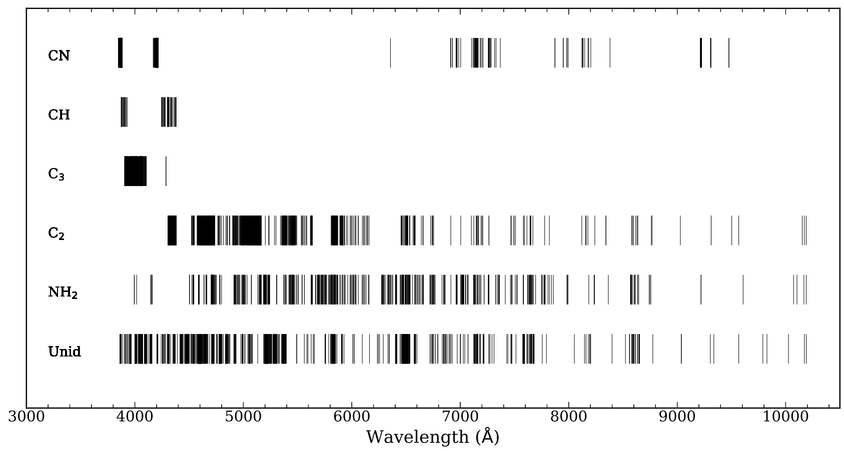

Figure 6.1: All identified lines for 46P for the epoch 2018-11-28

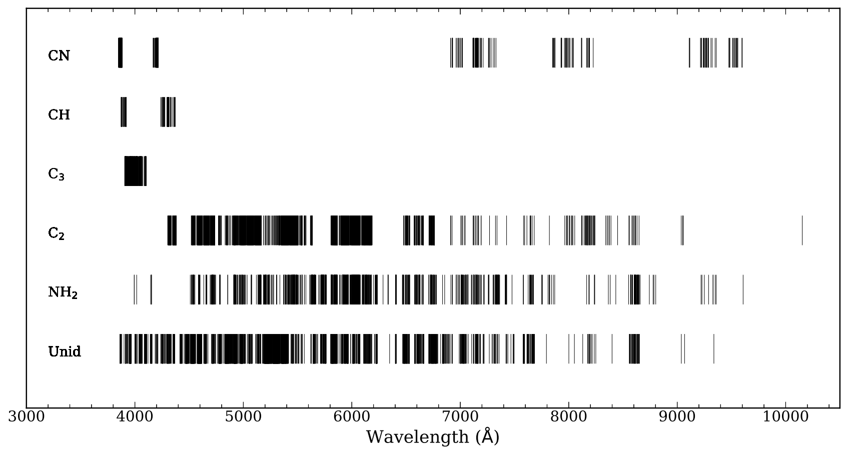

Figure 6.2: All identified lines for C/2015 V2 for the epoch 2017-05-28

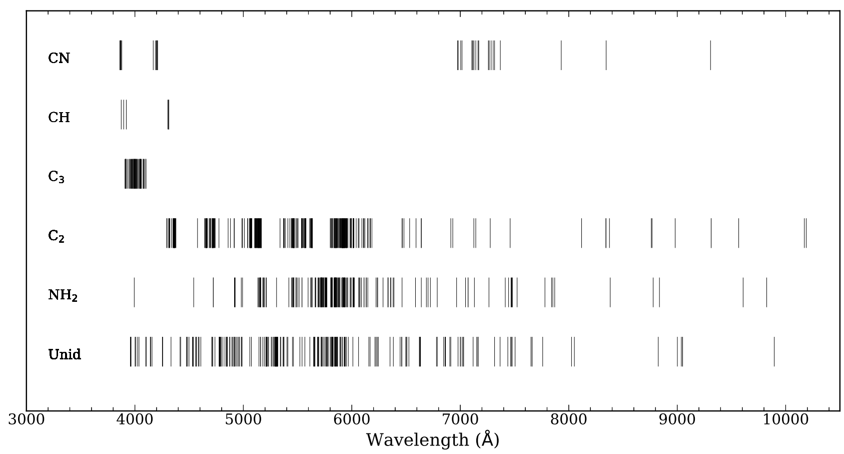

Figure 6.3: All identified lines for 38P for the epoch 2018-11-28

CN, C_3, CH, C_2 and NH_2 were observed in all the comets while emissions from CH^+ and CO^+ were not strong enough to be distinguished from the noise in the spectrum.

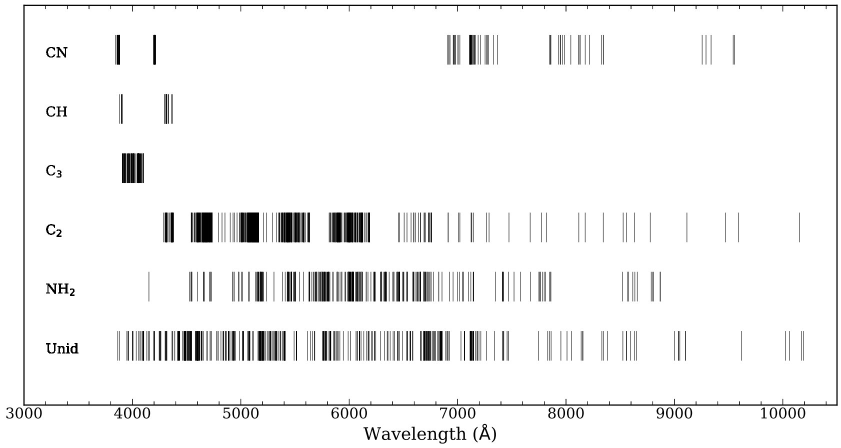

Figure 6.4: All identified lines for 41P for the epoch 2017-02-22

The most prominent cometary emission features corresponds to CN and C_2. Owing to the very long wavelength range of the HESP instrument, we were able to observe the two different electronic band system of CN, the violet system ($B^2\Sigma^+$-$X^2\Sigma^+$) and the red system ($A^2\Pi^+$-$X^2\Sigma^+$) and the Swan system of C_2 which is most dominant in the green, orange and red region of the cometary spectrum. The lines corresponding to NH_2 emissions are most prominent in the red region of the spectrum but mostly blended with C_2 emissions when observed in low resolution. The high resolution of the instrument helps us to split these emissions from the different Swan bands of C_2. Efforts have been made to compute the Ortho-to-Para ratio (OPR) of various transitions of NH_2 for certain comets. The strength of the emission lines depends on the activity in the comet which directly affects the number of lines identified (at 3σ level). Large number of lines have been identified in certain epochs of comet 46P and C/2015 V2 owing to their brightness as compared to the fainter comets (at the time of observation) 41P and 38P.

Differences observed in the relative strengths of the emission lines in different epochs can be majorly due to the varying heliocentric distance while the difference in line strength between spectra observed in Fibre 1 and 2 would be solely due to the corresponding internal physical and chemical conditions in the coma. Employing a higher resolution is effective in splitting a large number of lines in various band while it was most efficient in separating the cometary oxygen line from telluric lines while the comets geocentric velocity was not large enough to induce the required Doppler shift in the lines to be observed in lower resolution of HESP. Even though there are infinite possibilities in using such a data set for detailed study of the comets, aim of the current work is to discuss in brief the various emissions detected in different comets observed, provide an overall understanding of few comets from the basic analysis of forbidden oxygen lines, NH_2 Ortho & Para lines and also provide a general idea regarding the capability of the HESP instrument in observing comets in high resolution.

6.3.1 Detected strong emissions

6.3.1.1 CN($B^2\Sigma^+$-$X^2\Sigma^+$) emission

As mentioned above, owing to the long wavelength range provided by the HESP instrument, we are able to observe the violet and red systems in the CN emission. The violet band is the strongest among both detected bands and clearly shows the P and R branch of emissions. Swings effect (Swings, 1941) plays a major role in the observed differences in the relative strength of the emission lines in different epochs. As mentioned in Manfroid et al. (2009), there are few CH lines blended in the P branch of the CN emission and requires much higher resolution to be resolved. The CN emission detected in the different comets observed are discussed below.

46P: The CN B-X (0-0) emission was the strongest band observed in all the epochs (see Figure.6.5). The observation on 2018-12-15 has been excluded in this case due to the comparatively low SNR in the band. Strong variations in the relative strengths of different emission lines are observed in spectra obtained from Fibre 1 and 2. For illustrative purpose, Figure.6.6 shows the CN band in the spectra obtained from both Fibre 1 and 2 for the epoch 2018-11-28. Such comparisons can be further used along with modelling to understand in detail the physical conditions and the chemical reactions occurring at two different locations in the coma.

V2: Strong emissions from the CN violet bands were observed in V2. Figure 6.7 represents the B-X (0-0) emission band observed across the dates of observation. Even though Swings effect plays major role in creating difference in the relative strength

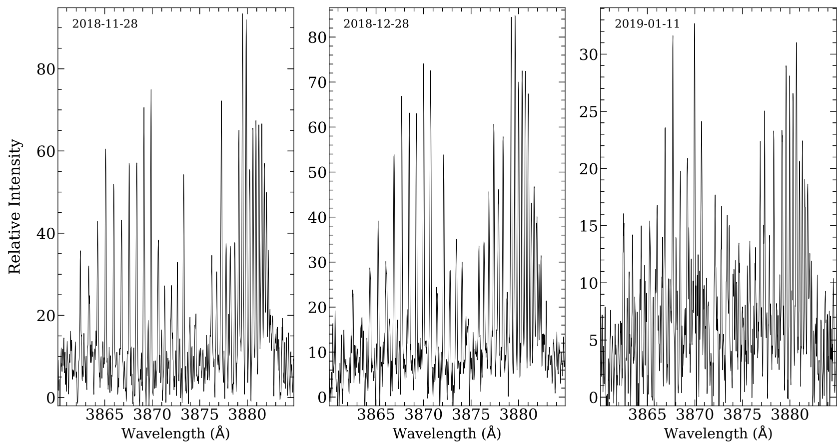

Figure 6.5: CN($\Delta v = 0$) emission observed in 46P during few observational epochs

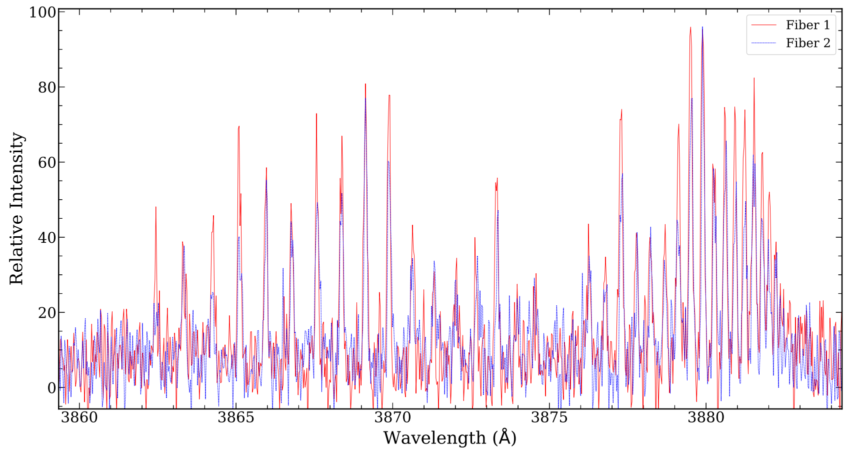

Figure 6.6: CN($\Delta v = 0$) band observed in Fibre 1 and Fibre 2 for 46P on 2018-11-28

of different emission lines from one epoch to another, a clear increase in the strength and definition of the P,R branches are observed as the comet approached perihelion. Figure.6.8 is a representation of the difference in emission between spectra extracted from Fibre 1 and Fibre 2 observed on 2017-05-28.

38P and 41P: The CN emissions were not so strong in comets 38P and 41P as compared to 46P and V2. The detected CN band in both the comets are shown in Figure.6.9

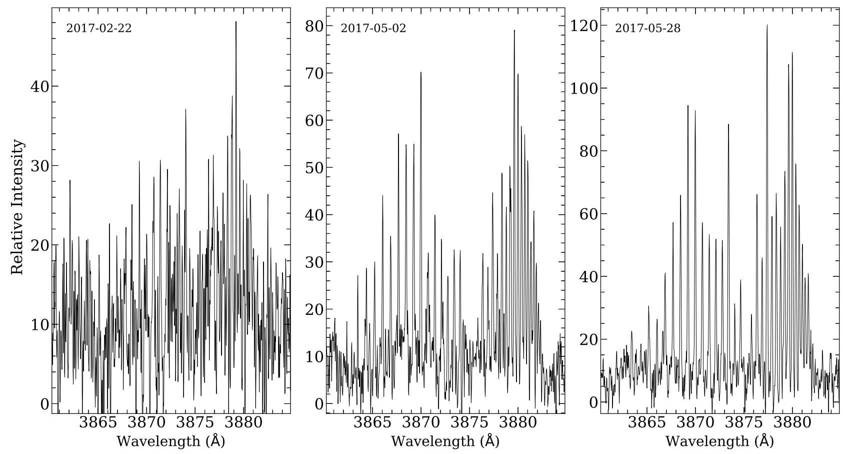

Figure 6.7: CN($\Delta v = 0$) emission observed in C/2015 V2 during all the observational epochs

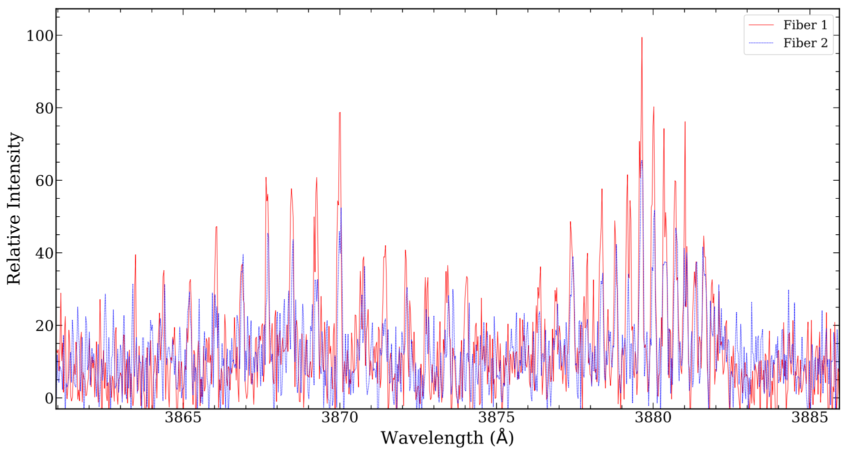

Figure 6.8: CN($\Delta v = 0$) band observed in Fibre 1 and Fibre 2 on 2017-05-28

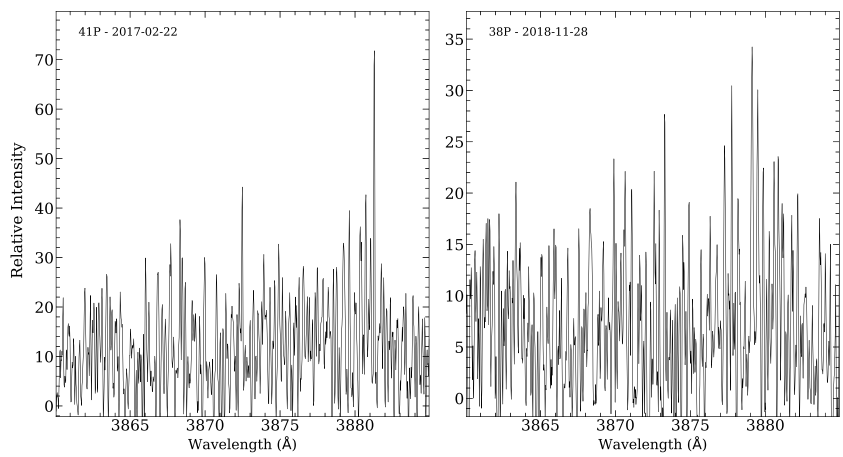

Figure 6.9: CN($\Delta v = 0$) band observed in comets 41P and 38P

6.3.1.2 C_2 emission

For most comets observed within a heliocentric distance of 2 AU, C_2 Swan band system is a dominant emission covering the green, orange and red regions of the cometary spectrum. Most of these bands are also highly blended with various NH_2 bands when observed at a resolution less than $\sim 10{,}000$. Various swan band systems like $C_2(\Delta\nu = 1)$, $C_2(\Delta\nu = 0)$, $C_2(\Delta\nu = -1)$ have been observed in most of the comets. The detection of the $C_2(\Delta\nu = 0)$ Swan band region (band head 5165 Å) observed in different comets are discussed below.

46P: 46P being a typical comet as discussed in Chapter.4, posses strong emission strength in the $C_2(\Delta\nu = 0)$ band. The variation in the band strength as the comet crossed perihelion is shown in Figure.6.10. The C_2 lines identified for the observation epoch 2018-11-28 is also shown along with it. It was observed that there are NH_2(0-5-0) band contamination within this C_2 emission band. Much higher resolution would be required to deblend these emissions.

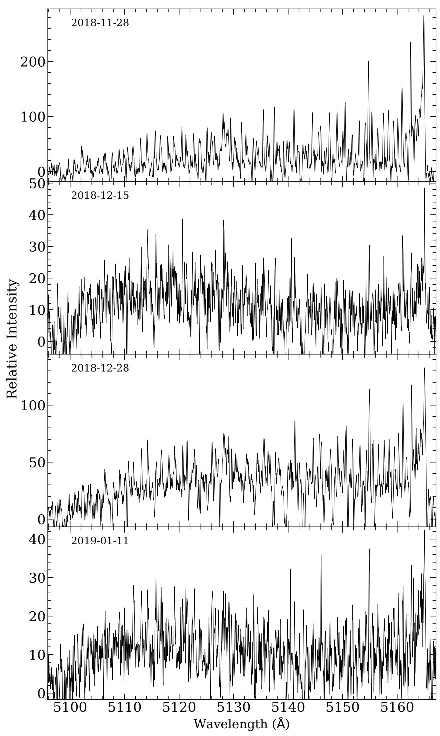

Figure 6.10: $C_2(\Delta\nu = 0)$ band in 46P during multiple epochs

We were able to observe the comet at a higher resolution (60000) on 2018-12-28. Certain lines which are observed as single lines in the medium-res mode of HESP are seen to split into multiple lines when observed in the high-res mode. Figure 6.11b represents one such observation in the C_2 emission. Only a small region of the band has been plotted for clarity. Observing a much brighter comet at this resolution could help us resolve and study the isotopic lines present in these regions.

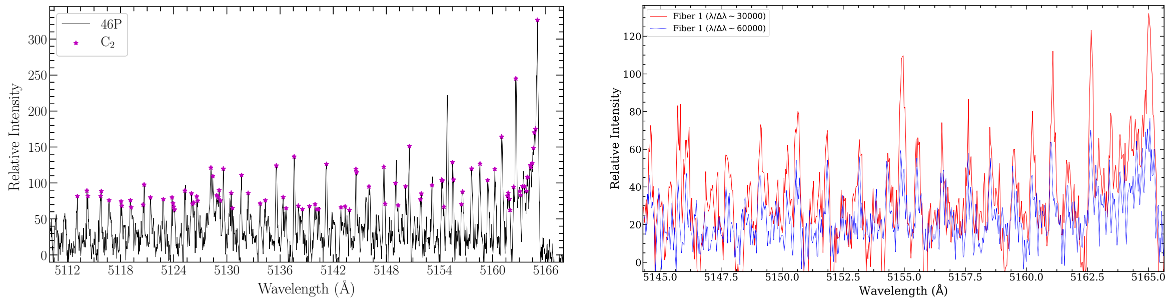

(a) C_2 lines identified for observation of 46P on 2018-11-28

(b) Comparison of C_2 lines observed in the high and low res on 2018-12-15

Figure 6.11: Analysis of the C_2 emission bands observed in 46P during certain epochs.

V2: The comet on its way into the inner Solar system was a major reason for the C_2 emission band to get stronger and more defined from one epoch to other. The major difference was seen in the band observed with the two fibres on 2018-05-28 (see Figure.6.12). Detailed studies are required to understand this striking difference in emission strength at two different locations in the coma.

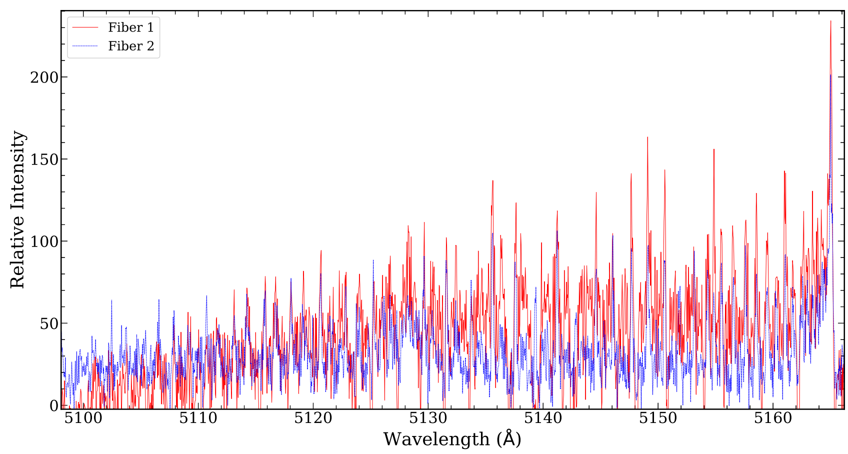

Figure 6.12: $C_2(\Delta\nu = 0)$ observed for V2 in Fibre 1 and Fibre 2

38P and 41P: Both the comets 38P and 41P being the fainter of the ones observed had a weaker C_2 band (see Figure.6.13). It was observed that the intensity of the C_2 band head was higher in 41P as compared to that in 38P.

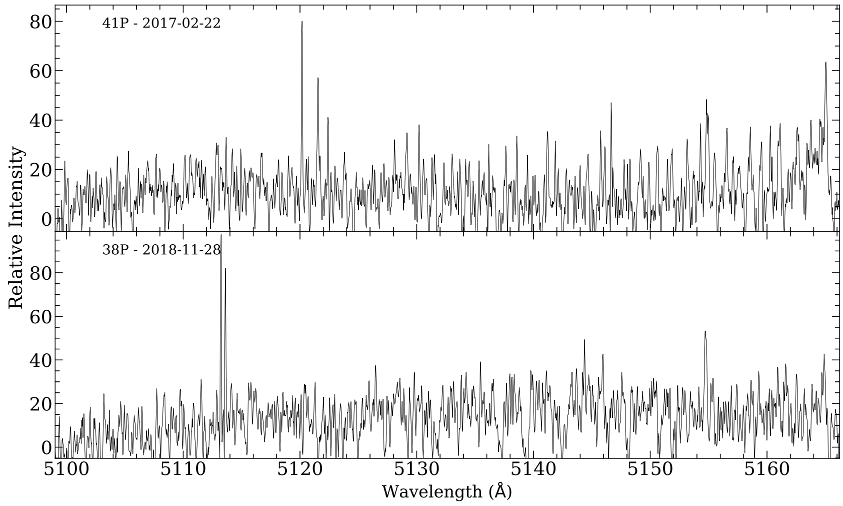

Figure 6.13: $C_2(\Delta v = 0)$ observed in comets 38P and 41P

6.3.1.3 C_3 emission

The C_3 emission band was seen to be strong enough only in certain epochs of 46P and C/2015 V2. Figure.6.14b shows how the strength of the band varies as the comet approached perihelion while Figure.6.14a illustrates the band observed in the comet before and after perihelion.

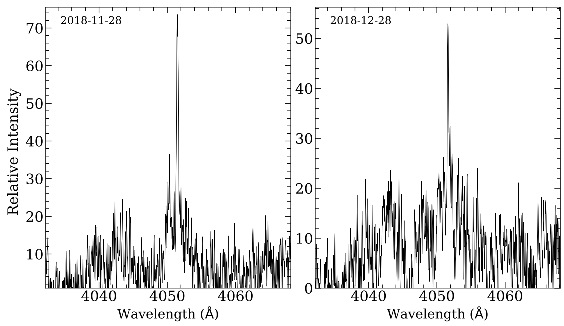

(a) C_3 emission band observed in 46P during few epochs

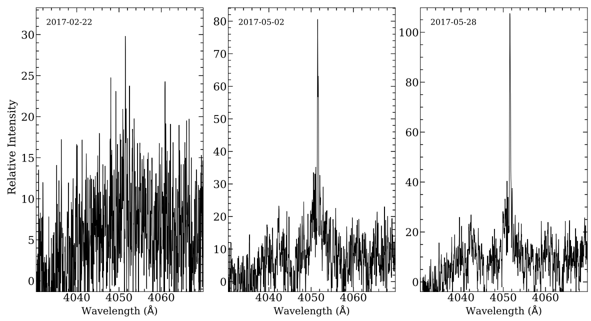

(b) C_3 emission band observed in V2 during few epochs

Figure 6.14: Comparison of the C_3 emission band observed in comets 46P and V2

6.3.1.4 CH emission

CH emission observed around 4300 Åis one band which is highly affected by the Swings effect. As a result, the line ratios vary drastically from epoch to epoch depending on the heliocentric velocity of the comet. In our case, CH emissions were clearly detected in both comets 46P and V2 (see figures.6.15 and 6.16a). At the same time, as seen in Figure.6.16b, the CH observed in V2 was observed to be stronger and defined as the comet was approaching perihelion. Even though the direct reason for such a strong detection is to be analysed in detail, it could be possible that the parent molecule responsible for the CH emission is more abundant in V2 than in 46P.

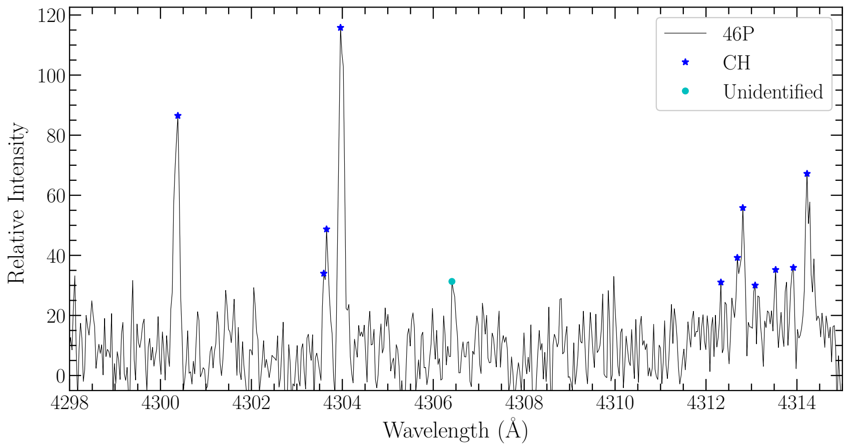

Figure 6.15: CH emission observed in 46P on 2018-11-28

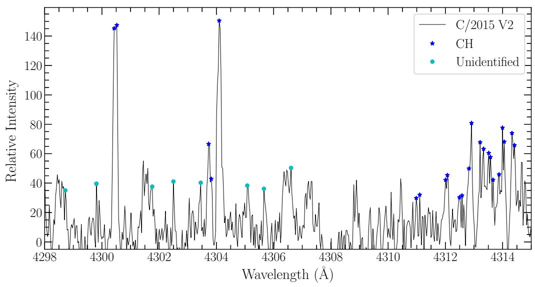

(a) CH observed in C/2015 V2 on 2017-05-28

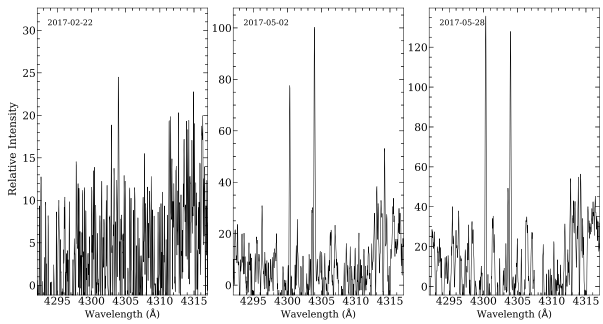

(b) CH emission observed in C/2015 V2 for different epochs

Figure 6.16: Analysis of CH emission bands observed in comet V2

6.3.1.5 NH_2 emissions

NH_2 emissions from different transitions are observed in plenty with good SNR in all the comet. It is observed to be present along a large range of wavelength blended amongst the C_2 Swan bands. Since ammonia is considered to be the sole parent of NH_2, the ortho-to-para abundance ratio (OPR) of ammonia is usually computed from the OPR of different transitions of NH_2 (Kawakita et al., 2004; Shinnaka et al., 2020, 2016). Even though the real implication of ammonia OPR is not yet known, the possibility of deriving the nuclear spin temperature of ammonia from OPR provides us an opportunity to understand the conditions in the solar nebula at the time of formation of the cometary material or the physio-chemical conditions in the inner-most coma or beneath the surface (Kawakita et al., 2004; Shinnaka et al., 2020).

46P: Having had its closest approach to Earth in about four centuries gave the biggest opportunity to study the various bands associated with the NH_2 emission present in the comet. Figures 6.17a, 6.17b and 6.17c represents the (0-10-0), (0-9-0) and (0-8-0) transitions present in the comet. With the help of the line lists given in Kawakita et al. (2004) and Shinnaka et al. (2020), the Ortho and Para lines were identified to perform a basic computation of the OPR of NH_2 as given in Table.6.2.

Table 6.2: NH_2 OPR measured in 46P for different epochs.

Date of observation	Band	Fibre 1	Fibre 2
2018-11-28	(0-9-0)	3.41	3.48
	(0-8-0)	3.18	–
2018-12-28/High-res	(0-9-0)	3.14	–
2018-12-28/Medium-res	(0-9-0)	3.84	–
Total Average		3.41	

The NH_2 bands from Fibre 2, wherever available, were also used to compute the corresponding OPR. From the average observed OPR of NH_2, the OPR of NH_3 was computed to be 1.205 through the relation mentioned in Shinnaka et al. (2016). This observed OPR(NH_3) is similar to that of certain comets reported in Shinnaka et al. (2016) and Hale-Bopp in Kawakita et al. (2004). This computed OPR(NH_3) would correspond to a nuclear spin temperature of $\sim$ 26 K. The error in these values are not significant in the current scenario since the OPR values are obtained by general computation and the spin temperature is generalised by comparison with various literature. The exact OPR and nuclear spin temperature can only be derived with the help of precise modelling techniques. As mentioned in Kawakita et al. (2007), further understanding of the implication of nuclear spin temperature in comets is required to have a comparative study of these values obtained in different comets. Whether a major difference of spin temperature between different dynamical classes is observed or not could vary the interpretation of these results.

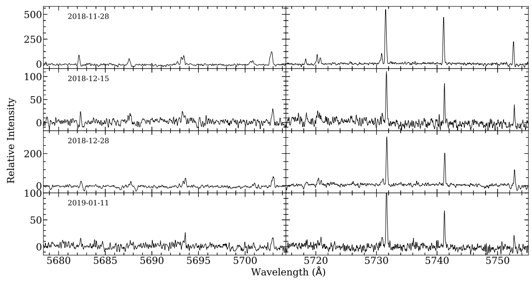

(a) NH_2(0-10-0) emission band region in 46P on different epochs.

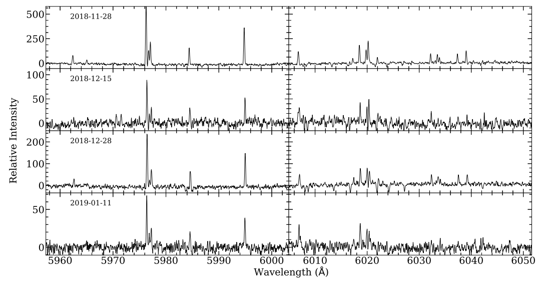

(b) NH_2(0-9-0) emission band region in 46P on different epochs

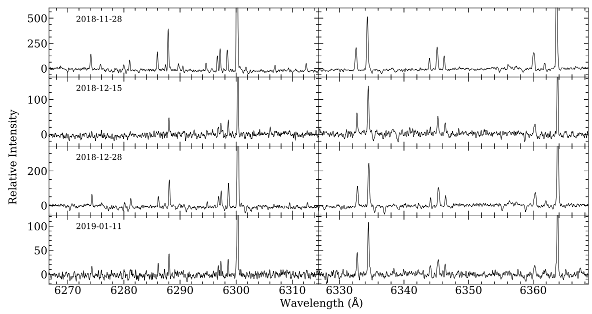

(c) NH_2(0-8-0) emission band region in 46P on different epochs

Figure 6.17: Various NH_2 band regions observed in 46P for different epochs

<u>V2</u>: The NH_2 (0-8-0) and (0-9-0) were observed in comet V2 for all the epochs (see Figure.6.18 for the observed (0-8-0) band), but the intensity in the individual Ortho and Para lines were not strong enough as in the case of 46P to perform the basic computation of OPR. Proper modelling techniques similar to those done in Moulane et al. (2020b), Shinnaka et al. (2020) and Kawakita et al. (2004) will have to be employed to synthesise the NH_2 spectrum matching the observed one using which the OPR can be computed.

<u>38P and 41P</u>: Similar to V2, the NH_2 (0-8-0) and (0-9-0) were detected in comets 38P and 41P (see figures.6.19a and 6.19b). Even though the computation of OPR would be difficult in the case of these comets, the difference in the relative strength of various

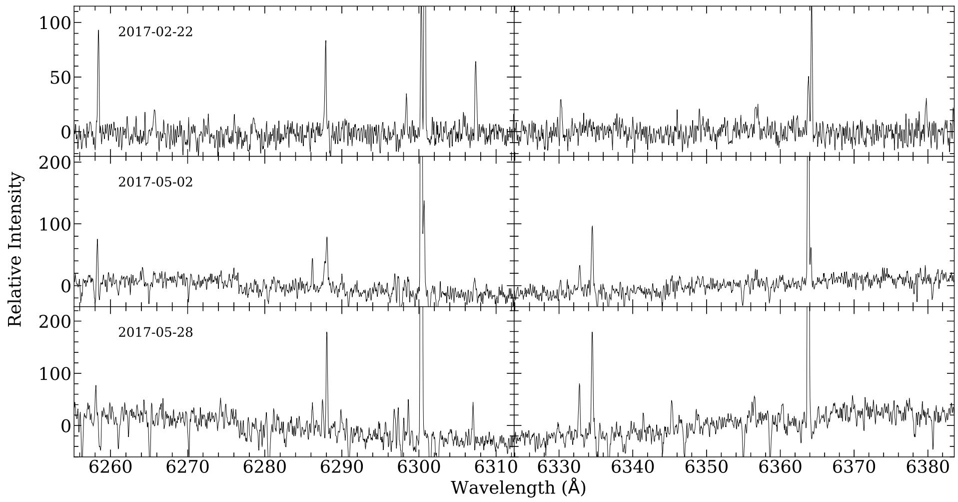

Figure 6.18: NH_2(0-8-0) emission band region observed in C/2015 V2 on different epochs

NH_2 lines between 38P and 41P can be used to differentiate the composition of an SPC and an HTC.

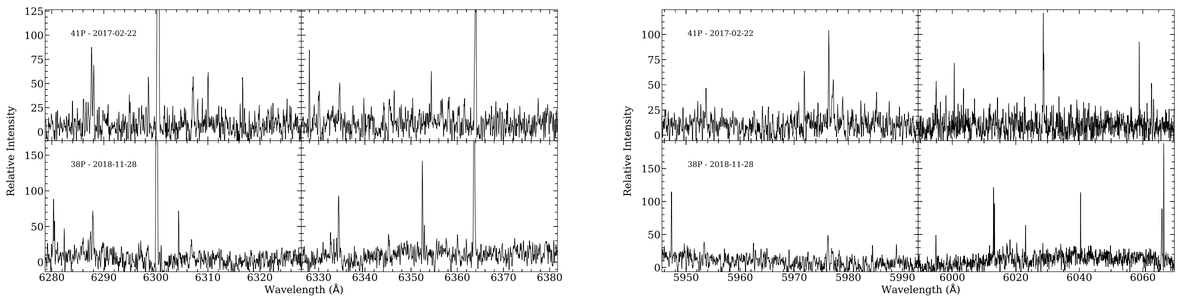

(a) NH_2(0-8-0) emission band region (b) NH_2(0-9-0) emission band region

Figure 6.19: Comparison of NH_2 bands observed in comets 41P and 38P.

6.3.1.6 O[I]

The most abundant materials present in comets, H_2O, CO_2 and CO all contain Oxygen, making it the most abundant element in comets. As the photo dissociation of all these molecules can produce Oxygen atoms, Festou & Feldman (1981) suggested that the strength of Oxygen emission lines present at 5577.339 Å, 6300.304 Å and 6363.776 Å can be used to analyse the basic compositional characteristics of a comets nucleus. The forbidden oxygen emission lines, the Green (G) and Red doublet (R), originates from the O(^{1}S) and O(^{1}D) levels respectively. Later, works carried out by Bhardwaj & Haider (2002), Bhardwaj & Raghuram (2012) and Raghuram & Bhardwaj (2014) defined that CO_2 and H_2O molecules contributed to the production of green line, while only H_2O molecule contributed to the red doublets. Hence, a ratio known as the G/R ratio was defined, which is the ratio of intensity of the green line to the sum of red doublets, to imply the possible major source of the detected Oxygen lines. The major source of Oxygen line is considered to be H_2O if the G/R is observed to be ~ 0.09 or less and CO_2 if it is much higher. The major catch here is that, for comets in which Oxygen lines are detected at far off heliocentric distances, the major source would be CO_2 as the temperature would not be ambient enough for water molecules to sublimate in large amount. As the comet moves in, the sublimation of water ice increases hence reducing the G/R. This means that G/R ratio is majorly dependent on the heliocentric distance. But, Decock et al. (2015) observed a nucleocentric dependence of G/R ratio in multiple comets. The G/R ratio was seen to be high ($\sim 0.1 - 0.2$) close to the nucleus within 100 km and drops of drastically at about 1000 km ($\sim 0.04 - 0.06$). Such differences in G/R ratio with nucleocentric distance is observed due to the high quenching of Oxygen atoms by the high density of H_2O molecules present in the inner coma (Bhardwaj & Raghuram, 2012). Such quenching mostly affects the atoms present in the O(^{1}D) level as its lifetime is much larger than those in O(^{1}S) (Raghuram & Bhardwaj, 2014) causing the increase in G/R close to the nucleus. At distances far enough from the nucleus where quenching is not a major factor, the actual value of the G/R ratio is observed. Cessateur et al. (2016) have also discussed the probability of including Oxygen molecule as a possible source of these Oxygen emissions. But, the effect of Oxygen molecule would be predominant in the inner coma within 400 km.

The forbidden oxygen emission lines, the Green (G) and Red doublet (R), originating from the O(^{1}S) and O(^{1}D) levels respectively are present both in comets and atmosphere. Since both cometary and telluric Oxygen lines fall at the same wavelength, it is nearly impossible to separate them in normal conditions. Even though the geocentric velocity of the comet induces a Doppler shift in the cometary Oxygen line separating it away from the telluric lines, fairly high enough resolution is required to probe them. In a special case, if the comet posses large geocentric velocity, it will be possible to separate the Oxygen lines even with a resolution of 30,000. Even though the 3 lines fall in 3 different orders of the spectrum, considering the fact that they are continuum corrected and fall more or less on the central part of the CCD, the effect of sensitivity can be considered minimal. On the other hand, the presence of certain C_2 lines blended along with the 5577.339 Å Oxygen lines may affect the computed G/R ratio. The synthetic spectrum of C_2 fabricated as mentioned in Decock et al. (2015) is to be removed from the observed spectrum in order to nullify this effect. The effect of these blends varies from comet to comet as the Carbon chain depletion varies in each of them. In the current case, a basic computation of the ratio has been performed to understand the general characteristics of the composition present in different comets. Even though a systematic study of change in G/R with nucleocentric distance is not possible in the case of HESP observations, the presence of 2 fibres 13 arcsec apart makes it feasible to measure the ratio at two different locations of the coma. This can prove important in analysing the effects of quenching on G/R ratio close to and away from the nucleus.

V2: As mentioned in Table.6.1, comet V2 was observed across 3 epochs with a resolution of 30,000. Out of the 3, the comet's geocentric velocity was large enough during the first two epochs to induce a fairly good Doppler shift so as to separate the cometary and telluric Oxygen lines. Figure.6.20 illustrates the Oxygen green and red doublets observed in V2 on 2017-02-22. The substantial separation between the Oxygen lines makes it easier to measure the intensities corresponding to the 3 lines with the help of Gaussian fitting and compute the G/R ratio. Table.6.3 provides the computed values for the two fibre inputs corresponding to the two different epochs. In the case of V2, during both the epochs, the geocentric distance was fairly large making it difficult to probe the inner coma. Since the physical aperture of Fibre 1 itself was greater than 1000 km during both the epochs, the G/R value corresponding to both Fibre 1 and 2 would in a way represent the actual value unaffected by the quenching effects. Hence, from the computed G/R values, it can be roughly implied that CO_2 was a major source for the production of Oxygen when the comet was at a geocentric distance of 1.78 AU after which H_2O started dominating as the comet approached 1 AU. The consistency in the measured values in both the fibres for the second epoch shows that the major effects of collisional quenching was well within $\sim$1000 km.

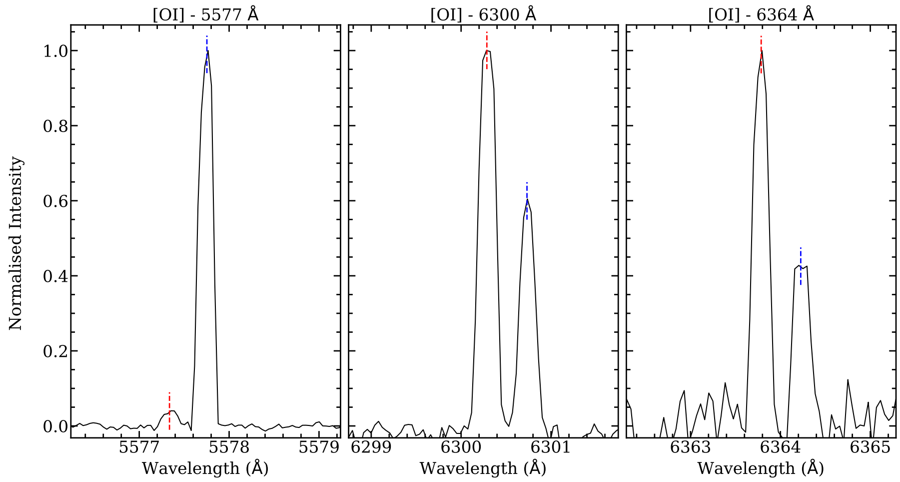

Figure 6.20: Green and red doublet [OI] forbidden lines observed in C/2015 V2 on 2017-02-22

46P: The geocentric velocity of the comet was not high enough during the first 3 epochs as the comet was having a close approach to Earth at the same time. Hence, the separation in the Oxygen lines induced by Doppler shift could not be probed by the 30,000 resolution for the first 3 epochs of observation. The observation of 46P in the 60,000 resolution on 2018-12-28 proved significant since the Oxygen line peaks could be separated. As shown in Figure.6.21, Gaussian deblending was used to measure the intensities of the cometary Oxygen lines and hence measure the G/R values. During the 2019-01-11 epoch of observation, the geocentric velocity played a major role in separating the lines to be detected in the 30,000 resolution. Still, the Gaussian deblending had to be incorporated as the separation was not evident enough as in the case of V2. The measured G/R values corresponding to both the fibres for the two epochs are given in Table.6.3. The historic closest approach 46P proved major in comparing the G/R values in the coma close to the nucleus and away from it. During both the epochs, Fibre 1 looked at the very inner part of the coma, around 100 km (due to seeing effects), and Fibre 2 was looking at a region more than $\sim$ 1000 km away from the nucleus. According to the study of variation in G/R values with nucleocentric distance for multiple comets as shown in Decock et al. (2015), these two regions correspond to different effects of quenching. Interestingly as expected, the G/R values measured for fibres probing two different locations in the coma vary largely. The consistency of the values measured for Fibre 1 and Fibre 2 on both the epochs of observation points

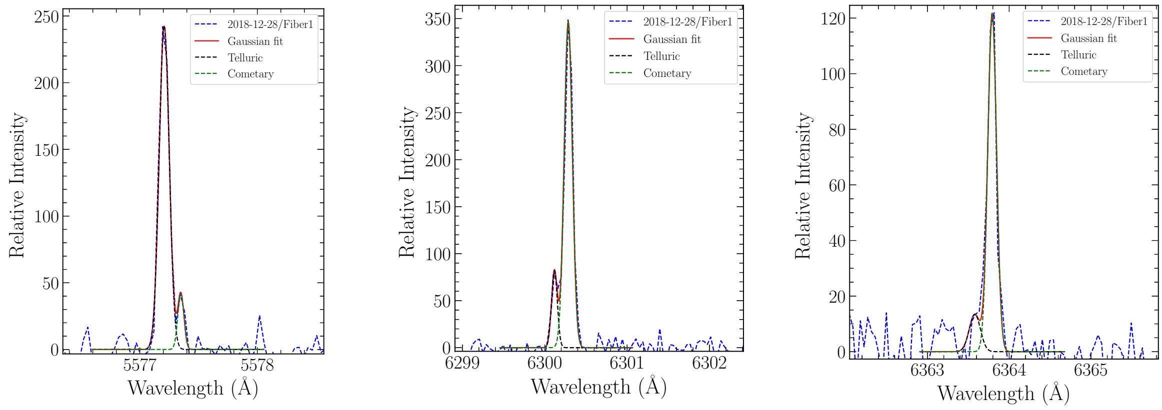

(a) [OI] 5577 Å (b) [OI] 6300 Å (c) [OI] 6364 Å

Figure 6.21: Green and red doublet [OI] forbidden lines observed in 46P on 2018-12-28 in high resolution mode.

to the major effect of collisional quenching in the inner parts of the coma. Similar to the works done by Decock et al. (2013) and Cessateur et al. (2016), further modelling can be incorporated to use these information to understand the abundance of CO_2 and Oxygen in the comet.

Table 6.3: Observational results of G/R

Comet	Date of observation	Fibre 1	Fibre 2
C/2015 V2	2017-02-22	–	0.09 ± 0.01
	2017-05-02	0.043 ± 0.005	0.041 ± 0.006
46P	2018-12-28	0.11 ± 0.01	0.05 ± 0.01
	2019-01-19	0.11 ± 0.01	0.06 ± 0.01

6.4 Conclusion

Out of all the identified comets, only a few have been observed in spectroscopic technique. Out of these, only a very few comets have been observed with a very high resolution to probe the different vibrational and rotational lines present in the different molecular emission bands. In this chapter, we have discussed the high resolution spectroscopy of 4 comets. The specific conclusions of the work are given below:

1. For the observed 4 comets, we have identified the lines present in the various molecular bands during different epochs.

2. The variation in the emission lines present in different molecular bands along the orbit of these comets have been laid out.

3. The green and red doublet forbidden oxygen lines in comets C/2015 V2 and 46P have been majorly probed to analyse their G/R ratio. The ratio computed for both comets point to H_2O being a major source for the Oxygen emissions.

4. Comet 46P having had a historic close approach to Earth enabled the analysis of G/R ratio at two different locations in the coma. From detailed analysis there is an indication of effects of quenching while comparing the values obtained close to the nucleus to that obtained further away from the nucleus.

5. The high SNR in 46P high resolution spectra helped in probing the different NH_2 bands present. They were used to compute the OPR to have a general understanding of the spin temperature present in the comet.

6. Detailed modelling techniques are to be employed with both NH_2 and Oxygen line analysis in order to remove all the possible blends to obtain the exact ratios and hence the apt understanding of the comet's composition.

Chapter 7

Interstellar visitor

7.1 Introduction

The various hypothesis regarding the existence of an interstellar comet population was discussed in Section.1.3.2. Section.1 emphasises the significance of comet observations and indicate that comparing comets from our Solar system with interstellar ones can shed light on the difference/similarity in the materials present in different proto-stellar systems. After centuries of comet observations and decades after the initial prediction by Sen & Rana (1993), Gennady Borisov on 30 August 2019, using his self-built 0.65 m telescope discovered a comet like body. This was later identified to be the first ever interstellar comet to be observed passing through the Solar system. The interstellar origin of the comet was confirmed from the very large eccentricity (e = *3.379*) and very high hyperbolic excess velocity (v $\sim$ 32 Km/s (Guzik et al., 2020)) possessed by the comet. The interstellar comet, initially identified as C/2019 Q4, was later named 2I/Borisov[1] by the IAU. Fitzsimmons et al. (2019) were the first to report the detection

[1]https://minorplanetcenter.net/mpec/K19/K19S72.html

of CN in the interstellar comet. Later, de León et al. (2020), Opitom et al. (2019a) and Kareta et al. (2020), have all reported the clear detection of CN along with an upper limit to the production rate of C_2(0-0) emissions. Lin et al. (2020a) and Bannister et al. (2020) have reported the clear detection of both CN and C_2 in their spectrum, with the latter work having the most detailed spectrum of 2I/Borisov reporting the detection of well-resolved C_2, NH_2 and CN emissions.

In this Chapter, we discuss the spectroscopic and imaging observations carried out from two Indian observatories during November and December 2019, to study the evolution of molecular emissions and also to put constraints on the physical characteristics of the rare interstellar comet 2I/Borisov. Section 7.2 describes the observations from both observatories. Section 7.3 discusses the data reduction and analysis methods used. Finally, we discuss the spectroscopic and imaging results in section 7.4.

7.2 Observations

Observations of the interstellar comet, 2I/Borisov, were carried out using the two Indian observatories, HCT and MIRO. The observational log, including the heliocentric distance, geocentric distance, phase angle and airmass at the time of observations are as given in Table.7.1. During the observation from HCT, apart from the comet and required calibration frames, Standard star HD74721 (A0V type) was observed for flux calibration. Separate sky frame was not obtained for the comet due to time constraints. Imaging observations were also carried out during the same epochs using the Johnson-Cousins *BVRI* filters. Multiple frames were obtained for each epoch, with exposure times varying over the range 120-300 s. Ru 149 photometric field was also observed in all above mentioned filters in order to perform photometric calibration of the comet images. Twilight flats and bias frames were also taken at regular intervals during the night to correct the pixel to pixel response and remove the bias offset respectively.

The optical imaging system (refer Section.2.2) was used during observations from MIRO. Imaging observation in the *BVRI* filters were carried out on 24^{th}, 25^{th} and 27^{th} of December 2019. Again, Ru 149 field was chosen as a standard star field to be used for photometric calibration. Twilight flats and bias frames necessary for basic reduction were obtained during all the nights.

Table 7.1: Observation Log for Interstellar comet 2I/Borisov

Date [UT]	Time [UT]	Telescope Facility	Heliocentric Distance (r_H) [AU]	Geocentric Distance (Δ) [AU]	Distance scale at photo-centre [Km/arcsecond]	Phase angle [°]	Airmass
30/11/2019	23.04	HCT	2.013	2.049	1486	28.08	1.83
22/12/2019	23.16	HCT	2.031	1.94	1407	28.56	2.6
24/12/2019	22.25	MIRO	2.039	1.938	1406	28.5	1.96
25/12/2019	21.62	MIRO	2.043	1.937	1405	28.45	2.23
27/12/2019	21.84	MIRO	2.05	1.936	1404	28.36	2.1

7.3 Data reduction and analysis

Careful reduction techniques are necessary to reduce, calibrate and extract information from the raw data of a comparatively faint comet. The following sub-sections discuss, in brief, the various steps used in the process of analysing the data obtained from spectroscopy and imaging.

7.3.1 Spectroscopy

The interstellar comet being a faint one does not give a spectrum with significant SNR. Hence, a single aperture with appropriate size so as to include the maximum signal is to be used to extract the spectrum. After the Standard reduction routines were performed, IRAF's *APALL* module was used to extract the 1D spectrum from the comet, calibration lamp and standard star frames. For both epochs, an aperture of 17.76″ (corresponding to 60 pixels, centred on the comet) was used to extract the comet spectrum. The corresponding physical distance at the photo-centre can be estimated using the distance scale column from Table.7.1. On analysing the profile along the slit, in the spatial axis, it appears that 2I/Borisov has an extent of about 20″. Taking this into account, we used an equal sized aperture for the comet and the sky in the same frame. The sky spectrum required for subtraction was extracted about 60″ away from the photo-centre, free from cometary emissions.

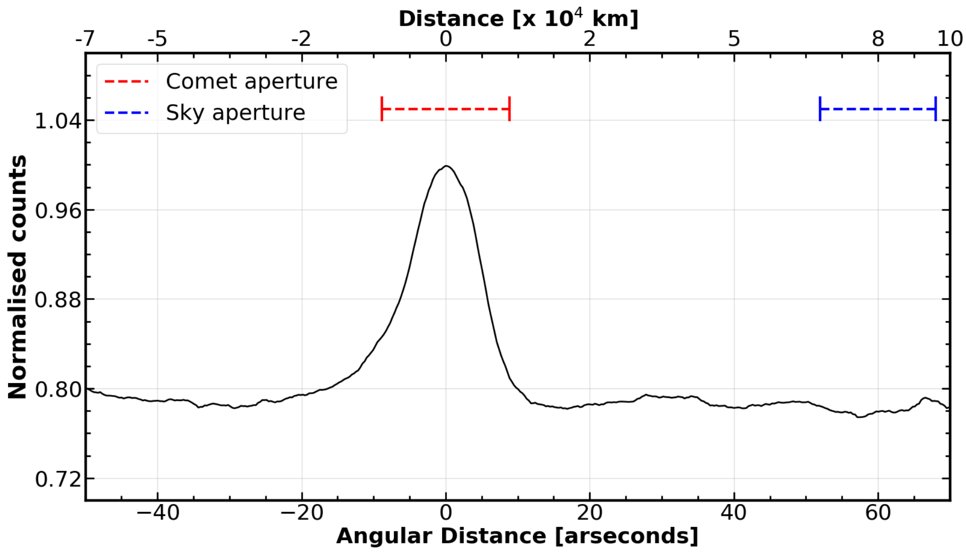

Figure 7.1: Profile along the slit (spatial direction) showing the locations of the apertures used for extracting the flux from the comet and the background sky.

Figure.7.1 depicts the positions of both these apertures over-plotted on the profile along the slit, in the spatial axis. The normalised wavelength calibrated spectra of both comet and sky, with a constant offset in the sky spectrum is shown in the top panel of Figure.7.2. The bottom panel depicts the corresponding sky corrected spectrum, with the detected emissions marked.

The extracted comet spectrum is calibrated and continuum subtracted by means explained in Section.2.3.1. A flux calibrated spectrum of the comet 2I/Borisov is shown in Figure.7.3, clearly indicating the presence of emissions from CN, C_2 and C_3 with the latter two highly depleted, similar to what has been observed by Opitom et al. (2019a), Lin et al. (2020a), Kareta et al. (2020), de León et al. (2020) and Bannister et al. (2020). The inset image represents the RGB view of the comet using the same instrument.
The computation of production rate and Haser factor for single aperture extraction is described in Section.B.2. The Haser factor for both the epochs were obtained from Schleicher's website for an aperture radius of 8.88″ (corresponding to 30 pixel, half the total aperture used). In order to adjust the Haser factor for the aperture used, the obtained value was adjusted for our aperture area of $1.92'' \times 17.76''$. The values for g

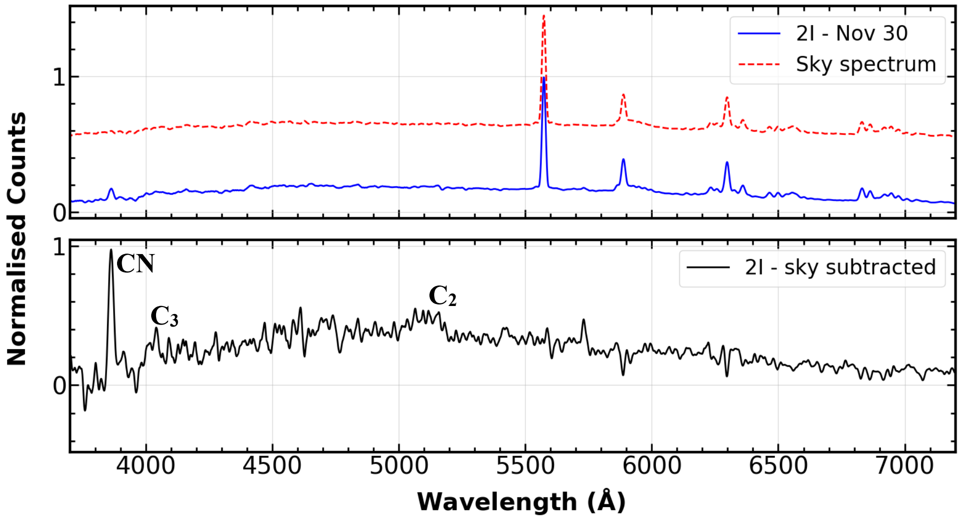

Figure 7.2: *Top panel* : Comet spectrum (blue solid line) and sky spectrum (red dashed line, with a constant offset) illustrating the presence of strong atmospheric telluric lines . *Bottom panel* : Comet spectrum after sky correction with the detected emissions marked.

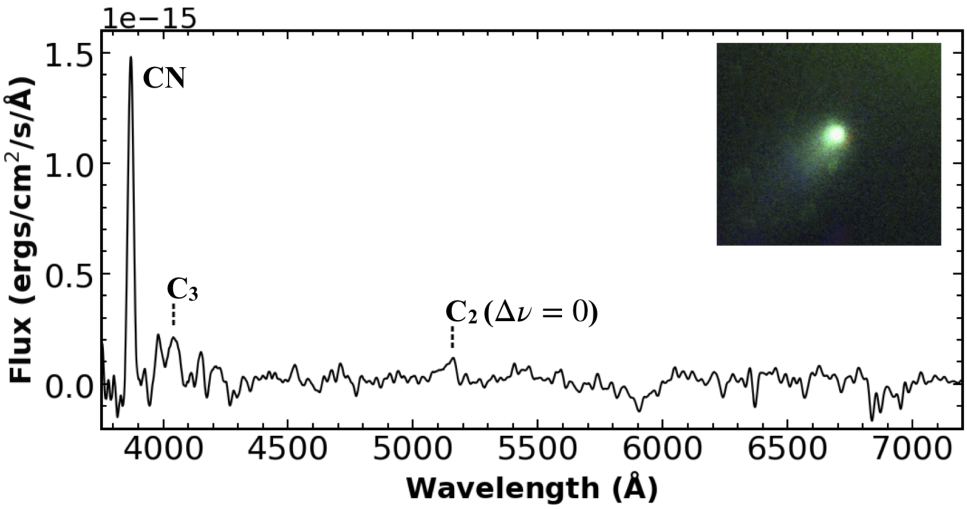

Figure 7.3: Optical spectrum of 2I/Borisov observed with the HFOSC instrument on HCT on 2019-12-22.965 UT. Inset shows the RGB colour composite view of the comet on the same night using images taken with HFOSC.

and τ at 1 AU taken from A'Hearn et al. (1995) and Schleicher (2010) were appropriately scaled and used to compute the production rates of the various molecular species.

7.3.2 Imaging

The self scripted Python routine whose steps are explained in Section.7.3.2 was used to perform all basic data reduction techniques on both comet and standard star images. The standard stars (Ru 149, Ru 149B, Ru 149D, Ru 149E) in the Ru149 field was used to compute the apparent magnitude of the comet on the respective epochs of observation. These computed values for different filters are tabulated in Table.7.3.

7.4 Results & discussion

7.4.1 Spectroscopy

From successful spectroscopic observations of the interstellar visitor, carried out on two epochs, pre and post perihelion, we detect the presence of CN radical, C_2 ($\Delta\nu = 0$) Swan band and C_3 emission (latter two being highly depleted) as shown in Figure.7.4. The production rates of CN, C_2 and C_3 computed for both epochs, as mentioned in Section 7.3.1, are listed in Table.7.2. The comet has been monitored in spectroscopy by various groups with heliocentric distance ranging from 2.7 to 2.02 AU. The current work reports the production rates for the comet pre and post perihelion and hence contributes a valuable data point towards studying the characteristics of the emissions in the comet post perihelion.

The production rate of CN, C_2 and C_3, reported in this work, pre-perihelion, is comparable with the values reported in other observations, as shown in Figure.7.5, with slight increase in the rate which can be accounted by the fact that the comet was approaching perihelion. Among the clear detection of C_2 as reported by Lin et al. (2020a), Bannister et al. (2020) and the current work, an increasing trend in the production rate can be observed, while it is difficult to compare the same with the upper limits reported in the other observations. Adding an important data point to

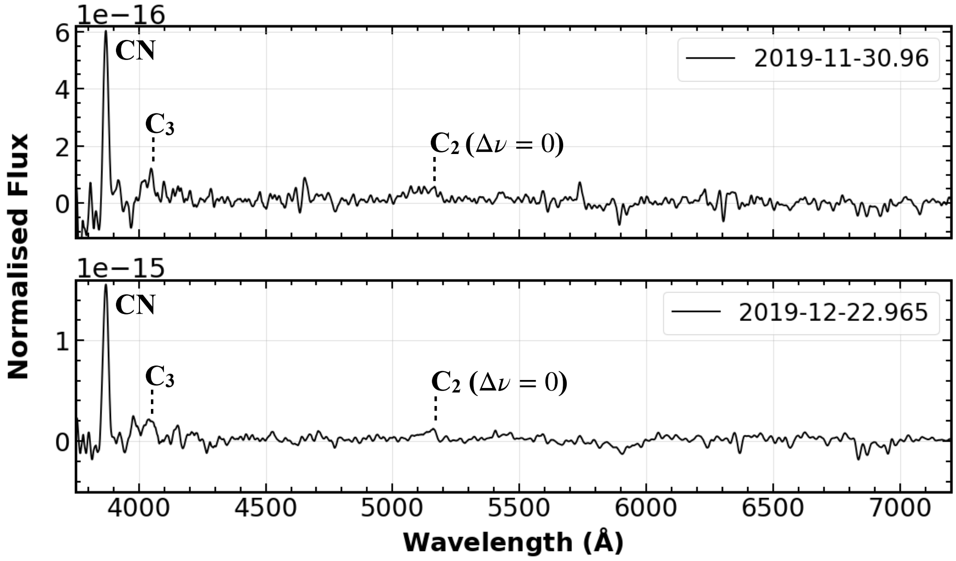

Figure 7.4: Optical spectra of 2I/Borisov as observed on the pre and post perihelion epochs.

the spectroscopic observation of the rare visit of the interstellar comet, the production rate of CN and C_3 shows drastic change with only a slight variation in that of C_2, post-perihelion. The production rate ratio, Q(C_2)/Q(CN), was computed for both the epochs and the comet was seen to be depleted in carbon chain molecules, according to the classification criterion defined by A'Hearn et al. (1995). Also, the comet can be classified as depleted in carbon chain molecules according to the criterion defined by Cochran et al. (2012), where the production rates of both C_3 and C_2 with respect to CN are considered. Figure.7.6 compiles the values of Q(C_2)/Q(CN) as reported from all the other observations with our own observations. It is interesting to observe that there is an increase in the production rate ratio with heliocentric distance (until perihelion), which is not common among Solar system comets for a minimal change in heliocentric distance (A'Hearn et al., 1995; Cochran et al., 2012). Along the orbit of the comet, the behaviour has changed from highly depleted to a moderately depleted comet, as it approached perihelion. Even though the production rate ratio, reported in our work, pre-perihelion, Q(C_2)/Q(CN) = 0.54, is comparable to the values reported by Bannister et al. (2020), it is surprising to observe that the value has dropped to Q(C_2)/Q(CN) = 0.34, post-perihelion, once again making the comet highly depleted in carbon chain molecules. Langland-Shula & Smith (2011) have reported the variation in production rate ratio (Q(C_2)/Q(CN)) with increasing heliocentric distance in a sample of Solar system comets. However, A'Hearn et al. (1995), Cochran et al. (1992) and Cochran et al. (2012) did not observe any variation in the production rate ratios for a *minimal* change in the heliocentric distance. In the current work, even though the production rate ratios are comparable within the errors, there is an indication of a possible asymmetry post-perihelion (see Figure.7.6). However, this cannot be confirmed with the limited post-perihelion data currently available.

As shown in Figure.7.5, we also notice an asymmetry in the production rates of CN and C_3 post-perihelion. Generally, such asymmetries in production rates are observed among the short period comets of our Solar system (eg. Opitom et al., 2017; A'Hearn et al., 1984a), close to perihelion. This asymmetry is expected either due to the illumination of different areas of the nucleus having different surface processing during their orbit or due to the presence of a less volatile surface, depleted in most of the molecules. Once these layers get disintegrated by the solar radiation, the less depleted surface of the comet gets exposed resulting in an increased flux in emissions. However, Bodewits et al. (2020) and Cordiner et al. (2020) report that 2I/Borisov has an extremely high abundance of carbon monoxide, implying that the surface of the comet has not undergone a sufficiently intense heat processing to cause the depletion of the top volatile surface. In addition, such high CO abundance is usually uncommon among the short period comets (Dello Russo et al., 2016). All these reported facts and the observed asymmetry in production rates around perihelion, makes us raise a question on the chemical homogeneity of the material present in the nucleus of 2I/Borisov or the difference in the volatile nature of the molecules present in the comet nucleus. Bannister et al. (2020) suggests a possibility of heterogeneous composition in the comet based on the observed increase in C_2 activity close to perihelion. Based on the observed very high abundance of CO in 2I/Borisov, Bodewits et al. (2020) points out the possibility of the comet having formed beyond the CO ice line of its parent stellar system. Since the results from the current work are also in agreement with the suggestions regarding the heterogeneity, it is possible that the comet was formed in a stellar system beyond the CO ice line undergoing a very inhomogeneous mixing of various volatile compounds present in the proto-stellar nebula.

A'Hearn & Cowan (1980) states that, since the parent molecules of C_2 are primarily contained in the grains of H_2O ice, the production of C_2 is directly related to the activity in the icy grains of H_2O, while production of CN and C_3 are not. Combi & Fink (1997) discuss the possibility of C_2 being produced from a primary parent molecule frozen in the icy mix of the nucleus and also directly from CHON grains at temperatures $\sim 500\,K$. In the current scenario where the perihelion distance of the comet is 2.0066 AU, the temperature from solar radiation would not be high enough for CHON grains to be a primary source for C_2. Also, the influence of CHON grains would result in a flattening of the spatial profile of C_2 as per the CHON grain halo (CGH) model proposed by Combi & Fink (1997). Such a spatial flattening has not been reported yet in the case of 2I/Borisov. On the other hand, Xing et al. (2020) reports that the water production in 2I/Borisov had increased drastically from November to December, close to perihelion and then decreased rapidly by December 21^{st}. With the contribution from CHON grains being ruled out, only the activity in H_2O ice can explain the increase in production rate of C_2 close to perihelion and hence the initial increase in Q(C_2)/Q(CN). The drop in the ratio post perihelion is due to an increased activity of CN while C_2 activity had not changed substantially. Results from our work also support the possibility reported by Bannister et al. (2020), regarding the heterogeneity in the comet nucleus. This would have resulted in a fresh layer, rich in carbon chain parent molecules trapped in the icy grains, being exposed and hence resulting in the steep increase of C_2 production rate along with the water production rate.

We also infer a possibility that, as the southern hemisphere of the nucleus was illuminated, after perihelion, a fresh unexposed area of the comet started sublimating as proposed by Kim et al. (2020). This resulted in the drastic increase in production rates of CN and C_3 with only a minimal change in the C_2 production rate owing to the reduced water production rate. Even though A'Hearn et al. (1986) and Fray et al. (2005) discusses the prospect of CHON grains being a possible parent source of CN, it can be ruled out in this case since the contribution would be very less due to the perihelion distance of the comet as discussed earlier. We also observe an abrupt discontinuity in the production rate of CN as compared to that for C_2 (see Figure.7.5). This strongly suggests that both of them come primarily from different sources as discussed by A'Hearn & Cowan (1980). This behaviour can also be considered as a confirmation, in this work, that the parent molecules of both CN and C_3 resides mainly in the comet nucleus whereas that of C_2 is mostly present in the icy grains of the coma. The difference in activity of C_3 and C_2 also confirms that the parent molecules of these emissions should be entirely different as mentioned in Yamamoto (1981).

Table 7.2: Activity of comet 2I/Borisov at different heliocentric distances

Date	Exposure	r_H	Δ	Production Rate (molec/sec)			Production rate ratio	Dust to gas ratio
[UT]	[s]	[AU]	[AU]	CN	$C_2(\Delta v = 0)$	C_3	Q(C_2)/Q(CN)	log[$(Af\rho)_R$/Q(CN)]
				$\times 10^{24}$	$\times 10^{24}$	$\times 10^{23}$		
2019-11-30.96	1800	2.013	2.049	3.36 ± 0.25	1.82 ± 0.60	1.97 ± 0.52	0.54 ± 0.18	-22.24 $\pm$ 0.12
2019-12-22.965	1800	2.031	1.94	6.68 ± 0.27	2.30 ± 0.82	7.14 ± 0.74	0.34 ± 0.12	-22.57 $\pm$ 0.12

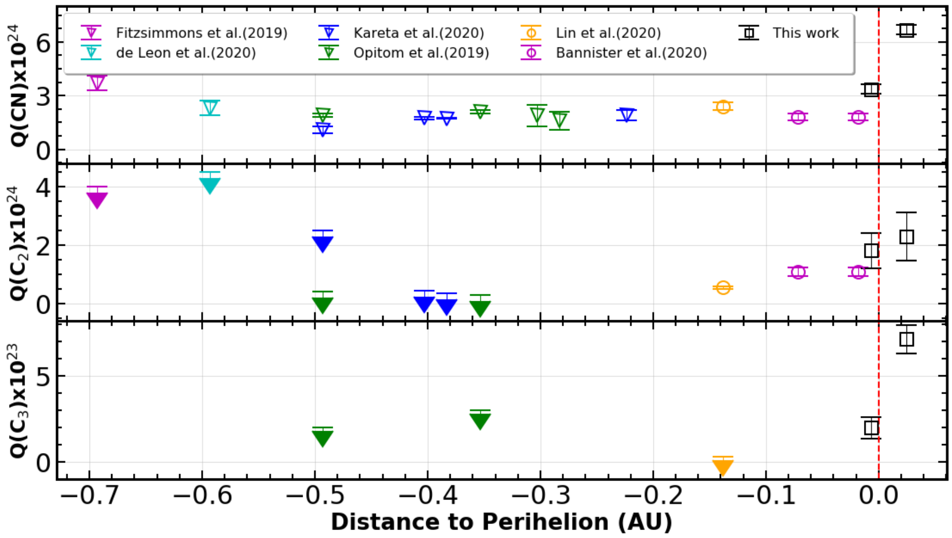

Figure 7.5: Comparison of pre-perihelion production rates (measurements/upper limits) of CN (upper panel), C_2 (middle panel) and C_3 (lower panel) reported in Fitzsimmons et al. (2019), Opitom et al. (2019a), Kareta et al. (2020), de León et al. (2020), Lin et al. (2020a) and Bannister et al. (2020) with the pre and post perihelion production rates of same molecules as computed in this work.

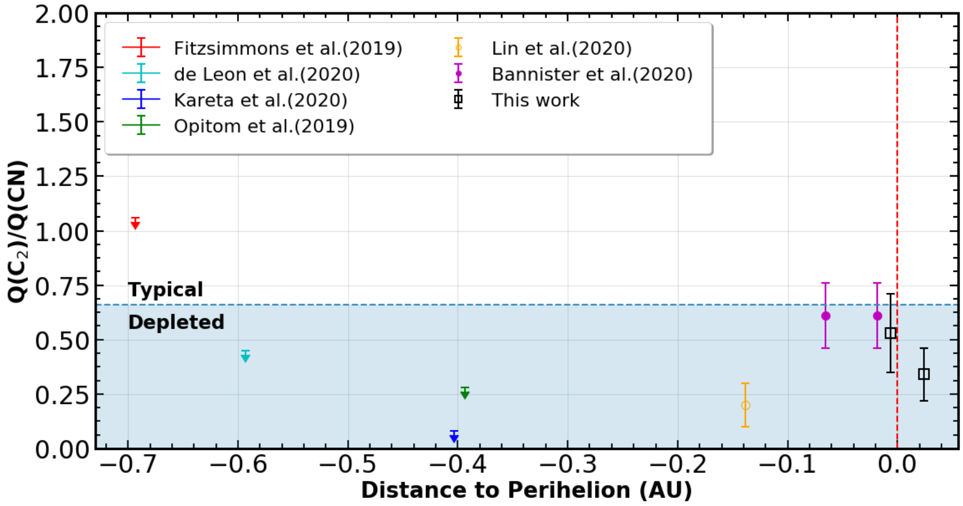

Figure 7.6: Cumulative comparison of the pre and post perihelion production rate ratio of C_2 and CN of 2I/Borisov observed in the current work with the values reported by Fitzsimmons et al. (2019), Opitom et al. (2019a), Kareta et al. (2020), de León et al. (2020), Lin et al. (2020a) and Bannister et al. (2020) while the comet was in an in-bound orbit. The shaded region represents the area of carbon chain depleted comets in our Solar system, for which $Q(C_2)/Q(CN) < 0.66$, as defined by A'Hearn et al. (1995). The red dashed vertical line represents the perihelion of the comet on 8th December 2019 with q$\sim$2.0066 AU.

7.4.2 Imaging

The comet was observed in imaging mode on 5 epochs (Table.7.1) in the Bessel's *BVRI* filters from both HCT and MIRO. The images were reduced and apparent magnitudes were computed as explained in section 7.3.2.

7.4.2.1 Optical colours and $Af\rho$

From the magnitudes computed, as given in Table.7.3, the optical colours of the comet were found to be; *(B-V)* = 0.80 ± 0.05, *(V-R)* = 0.49 ± 0.04, *(R-I)* = 0.53 ± 0.03 *(B-R)* = 1.29 ± 0.06. These colours are in good agreement with the colours reported by Jewitt & Luu (2019), which are slightly redder than the solar colours (Holmberg et al., 2006) and similar to that of 1I/'Oumuamua (Jewitt et al., 2017b). The colours of the

Table 7.3: Apparent magnitude (m), absolute magnitude (H), effective scattering cross section (C_e) and $Af\rho$ computed for various observational epochs

Date [UT]	m[a] B	m[a] V	m[a] R	m[a] I	H_R^b	C_e[Km^2]	$Af\rho$ [cm] B	$Af\rho$ [cm] V	$Af\rho$ [cm] R	$Af\rho$ [cm] I
2019-11-30	17.41 ± 0.08	16.59 ± 0.07	16.16 ± 0.10	15.64 ± 0.06	12.16 ± 0.07	157 ± 12	107 ± 3	110 ± 3	120 ± 4	138 ± 5
2019-12-22	17.62 ± 0.08	16.86 ± 0.07	16.31 ± 0.09	15.79 ± 0.06	12.39 ± 0.06	127 ± 9	80 ± 2	87 ± 3	97 ± 3	124 ± 5
2019-12-24	–	–	16.37 ± 0.14	15.81 ± 0.07	12.46 ± 0.10	118 ± 13	–	–	94 ± 2	120 ± 3
2019-12-25	17.72 ± 0.22	16.9 ± 0.17	16.41 ± 0.15	–	12.56 ± 0.11	108 ± 12	66 ± 5	86 ± 2	95 ± 2	–
2019-12-27	–	–	16.44 ± 0.14	–	12.58 ± 0.10	106 ± 11	–	–	94 ± 2	–

[a] An aperture size of 10,000 Km has been used on all epochs for all filters to compute the magnitude

[b] Absolute magnitude computed using Eq.7.1 from the corresponding apparent magnitude in R filter

interstellar comet are also surprisingly similar to the mean colours of long period comets in the Solar system (Jewitt, 2015). The *(B-V)*, *(V-R)* and *(R-I)* colours, after transformation to the SDSS photometric system as described in Jordi et al. (2006), also compares within uncertainties in measurement to the colours reported by Bolin et al. (2020) and Hui et al. (2020). The available magnitudes were also used to compute $Af\rho$, a proxy to the amount of dust produced (A'Hearn et al., 1984b). The obtained values of $Af\rho$ (see Table.7.3), for 30th November and 22nd December, in V band is found to be similar to the values reported by Xing et al. (2020), for the same wavelength band, during nearby epochs (1st December and 21st December respectively). The equation for average slope of the curve of reflectivity, as mentioned in A'Hearn et al. (1984b), when used with the observed magnitudes provides a slope $S' = (9.9 \pm 1.2)\%/10^3$ Å for the red-end (6400-7900 Å) and $S' = (13.5 \pm 1.5)\%/10^3$ Å for the blue-end (4200 - 5500 Å). The observed average slope at the red end is consistent with the values reported by Lin et al. (2020a) [$S' = 9.2\%/10^3$Å], de León et al. (2020) [$S' = (10 \pm 1)\%/10^3$Å], Kareta et al. (2020) [$S' = 11\%/10^3$Å] and Hui et al. (2020) [$S' = (10.6 \pm 1.4)\%/10^3$Å]. These values of spectral slope of 2I/Borisov suggests that the dust composition present in the cometary coma could be similar to those observed in the D-type asteroids (Licandro et al., 2018), a suggestion first proposed by de León et al. (2019) from their spectroscopic observations of 2I/Borisov. The observed slope at the blue end cannot be compared with the values reported through spectroscopy, since the magnitudes measured using the broad band filters, *B & V*, would be largely affected by the emissions from CN and C_2 respectively. The dust-gas ratio, as shown in Table.7.2 is also similar to the dust-gas ratio of carbon chain depleted Solar system comets (A'Hearn et al., 1995). These are clear indications of the similarity in dust composition of 2I/Borisov with Solar system comets implying a high possibility of the comet formation process similar to Solar system happening in other stellar systems.

7.4.2.2 Absolute magnitude and effective scattering cross section

The apparent magnitude is a function of the heliocentric distance, geocentric distance and the phase angle at the time of observation. Hence, the absolute magnitude (H), which corresponds to the magnitude of the comet at a heliocentric and geocentric distance of 1 AU and a phase angle of 0°, given by

$$H = m - 5log(r_H\Delta) + 2.5log[\phi(\alpha)], \tag{7.1}$$

was computed. Here m is the apparent magnitude in the respective filter, r_H is the heliocentric distance, Δ is the geocentric distance and $\phi(\alpha)$ is the phase function[2] corresponding to the phase angle at the time of observation, as defined in Schleicher & Bair (2011). The R band absolute magnitude can be used to compute the effective scattering cross section in order to investigate the nature of activity in the comet. The effective scattering cross section (C_e) is computed using the following equation;

$$C_e = \frac{\pi r_0^2}{p} 10^{0.4[m_{\odot,R} - H_R]}, \tag{7.2}$$

where r_0 is the mean Earth-Sun distance in Km, p is the geometric albedo of the cometary dust and $m_{\odot,R}$ is the solar apparent magnitude in the R band. Using the values of $r_0 = 1.5 \times 10^8$ Km and $m_{\odot,R} = -26.97$ from Willmer (2018), the above equation reduces to $C_e = (1.15 \times 10^6/p) \times 10^{-(0.4H_R)}$. For this work, the albedo (p) of the comet

[2]Composite Dust Phase Function for Comets https://asteroid.lowell.edu/comet/dustphaseHM_table.txt

was chosen as 0.1, typical for comet dust (Zubko et al., 2017), as used in Jewitt & Luu (2019), Hui et al. (2020) and Bolin et al. (2020). Figure.7.7 depicts the decreasing trend in the scattering cross section as a function of days in the year 2019. The grey dashed line at 342nd day represents the perihelion of the comet (8/12/2019) and the solid dashed line represents a linear least-squares fit, having a best fit slope $d(C_e)/dt = -1.77 \pm 0.22$ Km^2 d^{-1}. A mean nuclear radius (r) can be computed for $C_e = 123\ Km^2$ as $r \leq 3.1$ Km. This value, in close agreement with the sizes reported by other groups (Fitzsimmons et al., 2019; de León et al., 2020; Jewitt & Luu, 2019), can only be considered as an upper limit since the photometric aperture used is highly influenced by the dust in the coma. For comparison, the variation in scattering cross section, when the comet was in bound, reported by Jewitt & Luu (2019), is also included in Figure.7.7, where an increasing trend is observed. As per the variation of cross section with heliocentric distance reported by Bolin et al. (2020), the cross section is seen to be increasing till the day when 2I crossed the water-ice line at 2.5 AU and decreasing later on. Clubbing the short range trends reported in Jewitt & Luu (2019) (before 2I crossed the water-ice line) and in this work (after 2I crossed the water-ice line) along with the larger range trend reported in Bolin et al. (2020), it is clear that there was a steady increase in the scattering cross section till the water-ice line beyond which it decreased systematically. This observation is not in agreement with the variation in scattering cross section reported by Hui et al. (2020), where the cross section is seen to be continuously reducing.

Further, making use of the rate of change in effective cross section, the rate of dust production can be calculated as,

$$\frac{dM}{dt} = \frac{4}{3}\rho\bar{a}\frac{d(C_e)}{dt}, \tag{7.3}$$

where ρ is the particle density, $\bar{a}$ is the mean particle size. In this work we have accepted the values of $\rho = 1g/cm^3$ (Jewitt & Luu, 2019) and $\bar{a} = 100\ \mu m$ (Jewitt & Luu, 2019; Hui et al., 2020). Substituting these values, we get the average net mass loss rate $dM/dt = -2.74 \pm 0.34\ kg\ s^{-1}$. This value depicts the rate of change in dust mass over the observed period. The value is negative since the dust produced from the comet is not able to compensate for the dust lost from the photometric aperture ($\rho \sim 10^4$ Km), implying that the absolute amount of dust production is reducing over the time period,

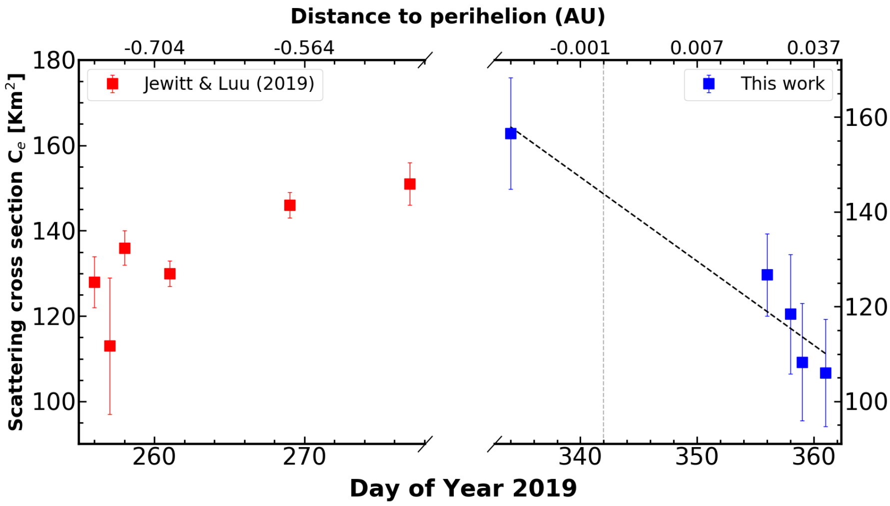

Figure 7.7: Variation of scattering cross section, computed using equation 7.2 as a function of time, expressed as Day of Year 2019, with Day 1 being January 1 2019. The top-axis is labelled with the distance to perihelion. The black dashed line is the best linear least-squares fit having a gradient -1.77 ± 0.22 Km^2/day. The vertical grey dashed line represents the perihelion of the comet. The red points are the scattering cross section as reported by Jewitt & Luu (2019) while the comet was approaching perihelion.

resulting in the comet getting fainter.

7.4.2.3 Connecting Afρ, dust production rate and sublimation flux

As mentioned in Cremonese et al. (2020), the following equation,

$$Af\rho = \frac{3AQ_d}{\rho v_d s_0}, \tag{7.4}$$

where A is the geometric albedo, v_d is the dust ejection velocity, ρ is the particle density and s_0 is the average particle size, can be used to convert the observed $Af\rho$ (in meter) (see Section B.1) into the dust production rate (Q_d). Using the same values for the parameters, as used in the previous section, we get a relation, $Q_d = 3.3v_d(Af\rho)$. Accepting the value of dust ejection velocity as $v_d \sim 8$ m s^{-1} (for epochs close to perihelion as reported by Hui et al., 2020), using Afρ values for V band, we obtain a dust production rate, $Q_d \sim 30$ kg s^{-1}. This absolute value of dust production rate is in agreement to the values reported in Cremonese et al. (2020), Jewitt et al. (2020b) and Kim et al. (2020). Considering this dust to be produced by water-ice sublimation, the patch of area supplying this dust can be computed as $A = Q_d/f_s$, where f_s is the specific rate of mass sublimation flux at equilibrium. According to Jewitt et al. (2015), the specific rate of mass sublimation flux at equilibrium, f_s $(Kg\ m^{-2}\ s^{-1})$, for a body at a heliocentric distance R is obtained from the equation,

$$\frac{F_{\odot}(1-A)}{R^2} cos\theta = \varepsilon\sigma T^4 + L(T) f_s, \tag{7.5}$$

where $F_{\odot}$ is the solar constant, A is the albedo, ε is the emissivity and $L(T)$ is the latent heat of sublimation of ice at temperature T. For the comet 2I/Borisov at 2.7 AU, Jewitt & Luu (2019) obtains $f_s = 4 \times 10^{-5}$ kg m^{-2} s^{-1}. Considering the change in temperature from 2.7 to 2.013 AU to be only $\Delta T \ \sim 30K$ (Henning & Weidlich, 1988), the value for latent heat of sublimation of water ice does not change significantly. Hence from Equation. 7.5, for the current work, we obtain the specific rate of mass sublimation flux to be $f_s = 7.2 \ \times \ 10^{-5}$ kg m^{-2} s^{-1}. Inserting this value in the above defined relation for area, provides $A = 0.4$ Km^2, which is equal to the surface area of a sphere of radius $r = 0.18$ Km. The computed nuclear radius is in good agreement with the lower limits reported in observations using the Neil Gehrels-Swift Observatory's Ultraviolet/Optical Telescope (Xing et al., 2020) and the Hubble Space Telescope (Jewitt et al., 2020a).

Assuming that the empirical relation mentioned in Jorda et al. (2008) holds for this interstellar comet, we can compute the water production rate from the visual V band magnitude (reduced to a geocentric distance of 1 AU). Using the observed reduced magnitudes, the expected water production rates (Q(H_2O)) for 30th November and 22nd December 2019 are $(9.7 \pm 0.9) \times 10^{26}$ molec/s and $(7 \pm 0.8) \times 10^{26}$ molec/s respectively. Even though the expected water production rate for 30th November is consistent, within uncertainties, with the observed rate reported by Xing et al. (2020) for 1st December, their reported rate on 21st December is much lower than expected from our observations for 22nd December. Emphasising on the fact that the empirical relation cannot be used to get precise measurements of water production rates, but only for order of magnitude estimates, we would like to point out that, such an unexpected drastic decrease in water production rate may be due to the heterogeneous composition of the nucleus, as discussed earlier, along with the low abundance of H_2O, uncommon in Solar system comets, as reported in Bodewits et al. (2020).

7.4.3 Conclusions

In this chapter we present the optical spectroscopic and imaging observations of the interstellar comet 2I/Borisov, before and after perihelion, using the 2-m HCT, Hanle and MIRO, 1.2 m Mt.Abu telescopes. Spectroscopic study shows clear emissions from CN, C_2 and C_3 pre and post perihelion and detects a drop in production rate ratio, $Q(C_2)/Q(CN)$ post perihelion. Imaging study reveals a systematically reducing $Af\rho$ and effective cross section, using which a possible size range of the nucleus has been computed. Using these observational results, we arrive at the following conclusions:

1. The computation of production rates of molecules CN, C_2 and C_3 shows an increase, comparable to the observations by other groups, as the comet approached perihelion with an asymmetry in the emission observed post perihelion.

2. The low value of the production rate ratio, $Q(C_2)/Q(CN)$, implies that the comet is depleted in carbon-chain molecules. The ratio had increased as the comet moved closer to perihelion, making it a moderately depleted one, with a later decrease in the ratio after perihelion passage.

3. We infer a chemical heterogeneity in the comet surface due to which there was a drastic surge in the C_2 emissions as the comet approached perihelion. We also infer that an initially unexposed surface of the comet would have been exposed to solar radiation post perihelion resulting in the substantial increase in the production rates of CN and C_3.

4. The $Af\rho$ values computed from the imaging observations, and hence the dust-to-gas ratio, are consistent with the numbers observed for Solar system comets, depleted in carbon-chain molecules. This may be an indication that the parent stellar system of 2I/Borisov would have undergone a formation process somewhat

similar to that of the Solar system.

5. The optical colours of the comet, *(B-V)* = 0.80 ± 0.05, *(V-R)* = 0.49 ± 0.04, *(R-I)* = 0.53 ± 0.03 *(B-R)* = 1.29 ± 0.06, are slightly redder than Solar and similar to the mean colour of large number of comets of our Solar system.

6. The water production rate computed using an empirical formula considering the V band magnitude, was found to match the rate reported before perihelion, but failed to match the rate reported after perihelion, due to a drastic drop in the observed water production rate. This maybe due to the fact that the empirical relation (only to get an order of magnitude estimate) is defined for Solar system comets and not applicable to 2I/Borisov, an interstellar comet with very low abundance in H_2O.

7. The possible size of the nucleus was deduced to be $0.18 \leq r \leq 3.1$ Km. This range is in very good agreement with the sizes reported by other groups.

8. Considering all the observational evidences, we infer that the comet 2I/Borisov was formed in a proto-stellar system undergoing a very inhomogeneous mixing of various volatile compounds beyond the CO ice line.

Chapter 8

Summary and Future work

8.1 Summary of results

This PhD study encompasses the observational study of a large number of comets belonging to various reservoirs. Multiple observational techniques like low resolution spectroscopy, high resolution spectroscopy, optical imaging and optical imaging polarimetry have been employed to study the different aspects of the comets. In order to ensure the proper utilisation of the data set, reduction and analysis pipelines have been self-scripted in PYTHON. Vast number of trial runs were required in converting the pipelines into a reliable one. During the various stages of this PhD, we have learned a lot regarding the observational and analytic study of minor bodies. In this work, certain comets have been studied individually while certain others have been studied in a collective manner. We were fortunate to have observed and reported the activity of the first Interstellar comet in the history of astronomy. This work has provided enormous experience in the field of observational astronomy as well as scientific data analysis. The conclusions/summary connected to each chapter are presented at the end of respective chapters.

Explicit understandings obtained from the complete data set presented in the thesis, along with comparison over an already available larger cometary database and investigation of certain general aspects are summarised below:

8.1.1 Collective understanding

As mentioned before, a large set of comets have been observed as a part of the thesis work. Hence, this provides us with an opportunity to collectively analyse the heliocentric variation as well as the interdependence of the various computed quantities such as production rates, production rate ratios, dust activity (denoted by Afρ) and dust to gas ratio distinctively for SPCs and LPCs. We also come forward to have a comparative and combined study of our dataset with those available from A'Hearn et al. (1995) and Cochran et al. (2012). The results and conclusions of these studies are given below:

1. The computed results of the production rates and production rate ratios of the major emissions present in the comet, CN, C_2 and C_3, for distinct epochs of different comets were combined in order to have a collective understanding of the heliocentric variation in these quantities. While Figure.8.1a shows that the variation of observed production rates with heliocentric distance is more evident in SPC than in LPC, Figure.8.1b shows that the production rate ratios are independent of heliocentric distance. Any sort of trend in the heliocentric variation of production rate ratios is evidently absent within our dataset. This is similar to what has been reported by A'Hearn et al. (1995), Cochran et al. (2012) and Langland-Shula & Smith (2011), for completely different datasets. This establishes that these ratios are due to the primordial composition of the comet rather than being influenced by evolutionary effects.

2. Origin of the different emissions detected in the comets still being an open question, analysing the inter dependency of the different molecular production rates, as shown in Figure.8.2, could be vital in the future studies of their photochemistry. Even though the different emissions are supposed to be produced by distinct par-

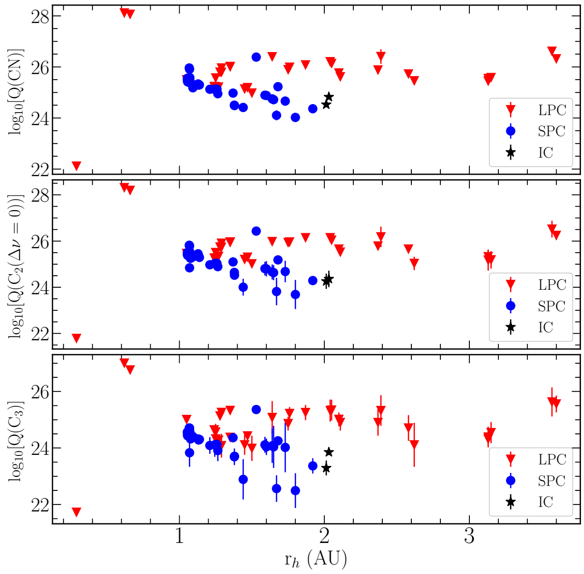

(a) Heliocentric variation observed for the production rates

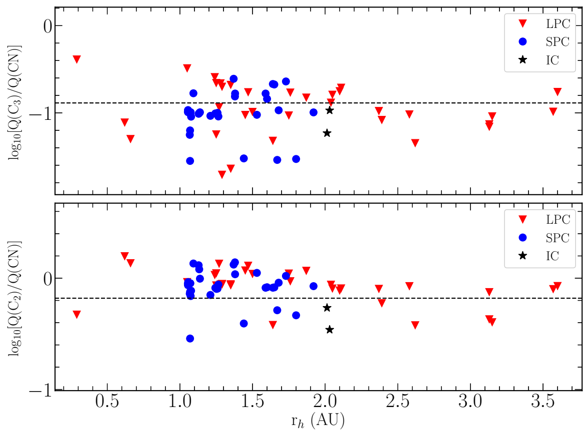

(b) Heliocentric variation observed for the production rate ratios. The black dashed lines in both the panels represents the border line separating the Typical and depleted class of comets.

Figure 8.1: Combined variation in the production rates and production rate ratios of various molecules as a function of heliocentric distance

ent molecules, the strong correlations of the activity observed in these molecules point to some interconnection between their parent molecules. Cochran et al. (2012) also reports similar strong trends for their observed dataset (see Figure.8.3 for comparison of trends in both data base). Interestingly, the activity observed in the first interstellar comet 2I/Borisov also fits well to this observed trend. Such inter dependencies can only be answered by considering the photochemistry in the comet as a whole rather than considering each molecule separately.
From Figures.8.2 and 8.3, it is clear that the activities observed in LPCs span over a larger range (HTCs being a clear part of them) while that of SPC is more or less constrained within a range. Major differences in the formation region of these two classes of comets could be a reason for this differentiation, which is yet to be completely understood.

3. Comets are made up of both dust and gas. Dust activity in comets could begin

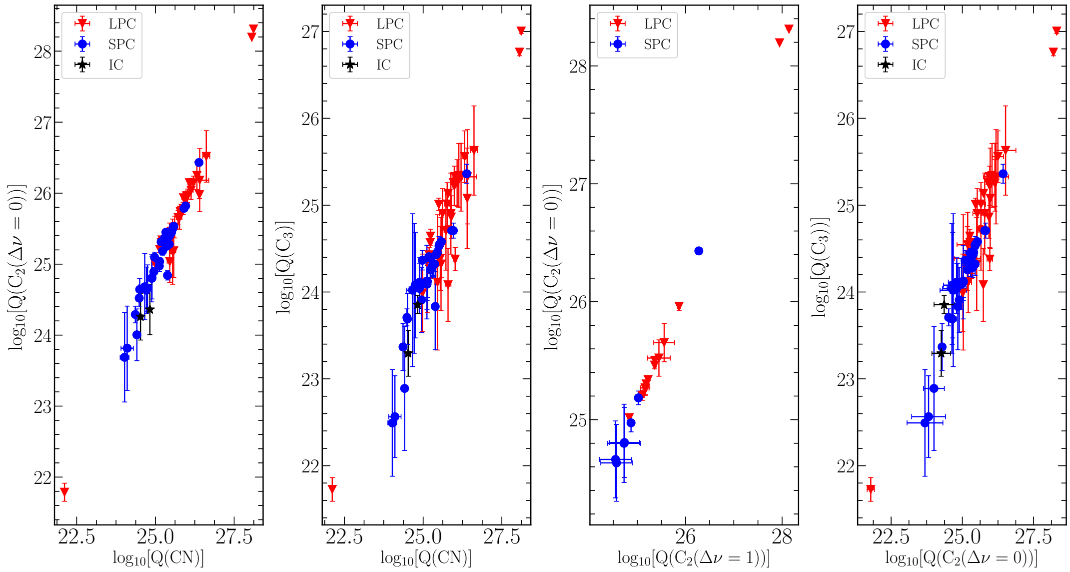

Figure 8.2: Comparison of the dependence of the different molecular production rates with each other

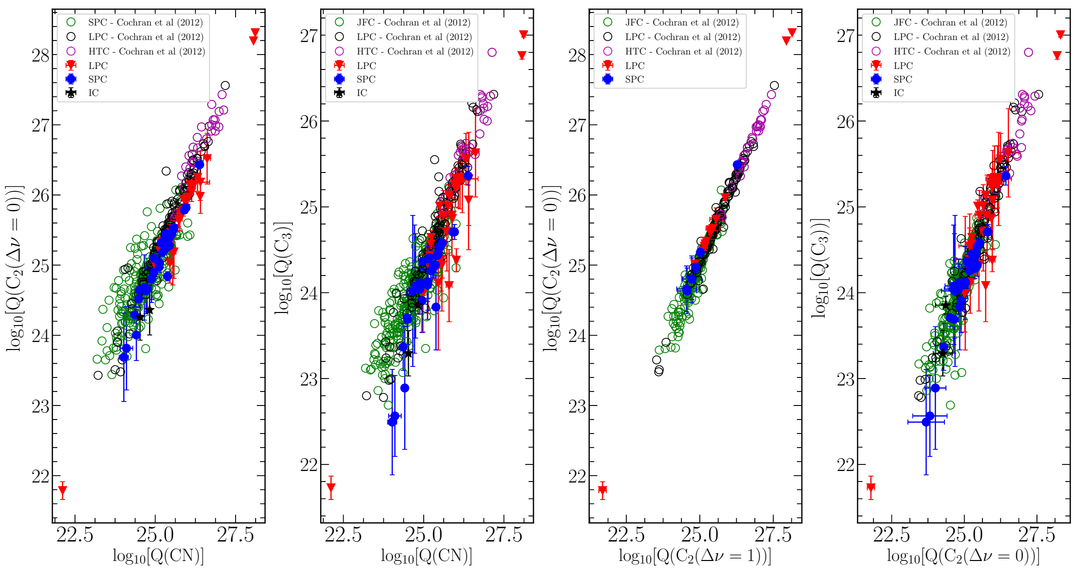

Figure 8.3: Comparison of the trends shown in Figure.8.2 with the data set available in Cochran et al. (2012)

well before the detection of the regular emissions in the optical regime due to other factors such as internal heat or activity in the other range of wavelengths. As the comet approaches perihelion, more volatile material would get sublimated due to the increased Solar heat, increasing the activity in the comet. From Figure.8.4a, it is seen that the dust activity observed in a comet is not strictly dependent on the heliocentric distance. Even though it is expected that the dust to gas ratio does not significantly vary for a particular comet with minimalistic change in heliocentric distance, over a large scale analysis, as shown in Figure.8.4b, it is seen that there is a sharp decline in dust to gas ratio for SPCs while the same in LPCs is more gradual. Points connected to certain comets have been marked as they have been considered to be outliers to the generally observed trend within LPC and SPC. As explained in certain other places in this thesis, this trend is simply because the surface of SPCs are generally more depleted in volatiles due to their multiple apparitions as compared to the fresh unexposed surface of LPCs. Hence, the increase in gaseous activity would be steeper in SPC as they get closer to perihelion (thereby loosing the depleted upper crust). Similar trends in dust to gas ratio have been reported in Langland-Shula & Smith (2011) as well. As seen here, even though the slopes of the trends are different, the ratios observed in both LPCs and SPCs span over similar ranges. Hence, differentiating comets based on dust to gas ratio would not be as apt as the production rate ratio classification.

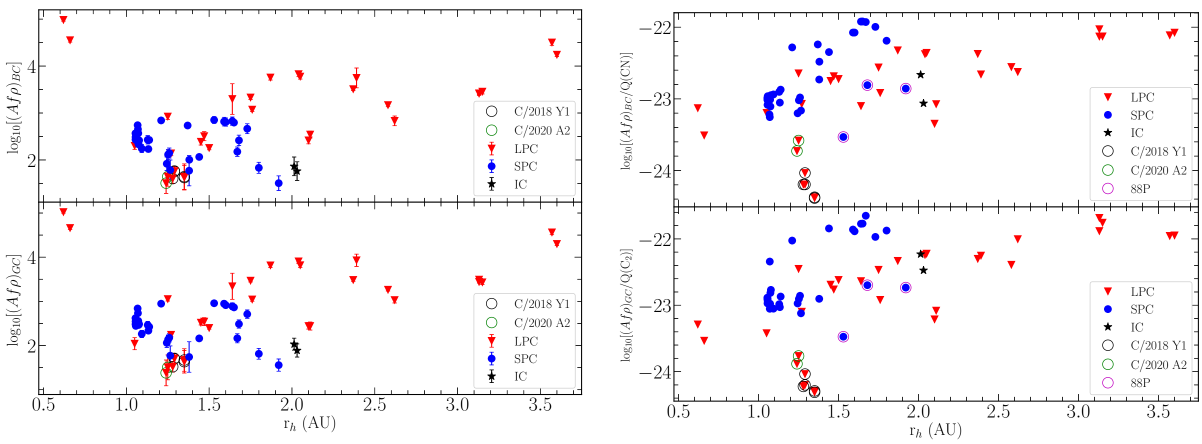

(a) Variation in the observed dust activity. (b) Variation in the observed dust to gas ratio.

Figure 8.4: Combined variation observed in dust activity and dust to gas ratio as a function of heliocentric distance.

4. It has been observed that A'Hearn et al. (1995) and Cochran et al. (2012) have defined, from their own vast observational dataset, the border line for the segregation of Typical and depleted class of comets. Figure.8.5 compares the distribution of the majorly used production rate ratios, $Q(C_2)/Q(CN)$ and $Q(C_3)/Q(CN)$,

reported in both these works, along with our dataset, in the form of a histogram. The limits differentiating the Typical and depleted class of comets, defined by both the works for the two production rate ratios have been marked. More or less, it can be seen that the limits would have been defined based on the peaks observed for the respective dataset.

Figure.8.6 represents the distribution of these production rate ratios for the combined dataset of the current work and the other two literature mentioned above. In both the cases, in order to avoid the effect of observational bias of certain comets on the total distribution, the average of the reported production rate ratios for a each comet has been used, assuming the ratios would not have changed drastically over the epochs. If the peak in the distribution is a factor deciding the limits for the classification, it is clear from Figure.8.6 that the limits deciding the class of comet based on Q(C_2)/Q(CN) requires a bit of refinement. It is necessary to have a complete dataset of activities reported for all the comets observed till date and look at it in a collective manner to fix the limits that can better classify the compositional class of the comet.

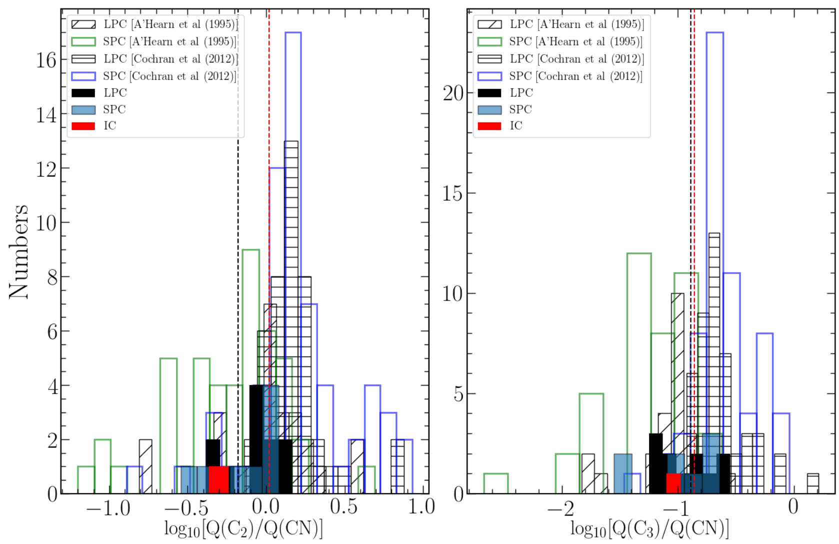

Figure 8.5: Separate histogram comparing the distribution of the comets observed in the current work and few other works for the two majorly used production rate ratios. The red dashed line represents the limit defined by Cochran et al. (2012) while the black dashed represents that of A'Hearn et al. (1995).

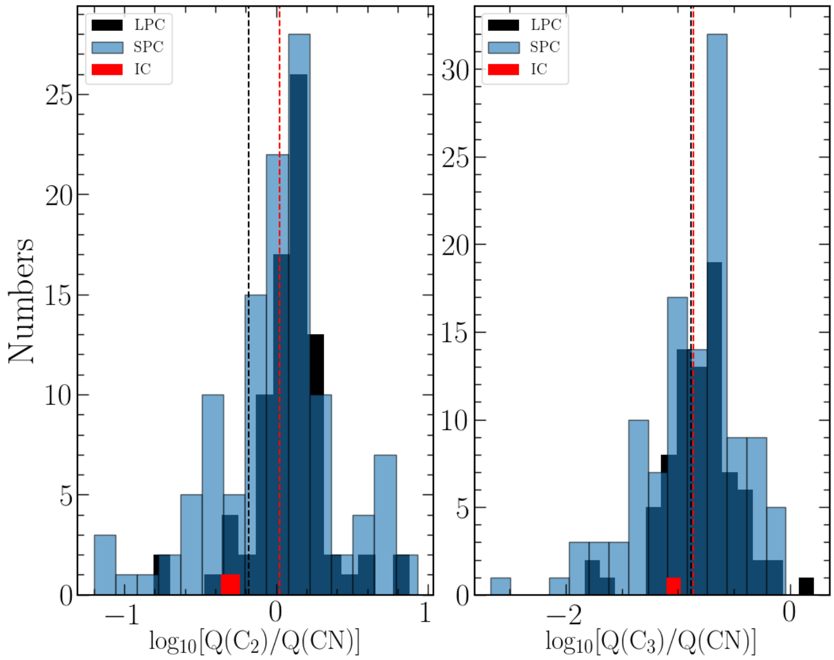

Figure 8.6: Histogram representing the combined dataset presented in Figure.8.5 illustrating the distribution of the two majorly used production rate ratios. The red dashed line represents the limit defined by Cochran et al. (2012) while the black dashed represents that of A'Hearn et al. (1995).

8.1.2 Non-Detection of ${N_2}^+$ as a mere observational constrain

The Proto-solar nebula is thought to have a large abundance in molecular nitrogen. If so, among H_2O, CO and H_2O in comets, N_2 should have been present in large amount. However, the presence of N_2 have been sparsely detected in comets from ground based observations (eg., Lutz et al., 1993). Either there is a mystery behind the absence of N_2 in comets or a reason for them not being detected. As mentioned in Section.2.3.1, our analysis method extracts spectra with fixed apertures along the long slit. Aravind et al. (2022) explains the construction of a full disk spectrum from a combination of these individual spectra. Hence, any minor emissions present in regions close to the nucleus would be suppressed by the other dominant gas and dust emissions in the full disk spectrum. Therefore, the presence of N_2 is usually observed from the detection of N_2^+ emissions in the ion tail. The ions which are formed close to the nucleus and later blown away into the ion tails are difficult to be detected within the coma due to the other dominant emissions. These emissions can be probed by analysing the spectrum extracted close to the photocentre with a seeing limited aperture. But, for comets at a relatively larger geocentric distance, spectrum extracted for the seeing limited aperture would itself correspond to a physical distance at the nucleus which would be dominated by the other strong emissions.

The current apparition of comet 46P was one such possibility of analysing the spectra extracted at locations close to the photocentre. The spectra obtained for epochs between 2018-11-28 and 2018-12-15 have very high SNR so that any detected peaks are well above the noise. Figure.8.7a illustrates the spectra of 46P observed on two different, blown up in the region of CN emission. As seen, similar to the detection reported in Lutz et al. (1993), there are doublet emissions at ~3914 Å which cannot be ascribed to any emissions other than N_2^+.

Similarly, comet C/2020 F3 which had a close approach to Earth is another candidate in which the presence of these emissions can be checked close to the nucleus due to the very high SNR of the spectrum. As shown in Figure.8.7b, even though the detection are not as evident as in 46P, minute features (doublets) are seen at regions around 3914 Å. At the same time, Lin et al. (2020b) have reported the detection of a Sodium tail in the comet's spectra observed on the same dates. Only a similar analysis of a spectrum acquired from a space observatory can resolve further as the seeing limited aperture would be highly dominated by the other strong emissions owing to the observed activity in the comet.

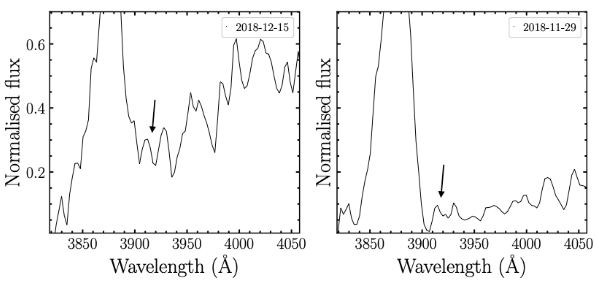

(a) 46P observed on two different epochs.

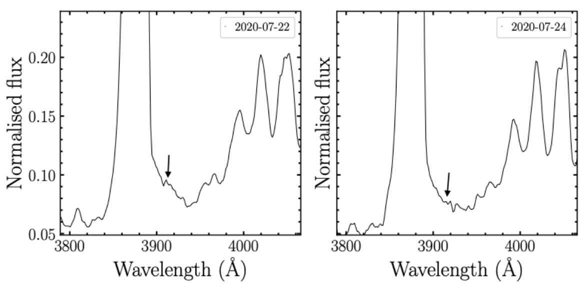

(b) F3 observed on two different epochs.

Figure 8.7: Comparison of the spectra extracted close to the nucleus for comets 46P and C/2020 F3 for CN region. The arrow marks the plausible detection of $N2^+$

8.1.3 Analysing the currently available Narrow band filter profiles.

The emission bands present in the comets are best understood through spectroscopic observations and modelling. The narrow band filter bands explained in 2.4 are defined upon careful analysis of these emission profiles. There is always room for improvement or improvisation in any system. In this work, we have used the low resolution spectrum of a number of bright comets that we observed to analyse the need for improvement in any of the HB filter profiles or the addition of a new filter corresponding to an emission which can help in the better understanding of the comet. With major comet missions like 'Comet Interceptor' coming up (Jones et al., 2022), such regular analysis and understanding of the cometary emissions and available filter profiles can prove to be critical. Figure.8.8 illustrates the spectra of a few comets overlaid with the bandpass of the narrow band filters available with us.

It is seen that the CN, C_2 and C_3 filters perform upto the mark for isolating and studying these emissions. Even though it is not clear, there is a chance that the BC and GC continuum filters can be contaminated from certain feeble emissions. Analysing the optical spectrum of different comets, we feel that filters dedicated to observe the NH_2(0-10-0) (5675 - 5775 Å) and NH_2(0-9-0) (5960 - 6050 Å) emission can be a major addition to observe an emission arising from regions very close to the nucleus. Proper understanding of the minute C_2 contamination in these regions can help in an accurate estimation of the activity in NH_2, which could be used to determine the ammonia composition in the comet. However, it is clear that spectroscopy is necessary to understand the general characteristics of a comet's emission before blindly observing them in the available filters.

8.2 Implication of the current work

It has been known for a long time that every comet is unique. Analysing the activity during every apparition of an already well studied SPC can also improve your understanding of the composition of the object. The results presented in this thesis brings out

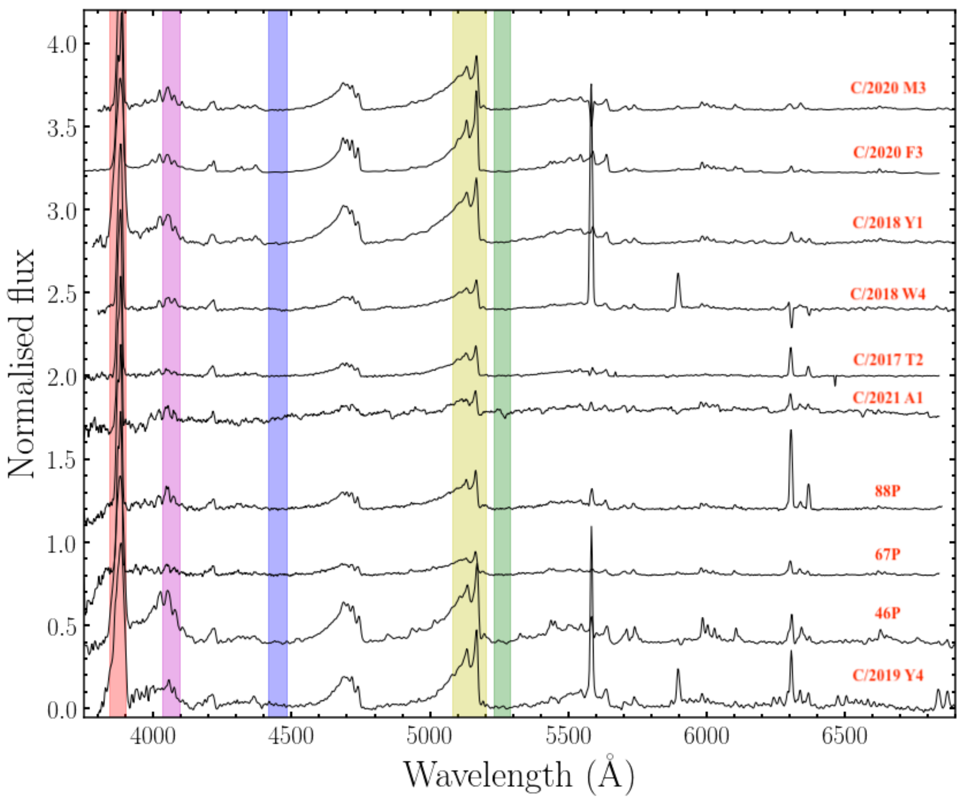

Figure 8.8: Comparison of optical spectra of different comets with the transmission bands pass of the available narrow band filters. The red, magenta, blue, yellow and green shaded regions corresponds to the bandwidth (fwhm) of CN, C_3, BC, C_2 and GC narrow band filters.

the importance of employment of multiple observational techniques on a single object to analyse different aspects of the comet. This work also exhibit the importance of low resolution spectroscopic observation of a comet, be it for a single epoch. Engaging bigger telescopes for similar observations for a larger fraction of all the detectable comets would help in getting a deeper understanding of the uniqueness of each cometary body and hence aid in better interpretation of the formation and distribution of the cometary bodies in the Solar system. A few of the major implications acquired from the current work are:

- As observed in comets 156P, 67P, 260P and C/2021 A1, there could be dust jets present in a comet's coma seen to have differences in Afρ profiles and vice versa. From the current observations, it is also seen that these dust jets can cause a distinction in the dust population within the coma resulting in variation of the observed polarisation (localised or radial) or colour. Combining the observed polarimetric data with different dust models can provide information regarding the physical and compositional characteristics of the dust present in the comet. Hence, simultaneous spectroscopic, imaging and polarimetric measurements are vital in having a wider understanding of the various features observed in comets.

- Long term observation of a comet is vital in analysing the activity in it as a function of distance from perihelion. Different comets can show different behaviours based on the composition and geometry. Long slit optical low resolution spectroscopy is efficient in obtaining a detailed understanding of the range of emissions occurring in the optical regime for each epoch. However, for historic apparitions similar to that of 46P, there could be direct effects of localised strong internal molecular jets which could affect the day to day computation of production rates. Keeping in mind that only a major variation in the production rate ratios along the orbit could point to a heterogeneous nucleus, comets 46P and C/2017 T2 are seen to have nearly homogeneous nucleus.
- Even though long term monitoring of comets are suggested, only a few comets would have availability over large range of heliocentric distance. Hence, spectroscopic observation of comets, even for one epoch, is vital in having a general idea regarding the composition of the comet. Similar observations for LPCs which will not be returning to the inner Solar system during the current lifetime is essential in adding points to the currently available comet dataset to improve the collective understanding of the activity in comets.
- Low resolution spectroscopy is effective in having a general understanding of the relative chemical abundance the comet but, to a large extend, different emissions are blended among each other. A higher resolution can help in separating these bands to have a deeper analysis of the various emissions present. The HESP instrument mounted on HCT is highly capable of having high resolution spectroscopic observation of comets with excessive scientific importance. The availability of two input fibers in HESP also favours the comparison of emissions occurring at two different locations in the coma.
- Various theories have been proposed regarding the existence of Interstellar comets.

It was not until 2019, the first comet belonging to this category was detected. From the spectroscopic observation of this comet, we were able to imply the similarity in composition of an interstellar comet to that of Solar system comets. The observed activity in the interstellar comet is seen to fit well with those observed in Solar system comets. This calls for the requirement of a combined understanding of the photochemistry occurring inside the coma.

8.3 Future works

The large scale survey of comets originating from various reservoirs using different observational techniques limits us from having a detailed analysis of the dataset available for each comet. The available dataset can be best utilised to have a better understanding of the activity of the individual comets at distinct epochs.

Specific ideas for the future work are listed below:

1. The low resolution spectrum available for the bright comets have to be analysed in detail to study the various emissions occurring in them and their variation between epochs. The column density profiles present in these comets will be used to model the parent and daughter scale lengths of each molecular species.

2. The high resolution spectroscopic technique will be used to study the reason for the variation in relative strength of emission lines between epochs as well as between the two fibers.

3. The peculiar long period comet, C/2017 K2, yet to have its perihelion in December 2022, have been followed in photometry for a very long time. We also have obtained imaging data in UV regime with the UVIT instrument onboard AstroSat. These dataset along with future data (spectrum and imaging) will be used to have a detailed analysis of the evolution of the comet's activity.

4. From this thesis work, it has been shown how important it is to get data for almost all available comets. Hence, the larger telescope facilities in the country, HCT, DOT and the upcoming PRL 2.5 m telescope, will be efficiently used to

predominantly observe a larger fraction of all the observable comets in different observational techniques.

5. The importance of broadband imaging polarimetry been discussed and portrayed in this thesis, efforts will be made to obtain spectro-polarimetric data for bright comets to analyse the polarisation present in the molecular emission bands.

It has been mentioned in different parts of the thesis that the fraction of comets observed to the total number is very small. Hence, an ever evolving database of the observed comets are required in order to have an improved understanding of these mysterious icy bodies. Even though the exact origin of the cometary bodies in the proto-Solar nebula is not clearly understood, independent and combined studies illustrated in this thesis point at a clear segregation between the SPCs and LPCs. A global database of the activities detected in all the observed comets would majorly help in having a collective/comprehensive picture of objects belonging to different reservoirs. Along with this, efforts will be made to model the parent and daughter scale lengths of different comets to search for any dependency on the origin of these bodies.
Modelling and laboratory studies of cometary ices that have been improving at very fast pace will be incorporated efficiently along with observational studies in an effort to understand in depth the pristine ices present in these bodies and their chemistry, which cannot be probed otherwise.

This page was intentionally left blank.

Appendix A

Python routine for spectrum extraction in low resolution spectroscopy

During any sort of large scale data extraction, extensive manual work can lead to unforced errors. These inevitable errors could lead to the computation of a wrong final result. When numerous comets are analysed and compared, it is to be made sure that they were extracted in an unbiased manner avoiding any possible manual error. Hence, a PYTHON code was scripted in order to extract the spectrum of comets corresponding to any user defined aperture or a series of apertures. The steps incorporated in the code while extracting the spectrum are:

1. Considers spectrum of the standard star and finds the centre in the spatial axis by fitting a Gaussian to the star profile as shown in Figure. A.1
2. In the same manner, the centre of multiple columns across the dispersion axis is computed and a polynomial is fitted to these points so as to produce a trace of the spectrum as shown in Figure.A.2. Figure.A.3 illustrates the final characteristic trace of the instrument, along the dispersion axis, overlaid on the raw spectrum image of a standard star.

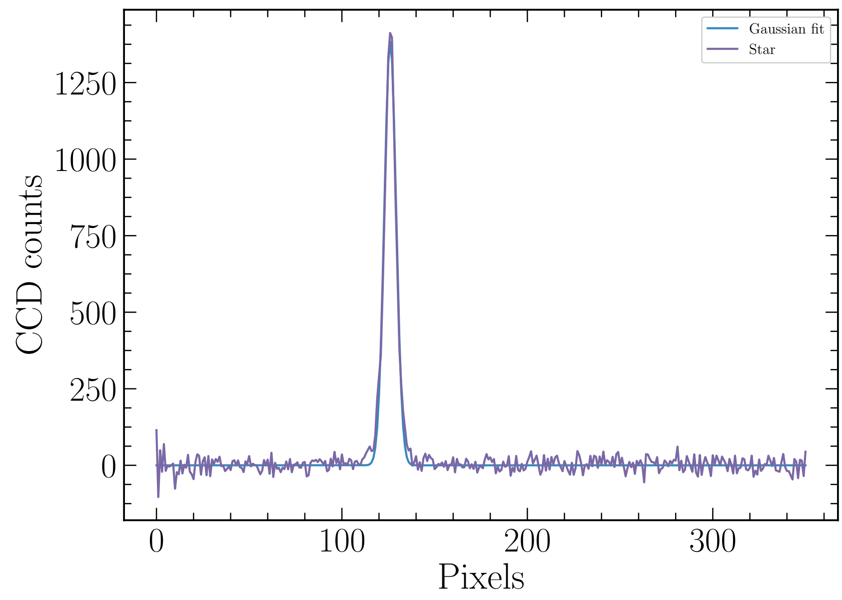

Figure A.1: Illustration of the gaussian fitting to the stellar profile where X axis denotes row number and Y axis denotes the counts in the CCD (across the spatial axis).

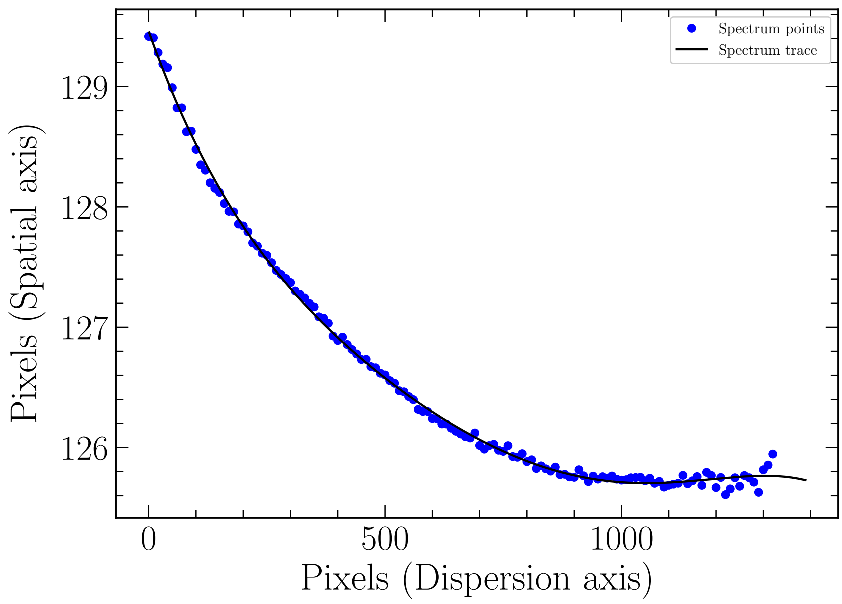

Figure A.2: Illustration of the polynomial fitting to the computed centres where X axis denotes column number and Y axis denotes the row numbers.

3. As a next step, an interactive window (see Figure.A.4) is used to select a possible centre of a column where the intensity of comet is maximum. Using this information, the trace found from standard star frame is scaled to reproduce the trace of the comet spectrum as shown in Figure.A.5.

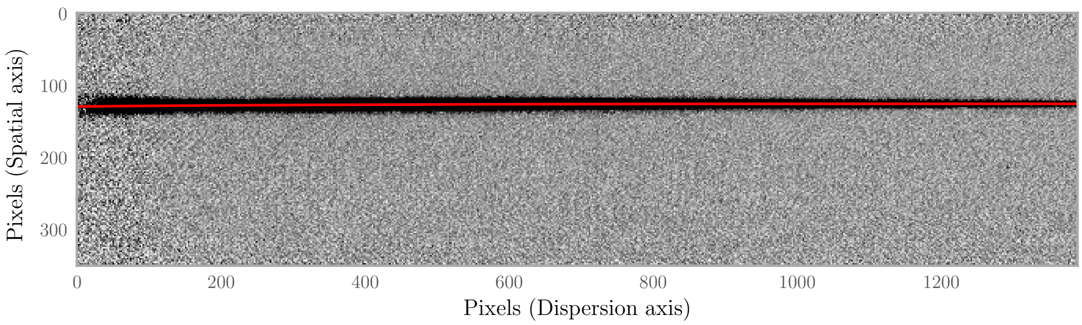

Figure A.3: Illustration of the computed trace along the dispersion axis overlaid on the standard star spectrum.

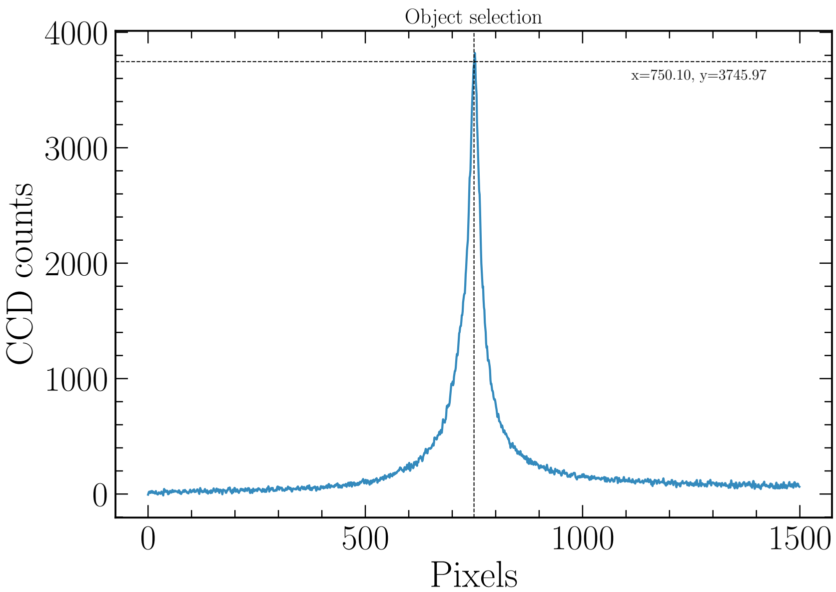

Figure A.4: Illustration of the interactive window used to select the maximum point in the spectrum.

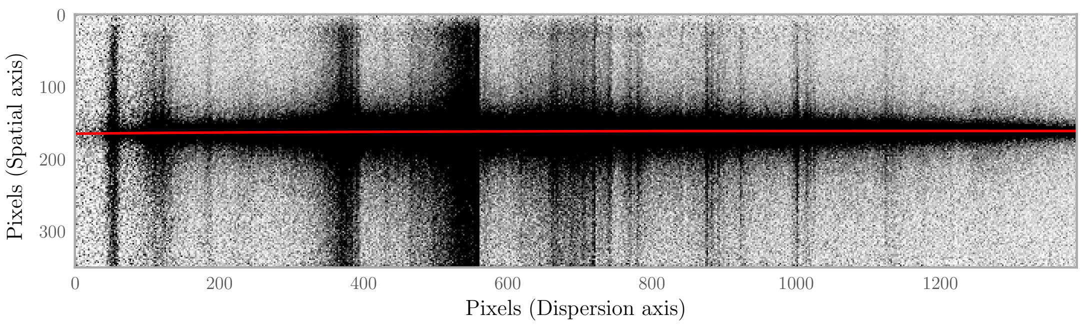

Figure A.5: The trace, previously computed, adjusted to trace the comet spectrum.

4. Once the trace of the comet has been established, the next step is to define apertures according to the users interest (for performing full disk conversion), based

on the comet's flux. Any integer number can be entered for the desired single apertures. Along with the selection of centre in the comet spectrum, in the interactive window, a rough end point should also be clicked, till where the user would want to put apertures. Using these inputs, now the corresponding apertures will be defined and displayed as shown in Figure.A.6. This same method can also be used to defined apertures on the other side of the spectrum so as to have a comparative study of the behaviour of the emissions on both sides of the spatial axis.

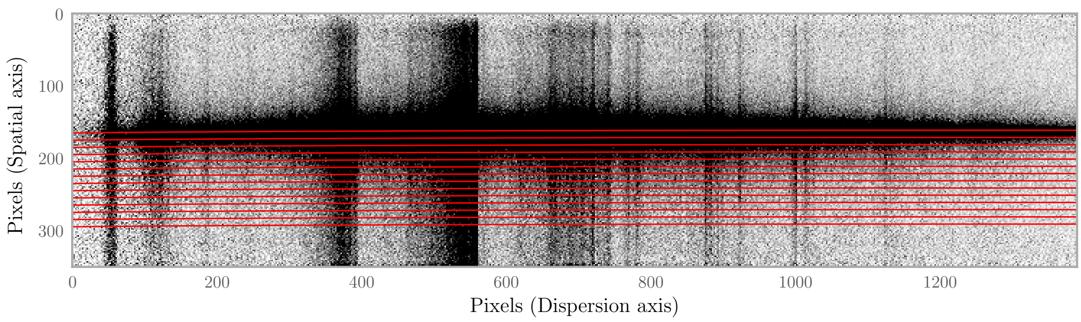

Figure A.6: The multiple apertures displayed till the desired end point, defined by the user

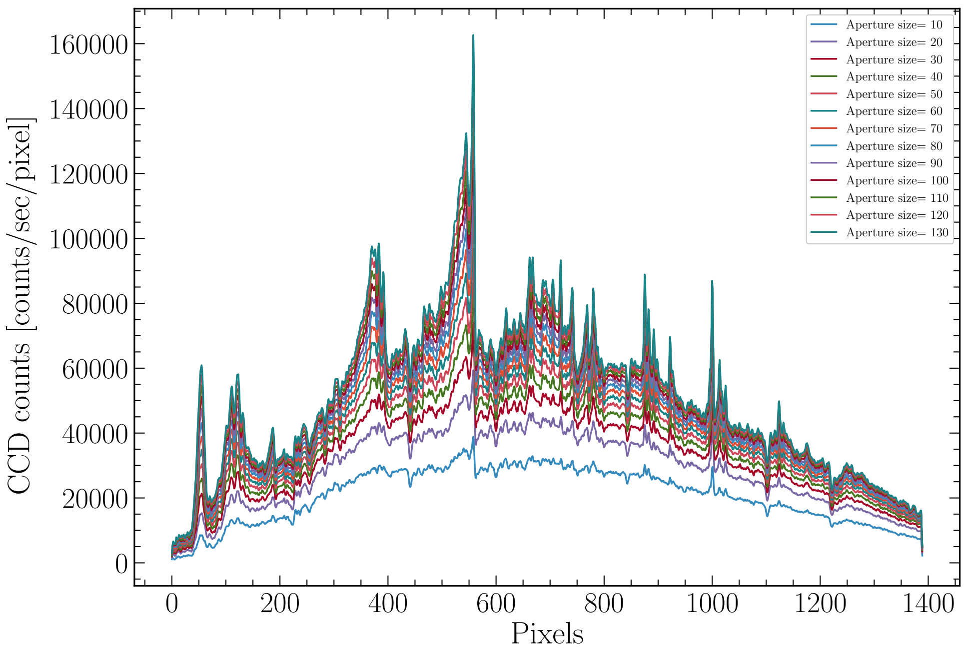

Figure A.7: Multiple spectra extracted corresponding to the apertures defined by the user.

5. As a final step in this code, now the spectra corresponding to the defined multiple apertures will be extracted (see Figure.A.7) and saved as fits file, to be used later for the wavelength calibration and flux calibration. Once these calibrations have been performed, they can be used to get the spectra corresponding to the individual columns of equal width at increasing distance from the photocenter or to get the total full disk flux (explained in the main text).

Previously, all these steps were performed in IRAF, which was time taking. There was also possibilities of more unforced errors since extra care had to be taken while defining the trace for each aperture, making the work more tedious. Now since the comet trace is defined straight from the standard star spectrum, it is very well defined. Also, the code gives the user full control over the size of the aperture to be chosen and the extent of spatial axis to be used to extract spectrum without any manual errors.

This page was intentionally left blank.

Appendix B

Computation of $Af\rho$ and Production rates

B.1 Afρ computation

Since the Afρ values are a proxy to the amount of dust present in the comet, they are computed for wavelength ranges corresponding to dust emission. Blue continuum (BC) and Green continuum (GC) are two such regions defined by Farnham et al. (2000). The parameter is directly measurable using the formula,

$$Af\rho = \frac{(2\Delta r)^2}{\rho}\frac{F_{\text{comet}}}{F_{\text{Sun}}}\frac{1}{S(\theta)}, \tag{B.1}$$

where Δ is the geocentric distance in kilometres, ρ the aperture size in kilometres, r is the heliocentric distance in AU, and F_{comet} is the observed cometary flux within the bandpass of the filter. F_{Sun} is the incident Solar flux at 1 AU integrated over the

bandpass of the filter and $S(\theta)$ is the phase function[1] corresponding to the phase angle at the time of observation, as defined in Schleicher & Bair (2011).
In imaging, the flux present in the continuum regions are directly observed by using the BC and GC filters. Here in spectroscopy, the data available is the total spectrum of the comet corresponding to increasing apertures and the transmission profile of the narrow band filters. Now, to obtain the cometary flux within the band pass of the narrow band filter, the spectrum of the comet was initially convolved with the transmission profile of the filter re-sampled to match the resolution of the instrument. Finally, the resulting spectrum was averaged over the bandpass of the narrow band filter as given by the equation

$$F_{\text{comet}} = \frac{\int_{\lambda_1}^{\lambda_2} I(\lambda)S(\lambda)d\lambda}{\int_{\lambda_1}^{\lambda_2} S(\lambda)d\lambda}. \tag{B.2}$$

Here, λ_1 and λ_2 are the wavelength range of the bandpass filter used, I(λ) is the flux as a function of wavelength and S(λ) is the transmission profile of the filter. The solar flux at 1 AU for the respective filter was obtained by using the magnitudes of the solar analogue stars given in Farnham et al. (2000). In this manner, Afρ corresponding to each increasing aperture in the required wavelength region can be obtained. The Afρ characteristic profile built like this provides information regarding the type of dust outflow present in the comet, steady state outflow or non-steady state outflow.
While using the imaging data in R and I filter, aperture photometry is performed to compute the apparent magnitude of the comet, as explained in Section.2.3.3, which is then used to determine the $Af\rho$. Apertures of increasing radius can be chosen to obtain the profile of $Af\rho$ similar to what is obtained while using spectroscopic data. Standard error in Afρ is computed by the propagation of errors present in the parameters mentioned in Equation.B.1.

[1] Composite Dust Phase Function for Comets: https://asteroid.lowell.edu/comet/dustphaseHM_table.txt

B.2 Haser model and computation of production rates

Optical spectrum can be obtained for both bright comets and faint comets by varying the exposure time. The advantage of bright comets is that the spectra can be extracted for fixed apertures at different distances from the photocentre to study the spatial variation of the emissions while only a single spectrum with a large enough aperture is possible for fainter comets. The computation of production rates of various molecular emissions differ slightly in both cases.

In the case of bright comets, strong emissions from $CN(\Delta\nu = 0)$, $C_3(\lambda 4050\text{Å})$, $C_2(\Delta\nu = +1)$ and $C_2(\Delta\nu = 0)$ can be observed. In order to compute the production rates of the various molecules detected, the spectra extracted to one side of the spatial axis with equal aperture size at different distances from the photocentre are used. The formula,

$$N(y) = \frac{4\pi}{g}\frac{F(y)}{\Omega}, \tag{B.3}$$

gives the column density (molecules per centimetre cube) corresponding to the flux (F) within the wavelength range of the molecule (defined by Langland-Shula & Smith (2011)) extracted from an aperture, at a distance y from the photocentre, subtending a solid angle Ω. The Solid angle, in steradians, is computed as the product of the slit width and the aperture size in radians. Here, g is the fluorescence efficiency (ergs per molecule per second). g at 1 AU for molecules C_2 and C_3 are taken from A'Hearn et al. (1995) and are scaled to r_h^{-2} in order to obtain the appropriate values to be used at the corresponding heliocentric distance (r_h). Schleicher (2010) have tabulated the g-factor of CN for different heliocentric distances and velocities. A double interpolation is performed on the provided table to obtain the exact g values for the corresponding heliocentric distance and velocity at the time of observation. Haser model (Haser, 1957) assumes a spherically symmetric coma with uniform outflow of gas to compute the total production rate for each molecular emission.

Langland-Shula & Smith (2011) and Venkataramani et al. (2016) have detailed a method to fit the Haser model to the observed column density profile in order to compute the production rate (molecules per second) of the corresponding molecule. The production rate Q, in molecules per second, is estimated using the minimum chi-square estimation between the observed column density and the theoretical column density computed using the equation,

$$N(y) = \frac{Q}{2\pi v_{\text{flow}}} \frac{\beta_0}{\beta_1 - \beta_0} \int_0^{\infty} \frac{1}{y^2 + z^2} \left(e^{-\beta_0 \sqrt{y^2+z^2}} - e^{-\beta_1 \sqrt{y^2+z^2}} \right) dz, \tag{B.4}$$

Here, y is the projected distance from the centre of the comet nucleus, v_{flow} is the outflow velocity in centimetre per second, z is in the line-of-sight direction, and β_0 and β_1 are the inverse of the parent and daughter molecule scale lengths in centimetres. The scale lengths of the parent (l_p) and daughter (l_d) molecules were taken from A'Hearn et al. (1995) and were scaled to r_h^2. During the computation of production rates, the most uncertain factor is the outflow velocity of gas and dust from the nucleus. There are various scaling laws which can be incorporated for the computation (Langland-Shula & Smith, 2011; Rosenbush et al., 2020; Whipple, 1978). In our work we adopt the outflow velocity relationship $v_{\text{flow}} = 0.85/\sqrt{r_h}$ as described in Cochran et al. (2012).

In the case of fainter comets where only a single spectrum can be extracted either to one side of the photocentre or centred on the comet, the area under the curve within the wavelength range covering the full emission bands of different molecules, as mentioned in Langland-Shula & Smith (2011), was used to obtain the total flux of the observed emissions. The uncertainties in the flux were obtained from the noise in the parts of the spectrum adjacent to the emission bands. The total number of molecules (N) present in the aperture used was calculated using,

$$N = \frac{4\pi\Delta^2}{g} \times F, \tag{B.5}$$

where g is the fluorescence efficiency, Δ is the geocentric distance and F is the total flux inside the aperture used for extraction. Haser model also provides a factor called the Haser factor which is the ratio of total number of molecules present in the aperture used to the total number of molecules present in the whole coma. The reciprocal of this factor, the Haser correction, can be used to extrapolate the observed flux so as to estimate the molecular abundance in the entire coma. This factor can be computed using the web calculator implemented by Prof. Schleicher on his website(`https://asteroid.lowell.edu/comet/`) for the corresponding aperture radius. Since the Haser factor is derived for a circular aperture, the obtained value is normalised to unit area and then multiplied by the area of the rectangular aperture used (slit width × aperture size). The total number of molecules is then divided by the lifetime of the daughter molecule (τ) to obtain the production rate. The values for g and τ at 1 AU were taken from A'Hearn et al. (1995) with proper scaling as mentioned above.

This page was intentionally left blank.

References

A'Hearn, M. F. & Cowan, J. J. 1975, Molecular production rates in comet Kohoutek., AJ, 80, 852 [Cited on page 56.]

A'Hearn, M. F. & Cowan, J. J. 1980, Vaporization in Comets - the Icy Grain Halo of Comet West, Moon and Planets, 23, 41 [Cited on pages 160 and 161.]

A'Hearn, M. F., Feaga, L. M., Keller, H. U., et al. 2012, Cometary Volatiles and the Origin of Comets, ApJ, 758, 29 [Cited on pages 28 and 29.]

A'Hearn, M. F., Feldman, P. D., Millis, R. L., & Stewart, A. I. F. 1984a, in Bulletin of the American Astronomical Society, Vol. 16, 638 [Cited on page 160.]

A'Hearn, M. F., Hoban, S., Birch, P. V., et al. 1986, Cyanogen jets in comet Halley, Nature, 324, 649 [Cited on page 161.]

A'Hearn, M. F., Millis, R. C., Schleicher, D. O., Osip, D. J., & Birch, P. V. 1995, The ensemble properties of comets: Results from narrowband photometry of 85 comets, 1976-1992, Icarus, 118, 223 [Cited on pages 4, 17, 21, 29, 56, 73, 84, 89, 90, 91, 92, 93, 98, 101, 102, 103, 104, 157, 159, 160, 163, 165, 172, 175, 176, 177, 193, 194, and 195.]

A'Hearn, M. F., Schleicher, D. G., Millis, R. L., Feldman, P. D., & Thompson, D. T. 1984b, Comet Bowell 1980b, AJ, 89, 579 [Cited on pages 4, 21, 48, 69, 74, and 164.]

A'Hearn, M. F., Thurber, C. H., & Millis, R. L. 1977, Evaporation of ices from Comet West., AJ, 82, 518 [Cited on page 56.]

Aravind, K., Halder, P., Ganesh, S., et al. 2022, Optical observations and dust modelling of comet 156P/Russell-LINEAR, Icarus, 383, 115042 [Cited on pages 24, 31, 77, 103, 126, 128, 129, and 177.]

Arpigny, C. 1964, The resonance-fluorescence excitation of the CO^{+} comet-tail bands of Comet Humason (1961e), Annales d'Astrophysique, 27, 406 [Cited on page 109.]

Bahcall, J. N. 1984, K giants and the total amount of matter near the sun, ApJ, 287, 926 [Cited on page 27.]

Bannister, M. T., Opitom, C., Fitzsimmons, A., et al. 2020, Interstellar comet 2I/Borisov as seen by MUSE: C_2, NH_2 and red CN detections, arXiv e-prints, arXiv:2001.11605 [Cited on pages 154, 156, 158, 159, 160, 161, 162, and 163.]

Bastien, P., Menard, F., & Nadeau, R. 1986, Linear polarization observations of P/Halley., MNRAS , 223, 827 [Cited on page 23.]

Basu, S. & Rana, N. C. 1992, Multiplicity-corrected Mass Function of Main-Sequence Stars in the Solar Neighborhood, ApJ, 393, 373 [Cited on page 27.]

Bauer, J. M., Gicquel, A., Kramer, E., & Meech, K. J. 2021, NEOWISE Observed CO and CO_2 Production Rates of 46P/Wirtanen During the 2018-2019 Apparition, The Planet. Sci. J., 2, 34 [Cited on page 84.]

Belton, M. J. S. & Melosh, J. 2009, Fluidization and multiphase transport of particulate cometary material as an explanation of the smooth terrains and repetitive outbursts on 9P/Tempel 1, Icarus , 200, 280 [Cited on page 28.]

Bessell, M. S. 2005, Standard photometric systems, Annu. Rev. Astron. Astrophys., 43, 293 [Cited on page 41.]

Bhardwaj, A. & Haider, S. A. 2002, Chemistry of O(^{1}D) atoms in the coma: implications for cometary missions, Advances in Space Research, 29, 745 [Cited on page 148.]

Bhardwaj, A. & Raghuram, S. 2012, A Coupled Chemistry-emission Model for Atomic Oxygen Green and Red-doublet Emissions in the Comet C/1996 B2 Hyakutake, ApJ, 748, 13 [Cited on page 148.]

Biesecker, D. A., Lamy, P., St. Cyr, O. C., Llebaria, A., & Howard, R. 1999, in AAS/Division for Planetary Sciences Meeting Abstracts, Vol. 31, AAS/Division for Planetary Sciences Meeting Abstracts #31, 14.04 [Cited on page 117.]

Blackwell, D. E. & Willstrop, R. V. 1957, A study of the monochromatic polarization of Comet Arend-Roland (1956 h), MNRAS , 117, 590 [Cited on page 23.]

Bockelée-Morvan, D., Biver, N., Schambeau, C. A., et al. 2022, Water, hydrogen cyanide, carbon monoxide, and dust production from distant comet 29P/Schwassmann-Wachmann 1, arXiv e-prints, arXiv:2205.11425 [Cited on page 109.]

Bodewits, D., Noonan, J. W., Feldman, P. D., et al. 2020, The carbon monoxide-rich interstellar comet 2I/Borisov, Nature Astronomy, 4, 867 [Cited on pages 160 and 169.]

Bolin, B. T., Lisse, C. M., Kasliwal, M. M., et al. 2020, Characterization of the Nucleus, Morphology, and Activity of Interstellar Comet 2I/Borisov by Optical and Near-infrared GROWTH, Apache Point, IRTF, ZTF, and Keck Observations, AJ, 160, 26 [Cited on pages 164 and 166.]

Brasser, R. & Morbidelli, A. 2013, Oort cloud and Scattered Disc formation during a late dynamical instability in the Solar System, Icarus , 225, 40 [Cited on page 10.]

Bregman, J. D., Witteborn, F. C., Allamandola, L. J., et al. 1987, Airborne and ground-based spectrophotometry of comet P/Halley from 5-13 micrometers, A&A , 187, 616 [Cited on page 23.]

Brown, M. E., Bouchez, A. H., Spinrad, A. H., & Johns-Krull, C. M. 1996, A high-Resolution Catalog of Cometary Emission Lines, AJ, 112, 1197 [Cited on page 133.]

Brownlee, D. 2014, The Stardust Mission: Analyzing Samples from the Edge of the Solar System, Annual Review of Earth and Planetary Sciences, 42, 179 [Cited on page 23.]

Brownlee, D., Tsou, P., Aléon, J., et al. 2006, Comet 81P/Wild 2 Under a Microscope, Science, 314, 1711 [Cited on page 23.]

Cambianica, P., Cremonese, G., Munaretto, G., et al. 2021, A high-spectral-resolution catalog of emission lines in the visible spectrum of comet C/2020 F3 (NEOWISE), A&A , 656, A160 [Cited on pages 51, 121, and 134.]

Cessateur, G., de Keyser, J., Maggiolo, R., et al. 2016, Photochemistry of forbidden oxygen lines in the inner coma of 67P/Churyumov-Gerasimenko, Journal of Geophysical Research (Space Physics), 121, 804 [Cited on pages 148 and 151.]

Ciesla, F. J. & Cuzzi, J. N. 2006, The evolution of the water distribution in a viscous protoplanetary disk, Icarus , 181, 178 [Cited on page 15.]

Cochran, A., Barker, E. S., & Cochran, W. 1980, Spectrophotometric observations of P/Schwassmann-Wachmann 1 during outburst, AJ, 85, 474 [Cited on page 109.]

Cochran, A. L., Barker, E. S., & Gray, C. L. 2012, Thirty years of cometary spectroscopy from McDonald Observatory, Icarus , 218, 144 [Cited on pages 4, 17, 21, 29, 73, 89, 98, 99, 101, 102, 103, 159, 160, 172, 173, 174, 175, 176, 177, and 194.]

Cochran, A. L., Barker, E. S., Ramseyer, T. F., & Storrs, A. D. 1992, The McDonald Observatory faint comet survey: Gas production in 17 comets, Icarus , 98, 151 [Cited on pages 4 and 160.]

Cochran, A. L. & Cochran, W. D. 1991, The first detection of CN and the distribution of CO^+ gas in the coma of Comet P/Schwassmann-Wachman 1, Icarus , 90, 172 [Cited on page 109.]

Cochran, A. L. & Cochran, W. D. 2002, A High Spectral Resolution Atlas of Comet 122P/de Vico, Icarus , 157, 297 [Cited on pages 3, 51, and 134.]

Cochran, A. L., Cochran, W. D., Barker, E. S., & Storrs, A. D. 1991, The development of the CO^+ coma of Comet P/Schwassmann-Wachmann 1, Icarus , 92, 179 [Cited on page 109.]

Cochran, A. L., Levison, H. F., Stern, S. A., & Duncan, M. J. 1995, The Discovery of Halley-sized Kuiper Belt Objects Using the Hubble Space Telescope, ApJ, 455, 342 [Cited on page 12.]

Cochran, A. L., Nelson, T., & McKay, A. J. 2020, What Does It Mean to be a "Depleted" Comet? High Spectral Resolution Observations of the Prototypical Depleted Comet 21P/Giacobini-Zinner from the McDonald Observatory, The Planet. Sci. J., 1, 71 [Cited on pages 99 and 134.]

Cohen, B. A., Swindle, T. D., & Kring, D. A. 2000, Support for the lunar cataclysm hypothesis from lunar meteorite impact melt ages, Science, 290, 1754 [Cited on page 13.]

Combi, M. R. & Fink, U. 1997, A Critical Study of Molecular Photodissociation and CHON Grain Sources for Cometary C_2, ApJ, 484, 879 [Cited on page 161.]

Combi, M. R., Mäkinen, T., Bertaux, J. L., Quémerais, E., & Ferron, S. 2021a, Water Production Rate of C/2020 F3 (NEOWISE) from SOHO/SWAN over Its Active Apparition, ApJ , 907, L38 [Cited on page 121.]

Combi, M. R., Mäkinen, T., Bertaux, J. L., et al. 2020, Comet 41P/Tuttle-Giacobini-Kresak, 45P/Honda-Mrkos-Pajdusakova, and 46P/Wirtanen: Water Production Activity over 21 yr with SOHO/SWAN, The Planet. Sci. J., 1, 72 [Cited on page 84.]

Combi, M. R., Shou, Y., Mäkinen, T., et al. 2021b, Water production rates from SOHO/SWAN observations of six comets: 2017-2020, Icarus , 365, 114509 [Cited on pages 84, 91, and 92.]

Cordiner, M. A., Milam, S. N., Biver, N., et al. 2020, Unusually high CO abundance of the first active interstellar comet, Nature Astronomy, 4, 861 [Cited on page 160.]

Cordiner, M. A., Remijan, A. J., Boissier, J., et al. 2014, Mapping the Release of Volatiles in the Inner Comae of Comets C/2012 F6 (Lemmon) and C/2012 S1 (ISON) Using the Atacama Large Millimeter/Submillimeter Array, ApJ , 792, L2 [Cited on page 17.]

Cremonese, G., Capria, M. T., & de Sanctis, M. C. 2007, Catalog of the emission lines in the visible spectrum of comet 153P/Ikeya-Zhang, A&A , 461, 789 [Cited on page 134.]

Cremonese, G., Fulle, M., Cambianica, P., et al. 2020, Dust Environment Model of the Interstellar Comet 2I/Borisov, ApJ , 893, L12 [Cited on pages 167 and 168.]

Cremonese, G., Huebner, W. F., Rauer, H., & Boice, D. C. 2002, Neutral sodium tails in comets, Advances in Space Research, 29, 1187 [Cited on page 19.]

de León, J., Licandro, J., de la Fuente Marcos, C., et al. 2020, Visible and near-infrared observations of interstellar comet 2I/Borisov with the 10.4-m GTC and the 3.6-m TNG telescopes, MNRAS , 495, 2053 [Cited on pages 154, 156, 162, 163, 164, and 166.]

de León, J., Licandro, J., Serra-Ricart, M., et al. 2019, Interstellar Visitors: A Physical Characterization of Comet C/2019 Q4 (Borisov) with OSIRIS at the 10.4 m GTC, Research Notes of the American Astronomical Society, 3, 131 [Cited on page 164.]

de Pater, I. & Lissauer, J. J. 2015, Planetary Sciences [Cited on pages 4 and 29.]

de Sanctis, M. C., Capria, M. T., & Coradini, A. 2002, in ESA Special Publication, Vol. 500, Asteroids, Comets, and Meteors: ACM 2002, ed. B. Warmbein, 39–42 [Cited on page 20.]

Decock, A., Jehin, E., Hutsemékers, D., & Manfroid, J. 2013, Forbidden oxygen lines in comets at various heliocentric distances, A&A , 555, A34 [Cited on page 151.]

Decock, A., Jehin, E., Rousselot, P., et al. 2015, Forbidden oxygen lines at various nucleocentric distances in comets, A&A , 573, A1 [Cited on pages 148, 149, and 150.]

Dello Russo, N., Kawakita, H., Vervack, R. J., & Weaver, H. A. 2016, Emerging trends and a comet taxonomy based on the volatile chemistry measured in thirty comets with high-resolution infrared spectroscopy between 1997 and 2013, Icarus , 278, 301 [Cited on page 160.]

Delsemme, A. H. 1987, Galactic Tides Affect the Oort Cloud - an Observational Confirmation, A&A , 187, 913 [Cited on page 10.]

DiSanti, M. A., Bonev, B. P., Dello Russo, N., et al. 2021, Volatile Composition and Outgassing in C/2018 Y1 (Iwamoto): Extending Limits for High-resolution Infrared Cometary Spectroscopy between 2.8 and 5.0 μm, The Planet. Sci. J., 2, 225 [Cited on page 113.]

Dolan, J. F. & Tapia, S. 1986, Wavelength dependence of position angle in polarization standards., PASP, 98, 792 [Cited on page 55.]

Donati, G. B. 1866, Observations and Elements of the Comet of December 9, 1865, MNRAS , 26, 81 [Cited on page 2.]

Dones, L., Brasser, R., Kaib, N., & Rickman, H. 2015, Origin and Evolution of the Cometary Reservoirs, Space Sci. Rev., 197, 191 [Cited on page 15.]

Douglas, A. E. 1951, Laboratory Studies of the λ 4050 Group of Cometary Spectra., ApJ, 114, 466 [Cited on page 3.]

Ehlert, S., Moticska, N., & Egal, A. 2019, Dust Production of Comet 21P/Giacobini-Zinner throughout Its 2018 Apparition, AJ, 158, 7 [Cited on pages 99 and 100.]

Everhart, E. 1967a, Comet discoveries and observational selection, AJ, 72, 716 [Cited on page 27.]

Everhart, E. 1967b, Intrinsic distributions of cometary perihelia and magnitudes, AJ, 72, 1002 [Cited on page 27.]

Faggi, S., Lippi, M., Camarca, M., et al. 2021, The Extraordinary Passage of Comet C/2020 F3 NEOWISE: Evidence for Heterogeneous Chemical Inventory in Its Nucleus, AJ, 162, 178 [Cited on page 121.]

Farnham, T. L. 2009, Coma morphology of Jupiter-family comets, Planet. Space Sci., 57, 1192 [Cited on pages 61 and 76.]

Farnham, T. L., Knight, M. M., Schleicher, D. G., et al. 2021, Narrowband Observations of Comet 46P/Wirtanen during Its Exceptional Apparition of 2018/19. I. Apparent Rotation Period and Outbursts, The Planet. Sci. J., 2, 7 [Cited on pages 84 and 88.]

Farnham, T. L., Schleicher, D. G., & A'Hearn, M. F. 2000, The HB Narrowband Comet Filters: Standard Stars and Calibrations, Icarus , 147, 180 [Cited on pages 34, 48, 57, 58, 63, 69, 191, and 192.]

Festou, M. & Feldman, P. D. 1981, The forbidden oxygen lines in comets, A&A , 103, 154 [Cited on page 147.]

Festou, M. C., Rickman, H., & West, R. M. 1993, Comets, A&A Rev., 4, 363 [Cited on pages 2 and 3.]

Fink, U. 2009, A taxonomic survey of comet composition 1985-2004 using CCD spectroscopy, Icarus , 201, 311 [Cited on pages 4, 21, and 102.]

Fitzsimmons, A., Hainaut, O., Meech, K. J., et al. 2019, Detection of CN Gas in Interstellar Object 2I/Borisov, ApJ , 885, L9 [Cited on pages 153, 162, 163, and 166.]

Fouchard, M., Froeschlé, C., Matese, J. J., & Valsecchi, G. B. 2006, Comparison between different models of galactic tidal effects on cometary orbits, Celestial Mechanics and Dynamical Astronomy, 96, 341 [Cited on page 10.]

Fray, N., Bénilan, Y., Cottin, H., Gazeau, M. C., & Crovisier, J. 2005, The origin of the CN radical in comets: A review from observations and models, Planet. Space Sci., 53, 1243 [Cited on page 161.]

Ganesh, S., Joshi, U. C., & Baliyan, K. S. 2009, Optical polarimetry of Comet NEAT C/2001 Q4, Icarus , 201, 666 [Cited on page 23.]

Ganesh, S., Joshi, U. C., Baliyan, K. S., & Deshpand e, M. R. 1998, Polarimetric observations of the comet Hale-Bopp, A&AS , 129, 489 [Cited on page 23.]

Ganesh, S., Rai, A., Aravind, K., et al. 2020, in Society of Photo-Optical Instrumentation Engineers (SPIE) Conference Series, Vol. 11447, Society of Photo-Optical Instrumentation Engineers (SPIE) Conference Series, 114479E [Cited on page 40.]

Garcia, R. S., Gil-Hutton, R., & García-Migani, E. 2020, Observational results for five short-period and five long-period comets, Planet. Space Sci., 180, 104779 [Cited on pages 74 and 75.]

Gomes, R., Levison, H. F., Tsiganis, K., & Morbidelli, A. 2005, Origin of the cataclysmic Late Heavy Bombardment period of the terrestrial planets, Nature, 435, 466 [Cited on pages 13 and 14.]

Greenberg, J. M. 1998, Making a comet nucleus, A&A , 330, 375 [Cited on page 16.]

Gronkowski, P. & Smela, J. 1998, The cometary outbursts at large heliocentric distances, A&A , 338, 761 [Cited on page 20.]

Guzik, P., Drahus, M., Rusek, K., et al. 2020, Initial characterization of interstellar comet 2I/Borisov, Nature Astronomy, 4, 53 [Cited on pages 28 and 153.]

Halder, P. & Ganesh, S. 2021, Modelling heterogeneous dust particles: an application to cometary polarization, MNRAS , 501, 1766 [Cited on pages 24, 77, 78, and 128.]

Hasegawa, I. & Nakano, S. 2003, Orbit of periodic comet 153P/Ikeya-Zhang, MNRAS , 345, 883 [Cited on page 7.]

Haser, L. 1957, Distribution d'intensité dans la tête d'une comète, Bulletin de la Societe Royale des Sciences de Liege, 43, 740 [Cited on page 193.]

Heisler, J. & Tremaine, S. 1986, The influence of the Galactic tidal field on the Oort comet cloud, Icarus , 65, 13 [Cited on page 10.]

Henning, T. & Weidlich, U. 1988, Temperature of Cometary Dust, Earth Moon and Planets, 41, 197 [Cited on page 168.]

Hills, J. G. 1981, Comet showers and the steady-state infall of comets from the Oort cloud., AJ, 86, 1730 [Cited on page 10.]

Holmberg, J., Flynn, C., & Portinari, L. 2006, The colours of the Sun, MNRAS , 367, 449 [Cited on page 163.]

Horner, J., Evans, N. W., & Bailey, M. E. 2004, Simulations of the population of Centaurs - I. The bulk statistics, MNRAS , 354, 798 [Cited on page 12.]

Huggins, W. 1868, Spectrum Analysis of Comet II. 1868., Astronomical register, 6, 169 [Cited on page 2.]

Hui, M.-T., Tholen, D. J., Kracht, R., et al. 2022, The Lingering Death of Periodic Near-Sun Comet 323P/SOHO, AJ, 164, 1 [Cited on page 117.]

Hui, M.-T. & Ye, Q.-Z. 2020, Observations of Disintegrating Long-period Comet C/2019 Y4 (ATLAS): A Sibling of C/1844 Y1 (Great Comet), AJ, 160, 91 [Cited on page 117.]

Hui, M.-T., Ye, Q.-Z., Föhring, D., Hung, D., & Tholen, D. J. 2020, Physical Characterization of Interstellar Comet 2I/2019 Q4 (Borisov), AJ, 160, 92 [Cited on pages 164, 166, and 167.]

Ivanova, O., Agapitov, O., Odstrcil, D., et al. 2019a, Dynamics of the CO^+ coma of comet 29P/Schwasmann-Wachmann 1, MNRAS , 486, 5614 [Cited on page 109.]

Ivanova, O., Luk'yanyk, I., Kolokolova, L., et al. 2019b, Photometry, spectroscopy, and polarimetry of distant comet C/2014 A4 (SONEAR), A&A , 626, A26 [Cited on pages 31 and 61.]

Ivanova, O., Luk'yanyk, I., Tomko, D., & Moiseev, A. 2021a, Photometry and long-slit spectroscopy of the split comet C/2019 Y4 (ATLAS), MNRAS , 507, 5376 [Cited on page 47.]

Ivanova, O., Luk'yanyk, I., Tomko, D., & Moiseev, A. 2021b, Photometry and long-slit spectroscopy of the split comet C/2019 Y4 (ATLAS), MNRAS , 507, 5376 [Cited on page 117.]

Ivanova, O., Rosenbush, V., Afanasiev, V., & Kiselev, N. 2017, Polarimetry, photometry, and spectroscopy of comet C/2009 P1 (Garradd), Icarus , 284, 167 [Cited on pages 31 and 61.]

Ivanova, O., Rosenbush, V., Luk'yanyk, I., et al. 2021c, Observations of distant comet C/2011 KP36 (Spacewatch): photometry, spectroscopy, and polarimetry, A&A , 651, A29 [Cited on pages 31 and 61.]

Ivanova, O. V., Luk'yanyk, I. V., Kiselev, N. N., et al. 2016, Photometric and spectroscopic analysis of Comet 29P/Schwassmann-Wachmann 1 activity, Planet. Space Sci., 121, 10 [Cited on pages 109 and 110.]

Ivanova, O. V., Skorov, Y. V., Korsun, P. P., Afanasiev, V. L., & Blum, J. 2011, Observations of the long-lasting activity of the distant Comets 29P Schwassmann-Wachmann 1, C/2003 WT42 (LINEAR) and C/2002 VQ94 (LINEAR), Icarus , 211, 559 [Cited on pages 20 and 109.]

Jehin, E., Moulane, Y., & Manfroid, J. 2021a, TRAPPIST C/2021 A1 (Leonard) comet production rates, The Astronomer's Telegram, 15128, 1 [Cited on page 126.]

Jehin, E., Moulane, Y., Manfroid, J., et al. 2021b, TRAPPIST comet production rates: 6P/d'Arrest, 67P/C-G, 4P/Faye, 19P/Borrelly, 57P/D-N-D, The Astronomer's Telegram, 15117, 1 [Cited on pages 98 and 102.]

Jehin, E., Moulane, Y., Manfroid, J., et al. 2022a, Outburst of comet C/2021 A1 (Leonard) on January 7, 2021, The Astronomer's Telegram, 15189, 1 [Cited on pages 125 and 126.]

Jehin, E., Moulane, Y., Manfroid, J., et al. 2022b, TRAPPIST comet production rates: 19P/Borrelly, 67P/C-G, 104P/Kowal 2, C/2019 L3 (ATLAS), and C/2021 A1 (Leonard), The Astronomer's Telegram, 15186, 1 [Cited on pages 102, 114, and 126.]

Jehin, E., Moulane, Y., Manfroid, J., et al. 2020a, TRAPPIST comet production rates: 88/Howell, C/2020 M3 (ATLAS), C/2020 S3 (Erasmus), 156P/Russell-LINEAR, The Astronomer's Telegram, 14174, 1 [Cited on pages 62, 104, and 124.]

Jehin, E., Moulane, Y., Manfroid, J., Pozuelos, F., & Hutsemekers, D. 2020b, TRAPPIST comet production rates: 88/Howell, C/2020 M3 (ATLAS), C/2020 S3 (Erasmus), 156P/Russell-LINEAR, The Astronomer's Telegram, 14101, 1 [Cited on pages 62, 74, 104, 124, and 126.]

Jewitt, D. 2009, The Active Centaurs, AJ, 137, 4296 [Cited on page 19.]

Jewitt, D. 2015, Color Systematics of Comets and Related Bodies, AJ, 150, 201 [Cited on pages 100, 126, and 164.]

Jewitt, D., Chizmadia, L., Grimm, R., & Prialnik, D. 2007, in Protostars and Planets V, ed. B. Reipurth, D. Jewitt, & K. Keil, 863 [Cited on page 19.]

Jewitt, D., Hsieh, H., & Agarwal, J. 2015, The Active Asteroids (University of Arizona Press), 221–241 [Cited on page 168.]

Jewitt, D., Hui, M.-T., Kim, Y., et al. 2020a, The Nucleus of Interstellar Comet 2I/Borisov, ApJ , 888, L23 [Cited on page 168.]

Jewitt, D., Hui, M.-T., Mutchler, M., et al. 2017a, A Comet Active Beyond the Crystallization Zone, ApJ , 847, L19 [Cited on page 20.]

Jewitt, D., Kim, Y., Mutchler, M., et al. 2021, Cometary Activity Begins at Kuiper Belt Distances: Evidence from C/2017 K2, AJ, 161, 188 [Cited on page 20.]

Jewitt, D., Kim, Y., Mutchler, M., et al. 2020b, Outburst and Splitting of Interstellar Comet 2I/Borisov, ApJ , 896, L39 [Cited on page 168.]

Jewitt, D. & Luu, J. 1997, in Astronomical Society of the Pacific Conference Series, Vol. 122, From Stardust to Planetesimals, ed. Y. J. Pendleton, 335 [Cited on page 12.]

Jewitt, D. & Luu, J. 2019, Initial Characterization of Interstellar Comet 2I/2019 Q4 (Borisov), ApJ , 886, L29 [Cited on pages 163, 166, 167, and 168.]

Jewitt, D., Luu, J., Rajagopal, J., et al. 2017b, Interstellar Interloper 1I/2017 U1: Observations from the NOT and WIYN Telescopes, ApJ , 850, L36 [Cited on pages 28 and 163.]

Jin, L., Arnett, W. D., Sui, N., & Wang, X. 2008, An Interpretation of the Anomalously Low Mass of Mars, ApJ , 674, L105 [Cited on page 13.]

Jones, G. H., Snodgrass, C., & Tubiana, C. 2022, in LPI Contributions, Vol. 2678, LPI Contributions, 2943 [Cited on page 179.]

Jorda, L., Crovisier, J., & Green, D. W. E. 2008, in Asteroids, Comets, Meteors 2008, Vol. 1405, 8046 [Cited on page 168.]

Jordi, K., Grebel, E. K., & Ammon, K. 2006, Empirical color transformations between SDSS photometry and other photometric systems, A&A , 460, 339 [Cited on page 164.]

Joshi, U. C., Baliyan, K. S., Ganesh, S., et al. 1997, A polarization study of comet Hyakutake (C/1996 B2)., A&A , 319, 694 [Cited on page 23.]

Joshi, U. C., Sen, A. K., Deshpande, M. R., & Chauhan, J. S. 1992, Photopolarimetric studies of Comet Austin, Journal of Astrophysics and Astronomy, 13, 267 [Cited on page 23.]

Kareta, T., Andrews, J., Noonan, J. W., et al. 2020, Carbon Chain Depletion of 2I/Borisov, ApJ , 889, L38 [Cited on pages 154, 156, 162, 163, and 164.]

Kawakita, H., Jehin, E., Manfroid, J., & Hutsemékers, D. 2007, Nuclear spin temperature of ammonia in Comet 9P/Tempel 1 before and after the Deep Impact event, Icarus , 187, 272 [Cited on page 146.]

Kawakita, H., Watanabe, J.-i., Furusho, R., et al. 2004, Spin Temperatures of Ammonia and Water Molecules in Comets, ApJ, 601, 1152 [Cited on pages 145 and 146.]

Kelley, M. S., Fernández, Y. R., Licandro, J., et al. 2013, The persistent activity of Jupiter-family comets at 3-7 AU, Icarus , 225, 475 [Cited on page 107.]

Kelley, M. S. P., Bodewits, D., & Y, Q. 2019a, Small outburst of comet 260P/McNaught, The Astronomer's Telegram, 13174, 1 [Cited on page 105.]

Kelley, M. S. P., Farnham, T. L., Li, J.-Y., et al. 2021, Six Outbursts of Comet 46P/Wirtanen, The Planet. Sci. J., 2, 131 [Cited on pages 84 and 88.]

Kelley, M. S. P., Lister, T., & Bodewits, D. 2019b, Small Apparent Outburst of Comet 123P/West-Hartley, The Astronomer's Telegram, 12380, 1 [Cited on page 106.]

Khandelwal, A., Chaturvedi, P., Chakraborty, A., et al. 2022, Discovery of an inflated hot Jupiter around a slightly evolved star TOI-1789, MNRAS , 509, 3339 [Cited on page 25.]

Kidger, M. R. 2004, Dust production and coma morphology of 67P/Churyumov-Gerasimenko during the 2002/2003 apparition. II. A comparative study of dust production in 46P/Wirtanen and 67P/Churyumov-Gerasimenko during their 2002/2003 apparition, A&A , 420, 389 [Cited on page 84.]

Kiefer, F., Lecavelier des Étangs, A., Vidal-Madjar, A., et al. 2017, Detection of a repeated transit signature in the light curve of the enigma star KIC 8462852: A possible 928-day period, A&A , 608, A132 [Cited on page 26.]

Kim, Y., Jewitt, D., Mutchler, M., et al. 2020, Coma Anisotropy and the Rotation Pole of Interstellar Comet 2I/Borisov, ApJ , 895, L34 [Cited on pages 161 and 168.]

Kiselev, N., Shubina, E., Velichko, S., et al. 2017, Compilation of Comet Polarimetry from Published and Unpublished Sources, NASA Planetary Data System [Cited on page 24.]

Kiselev, N. N. & Chernova, G. P. 1978, Polarization of the radiation of comet West, 1975n, Soviet Ast., 22, 607 [Cited on page 23.]

Kiselev, N. N. & Chernova, G. P. 1981, Phase functions of polarization and brightness and the nature of cometary atmosphere particles, Icarus , 48, 473 [Cited on page 23.]

Knight, M. M., Schleicher, D. G., & Farnham, T. L. 2021, Narrowband Observations of Comet 46P/Wirtanen during Its Exceptional Apparition of 2018/19. II. Photometry, Jet Morphology, and Modeling Results, The Planet. Sci. J., 2, 104 [Cited on pages 84, 89, and 90.]

Kolokolova, L., Hanner, M. S., Levasseur-Regourd, A. C., & Gustafson, B. Å. S. 2004, in Comets II, ed. M. C. Festou, H. U. Keller, & H. A. Weaver, 577 [Cited on page 23.]

Korsun, P. P., Ivanova, O. V., & Afanasiev, V. L. 2008, C/2002 VQ94 (LINEAR) and 29P/Schwassmann-Wachmann 1 — CO^+ and N^+_2 rich comets, Icarus , 198, 465 [Cited on page 109.]

Kresak, L. 1992, Are there any comets coming from interstellar space?, A&A , 259, 682 [Cited on page 26.]

Krishna Swamy, K. S. 1979, Intensities of A-X and B-X bands of Co and CO^+ in comets., ApJ, 227, 1082 [Cited on page 109.]

Krishnakumar, A., Angchuk, D., Venkataramani, K., et al. 2020, CN, C2, C3 production rates of Comet C/2020 F3 (NEOWISE) as observed from Himalayan Chandra Telescope, Hanle, India, The Astronomer's Telegram, 13897, 1 [Cited on page 121.]

Kulyk, I., Korsun, P., Rousselot, P., Afanasiev, V., & Ivanova, O. 2016, P/2008 CL94 (Lemmon) and P/2011 S1 (Gibbs): comet-like activity at large heliocentric distances, Icarus , 271, 314 [Cited on page 19.]

Kupperman, D. G., Paxton, L. J., Carbary, J., et al. 1998, On the sodium tail of comet Hale-Bopp (C/1995 O1), Geophys. Res. Lett., 25, 3261 [Cited on page 19.]

Kurucz, R. L., Furenlid, I., Brault, J., & Testerman, L. 1984, Solar flux atlas from 296 to 1300 nm [Cited on page 47.]

Lambert, D. L. & Danks, A. C. 1983, High-resolution spectra of C2 Swan bands from comet West 1976 VI, ApJ, 268, 428 [Cited on page 133.]

Landolt, A. U. 1992, UBVRI Photometric Standard Stars in the Magnitude Range $11.5 < V < 16.0$ Around the Celestial Equator, AJ, 104, 340 [Cited on pages 52 and 65.]

Langland-Shula, L. E. & Smith, G. H. 2011, Comet classification with new methods for gas and dust spectroscopy, Icarus , 213, 280 [Cited on pages 4, 21, 48, 84, 98, 159, 172, 175, 193, and 194.]

Lara, L. M., Licandro, J., Oscoz, A., & Motta, V. 2003, Behaviour of Comet 21P/Giacobini-Zinner during the 1998 perihelion, A&A , 399, 763 [Cited on page 99.]

Lara, L. M., Tozzi, G. P., Boehnhardt, H., DiMartino, M., & Schulz, R. 2004, Gas and dust in Comet C/2000 WM1 during its closest approach to Earth: Optical imaging and long-slit spectroscopy, A&A , 422, 717 [Cited on page 74.]

Larson, S. M. & Slaughter, C. D. 1992, in Asteroids, Comets, Meteors 1991, ed. A. W. Harris & E. Bowell, 337 [Cited on page 75.]

Lecavelier Des Etangs, A., Vidal-Madjar, A., & Ferlet, R. 1999, Photometric stellar variation due to extra-solar comets, A&A , 343, 916 [Cited on page 25.]

Lee, S. & Pak, S. 2006, Flux Calibration Method of Slit Spectrometer of Extended Sources, Journal of Korean Astronomical Society, 39, 151 [Cited on page 40.]

Levison, H. F. 1996, in Astronomical Society of the Pacific Conference Series, Vol. 107, Completing the Inventory of the Solar System, ed. T. Rettig & J. M. Hahn, 173–191 [Cited on pages 8 and 9.]

Levison, H. F., Dones, L., Chapman, C. R., et al. 2001a, Could the Lunar "Late Heavy Bombardment" Have Been Triggered by the Formation of Uranus and Neptune?, Icarus , 151, 286 [Cited on page 13.]

Levison, H. F., Dones, L., & Duncan, M. J. 2001b, The Origin of Halley-Type Comets: Probing the Inner Oort Cloud, AJ, 121, 2253 [Cited on pages 10 and 11.]

Levison, H. F. & Duncan, M. J. 1997a, From the Kuiper Belt to Jupiter-Family Comets: The Spatial Distribution of Ecliptic Comets, Icarus , 127, 13 [Cited on pages 11 and 12.]

Levison, H. F. & Duncan, M. J. 1997b, From the Kuiper Belt to Jupiter-Family Comets: The Spatial Distribution of Ecliptic Comets, Icarus , 127, 13 [Cited on page 61.]

Levison, H. F. & Morbidelli, A. 2003a, The formation of the Kuiper belt by the outward transport of bodies during Neptune's migration, Nature, 426, 419 [Cited on page 12.]

Levison, H. F. & Morbidelli, A. 2003b, The formation of the Kuiper belt by the outward transport of bodies during Neptune's migration, Nature, 426, 419 [Cited on page 12.]

Licandro, J., Popescu, M., de León, J., et al. 2018, The visible and near-infrared spectra of asteroids in cometary orbits, A&A , 618, A170 [Cited on page 164.]

Lin, D. N. C. & Papaloizou, J. 1986, On the Tidal Interaction between Protoplanets and the Protoplanetary Disk. III. Orbital Migration of Protoplanets, ApJ, 309, 846 [Cited on page 15.]

Lin, H. W., Lee, C.-H., Gerdes, D. W., et al. 2020a, Detection of Diatomic Carbon in 2I/Borisov, ApJ , 889, L30 [Cited on pages 154, 156, 158, 162, 163, and 164.]

Lin, Z.-Y., Kelley, M. S. P., & Ip, W.-H. 2021, An outburst of Comet 4P/Faye, The Astronomer's Telegram, 14967, 1 [Cited on page 98.]

Lin, Z.-Y., Wang, C., Ip, W.-H., et al. 2020b, The Sodium Emission of comet C/2020 F3 (NEOWISE) observed at KenTing and Lulin observatory, The Astronomer's Telegram, 13886, 1 [Cited on pages 19 and 178.]

Lutz, B. L., Womack, M., & Wagner, R. M. 1993, Ion Abundances and Implications for Photochemistry in Comets Halley (1986 III) and Bradfield (1987 XXIX), ApJ, 407, 402 [Cited on pages 109, 177, and 178.]

Luu, J., Marsden, B. G., Jewitt, D., et al. 1997, A new dynamical class of object in the outer Solar System, Nature, 387, 573 [Cited on page 12.]

Lyttleton, R. A. 1951, On the structure of comets and the formation of tails, MNRAS , 111, 268 [Cited on page 3.]

Magnani, L. & A'Hearn, M. F. 1986, CO + Fluorescence in Comets, ApJ, 302, 477 [Cited on page 109.]

Manfroid, J., Jehin, E., Hutsemékers, D., et al. 2009, The CN isotopic ratios in comets, A&A , 503, 613 [Cited on page 138.]

Manzini, F., Ochner, P., Oldani, V., & Bedin, L. R. 2020, Concentric structures in the inner coma of comet C/2017 T2 (PANSTARRS), The Astronomer's Telegram, 13698, 1 [Cited on pages 84 and 92.]

Manzini, F., Oldani, V., Crippa, R., et al. 2014, Comet McNaught (260P/2012 K2): spin axis orientation and rotation period, Ap&SS, 351, 435 [Cited on page 105.]

Manzini, F., Oldani, V., Ochner, P., et al. 2021, Coma morphology and dust emission pattern of comet C/2020 F3 (NEOWISE), MNRAS , 506, 6195 [Cited on page 121.]

Marsden, B. G., Sekanina, Z., & Everhart, E. 1978, New osculating orbits for 110 comets and analysis of original orbits for 200 comets., AJ, 83, 64 [Cited on page 26.]

Marshall, D., Rezac, L., Hartogh, P., Zhao, Y., & Attree, N. 2019, Interpretation of heliocentric water production rates of comets, A&A , 623, A120 [Cited on page 73.]

Maslov, A. I. 2021, Polarization of comet C/2020 F3 (NEOWISE) in the red region of the spectrum, Astronomicheskij Tsirkulyar, 1648, 1 [Cited on page 121.]

Masset, F. & Snellgrove, M. 2001, Reversing type II migration: resonance trapping of a lighter giant protoplanet, MNRAS , 320, L55 [Cited on pages 13 and 15.]

Mazzotta Epifani, E. & Palumbo, P. 2011, The dust coma environment of the short period comets 32P/Comas Solá, 56P/Slaughter-Burnham, and 78P/Gehrels 2 from ground-based observations, A&A , 525, A62 [Cited on page 74.]

McGlynn, T. A. & Chapman, R. D. 1989, On the Nondetection of Extrasolar Comets, ApJ , 346, L105 [Cited on pages 26 and 27.]

McKay, A. J., DiSanti, M. A., Cochran, A. L., et al. 2021, Quantifying the Hypervolatile Abundances in Jupiter-family Comet 46P/Wirtanen, The Planet. Sci. J., 2, 21 [Cited on page 84.]

McKeegan, K. D., Aléon, J., Bradley, J., et al. 2006, Isotopic Compositions of Cometary Matter Returned by Stardust, Science, 314, 1724 [Cited on page 23.]

Meech, K. J., Kleyna, J. T., Hainaut, O., et al. 2017a, CO-driven Activity in Comet C/2017 K2 (PANSTARRS), ApJ , 849, L8 [Cited on pages 19 and 20.]

Meech, K. J., Pittichová, J., Bar-Nun, A., et al. 2009, Activity of comets at large heliocentric distances pre-perihelion, Icarus , 201, 719 [Cited on pages 19 and 20.]

Meech, K. J., Weryk, R., Micheli, M., et al. 2017b, A brief visit from a red and extremely elongated interstellar asteroid, Nature, 552, 378 [Cited on page 28.]

Micheli, M., Farnocchia, D., Meech, K. J., et al. 2018, Non-gravitational acceleration in the trajectory of 1I/2017 U1 ('Oumuamua), Nature, 559, 223 [Cited on page 28.]

Montmerle, T., Augereau, J.-C., Chaussidon, M., et al. 2006, From Suns to Life: A Chronological Approach to the History of Life on Earth 3. Solar System Formation and Early Evolution: the First 100 Million Years, Earth Moon and Planets, 98, 39 [Cited on page 13.]

Morbidelli, A. 2005, Origin and Dynamical Evolution of Comets and their Reservoirs, 35th Saas Fee course on "Trans-Neptunian Objects and Comets", arXiv e-prints, astro [Cited on pages 11, 12, and 15.]

Morbidelli, A. & Crida, A. 2007, The dynamics of Jupiter and Saturn in the gaseous protoplanetary disk, Icarus , 191, 158 [Cited on page 13.]

Morbidelli, A., Levison, H. F., Tsiganis, K., & Gomes, R. 2005, Chaotic capture of Jupiter's Trojan asteroids in the early Solar System, Nature, 435, 462 [Cited on page 13.]

Morbidelli, A., Tsiganis, K., Crida, A., Levison, H. F., & Gomes, R. 2007, Dynamics of the Giant Planets of the Solar System in the Gaseous Protoplanetary Disk and Their Relationship to the Current Orbital Architecture, AJ, 134, 1790 [Cited on pages 13 and 14.]

Morrison, N. D., Knauth, D. C., Mulliss, C. L., & Lee, W. 1997, High-Resolution Optical Spectra of the Head of the Comet C/1996 B2 (Hyakutake), PASP, 109, 676 [Cited on page 134.]

Moulane, Y., Jehin, E., José Pozuelos, F., et al. 2020a, in European Planetary Science Congress, EPSC2020–419 [Cited on pages 84, 92, 112, 113, and 117.]

Moulane, Y., Jehin, E., Rousselot, P., et al. 2020b, Photometry and high-resolution spectroscopy of comet 21P/Giacobini-Zinner during its 2018 apparition, A&A , 640, A54 [Cited on pages 99, 100, and 146.]

Mumma, M. J. & Charnley, S. B. 2011, The Chemical Composition of Comets—Emerging Taxonomies and Natal Heritage, ARA&A, 49, 471 [Cited on page 17.]

Mumma, M. J., Disanti, M. A., dello Russo, N., et al. 2002, in ESA Special Publication, Vol. 500, Asteroids, Comets, and Meteors: ACM 2002, ed. B. Warmbein, 753–762 [Cited on page 16.]

Mumma, M. J., McLean, I. S., DiSanti, M. A., et al. 2001, A Survey of Organic Volatile Species in Comet C/1999 H1 (Lee) Using NIRSPEC at the Keck Observatory, ApJ, 546, 1183 [Cited on page 17.]

Myers, R. V. 1985, Polarization of comets at small phase angles, Icarus , 63, 206 [Cited on page 23.]

Myers, R. V. & Nordsieck, K. H. 1984, Spectropolarimetry of comets Austin and Churyumov-Gerasimenko, Icarus, 58, 431 [Cited on page 78.]

Nesvorný, D., Vokrouhlický, D., Dones, L., et al. 2017, Origin and Evolution of Short-period Comets, ApJ, 845, 27 [Cited on pages 11 and 12.]

Noonan, J. W., Harris, W. M., Bromley, S., et al. 2021, FUV Observations of the Inner Coma of 46P/Wirtanen, The Planet. Sci. J., 2, 8 [Cited on page 84.]

Öhman, Y. 1939, On some observations made with a modified Pickering polarigraph, MNRAS , 99, 624 [Cited on page 23.]

Öhman, Y. 1941, Measurements of polarization in the spectra of comet Cunningham (1940 C) and comet Paraskevopoulos (1941 C), Stockholms Observatoriums Annaler, 13, 11.1 [Cited on page 23.]

Oort, J. H. 1950, The structure of the cloud of comets surrounding the Solar System and a hypothesis concerning its origin, Bull. Astron. Inst. Netherlands, 11, 91 [Cited on pages 3, 4, 10, and 26.]

Opitom, C., Fitzsimmons, A., Jehin, E., et al. 2019a, 2I/Borisov: A C_2-depleted interstellar comet, A&A , 631, L8 [Cited on pages 154, 156, 162, and 163.]

Opitom, C., Hutsemékers, D., Jehin, E., et al. 2019b, High resolution optical spectroscopy of the N_2-rich comet C/2016 R2 (PanSTARRS), A&A , 624, A64 [Cited on pages 19 and 109.]

Opitom, C., Jehin, E., Hutsemékers, D., et al. 2021, The similarity of the interstellar comet 2I/Borisov to Solar System comets from high-resolution optical spectroscopy, A&A , 650, L19 [Cited on page 134.]

Opitom, C., Snodgrass, C., Fitzsimmons, A., et al. 2017, Ground-based monitoring of comet 67P/Churyumov-Gerasimenko gas activity throughout the Rosetta mission, MNRAS , 469, S222 [Cited on pages 73 and 160.]

Osborn, W. H., A'Hearn, M. F., Carsenty, U., et al. 1990, Standard stars for photometry of comets, Icarus , 88, 228 [Cited on page 56.]

Pavlenko, Y., Shubina, O., Kulyk, I., et al. 2021, Exocometary Activity Around Stars at Different Evolutionary Stages: Current Issues, Kinematics and Physics of Celestial Bodies, 37, 64 [Cited on page 26.]

Picazzio, E., de Almeida, A., Andrievskii, S. M., Churyumov, K. I., & Luk'yanyk, I. V. 2002, in ESA Special Publication, Vol. 500, Asteroids, Comets, and Meteors: ACM 2002, ed. B. Warmbein, 713–716 [Cited on page 134.]

Picazzio, E., Luk'yanyk, I. V., Ivanova, O. V., et al. 2019, Comet 29P/Schwassmann-Wachmann 1 dust environment from photometric observation at the SOAR Telescope, Icarus , 319, 58 [Cited on pages 109 and 110.]

Pittichová, J., Woodward, C. E., Kelley, M. S., & Reach, W. T. 2008, Ground-Based Optical and Spitzer Infrared Imaging Observations of Comet 21P/GIACOBINI-ZINNER, AJ, 136, 1127 [Cited on page 99.]

Pollack, J. B., Hubickyj, O., Bodenheimer, P., et al. 1996, Formation of the Giant Planets by Concurrent Accretion of Solids and Gas, Icarus , 124, 62 [Cited on page 15.]

Prialnik, D. & Bar-Nun, A. 1992, Crystallization of amorphous ice as the cause of Comet P/Halley's outburst at 14 AU, A&A , 258, L9 [Cited on page 20.]

Protopapa, S., Kelley, M. S. P., Woodward, C. E., & Yang, B. 2021, Nondetection of Water-ice Grains in the Coma of Comet 46P/Wirtanen and Implications for Hyperactivity, The Planet. Sci. J., 2, 176 [Cited on page 84.]

Raghuram, S. & Bhardwaj, A. 2014, Photochemistry of atomic oxygen green and red-doublet emissions in comets at larger heliocentric distances, A&A , 566, A134 [Cited on page 148.]

Rappaport, S., Vanderburg, A., Jacobs, T., et al. 2018, Likely transiting exocomets detected by Kepler, MNRAS , 474, 1453 [Cited on page 26.]

Rebollido, I., Eiroa, C., Montesinos, B., et al. 2020, Exocomets: A spectroscopic survey, A&A , 639, A11 [Cited on page 26.]

Rickman, H. 2010, in Lecture Notes in Physics, Berlin Springer Verlag, ed. J. Souchay & R. Dvorak, Vol. 790, 341–399 [Cited on page 12.]

Rosenbush, V., Ivanova, O., Kleshchonok, V., et al. 2020, Comet 2P/Encke in apparitions of 2013 and 2017: I. Imaging photometry and long-slit spectroscopy, Icarus , 348, 113767 [Cited on page 194.]

Rosenbush, V., Kiselev, N., Husárik, M., et al. 2021a, Photometry and polarimetry of comet 46P/Wirtanen in the 2018 apparition, MNRAS , 503, 4297 [Cited on page 84.]

Rosenbush, V., Kiselev, N., Husárik, M., et al. 2021b, Photometry and polarimetry of comet 46P/Wirtanen in the 2018 apparition, MNRAS , 503, 4297 [Cited on page 90.]

Rosenbush, V. K., Ivanova, O. V., Kiselev, N. N., Kolokolova, L. O., & Afanasiev, V. L. 2017, Spatial variations of brightness, colour and polarization of dust in comet 67P/Churyumov-Gerasimenko, MNRAS , 469, S475 [Cited on pages 55, 71, 78, 79, and 102.]

Roth, N. X., Milam, S. N., Cordiner, M. A., et al. 2021, Rapidly Varying Anisotropic Methanol (CH_3OH) Production in the Inner Coma of Comet 46P/Wirtanen as Revealed by the ALMA Atacama Compact Array, The Planet. Sci. J., 2, 55 [Cited on pages 84 and 89.]

Samarasinha, N. H., Larson, S., & Beshore, E. 2006, in AAS/Division for Planetary Sciences Meeting Abstracts, Vol. 38, AAS/Division for Planetary Sciences Meeting Abstracts #38, 29.13 [Cited on page 75.]

Schleicher, D. G. 2010, The Fluorescence Efficiencies of the CN Violet Bands in Comets, AJ, 140, 973 [Cited on pages 157 and 193.]

Schleicher, D. G. 2022, Comet 21P/Giacobini-Zinner: Narrowband Photometry of the Prototype of Carbon-chain Depleted Comets at Multiple Apparitions, The Planet. Sci. J., 3, 143 [Cited on pages 99 and 100.]

Schleicher, D. G. & Bair, A. N. 2011, The Composition of the Interior of Comet 73P/Schwassmann-Wachmann 3: Results from Narrowband Photometry of Multiple Components, AJ, 141, 177 [Cited on pages 165 and 192.]

Schleicher, D. G. & Farnham, T. L. 2004, Photometry and imaging of the coma with narrowband filters, Comets II, 449 [Cited on page 75.]

Schleicher, D. G., Knight, M. M., & Skiff, B. A. 2020, in AAS/Division for Planetary Sciences Meeting Abstracts, Vol. 52, AAS/Division for Planetary Sciences Meeting Abstracts, 111.05 [Cited on pages 84, 104, and 121.]

Schmidt, G. D., Elston, R., & Lupie, O. L. 1992, The Hubble Space Telescope Northern-Hemisphere Grid of Stellar Polarimetric Standards, AJ, 104, 1563 [Cited on pages 54, 67, and 71.]

Schulz, R. 2005, A Target for Rosetta, Highlights of Astronomy, 13, 743 [Cited on page 84.]

Schwarz, G., Cosmovici, C., Mack, P., & Ip, W. 1989, Image processing techniques for gas morphology studies in the coma of Comet Halley, Advances in Space Research, 9, 217 [Cited on page 75.]

Schwarzschild, K. & Kron, E. 1911, On the Distribution of Brightness in the Tail of Halley's Comet, ApJ, 34, 342 [Cited on page 2.]

Sekanina, Z. 1976, A Probability of Encounter With Interstellar Comets and the Likelihood of Their Existence, Reports of Accomplishments of Planetology Programs, 1975-1976. [Cited on page 26.]

Sekanina, Z. 1987, in ESA Special Publication, Vol. 278, Diversity and Similarity of Comets, ed. E. J. Rolfe, B. Battrick, M. Ackerman, M. Scherer, & R. Reinhard, 315–322 [Cited on page 76.]

Sekanina, Z. & Chodas, P. W. 2012, Comet C/2011 W3 (Lovejoy): Orbit Determination, Outbursts, Disintegration of Nucleus, Dust-tail Morphology, and Relationship to New Cluster of Bright Sungrazers, ApJ, 757, 127 [Cited on page 117.]

Sekanina, Z. & Kracht, R. 2014, Disintegration of Comet C/2012 S1 (ISON) Shortly Before Perihelion: Evidence from Independent Data Sets, arXiv e-prints, arXiv:1404.5968 [Cited on page 117.]

Sekanina, Z. & Larson, S. M. 1984, Coma morphology and dust-emission pattern of periodic Comet Halley. II - Nucleus spin vector and modeling of major dust features in 1910, AJ, 89, 1408 [Cited on page 75.]

Seligman, D. Z., Rogers, L. A., Cabot, S. H. C., et al. 2022, The Volatile Carbon to Oxygen Ratio as a Tracer for the Formation Locations of Interstellar Comets, arXiv e-prints, arXiv:2204.13211 [Cited on page 12.]

Sen, A. K., Deshpande, M. R., Joshi, U. C., Rao, N. K., & Raveendran, A. V. 1991, Polarimetry of Comet P/Halley - Properties of dust, A&A , 242, 496 [Cited on page 23.]

Sen, A. K. & Rana, N. C. 1993, On the missing interstellar comets, A&A , 275, 298 [Cited on pages 27 and 153.]

Sharma, K., Kelley, M. S. P., Joharle, S., et al. 2021, Outbursts of Comet 67P/Churyumov-Gerasimenko, Research Notes of the American Astronomical Society, 5, 277 [Cited on page 102.]

Shinnaka, Y., Kawakita, H., Jehin, E., et al. 2016, Ortho-to-para abundance ratios of NH_2 in 26 comets: implications for the real meaning of OPRs, MNRAS , 462, S124 [Cited on page 145.]

Shinnaka, Y., Kawakita, H., & Tajitsu, A. 2020, High-resolution Optical Spectroscopic Observations of Comet 21P/Giacobini-Zinner in Its 2018 Apparition, AJ, 159, 203 [Cited on pages 99, 134, 145, and 146.]

Shustov, B., Sachkov, M., Gómez de Castro, A. I., et al. 2018, Comets in UV, Ap&SS, 363, 64 [Cited on pages 20 and 73.]

Smith, A. J., Anish Roshi, D., Manoharan, P., et al. 2021, Detection of OH 18 cm Emission from Comet C/2020 F3 NEOWISE Using the Arecibo Telescope, The Planet. Sci. J., 2, 123 [Cited on page 121.]

Sriram, S., Kumar, A., Surya, A., et al. 2018, in Society of Photo-Optical Instrumentation Engineers (SPIE) Conference Series, Vol. 10702, Ground-based and Airborne Instrumentation for Astronomy VII, ed. C. J. Evans, L. Simard, & H. Takami, 107026K [Cited on page 43.]

Stalin, C. S., Hegde, M., Sahu, D. K., et al. 2008, Night sky at the Indian Astronomical Observatory during 2000–2008, Bulletin of the Astronomical Society of India, 36, 111 [Cited on page 52.]

Stephens, D. C. & Noll, K. S. 2006, Detection of Six Trans-Neptunian Binaries with NICMOS: A High Fraction of Binaries in the Cold Classical Disk, AJ, 131, 1142 [Cited on page 11.]

Stern, S. A. 2003, The evolution of comets in the Oort cloud and Kuiper belt, Nature, 424, 639 [Cited on page 5.]

Stern, S. A. & Colwell, J. E. 1997, Collisional Erosion in the Primordial Edgeworth-Kuiper Belt and the Generation of the 30-50 AU Kuiper Gap, ApJ, 490, 879 [Cited on page 12.]

Stern, S. A. & Weissman, P. R. 2001, Rapid collisional evolution of comets during the formation of the Oort cloud, Nature, 409, 589 [Cited on page 10.]

Swamy, K. S. K. 2010, Physics of Comets (3rd Edition) [Cited on pages 19 and 133.]

Swan, W. 1857, Ueber die prismatischen Spectra der Flammen von Kohlenwasserstoffverbindungen, Annalen der Physik, 176, 306 [Cited on page 133.]

Swings, P. 1941, Complex structure of cometary bands tentatively ascribed to the contour of the solar spectrum, Lick observatory bulletin, 19, 131 [Cited on pages 2 and 138.]

Swings, P. 1942, Spectra of Comets, PASP, 54, 123 [Cited on page 3.]

Swings, P. 1943, The physical chemistry of comets, Popular Astronomy, 51, 412 [Cited on page 3.]

Swings, P., McKellar, A., & Minkowski, R. 1943, Cometary Emission Spectra in the Visual Region., ApJ, 98, 142 [Cited on page 3.]

Swings, P. & Struve, O. 1943, The Spectrum of Comet Whipple 2 (1942f), PASP, 55, 150 [Cited on page 3.]

Tancredi, G. & Rickman, H. 1992, in IAU Symposium, Vol. 152, Chaos, Resonance, and Collective Dynamical Phenomena in the Solar System, ed. S. Ferraz-Mello, 269 [Cited on page 61.]

Taylor, M. B. 2006, in Astronomical Society of the Pacific Conference Series, Vol. 351, Astronomical Data Analysis Software and Systems XV, ed. C. Gabriel, C. Arviset, D. Ponz, & S. Enrique, 666 [Cited on page 51.]

Tisserand, F. 1889, Mémoires et observations. Sur la théorie de la capture des comètes périodiques. [Suite et fin (^{1}).], Bulletin Astronomique, Serie I, 6, 289 [Cited on page 8.]

Tozzi, G. P., Boehnhardt, H., & Lo Curto, G. 2003, Imaging and spectroscopy of comet C/2001 Q4 (NEAT) at 8.6 AU from the Sun, A&A , 398, L41 [Cited on page 74.]

Tsiganis, K., Gomes, R., Morbidelli, A., & Levison, H. F. 2005, Origin of the orbital architecture of the giant planets of the Solar System, Nature, 435, 459 [Cited on pages 13 and 14.]

van der Helm, E. & Jeffers, S. V. 2012, Dynamical and collisional evolution of Halley-type comets, Icarus , 218, 448 [Cited on page 11.]

van Dokkum, P. G. 2001, Cosmic-Ray Rejection by Laplacian Edge Detection, PASP, 113, 1420 [Cited on page 44.]

Venkataramani, K. 2019, PhD thesis, Astronomy & Astrophysics Division, Physical Research Laboratory, Ahmedabad, India [Cited on pages 39 and 57.]

Venkataramani, K., Ganesh, S., & Baliyan, K. S. 2020, Ionic emissions in comet C/2016 R2 (Pan-STARRS), MNRAS , 495, 3559 [Cited on pages 19, 109, 119, and 120.]

Venkataramani, K., Ghetiya, S., Ganesh, S., et al. 2016, Optical spectroscopy of comet C/2014 Q2 (Lovejoy) from the Mount Abu Infrared Observatory, MNRAS , 463, 2137 [Cited on pages 20, 73, 120, and 193.]

Walsh, K. J., Morbidelli, A., Raymond, S. N., O'Brien, D. P., & Mandell, A. M. 2011, A low mass for Mars from Jupiter's early gas-driven migration, Nature, 475, 206 [Cited on pages 13 and 14.]

Wang, J. H. & Brasser, R. 2014, An Oort Cloud origin of the Halley-type comets, A&A , 563, A122 [Cited on pages 10 and 11.]

Weiler, M. 2012, The chemistry of C_3 and C_2 in cometary comae. I. Current models revisited, A&A , 538, A149 [Cited on page 3.]

Weissman, P. R. 1980, Stellar perturbations of the cometary cloud, Nature, 288, 242 [Cited on page 10.]

Weissman, P. R. 1983, Dynamical evolution of the Oort cometary cloud., Highlights of Astronomy, 6, 363 [Cited on page 27.]

Whipple, F. L. 1950, On tests of the icy conglomerate model for comets., AJ, 55, 83 [Cited on page 3.]

Whipple, F. L. 1978, Rotation period of comet Donati, Nature, 273, 134 [Cited on page 194.]

Willacy, K., Turner, N., Bonev, B., et al. 2022, Comets in context: Comparing comet compositions with protosolar nebula models, arXiv e-prints, arXiv:2204.07517 [Cited on page 28.]

Willmer, C. N. A. 2018, The Absolute Magnitude of the Sun in Several Filters, ApJS, 236, 47 [Cited on page 165.]

Womack, M., Sarid, G., & Wierzchos, K. 2017, CO in Distantly Active Comets, PASP, 129, 031001 [Cited on page 19.]

Wright, A. W. 1881a, Polariscopic observations of Comet C, 1881, American Journal of Science, 22, 372 [Cited on page 23.]

Wright, A. W. 1881b, The polarization of light from Comet B, 1881, American Journal of Science, 22, 142 [Cited on page 23.]

Wurm, K. 1939, On the Interpretation of the Spectra of Comets and Their Forms., The Astrophysical Journal, 89, 312 [Cited on page 3.]

Xing, Z., Bodewits, D., Noonan, J., & Bannister, M. T. 2020, Water Production Rates and Activity of Interstellar Comet 2I/Borisov, ApJ , 893, L48 [Cited on pages 161, 164, and 168.]

Yabushita, S. & Hasegawa, I. 1978, A note on the possible origin of comets in an interstellar gas cloud, MNRAS , 185, 549 [Cited on page 26.]

Yamamoto, T. 1981, On the photochemical formation of CN, C_2, and C_3 radicals in cometary comae, Moon and Planets, 24, 453 [Cited on pages 3 and 162.]

Ye, Q., Jewitt, D., Hui, M.-T., et al. 2021, Disintegration of Long-period Comet C/2019 Y4 (ATLAS). I. Hubble Space Telescope Observations, AJ, 162, 70 [Cited on page 117.]

Ye, Q. & Zhang, Q. 2020, Possible Disintegration of Comet C/2019 Y4 (ATLAS), The Astronomer's Telegram, 13620, 1 [Cited on page 117.]

Zhang, H. W., Zhao, G., & Hu, J. Y. 2001, A catalogue of emission lines in spectra of Comet C/1995 O1 (Hale-Bopp), A&A , 367, 1049 [Cited on page 134.]

Zhang, Q., Ye, Q., Farnham, T. L., & Holt, C. E. 2022, Disintegration of Near-Sun Comet C/2021 O3 (PANSTARRS), The Astronomer's Telegram, 15358, 1 [Cited on page 117.]

Zhang, Q., Ye, Q., Vissapragada, S., Knight, M. M., & Farnham, T. L. 2021, Preview of Comet C/2021 A1 (Leonard) and Its Encounter with Venus, AJ, 162, 194 [Cited on page 125.]

Zieba, S., Zwintz, K., Kenworthy, M. A., & Kennedy, G. M. 2019, Transiting exocomets detected in broadband light by TESS in the β Pictoris system, A&A , 625, L13 [Cited on page 26.]

Zubko, E., Videen, G., Hines, D. C., & Shkuratov, Y. 2016, The positive-polarization of cometary comae, Planet. Space Sci., 123, 63 [Cited on page 23.]

Zubko, E., Videen, G., Shkuratov, Y., & Hines, D. C. 2017, On the reflectance of dust in comets, J. Quant. Spec. Radiat. Transf., 202, 104 [Cited on page 166.]

Zubko, E., Zheltobryukhov, M., Chornaya, E., et al. 2020, Polarization of disintegrating Comet C/2019 Y4 (ATLAS), MNRAS , 497, 1536 [Cited on pages 23 and 128.]